Modern Raman Microscopy
Technique and Practice

Alexander Rzhevskii

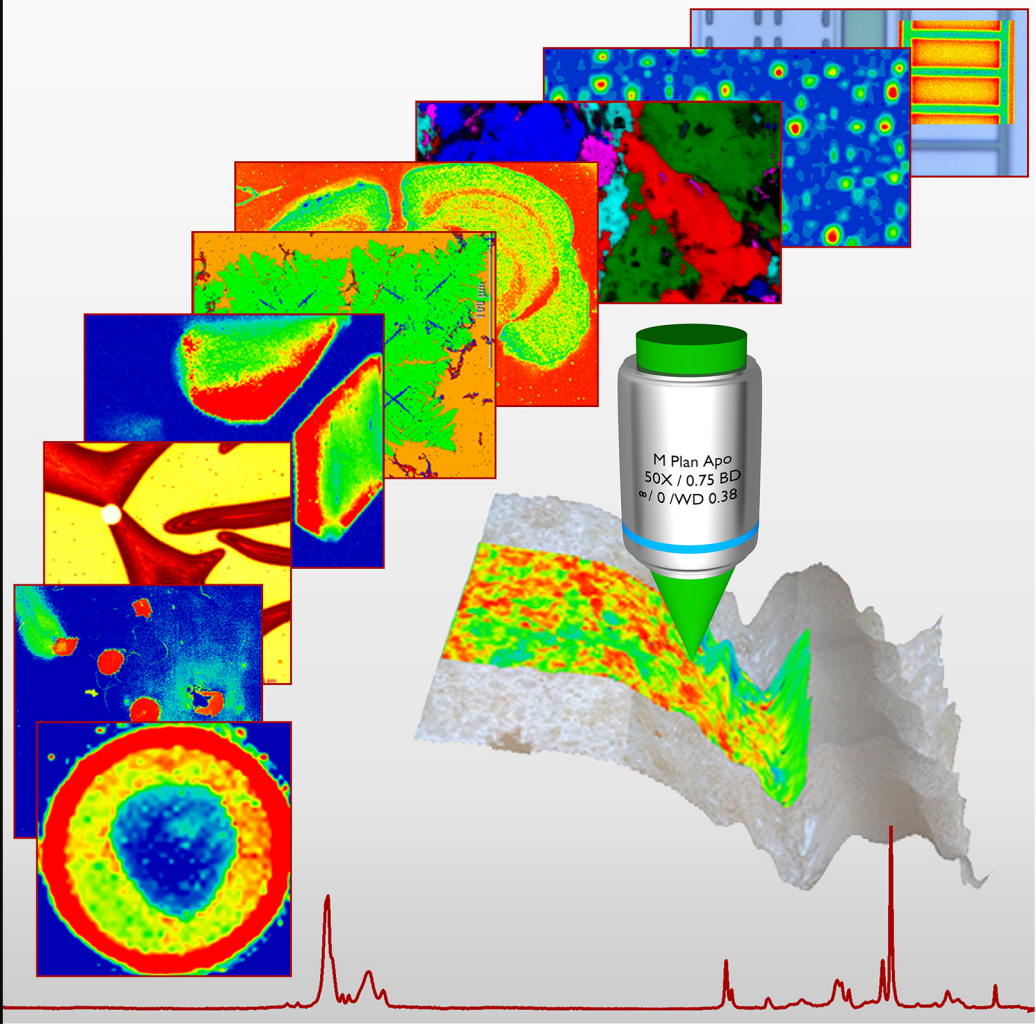

Modern Raman Microscopy

Modern Raman Microscopy:

Technique and Practice

By

Alexander Rzhevskii

Cambridge
Scholars
Publishing

Modern Raman Microscopy: Technique and Practice

By Alexander Rzhevskii

This book first published 2021

Cambridge Scholars Publishing

Lady Stephenson Library, Newcastle upon Tyne, NE6 2PA, UK

British Library Cataloguing in Publication Data
A catalogue record for this book is available from the British Library

ISBN (10): 1-5275-6784-2
ISBN (13): 978-1-5275-6784-9

Dedicated to Mechislav and Bronislav Rzhevskii

TABLE OF CONTENTS

PREFACE

In 1928, Sir C.V. Raman discovered the phenomenon of inelastic light scattering. The radiation scattered by molecules contains photons of the same frequency as the incident radiation, as well as photons with frequencies shifted with respect to that of the incident radiation. The frequency change was named the Raman effect after Sir Raman, and the phenomenon of scattering these photons is called Raman scattering. In 1928, Sir C.V. Raman was awarded the Nobel Prize for his discovery. The Raman effect formed the basis of a new method of vibrational spectroscopy and, by the end of the 1930s, Raman spectroscopy has become the experimental method for nondestructive chemical analysis.

IR spectroscopy surpassed Raman spectroscopy after World War II, when the development of sensitive IR detectors and advances in electronics made IR spectroscopy easier to use. Measurements using IR spectroscopy became routine, while Raman spectroscopy still required sophisticated equipment, skilled operators and a dark room.

With the development of lasers in the 1960s, interest in Raman spectroscopy rose again, but its application was mostly limited to research laboratories. Skilled operators were still required to collect simple spectra, and the process was rather labor intensive.

The subsequent progress in Raman instrumentation, such as the introduction of sensitive charge-coupled devices for detection of inelastically scattered light and holographic filters for the rejection of elastically scattered

(Rayleigh) radiation, marked the beginning of the renaissance of Raman spectroscopy as a routine laboratory technique.

Confocal optical microscopy, which was pioneered by Marvin Minsky in 1955, and the coupling of a Raman spectrometer with a conventional optical microscope, commercially realized as the Molecular Optical Laser Examiner (MOLE) in 1976, opened up a new era in confocal Raman microscopy. It provided nondestructive analysis of the interior of optically transparent and translucent objects, as well as novel materials and systems at the microscopic level.

Modern confocal Raman scanning microscopy, which allows one to acquire two-dimensional and three-dimensional spectrochemical images of samples, is a unique method not only due to the information obtained but also in terms of the technologies involved in this technique. Indeed, the experimental implementation of this technology combines methods of spectroscopy, optics, electronics, mechanics and microscopy. The power and diversity of this technology also allow it to be used for a wide range of applications: from cell biology, forensic science and analysis of works of art to material science and the study of substances in various states, as well as under external impacts in real time.

Today, confocal Raman microscopes are computer-driven instruments equipped with multiple laser excitation sources, precise sample scanning mechanisms, white light and Raman polarization capabilities, automatic alignment and calibration procedures. These advantages make the measurements of Raman spectra and the acquisition of spectrochemical images with a spatial resolution at the diffraction limit of light a routine procedure. Advanced algorithms for the processing of spectral data arrays

and the availability of a wide range of Raman spectral libraries facilitate the representation and interpretation of the results.

The purpose of this book is to familiarize a wide circle of experimenters with the fundamentals of the technique and practice of confocal Raman microscopy and imaging. The author has tried to present the theory of Raman spectroscopy, instrumentation, principles of operation and the main characteristics of confocal Raman microscopes in a thorough but accessible form. Examples of the application of Raman microscopy and imaging for some of the most frequently used applications are provided.

The first chapter of this book is devoted to the basics of vibrational spectroscopy. Although the main vibrational spectroscopy techniques, such as Raman and modern FTIR spectroscopies, are complementary, it is necessary to understand their benefits for the optimal choice of the spectral method when studying specific chemical compounds and samples.

The second chapter describes the main components of Raman microscopes and the basic principles of their operations. The importance of choosing the most optimal components and the proper configuration of Raman microscopes is emphasized in order to obtain the best possible experimental results for specific applications.

The third chapter provides the specifics of Raman microscopes' confocal design. It highlights the importance of maintaining these instruments in a technical condition that ensures their maximum performance and capabilities. A separate part of this chapter is devoted to the different manufacturers of commercial confocal Raman microscopes, listing the models of the instruments produced, their main characteristics and capabilities.

In the final, fourth chapter, some examples of applications of confocal Raman microscopy and imaging are given, which illustrate the possibilities of this technique for obtaining two- and three-dimensional spectrochemical images of “real world” objects in order to study their spatial structure, composition and properties.

This book is intended for a wide circle of experimenters from a diversity of disciplines, who are using or intending to use confocal Raman spectroscopy and imaging methods in their work. Since this book was written for experimenters with different backgrounds, the author did not provide an exhaustive bibliography on the topics discussed. References are given, as a rule, only to the results of research over the past 10–15 years where the problem was presented most fully (mainly reviews) and to some classical primary sources. The author hopes that this book will be beneficial for novice Raman microscopy users and serve as a reference resource for experienced spectroscopists.

ACKNOWLEDGEMENTS

I am grateful to Dr. Ellen Misseo for her kind assistance in writing this book and for her valuable remarks and corrections. I would also like to thank Vadim Pushkarchuk and Pavel Ermakovich for their inestimable help in creating illustrations for this book.

CHAPTER ONE

FUNDAMENTALS OF THE RAMAN EFFECT AND RAMAN SPECTROSCOPY

1.1. The sky is blue and the sunset is red due to light being scattered

The interaction of light, a form of electromagnetic radiation, with matter results in the reflection, absorption, transmission and scattering of light. In some cases, this interaction also results in photoluminescence, that is, the light emissions at longer wavelengths than that of the incident light. It is generally accepted that the phenomenon known as the molecular scattering of light was first considered and explained in the works of Lord Rayleigh, who, among other aspects of scattering theory, calculated the degree of light scattered by molecules of atmospheric dust-free gases. John William Strutt, the future famous physicist Lord Rayleigh, was challenged by James Clerk Maxwell to explain the blue colour of the sky; he addressed this issue from the viewpoint of the wave theory of light. According to Rayleigh, a light wave propagating in the atmosphere causes oscillations in air molecules followed by the emission of light waves. Each molecule is independent of other emitters of secondary waves, and to calculate the intensity of the scattered light, it is enough to sum up the secondary radiation of individual molecules. He found that the amount of the scattered light I was inversely proportional to the fourth power of wavelength λ of the light for the particles that were much smaller than the wavelength:

$$I \propto {}^{1}/_{\lambda^4}\,. \qquad (1.1)$$

We will be referring to this dependence, which was established by Rayleigh in 1871, through the text of this book, as it plays an important role in the spectroscopy of scattered light. Since the portion of the electromagnetic spectrum visible to the human eye occupies the wavelength range from about 400 (violet) to 800 (dark red) nanometers (nm), then, for example, the blue light of 450 nm is scattered more intensely than the red light of 670 nm by a factor of $(670/450)^4 \approx 5$. Thus, Rayleigh first successfully explained the blue colour of the sky—the blue colour has a shorter wavelength than the red and yellow, so the blue rays of the sunlight are scattered stronger. When we look overhead to the sky on a clear cloudless day, not directly to the sun, the sky appears to be blue because we observe the light scattered by the molecules in the atmosphere, and scattered light is mostly blue. When we look in the direction of the sun at the sunset or sunrise, we see red and orange colours because the light from the sun passes a long distance through the atmosphere and the blue light scatters out and away from the line of observation.

The scattering of light by molecules, which Rayleigh studied to explain the blue colour of the sky, occurs without changing the frequency of the light––the frequency of the scattered light is equal to the frequency of the incident. Such scattering is called elastic since the state of the molecule after scattering is the same as before. This is the dominant scattering of light by particles much smaller than the wavelength of the radiation, and this process is called Rayleigh scattering. The scattering occurs in all directions uniformly and can be extended to scattering from the particles up to about a tenth of the wavelength of light. Another type of elastic scattering, Mie

scattering, occurs from spherical particles with dimensions comparable to or slightly larger than the wavelength of the incident light. In this process, the scattered radiation does not depend much on the wavelength. This effect gives rise to the scattered white light seen in clouds, mist or fog, and the bright whiteness of snow.

In 1923, the Austrian physicist Adolf Smekal published a theoretical paper in which he gave a clear prediction of the phenomenon of inelastic scattering of photons of light by atoms and molecules (Smekal 1923). Smekal suggested that, as the result of scattering, shorter and longer wavelengths would appear in addition to the original wavelength of light. Smekal also assigned the frequency shift between the incident and scattered light to the energy difference between the two states of the molecule: before and after scattering. The Dutch, Hans Kramers, and the German, Werner Heisenberg, strengthened the prediction of Smekal in a more expanded form (Kramers and Heisenberg 1925), which was later followed by the quantum-mechanical descriptions proposed by English theoretical physicist Paul Dirac (Dirac and Fowler 1927).

According to quantum theory, atoms and molecules can only take on certain discrete values of energy E_0, E_1, etc. If an inelastic collision of a photon having an initial energy hv_0 (h is the Plank constant, v_0 is the electromagnetic frequency) with an unexcited molecule located at the lower energy level E_0 occurs, then the photon excites the molecule to a higher energy level E_1. After such a collision, the photon scatters away from the molecule with reduced energy (here, the "r" index denotes the word "red"):

$$hv_r = hv_0 - (E_1 - E_0) \, . \tag{1.2}$$

If an inelastic collision of a photon with an already excited molecule occurs, then the molecule may undergo a transition from the level E_1 to the level E_0, and the photon scatters with increased energy (the "*b*" index means "blue"):

$$h\nu_b = h\nu_0 + (E_1 - E_0) . \quad (1.3)$$

In the first case, a quantum of intramolecular energy is subtracted from the initial energy of the light photon and, in the second case, the addition of this quantum occurs. In the first case, the frequency of the scattered photon appears to be less than the frequency of the photon incident on the molecule:

$$\nu_r = \nu_0 - \frac{E_1 - E_0}{h}, \quad (1.4)$$

and in the second, it is greater:

$$\nu_b = \nu_0 + \frac{E_1 - E_0}{h}. \quad (1.5)$$

Thus, together with the frequency ν_0 that exists as the result of the elastic collisions of photons with molecules, the frequencies ν_r and ν_b should appear in the scattered light. Correspondingly, in the spectrum of scattered light, two spectral lines (satellites) symmetrically shifted with respect to the centre line with a frequency ν_0 should be anticipated. The red satellite ν_r arises at longer wavelengths (this is why it is called "red") as a result of the collisions of photons with molecules in a ground state, while the blue ν_b at shorter wavelengths (thus, "blue") is due to collisions with excited molecules.

French physicists J. Cabannes, P. Daure and Y. Rocard were the first to try to experimentally confirm the predictions of the theorists, but they failed to measure the light of low intensity in gases.

The effect of inelastic scattering in liquids and vapours was first experimentally discovered by Chandrasekhara Venkata Raman and Kariamanickam Srinivasa Krishnan and reported in March of 1928 in "Nature" (Raman and Krishnan 1928). In this first work, Raman and Krishnan used a simple yet elegant experimental setup in which sunlight was focused by a telescope on scattering materials, thoroughly purified liquids or dust-free gases, and the method of complementary light filters was applied to visually observe "a modified scattered radiation":

> "A blue-violet filter, when coupled with a yellow-green filter and placed in the incident light, completely extinguished the track of the light through liquid or vapour. The reappearance of the track when the yellow filter is transferred to a place between it and the observer's eye is proof of the existence of a modified scattered radiation" (Fig. 1-1).

Initially, Raman and Krishnan were looking for a new type of secondary radiation, as they assumed that there was an optical analogue to the Compton effect observed when X-rays are scattered by some materials. Nevertheless, they examined more than sixty common liquids and vapours and detected the modified scattered radiation with a changed frequency in each of the liquids to a greater or lesser degree.

In the same year, Russian physicists G.S. Landsberg and L.I. Mandelstam detected the phenomenon in crystals and published their work in a German-language journal "Die Naturwissenschaften" ("The Natural Sciences") in July (Landsberg and Mandelstam 1928). They used a spectroscopic method of detection: an intense beam of light from a mercury lamp passed through a quartz crystal, and the light scattered off the crystal at 90° angle to the incident beam was investigated using a spectrograph. It was found that, in all spectrograms, each spectral line of mercury was accompanied by a

clearly observed satellite with a slightly longer wavelength. Soon after, Cabannes and Daure (Cabannes and Daure 1928) confirmed the discovery made by Raman and Krishnan, while Rocard published the first theoretical explanation of the phenomenon (Rocard 1928).

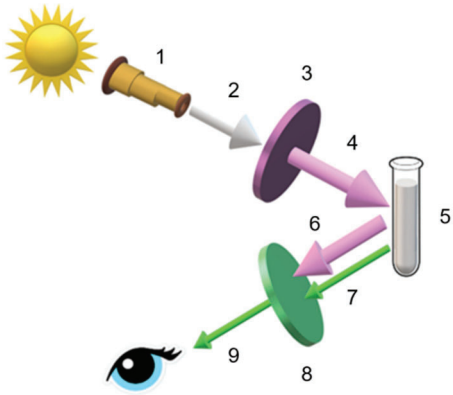

Figure 1-1. Sir Chandrasekhara Venkata Raman, the recipient of the Nobel Prize for Physics in 1930, and the schematic of his remarkable experiment described in "Nature": 1 – telescope, 2 – incident sunlight (white) as the excitation light, 3 – blue-violet filter, 4 – blue-violet light transmitted through the filter, 5 – sample, 6 – unmodified (elastically) scattered light, 7 – modified (inelastically) scattered light, 8 – yellow-green filter, 9 –modified (inelastically) scattered yellow-green light passed through the filter to the observer's eye.

It should be emphasized that all three groups of scientists from India, Russia and France, which investigated the phenomenon of molecular scattering of light, conducted their work entirely independently of each other.

Sir Chandrasekhara Venkata Raman was awarded the Nobel Prize for Physics in 1930 for his remarkable experimental discovery and proof of the universal character of this effect by investigating a large number of solids

and liquids, and the first publication of a spectrum of scattered light with changing frequencies. Raman scattering is named after him.

The intriguing history of this discovery, the Nobel Prize nomination and the award decision that underlined the importance of prompt research publications, relations and communications in the scientific community, with vast references to the original publications may be found elsewhere (Fabelinskii 1998, Singh and Reiss 2001, Singh 2018).

In 2028, the scientific community and the researchers dealing with molecular spectroscopy throughout the world will be celebrating the 100th anniversary of the outstanding discovery of the Raman effect. The author hopes that this book will still be available and useful at that time.

1.1.1. Fundamentals of Raman scattering

Historically, Raman scattering has been approached both in terms of classical electromagnetic and quantum-mechanical theories. In the classical approach, light is treated as an electromagnetic wave that propagates through and interacts with a matter. In turn, the matter is considered as consisting of atoms or molecules representing an assembly of independent harmonic oscillators. As is known, a molecule consists of positively charged nuclei surrounded by a negatively charged cloud of electrons. Although the total charge on a molecule is zero, positive and negative charges often do not entirely overlap. The molecules with these charges separated by small distances have a permanent dipole moment.

In this chapter, the GaussView 6 software package was used to visualise electrostatic potential maps of small molecules, such as diatomic O_2, triatomic CO_2 and H_2O. The full geometry optimization of the electrostatic

potential of the molecules with and without an external electric field, as well as the dipole moment and the polarizability changes during the molecular vibrations were performed using the Gaussian 16 computational chemistry software package (Gaussian n.d.). All calculations (Pushkarchuk 2019) were carried out using Density Functional Theory (DFT). Becke's three-parameter exchange functional in combination with the Lee-Yang-Parr correlation functional (B3LYP) and 6-31+G(3d) basis set were used (DFT/B3LYP/6-31+G(3d) level of the theory).

Consider a homonuclear diatomic molecule in an oscillating electric field, as shown in Figure 1-2.

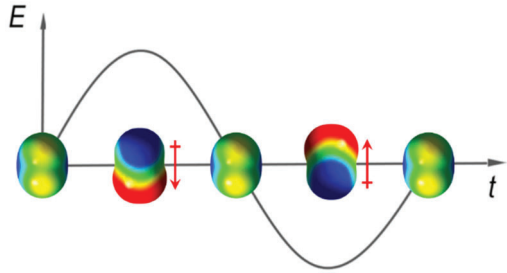

Figure 1-2. Interaction of the electric field E of the light wave with a homonuclear diatomic molecule. The perturbation of the electron cloud with time t results in a periodic separation of the centres of positive and negative charges within the molecule, which creates an induced dipole moment indicated by red vertical arrows.

The homonuclear diatomic molecule has no permanent dipole moment μ and, in the absence of an external electric field or when the amplitude of the electric field is equal to zero, the centre of the negative charge of the electron cloud coincides with the centre of the positively charged nuclei. The electric field of the light wave E oscillates with time t as a cosine function

$$E = E_0 \cos(2\pi \nu_0 t) , \tag{1.6}$$

where E_0 is the magnitude of the electric field and ν_0 is the frequency of the light wave in Hz ($\nu = c/\lambda$, where c is the speed, and λ is the wavelength of light). The oscillating electric field perturbs the cloud of electrons surrounding the nuclei and displaces the centre of the electron cloud relative to the centre of the nuclei. The high and low electron density distribution is shown in red and blue, respectively. The displacement results in an induced dipole moment. In the literature, it is sometimes referred to as induced polarization and, to distinguish it from the permanent dipole moment usually indicated by μ, it is denoted as p:

$$p = \alpha E , \tag{1.7}$$

where α is the polarizability of the molecule. As follows from the equations (1.6) and (1.7), the oscillation of the induced dipole moment p occurs with the frequency ν_0 of the light wave:

$$p = \alpha E_0 \cos(2\pi \nu_0 t) . \tag{1.8}$$

The polarizability α of the molecule is an important parameter in the classical theoretical consideration of the Raman effect. The polarizability can be described as a measure of deformability of the electron cloud in the molecule or, in other words, how easily the electron cloud can be distorted by the electric field of light interacting with the molecule. The polarizability α is not constant because the vibrations of atoms in the molecule can cause it to alter. During the vibration, the diatomic molecule is being consecutively compressed and extended. The configuration of the electron cloud is not the same at the two extremes of the vibration, so a change in polarizability occurs. However, the change happens at the frequency of

molecular vibrations ν_{vib}, which is much lower than the frequency of the light wave ν_0. If the molecule is vibrating as a harmonic oscillator with a frequency ν_{vib}, then the displacement of nuclei q relative to an equilibrium position is given by the similar cosine function:

$$q = q_0 \cos(2\pi \nu_{vib} t)\,, \tag{1.9}$$

where q_0 is the amplitude of vibration. For a diatomic molecule, such as O_2, N_2 and H_2, the displacement is about 10% of the distance between the nuclei at their equilibrium position. For such small displacements, the polarizability of the diatomic molecule can be described as a linear function of the displacement q. It can be expanded as a Taylor series around its equilibrium position $q = 0$ in which the higher-order terms can be neglected:

$$\alpha = \alpha_0 + \left(\frac{\partial \alpha}{\partial q}\right)_0 q + \cdots, \tag{1.10}$$

where α_0 is the polarizability at the equilibrium position of the nuclei and the derivative $(\partial\alpha/\partial q)_0$ is the rate of change of the polarizability α upon the displacement of nuclei q from the equilibrium position $q=0$. Figure 1-3 illustrates the polarizability of a diatomic molecule during its vibration. For clarity, the displacement of nuclei from their equilibrium position defined by the bond length l in the compressed (l-q_0) and the extended (l+q_0) states is exaggerated. When the molecule is compressed, the electron cloud is imagined as mostly localized around the nuclei (the high and the low electron densities are close to each other) and therefore cannot be much distorted by an external electric field E. In contrast, when the molecule is expanded, the electron cloud appears to be delocalized (the high and the low electron densities are much further apart) and can thus be more readily

displaced by the electric field. Consequently, polarizability increases as the distance between the nuclei (bond length) elongates.

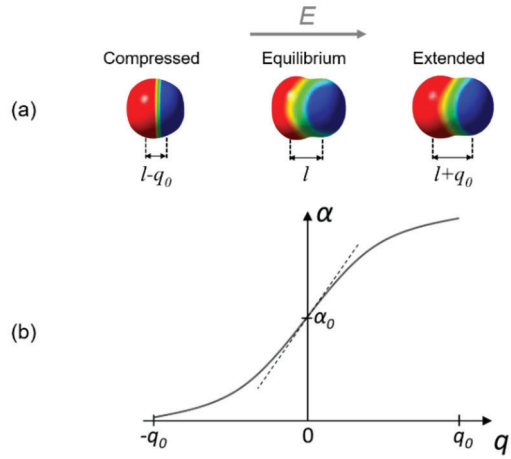

Figure 1-3. Polarizability of a diatomic molecule in an external electrical field E during its vibration. (a) The change of the electron density distribution: the high and the low electron density are shown in red and blue, respectively. (b) The graph representing the polarizability α as a function of displacement q (solid curve) and the derivative of polarizability $(\partial\alpha/\partial q)_0$ near the equilibrium position (dotted line).

Combining (1.8) through (1.10), and taking into account the known trigonometric equation $cos(2\pi\nu_0 t)cos(2\pi\nu_{vib}t) = 1/2cos[2\pi(\nu_0+\nu_{vib})]+1/2cos[2\pi(\nu_0-\nu_{vib})]$, the expression for the oscillating induced dipole moment takes the following form:

$$p = \alpha E_0 \cos(2\pi\,\nu_0 t) = \alpha_0 E_0 \cos(2\pi\,\nu_0 t) + \left(\frac{\partial\alpha}{\partial q}\right)_0 q E_0 \cos(2\pi\,\nu_0 t) = \tag{1.11}$$

$$= \alpha_0 E_0 \cos(2\pi\, \nu_0 t) +$$

$$\left(\frac{\partial \alpha}{\partial q}\right)_0 q_0 E_0 \cos(2\pi\, \nu_0 t) \cos(2\pi\, \nu_{vib} t) =$$

$$= \alpha_0 E_0 \cos(2\pi\, \nu_0 t) + \frac{1}{2}\left(\frac{\partial \alpha}{\partial q}\right)_0 q_0 E_0 \cos[2\pi\, (\nu_0 + \nu_{vib}) t] +$$

$$\frac{1}{2}\left(\frac{\partial \alpha}{\partial q}\right)_0 q_0 E_0 \cos[2\pi\, (\nu_0 - \nu_{vib}) t] \,.$$

The oscillating induced dipole moment represents a source that gives rise to scattered light. As follows from (1.11), there are three components in the scattered light. The first component has the same frequency ν_0 as the incident light and corresponds to Rayleigh scattering, which is the dominant effect. The two other components are shifted with respect to the frequency of the incident light by plus or minus the frequency of the molecular vibration and correspond to Raman scattering. The increase in frequency is referred to as an anti-Stokes (ν_{aS}) shift and the decrease in frequency is known as a Stokes (ν_S) shift:

$$\nu_{aS} = \nu_0 + \nu_{vib} \,, \qquad \nu_S = \nu_0 - \nu_{vib} \,. \tag{1.12}$$

This terminology originates from the shift between the frequencies of the absorption and emission, which was observed by Irish physicist George Gabriel Stokes in the phenomenon of fluorescence in 1852 and named in his honour. According to Stokes' rule, the frequency of fluorescent light is always smaller or equal to that of the exciting light. Thus, the Stokes frequency corresponds to Stokes' rule, and the anti-Stokes frequency contradicts it. By analogy, this nomenclature was accepted for the Raman effect, although it differs from fluorescence.

The classical description correctly explains the frequencies of Rayleigh and Raman components in scattered light, provides a pictorial representation of the polarizability of molecules and predicts some other aspects of the scattering phenomenon. The energy emitted by an oscillating electric dipole per unit of time and integrated over a sphere enclosing the dipole is given by a known equation from the classical theory of radiation:

$$W = \frac{32\pi^4\nu_0^4}{3c^4}\,\alpha_0^2E_0^2cos^2(2\pi\nu_0 t)\,.$$

Averaging by time, the total energy elastically scattered by the induced dipole is as follows:

$$\bar{W}_R = \frac{16\pi^4\nu_0^4}{3c^4}\,\alpha_0^2E_0^2\,,$$

since the average of cosine $\overline{cos^2(2\pi\nu_0 t)}$ = ½. Similarly, and taking into consideration factor ½ for the terms of Raman scattering in (1.11), the total time-averaged energies inelastically scattered with Stokes and ant-Stokes shifts can be presented, correspondingly, as

$$\bar{W}_S = \frac{4\pi^4(\nu_0 - \nu_{vib})^4}{3c^4}\left(\frac{\partial\alpha}{\partial q}\right)^2 q_0^2E_0^2 \qquad (1.13)$$

and

$$\bar{W}_{aS} = \frac{4\pi^4(\nu_0 + \nu_{vib})^4}{3c^4}\left(\frac{\partial\alpha}{\partial q}\right)^2 q_0^2E_0^2\,. \qquad (1.14)$$

Thus, the total energy of light scattered by a single molecule is proportional to the fourth power of the frequency, the square of the amplitude of the electric field E_0 of the incident light and the square of the polarizability of the molecule. Since, if plotted in the coordinate axes of Figure 1-3, $(\partial\alpha/\partial q)_0$

appears to be much smaller than α_0, then Raman scattering is also predicted to be much weaker than Rayleigh scattering.

However, one of the major limitations of the classical theory is the inference that the energies of Stokes and corresponding anti-Stokes Raman components should be approximately the same. Indeed, dividing the expression (1.13) by (1.14) the ratio results in

$$\frac{\bar{W}_S}{\bar{W}_{aS}} = \frac{(\nu_0 - \nu_{vib})^4}{(\nu_0 + \nu_{vib})^4} \approx 1 .$$

Another limitation of the classical theory is that it does not take the real physical states of the molecules involved in the interaction with the incident light into consideration. The basic concepts of the classical consideration of Rayleigh and Raman scattering are illustrated in Figure 1-4.

This and other limitations of the classical approach can be overcome exclusively in frames of the quantum-mechanical theory that reveals the reality of physics on a molecular scale by introducing the quantized energy states of both the radiation and molecules. The quantum theory considers radiation and the molecule together as a complete system and describes how energy is transferred between the radiation and the molecule as a result of the interaction. The molecule is described by the Schrödinger equation, which takes the movement of electrons, the vibrations of atoms relative to each other in a molecule and the rotation of the molecule as a whole into account. A detailed quantum-mechanical description of the Raman effect is rather complicated and beyond the scope of this book. Although there are many detailed texts on the quantum-mechanical interpretation of Raman scattering, the reader is referred to the book by Long (Long 2002), which

presents a unified theoretical approach in a complete and comprehensible form.

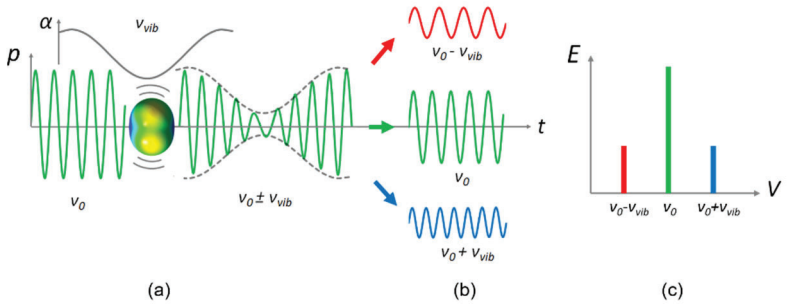

Figure1-4. Schematic representation of basic concepts of the classical theory of Rayleigh and Raman scattering. (a) The incident light induces the dipole moment p in the molecule and makes it oscillate at the frequency v_0 of the incident light. The vibration of nuclei at a much lower frequency v_{vib} changes the polarizability α of the molecule. As a result, the amplitude of the lightwave reemitted by the induced dipole moment is modulated. (b) The amplitude-modulated wave has three components: the carrier wave of the frequency v_0 (Rayleigh scattering), two sidebands with the frequencies $v_0 - v_{vib}$ (Stokes Raman scattering) and $v_0 + v_{vib}$ (anti-Stokes Raman scattering), which are shown as cosine waves in the time domain t. (c) The same components of scattered light in the frequency domain V are denoted by the colours corresponding to the Stokes (red) and anti-Stokes (blue) Raman shifts with respect to the Rayleigh component (green) of unchanged frequency. Note, the amplitudes of the Stokes and anti-Stokes Raman components are equal.

According to quantum mechanics, an isolated molecule can only exist in quantized energy states that, in the general case, can be represented by electronic, vibrational and rotational levels of energy. The quantized energy levels of molecules and transitions between them when interacting with photons of light can be graphically represented in the form of a Jablonski

diagram. In the diagram introduced by and named after the Polish physicist Aleksander Jablonski, the states are arranged vertically by energy and grouped horizontally by corresponding transitions. As mentioned earlier, in the quantum-mechanical interpretation proposed by Kramers, Heisenberg and Dirac, the Raman effect is described as an inelastic scattering of a photon by a vibrating molecule. Figure 1-5 illustrates the process formulated in the sequence of simple equations (1.2)–(1.5) above and determines some additional information.

For the sake of simplicity, consider a ground electronic state E_0 with only two corresponding vibrational levels of energy denoted by quantum numbers 0 and 1 for the ground and excited level, respectively. The rotational energy levels are ignored since their energy is significantly lower than the energy of vibrations, and the rotation motion is hindered in a condensed matter. The incident photon excites the molecule from an initial energy state to a virtual E_{virt} state, as shown in Figure 1-5(b). A virtual state is a very short-lived intermediate quantum state that is not defined by a strict molecular energy value. From the virtual state, the molecule instantaneously relaxes back to a vibrational level in the ground E_0 electronic state and emits a photon of light. When the relaxation occurs, there are three possible situations. First, the molecule is excited from and then relaxes down to the same ground vibrational level 0 and reemits a photon of light with the energy equal to that of the incident photon. As we know, this is an elastic process that corresponds to Rayleigh scattering with the unchanged frequency of the light. The other two situations result in the inelastic scattering of the incident photon that alters its energy. If the molecule is excited by a photon from

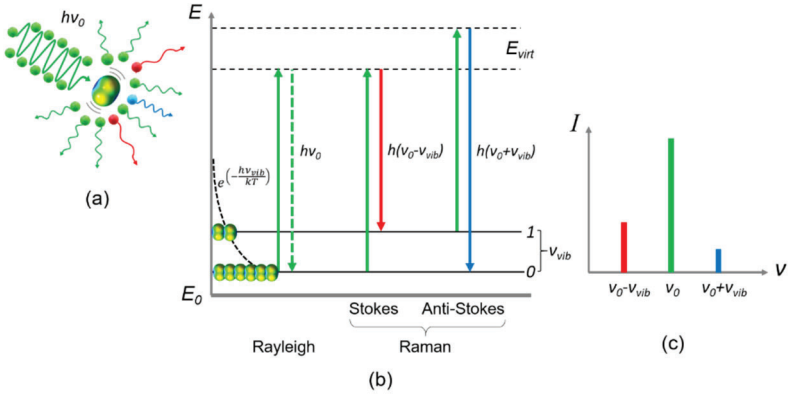

Figure 1-5. Schematic representation of quantum-mechanical interpretation of Rayleigh and Raman scattering. (a) The incident photons of light with the energy $h\nu_0$ being scattered off by the vibrating molecule: the green corpuscles symbolize photons with unchanged $h\nu_0$, whereas the red and blue ones imply photons in Stokes and anti-Stokes Raman scattering, respectively. (b) Jablonski diagram illustrating transition between the vibration energy levels accompanied by the absorption of an incident photon and emission of a scattered photon: Rayleigh scattering with unchanged energy $h\nu_0$, Stokes Raman scattering with red-shifted photon $h(\nu_0 - \nu_{vib})$ and anti-Stokes Raman scattering with blue-shifted photon $h(\nu_0 + \nu_{vib})$. The left inset sketches the population of the vibrational levels given by the exponential Boltzmann distribution. (c) The illustration of the higher intensity of Stokes Raman (red) scattering with regards to anti-Stokes Raman (blue) scattering as follows from the Boltzmann distribution.

level 0 and then relaxes to level 1, then the molecule gains energy and reemits a photon of lesser energy (referred to as being “red”-shifted) that corresponds to Stokes Raman scattering. The third possible situation realizes when the molecule is excited from level 1 and then relaxes down to level 0, thus losing its energy and reemitting a photon of light with higher

energy than the incident photon. This situation with the "blue"-shifted photon corresponds to anti-Stokes Raman scattering.

A quantum mechanical approach correctly predicts the difference in intensity between Stokes and anti-Stokes Raman scattering, as illustrated in Figure 1-5(c). Indeed, the intensity of Raman scattering is proportional to the number of molecules being illuminated. Therefore, the intensity of Stokes Raman scattering is proportional to the number of molecules N_0 occupying the ground level 0, whereas the intensity of anti-Stokes Raman is proportional to the number of molecules N_1 occupying the excited level 1. At thermal equilibrium, the population of excited vibrational levels decreases exponentially with the difference between the energy of excited and ground levels following the Boltzmann distribution which, in case of $h(\nu_1 - \nu_0) = h\nu_{vib}$ for levels 1 and 0, is given by

$$\frac{N_1}{N_0} = e^{\left(-\frac{h\nu_{vib}}{kT}\right)},$$

where h is the Planck's constant, k is the Boltzmann's constant (k=1.38064852·10^{-23} J·K^{-1}), and T is the temperature in Kelvin. At room temperature, the ground vibrational energy level is always more populated than the excited one. Accordingly, there is a much higher probability that photons will be scattered with Stokes shift, and the intensity ratio of Stokes (I_S) to anti-Stokes (I_{aS}) Raman scattering depends on the separation between the vibration energy levels and the temperature following Boltzmann equation:

$$\frac{I_S}{I_{aS}} = \frac{(\nu_0 - \nu_{vib})^4}{(\nu_0 + \nu_{vib})^4}\, e^{\left(-\frac{h\nu_{vib}}{kT}\right)} \gg 1\,. \qquad (1.15)$$

At normal temperatures, this ratio is very large, and anti-Stokes Raman scattering is very weak compared to Stokes Raman scattering. At higher temperatures, the ratio decreases and anti-Stokes Raman scattering increases noticeably.

When the light propagates through a matter, the light photons tend not to interact with the molecules of the matter but rather pass through. Only one photon out of about a thousand incident photons is usually scattered by the molecules. Of the scattered photons, an overwhelming majority is elastically scattered, keeping the same energy as the incident photons. Only one of a million scattered photons changes the energy through an inelastic interaction with the molecules. Therefore, in Raman scattering, the number of photons is about one photon of a billion incident photons.

Regardless of the challenge in practical detection of the weak Raman effect, there are few physical phenomena that have received such wide scientific and practical application as Raman scattering. Scores of books and thousands of articles dedicated to studying all aspects of this fundamental optical phenomenon are the best evidence of the scientific and practical significance of its discovery, which is a worthy testament to the scientist who determined it. The Raman effect formed the basis of the whole direction of vibrational spectroscopy—Raman spectroscopy.

Despite quantum mechanics giving a more complete description of the Raman scattering phenomenon than the classical theory, we will be using the most widely accepted and explanatory models from both theories to illustrate the fundamentals of Raman spectroscopy.

1.2. Fundamentals of Raman spectroscopy

1.2.1. Selection rules in vibrational spectra

The most detailed knowledge of molecular structure is obtained from molecular spectroscopy—the study of the emission, absorption and scattering of electromagnetic radiation by molecules by way of measuring and analyzing the corresponding spectra. In general, a molecular spectrum is composed of bands that are groups of closely spaced spectral lines. The reason for such an appearance is that besides the energy of the electron shell E_e, the molecule possesses the energy of vibration E_{vib} and rotation E_{rot}, so the total energy of the molecule E can be represented as the sum of these energies:

$$E = E_e + E_{vib} + E_{rot} .$$

The processes of emission, absorption and scattering of light affect the amounts of these types of energy, which are manifested in the molecular spectra. The most important circumstance in the division of energy into parts is the different order of magnitude of the energy constituents. The electron energy of a molecule, which has the same order of magnitude as in an atom, is much larger than the vibrational energy, and the vibrational energy, in turn, is much larger than the rotational energy:

$$E_e \gg E_{vib} \gg E_{rot} .$$

A quantum mechanical estimate of the orders of magnitude of the individual energy constituents was first performed by Born and Oppenheimer in 1927. They showed that

$$E_e : E_{vib} : E_{rot} = 1 : \beta : \beta^2 ,$$

where $\beta = \sqrt{\frac{m_e}{m}}$, m_e is the mass of the electron and m is the mass of atoms. Due to the smallness of the electron mass compared to the mass of the nuclei (for hydrogen, the ratio is 1/1836), the following relationship is approximately satisfied:

$$E_e : E_{vib} : E_{rot} = 10000 : 100 : 1 .$$

If expressed in cm^{-1} (or eV), $E_e \sim 10000$ cm^{-1} (~ 1 eV), $E_{vib} \sim 1000$ - 100 cm^{-1} (~ 0.1 – 0.01 eV), and $E_{rot} \sim 10$ - 1 cm^{-1} (~ 0.001 – 0.0001 eV). Thus, based on the separation of the energy of molecules into the constituents and taking the order of their magnitudes into account, the nature of molecular spectra in different frequency ranges is easily explained: the electronic transitions correspond to the visible and UV spectral regions (100,000–10,000 cm^{-1}), vibrational ones correspond to the infrared (4000–100 cm^{-1}) and rotational ones to the far-infrared (100–1 cm^{-1}) region.

The most important consequence of the small mass of the electron compared to the mass of the nuclei is that the electrons move much faster in the molecule than the nuclei. Due to the slow motion of the nuclei, it is a physically reasonable approximation to consider the motion of electrons relative to a fixed arrangement of the nuclei (adiabatic approximation). Electronic energy, which is the sum of the energy of electron motion in the electric field of the fixed nuclei and the energy of the electron-nuclear interactions, plays the role of potential energy in the Schrödinger equation.

Vibrational spectroscopy is the most significant portion of molecular spectroscopy because it provides complete information about the structure and properties of molecules by studying the vibrations and interactions of chemical bonds that associate atoms into molecules. There are three types

of vibrational spectroscopy—infrared (IR), Raman and electron energy loss (EELS) spectroscopy. EELS is a niche technique for probing vibrational modes of atoms and molecules on solid surfaces, typically in a vacuum, but IR and Raman represent universal tools for the determination and identification of molecular structure in virtually any type of samples and environments. Both methods are complementary, as they provide comprehensive information on molecular vibrations. The synergy of the methods will be discussed below in terms of their similarities and differences.

A simple classical approach can be used to explain if a normal vibration results in a corresponding IR or/and Raman spectral band. This approach takes the changes in the dipole moment and the polarizability during the molecular vibration into consideration. The dipole moment arises from the difference in electronegativity of atoms composing chemical bonds and due to non-uniform distributions of positive and negative charges on the various atoms. The magnitude of the dipole moment of an individual chemical bond composed of atoms that have different electronegativity is given by

$$\mu = Ql\,,$$

where Q is a charge and l is the distance between the atoms. Thus, the dipole moment is a measure of the charge asymmetry of a molecule. The total dipole moment of a polyatomic molecule is a vector sum of the individual dipole moments of chemical bonds. The dipole moment oscillates during molecular vibration with the frequency of the vibration:

$$\mu = \mu_0\, cos(2\pi\, \nu_{vib} t)\,,$$

where μ_0 is the permanent dipole moment in the equilibrium state of the molecule. The classical electromagnetic theory requires that for a molecule to absorb the light, the change in the dipole moment with respect to displacement during the vibration (the first derivative) must be non-zero:

$$\left(\frac{\partial \mu}{\partial q}\right)_0 \neq 0\,, \tag{1.16}$$

and the corresponding vibration is said to be IR-active.

As shown above, the interaction of light with a molecule leads to the appearance of an induced dipole moment, even if there may be no permanent dipole moment. An important consequence of equations (1.13) and (1.14) is that for Raman scattering to occur, the vibration that changes the polarizability α with the displacement of nuclei q must be non-zero:

$$\left(\frac{\partial \alpha}{\partial q}\right)_0 \neq 0\,, \tag{1.17}$$

and the vibration is said to be Raman-active. By contrast, if the molecular vibration does not cause a variation in the polarizability α, then there is no amplitude modulation of the dipole moment oscillation shown in Figure 1-4, and there is no Raman Stokes and anti-Stokes radiation. Such vibration is called Raman-inactive.

The necessary conditions (1.16) and (1.17) for a vibration to be active are often termed the gross or major selection rules, respectively, for IR absorption and Raman scattering. In a polyatomic molecule, the vibrations that bring on a net change in a dipole moment are IR-active, and those that induce polarizability changes are Raman-active. Obviously, some

vibrations can be both Raman- and IR-active (Wilson Jr., Decius and Cross 1955).

1.2.2. Ellipsoid of polarizability

The notion of the ellipsoid of polarizability helps to visualize how the polarizability of a molecule changes during its vibrations and to figure out whether or not a given vibration is Raman-active. In the general case of an arbitrary orientation of a molecule with respect to the x-, y- and z-axes in a Cartesian system of coordinates, an electric field E oriented in the x-direction induces a dipole moment p with x-, y- and z-components in accordance with (1.7):

$$p_x = \alpha_{xx}E_x \, , p_y = \alpha_{yx}E_x \, , p_z = \alpha_{zx}E_x \, . \tag{1.18}$$

Hence, if the electric field is in the x-direction, the dipole moment is not necessarily induced in the same direction but rather has x-, y- and z-components individually proportional to E_x. Similarly, for the electric field in the y- and z-directions, the components of p are respectively given by:

$$p_x = \alpha_{xy}E_y \, , p_y = \alpha_{yy}E_y \, , p_z = \alpha_{zy}E_y \tag{1.19}$$

$$p_x = \alpha_{xz}E_z \, , p_y = \alpha_{yz}E_z \, , p_z = \alpha_{zz}E_z \tag{1.20}$$

Consequently, if E has components along x, y and z-axes, the resulting components of p represent the sum of the corresponding contributions from (1.18), (1.19) and (1.20):

$$\begin{aligned} p_x &= \alpha_{xx}E_x + \alpha_{xy}E_y + \alpha_{xz}E_z \\ p_y &= \alpha_{yx}E_x + \alpha_{yy}E_y + \alpha_{yz}E_z \, . \\ p_z &= \alpha_{zx}E_x + \alpha_{zy}E_y + \alpha_{zz}E_z \end{aligned} \tag{1.21}$$

The three linear equations (1.21) can be written in the form of matrix equation:

$$\begin{bmatrix} p_x \\ p_y \\ p_z \end{bmatrix} = \begin{bmatrix} \alpha_{xx}\ \alpha_{xy}\ \alpha_{xz} \\ \alpha_{yx}\ \alpha_{yy}\ \alpha_{yz} \\ \alpha_{zx}\ \alpha_{zy}\ \alpha_{zz} \end{bmatrix} \begin{bmatrix} E_x \\ E_y \\ E_z \end{bmatrix}. \qquad (1.22)$$

In a compact form, the relation between p and E (1.21) may be written as:

$$p_i = \sum_j \alpha_{ij} E_j\ , \qquad (1.23)$$

where the subscripts i and j each stands for any one of the three possible indexes x, y and z. The array of the coefficients α_{ij} in (1.23) or the matrix in (1.22) in the format

$$\begin{bmatrix} \alpha_{xx}\ \alpha_{xy}\ \alpha_{xz} \\ \alpha_{yx}\ \alpha_{yy}\ \alpha_{yz} \\ \alpha_{zx}\ \alpha_{zy}\ \alpha_{zz} \end{bmatrix} \qquad (1.24)$$

is considered to be a tensor—in this case, the polarizability tensor. The behaviour of the induced dipole moment of a molecule is then defined by the coefficients α_{ij}. Generally speaking, all the coefficients α_{ij} will be different for a different system of coordinates. However, it can be shown strictly mathematically and derived logically that if the same electric field E is specified in the new coordinate system, the induced polarization should stay the same. In other words, the induced dipole moment p is defined completely by the components of the polarization tensor α_{ij} with respect to an arbitrarily selected set of mutually perpendicular axes.

Usually, the tensor of polarizability is symmetrical, which means its coefficients are $\alpha_{ij}=\alpha_{ij}$ in (1.23) and, respectively, $\alpha_{xy}=\alpha_{yx}$, $\alpha_{xz}=\alpha_{zx}$ and

$\alpha_{yz}=\alpha_{zy}$ in (1.24). Consequently, this tensor will be defined by the six coefficients: α_{xx}, α_{yy}, α_{zz}, α_{xy}, α_{xz} and α_{yz}. One can always choose the moveable orthogonal coordinates a, b and c associated with the molecule so that the three nondiagonal coefficients are equal to zero. The polarization tensor (in fact, any multidimensional symmetric tensor of the 2nd rank) can be then reduced to the diagonal matrix form with only three non-zero components α_a, α_b and α_c in such orthogonal axes a, b and c:

$$\begin{bmatrix} \alpha_a & 0 & 0 \\ 0 & \alpha_b & 0 \\ 0 & 0 & \alpha_c \end{bmatrix}.$$

The axes a, b and c are termed "principal" axes that can often be chosen so that they are related to the symmetry axes of a molecule. If the molecule rotates with the principal axes, the coefficients α_a, α_b and α_c do not change. Since the energy in the electric field is proportional to the square of its intensity E^2, the energy that is required to polarize the molecule U with respect to these axes is given by a simple equation

$$U = \frac{1}{2}(\alpha_a E_a^2 + \alpha_b E_b^2 + \alpha_c E_c^2)\,. \qquad (1.25)$$

The geometrical interpretation of this equation and, respectively, the polarizability follows directly from the comparison with the standard equation for an ellipsoid in a Cartesian system of coordinate coinciding with the principal axes X, Y and Z:

$$\frac{X^2}{a^2} + \frac{Y^2}{b^2} + \frac{Z^2}{c^2} = 1\,. \qquad (1.26)$$

The coefficients a, b and c are linear segments equal to half the lengths of the principal axes enclosed within the ellipsoid. If we rewrote (1.25) in accordance with (1.26) as

$$U = \frac{1}{2}\left(\frac{E_a^2}{\left(1/\sqrt{\alpha_a}\right)^2} + \frac{E_b^2}{\left(1/\sqrt{\alpha_b}\right)^2} + \frac{E_c^2}{\left(1/\sqrt{\alpha_c}\right)^2}\right),$$

then the polarizability of a molecule can be represented in the form of an ellipsoid called a polarizability ellipsoid, as shown in Figure 1-6(a). Note that the axes of the ellipsoid are inversely proportional to the square roots of the coefficients of the polarizability tensor (Wong 1994). Since the electrons are more polarizable in the direction of a chemical bond (a larger α_{ij}), the shortest axes of the polarizability ellipsoid correspond to the directions of the easiest polarization as shown in Figure 1-3(b) for a diatomic molecule.

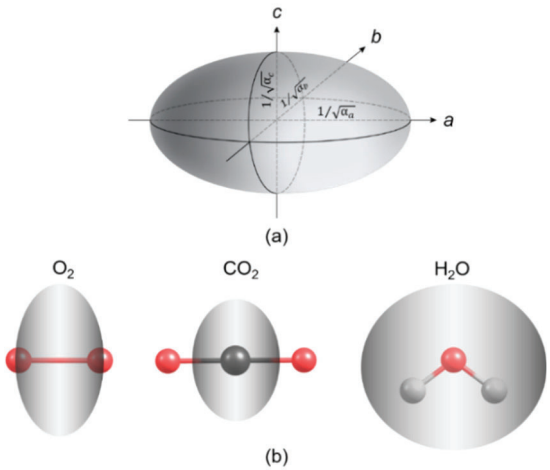

Figure 1-6. The ellipsoid of the polarizability. (a) Half the lengths of the principal axes are inversely proportional to the square roots of the coefficients of the polarizability tensor. (b) The polarizability ellipsoid for the molecules O_2, CO_2 and H_2O in the equilibrium state.

1.2.3. Normal modes of molecular vibrations

Spectroscopists tend to treat the molecule as a dynamic system and classify its vibrational motions by normal modes. The normal vibrational modes are usually considered as collective, concerted motions of the atoms when all the atoms pass through their equilibrium positions at the same time keeping the centre of the molecule's mass unaffected. Each mode can be differentiated by the relative movements of the atoms in a molecule as stretching that alters the length of chemical bonds (ν) and deformation or bending (δ) that changes the bond angles while keeping the bond length unaffected. The vibrations can be additionally subdivided into symmetric (s), asymmetric (as), in-plane (δ), out-of-plane (γ) and degenerated (e) types. The deformation modes are often regarded as twisting, rocking and wagging vibrations of a group of atoms in a molecule. The normal modes are independent, i.e., synchronous motions of atoms or groups of atoms in a molecule occur without causing changes in any of the other modes. For example, the symmetric and asymmetric stretching vibrations of CO_2, in which the oxygen atoms are displaced while the carbon atom remains stationary, represent two of the normal modes of this molecule shown below.

The number of normal modes for a molecule composed of N atoms is defined by its internal degrees of freedom and results in well-known 3N - 6 and 3N - 5 quantities for nonlinear and linear molecules, respectively. Indeed, each atom has three degrees of freedom, corresponding to motions along any of the three Cartesian coordinate axes x, y and z. A polyatomic molecule of N atoms thus has 3N degrees of freedom. Three of these 3N degrees of freedom correspond to the translational motion of the entire molecule through space. The remaining 3N - 3 degrees of freedom

constitute rotational and vibrational motions. For a nonlinear molecule, the rotational motions around the three mutually perpendicular x-, y- and z-axes correspond to the three rotational degrees of freedom so that the residual 3N - 6 degrees of freedom constitute vibrational motions. For a linear molecule, the rotation around its principal (internuclear) axis of symmetry leaves the molecule unchanged so that there are only two rotational degrees of freedom, thereby resulting in 3N - 5 degrees of freedom for vibrations.

The changes of the dipole moment and the polarizability during the vibration of small molecules such as diatomic O_2, linear CO_2 and nonlinear H_2O are illustrated in Table 1-1. The dipole moment of a molecule is a vector quantity that can be represented by an arrow where the length of the arrow is proportional to its magnitude, and the arrow's head points its direction. The vibration is IR-active if the magnitude or direction of the dipole moment changes. In contrast, a normal vibration is Raman-active if the size, shape or orientation of the polarizability ellipsoid changes during the vibration. In a homonuclear diatomic molecule, such as O_2, H_2 or N_2, there is no permanent dipole moment in their equilibrium states. The vibration of the only truly covalent nonpolar bond does not change the dipole moment such that the derivative of the dipole moment (1.16) is zero, and the vibrations of these molecules are not IR-active. However, the polarizability of the molecules changes with the nuclear displacement (Fig. 1-3), and the vibration results in a non-zero derivative at the equilibrium position (1.17). As shown for the O_2 molecule, the polarizability ellipsoid noticeably changes alongside the bond and, therefore, the vibration is Raman-active.

Table 1.1. Vibration modes, ellipsoids of polarizability, dipole moments and vibrational frequencies experimentally observed in Raman and IR spectra of small molecules in the gas phase: ν_a – symmetric stretching, ν_{as} – asymmetric stretching and δ – bending vibrations. Blue arrows indicate the dipole moments.

Molecule	Vibration modes, ellipsoids of polarizability and dipole moments	Frequency, cm^{-1}	
		R	IR
O_2	ν_s 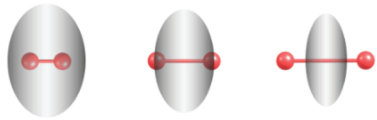	1556	
CO_2	ν_s 	1330*	
	ν_{as} 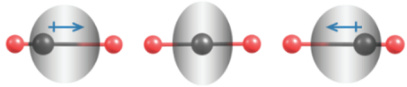		2349
	δ 		667
H_2O	ν_s 	3652	3652
	ν_{as} 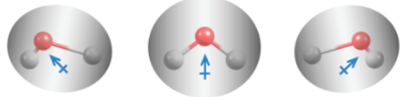	3756	3756
	δ 	1595	1595

* Observed as spectral doublet due to the Fermi resonance (see Fig. 1-9).

In the symmetric stretching vibration of the CO_2 molecule, the strength of how tightly the electrons are bound to the nuclei is different between the

compressed and extended geometries of the molecule. Consequently, the polarizability changes during the vibration, and this vibrational mode is Raman-active. In contrast, there is no change in the dipole moment during the vibration as the dipole moments of individual C-O bonds are equal in magnitude but opposite in sign and, therefore, the vibration is inactive in IR. In the asymmetric stretching vibrations, the compression of the individual C-O bond on one or another side produces an equal decrease in the polarizability of the molecule alongside the bond. Thus, the asymmetric stretching vibration is Raman-inactive. In contrast, the dipole moment arises and changes the direction to the opposite one when the molecule passes the equilibrium position so that the vibration is IR-active. For the bending vibration, it is obvious that the polarizability increases equally and independent of the direction of bending. Therefore, the vibration is inactive in Raman. However, the dipole moment arises and changes its direction so that the vibration is IR-active.

Unlike O_2 and CO_2 molecules, all the three vibrational modes of the H_2O molecule appear to be both Raman- and IR-active as the vibrational motion causes both the change of the polarizability ellipsoid and the dipole moment. Indeed, the symmetric stretching vibration causes the change of the ellipsoid of the polarizability in size and shape, the asymmetric stretching in orientation and the bending vibration in size and shape. Similarly, the dipole moment changes its magnitude and direction. When the bond is stretched out, which causes the hydrogen atoms to be situated further away from the oxygen atom, the molecule will be polarized more easily. In contrast, when the hydrogen atoms at the other extreme are situated closer to the oxygen atom, the molecule will be less easy to polarize. In principle, a similar conceptual approach of dissecting molecular dipoles and polarizabilities

into the dipoles and polarizabilities of chemical bonds can be pursued for large molecules.

The schematic representations of the polarizability ellipsoids in Table 1-1 are based on the results of calculations performed using a Gaussian 16, which are referenced above.

1.2.4. Frequencies and transitions in vibrational spectra

The frequencies of the vibrations of atoms in molecules can be predicted using a harmonic oscillator approximation in the framework of classical mechanics. Consider a simple model of a diatomic molecule that consists of two positive nuclei and electrons forming an electron shell around the nuclei. The existence of a stable molecule is a consequence of the equilibrium of two forces. On the one hand, there is a repulsion between the positively charged nuclei of both atoms and between the negative electron clouds. On the other hand, the nucleus of one atom attracts the electrons of another one and vice versa. Two atoms are located at an average internuclear distance at which these forces are equilibrated, and the potential energy of the system reaches a minimum. The average internuclear distance is called the equilibrium distance or the bond length. When atoms approach each other, repulsive forces quickly increase, and when the atoms move away from each other, attractive forces increase. The force that returns the nuclei to the equilibrium position, in the first approximation, is proportional to their displacement following the known analogy with Hooke's law for an elastic mechanical spring:

$$F = -kq\,,$$

where F is the elastic force, k is the force constant (spring stiffness), and q is the displacement of the nuclei from the equilibrium position (spring extension or compression) during the vibration. In a model of a diatomic molecule or a chemical bond between two atoms with masses m_1 and m_2 connected by a massless spring, each atom oscillates along the spring axis with different amplitudes, but the same frequency and both atoms go through their equilibrium position simultaneously. A system satisfying this condition is the classic example of a harmonic oscillator. The potential energy curve of a harmonic oscillator is a parabola and is defined by the following formula:

$$U(q) = \frac{1}{2}kq^2 . \tag{1.27}$$

Note that the oscillatory motion of a system of two nuclei with masses m_1 and m_2 relative to each other can be easily reduced to the oscillation of one mass M relative to the equilibrium position. The mass M is called a reduced or an effective mass and is defined by the ratio

$$M = \frac{m_1 m_2}{m_1 + m_2}.$$

The frequency of a harmonic oscillator derived from Hook's spring law and Newton's second law of motion is given in Hz by

$$\nu = \frac{1}{2\pi}\sqrt{\frac{k}{M}}. \tag{1.28}$$

According to classical electrodynamics, such oscillations cause emission or absorption of electromagnetic radiation at the same frequency. However, as we know, the quantum theory specifies that molecules can only exist in

quantized energy states. Thus, the vibrational energy is not continuously variable but, instead, can only have certain discrete values. The emission or absorption of electromagnetic radiation occurs during the transitions between discrete energy levels. The energies of these levels obtained as a result of solving the Schrödinger equation are expressed in the following form:

$$E_{vi} = h\nu_i \left(v_i + \frac{1}{2}\right),$$

where ν_i is the frequency of a particular vibration mode, and v_i is the quantum number of the energy level (v_i = 0,1,2, …). Thus, the harmonic oscillator has a set of equidistant levels and its zero energy at $v_i = 0$ is not equal to zero. Detailed consideration of the wave functions of the harmonic oscillator leads to the selection rules $\Delta v_i = \pm 1$. Consequently, for a molecule represented by an idealized harmonic oscillator, so-called fundamental vibration is only allowed with the frequency defined by the equation (1.28).

However, for vibrations of a real molecule, the approximation of the harmonic oscillator is no longer valid because it does not forecast the appearance of overtones and combination frequencies of the molecular vibrations observed in practice. With an increase in the amplitude of vibration in the molecule, the potential energy curve cannot have a parabolic shape for large q in (1.27). Indeed, at a very small distance between the atoms, when $q \ll 0$, an extra repulsive effect comes into play, which prevents the atoms from being forced together. From the other side, when the bond between the atoms is being stretched too far, so that $q \gg 0$, it will break in the long run. As a result, when the energy of the vibration reaches the value of the dissociation energy, the molecule is cleaved into atoms.

Thus, at higher vibrational energies, which correspond to larger displacements from an equilibrium position, it becomes more difficult to compress the chemical bond than stretch it. For large vibrational amplitudes, expression (1.27) is no longer suitable for potential energy, and it is necessary to take anharmonicity of the oscillations expressed by higher-order terms in the Taylor expansion for the function of potential energy into account:

$$U(q) = \frac{1}{2}kq^2 + k_1q^3 + k_2q^4 + \dots ,$$

where the term $\frac{1}{2}kq^2$ corresponds to the harmonic part of the potential energy and the terms $k_1q^3 + k_2q^4 + \dots$ are responsible for anharmonicity. The theoretical calculation of these terms and, consequently, those of the potential energy curves is quite difficult. The most convenient analytical expression that satisfactorily approximates the experimental *U(q)* curves for relatively light diatomic molecules was proposed by the American physicist Philip Morse (Morse 1929):

$$U(q) = D_0\left(1 - e^{-\beta q}\right)^2 , \qquad (1.29)$$

where D_0 is the dissociation energy measured from the curve minimum, β is the parameter that defines the width of the function, and q is the displacement of atoms. In the Morse potential function, the curve deviates from parabolic symmetry and realistically results in dissociation. The potential energy curves of a diatomic molecule in harmonic (Hook's form) and anharmonic (Morse form) approximations along with a space-filling model of a diatomic molecule in compressed, equilibrated, stretched and dissociated states as a function of displacement of atoms from its equilibrium distance are shown in Figure 1-7(a).

The function proposed by Morse leads to the two-term expression for the vibrational energy levels of the molecule

$$E_{vi} = h\nu_i\left(v_i + \frac{1}{2}\right) - h\nu_i x_i\left(v_i + \frac{1}{2}\right)^2, \qquad (1.30)$$

where x_i is the anharmonicity constant that typically has values between 0.001 and 0.03 depending on the molecule and the mode of vibration (e.g., for the molecule of H_2, the anharmonicity constant x_i has one of the highest value equal to 0.0285). In this equation, the second term accounted for anharmonicity is always negative. Consequently, anharmonicity lowers the energy level values. As a result, with an increasing quantum number v_i, the energy levels in the potential well are condensed and converge to an energy equal to the dissociation energy. Thus, the separation between the adjacent vibrational levels becomes smaller at higher vibrational energies until the energy finally reaches the level of dissociation. The effect of anharmonicity mitigates the selection rules so that not only the fundamental transitions between the adjacent levels are allowed ($\Delta v_i = \pm 1$), but overtones ($\Delta v_i = \pm 2, \pm 3, \ldots$) and combination ($\Delta v_i = 1$, $\Delta v_j = 1$, where i and j represent different vibration modes) frequencies of molecular vibrations appear. Anharmonicity may also result in the interaction of a fundamental vibration with an overtone known as Fermi resonance. The first overtone ($\Delta v_i = \pm 2$) is approximately equal to twice the frequency of the corresponding fundamental vibration. The combination transitions result from the addition of two different fundamental vibrations. The fundamental transition, the first overtone and the formation of combination frequency upon light absorption are shown in Figure 1-7(b-d). The transitions corresponding to the processes of Rayleigh, Stokes and anti-Stokes Raman scattering are shown in Figure 1-7(e-g).

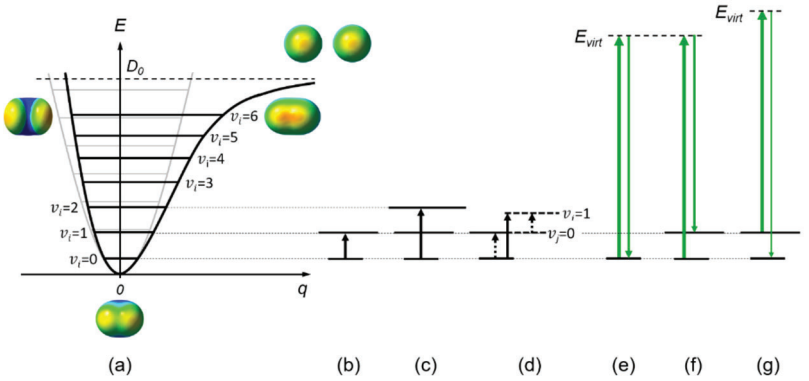

Figure 1-7. The potential energy of a diatomic molecule and the vibrational transitions. (a) $E=U(q)$ is a function of displacement q of atoms from its equilibrium position denoted by 0 for harmonic (grey) and anharmonic (black) oscillators, where D_0 is the dissociation energy. The space-filling models represent the diatomic molecule in compressed, equilibrated, stretched and dissociated states at the corresponding values of q. The quantum number $v_i=0,1,2,..$ designates the vibrational energy levels. (b) The fundamental transition $v_i=0 \rightarrow 1$. (c) The first overtone $v_i=0 \rightarrow 2$. (d) The combination frequency $v_i=0 \rightarrow 1 + v_j=0 \rightarrow 1$, where j corresponds to another vibration mode. (e) Rayleigh scattering. (f) Raman Stokes scattering. (g) Raman anti-Stokes scattering. E_{virt} designates the virtual energy levels. Note that the different thicknesses of the vertical green lines in the diagrams (e–g) imply substantially different intensities of the excitation and the corresponding scattering processes $I_0>I_R>I_S>I_{aS}$.

1.2.5. Intensities in vibrational spectra

The transitions between the quantized vibrational levels can be experimentally observed in the IR and Raman spectra of a sample as the corresponding spectral bands upon excitation of the sample with light.

In IR spectra, the absorption of light by molecules of the sample is measured as a function of the frequency of light. The sample absorbance A obeys the Lambert-Beer law that establishes the relationship

$$A = \varepsilon C d\,, \tag{1.31}$$

where ε is called the extinction coefficient, C is the concentration of the molecules, and d is the pathlength that light travels through the sample. The extinction coefficient ε, which is also known as absorptivity, characterizes the ability of molecules or chemical bonds to absorb light at a given frequency. The coefficient is proportional to the square of the change in the dipole moment with respect to displacement during the normal vibration:

$$\varepsilon \propto \left(\frac{\partial \mu}{\partial q}\right)^2 . \tag{1.32}$$

The absorbance A can be expressed via the sample transmittance T as

$$A = log_{10}\frac{1}{T} = log_{10}\frac{I_0}{I}\,, \tag{1.33}$$

where $T = {}^{I}/_{I_0}$, and I and I_0 denote the intensities of the incident light and the light transmitted through the sample, respectively. In practice, the sample transmittance is often calculated in % as

$$T(\%) = \frac{I}{I_0} \times 100\,,$$

although *T(%)*, in contrast to A, is not linearly related to the concentration C. Thus, the IR spectrum represents a plot of absorbance A or transmittance *T(%)* vs. the absolute frequency.

In the Raman spectra, the intensity of light scattered by molecules of a sample is also measured as a function of the frequency of light. Since the intensity of light is related to the energy carried by the light wave as

$$I = cE^2 ,$$

where c is the speed of light, and E is the amplitude of the electric field of the light wave, then the intensity of Raman light scattered by N molecules in the sample can be derived from (1.13–1.14) by substituting E_0^2 with I_0 and written as

$$I_{S,aS} \propto I_0 N(\nu_0 \mp \nu_{vib})^4 \left(\frac{\partial \alpha}{\partial q}\right)^2 , \tag{1.34}$$

where I_0 and ν_0 are the intensity and the frequency of the excitation light, respectively. The dependence (1.34) can be presented in the form to some extent analogous to the Lambert-Beer law (1.31) so that

$$I_R = KI_0\sigma CV , \tag{1.35}$$

where K is a parameter mostly determined by experimental conditions of measurement, C is the concentration of the molecules in the sample, and V is the sampling volume, i.e., the volume from which the scattered light is collected and measured. However, in contrast to the Lambert-Beer law, the intensities of Raman bands linearly depend on the intensity I_0 of excitation light. The coefficient σ defined as

$$\sigma \propto (\nu_0 \mp \nu_{vib})^4 \left(\frac{\partial \alpha}{\partial q}\right)^2 \tag{1.36}$$

characterizes the ability of a molecule or chemical bond to scatter light at a given frequency of vibration ν_{vib} and is called a Raman scattering cross-section.

The absorptivity ε and Raman cross-section σ play a somewhat similar role in both methods of vibrational spectroscopy. These coefficients are a measure for the probability of a specific transition to occur and characterize the intrinsic properties of molecules or chemical bonds to absorb and scatter light. Namely, ε and σ define the presence of spectral bands as well as their strengths and weaknesses since the coefficients are related to the terms (1.16) and (1.17) accountable for the selection rules, correspondingly, in IR and Raman spectra. However, the Raman cross-section σ strongly depends on the excitation frequency being proportional to its fourth power. That is, for a given sample, replacing a 1064 nm laser with a 532 nm laser (both of which are popular choices for Raman spectroscopy) increases the scattering cross-section by a factor of 16. Thus, an important outcome of expressions (1.35) and (1.36) is that the intensities of Raman bands can be increased by increasing the frequency ν_0 or the intensity (the light flux power density) I_0 of excitation light. Nevertheless, as in IR, the intensities of spectral bands are proportional to the concentration of an analyte C, making Raman spectroscopy well suitable for quantitative analysis.

In contrast to IR, the frequencies in Raman spectra are usually calculated as a Raman shift, i.e., the difference between the frequencies of excitation light and Raman transitions. Following (1.12), in Stokes ($\nu_0 - \nu_S = \nu_0 - (\nu_0 - \nu_{vib}) = \nu_{vib}$) and anti-Stokes ($\nu_0 - \nu_{aS} = \nu_0 - (\nu_0 + \nu_{vib}) = -\nu_{vib}$) regions, the vibrational frequencies result in quantities with the sign "plus" and "minus", respectively. Thus, in the Raman spectrum, the intensities along the ordinate axis are plotted vs. the Raman shift along the abscissa axis, and the shift appears to be independent of the frequency of excitation light.

From Figure 1-7 is evident that for transitions between the corresponding energy levels, for example, $v_i=0 \rightarrow 1$, the Raman shift is equivalent to the

frequency of the IR absorption. This similarity forms the basis for the interpretation of Raman and IR spectra, as well as their complementary and confirmatory role.

Spectroscopists prefer to define the abscissa scale of vibrational spectra in wavenumbers $\bar{\nu}$ expressed in cm^{-1} units, which is sometimes called the reciprocal centimetre, as this unit is the reciprocals of a wavelength. It indicates the number of the light wavelengths that fit into the distance of one centimetre and is given by:

$$\bar{\nu} = \frac{1}{\lambda} = \frac{\nu}{c}\,, \tag{1.37}$$

where c is the velocity of light in cm per second. The frequency of a fundamental vibration of a diatomic molecule can be predicted with a good degree of approximation by equation (1.28) and expressed in cm^{-1} units by

$$\bar{\nu} = \frac{1}{2\pi c}\sqrt{\frac{k}{M}}\,. \tag{1.38}$$

The wavenumber $\bar{\nu}$ has the advantage of being linear with respect to the energy of electromagnetic waves. Wavenumbers $\bar{\nu}$ and wavelength λ can be interconverted following the equation

$$\bar{\nu}\,[cm^{-1}] = \frac{1}{\lambda[\mu m]} \times 10^4\,.$$

A Fourier-transform infrared (FTIR) spectrometer is used most often to measure IR spectra. There is a vast literature devoted to the measurement of IR spectra and, in particular, the principles of operation of modern FTIR

spectrometers. One of the most comprehensive descriptions of the practice of FTIR spectroscopy can be found in the book by Griffiths and de Haseth (Griffiths and de Haseth 2007). Raman spectra are measured using Raman spectrometers that will be introduced in the next chapter.

Figure 1-8 shows the Raman spectrum of a silicon (Si) wafer in Stokes and anti-Stokes regions. In the Stokes region, the so-called first-order Raman spectrum manifests a strong band at 520.7 cm^{-1} arising from the fundamental transition assigned to the triply degenerate, long-wavelength transverse optical (TO) phonon. The second-order Raman band corresponding to the first overtone is much weaker and is observed at ~ 960 cm^{-1}. In the anti-Stokes region, the only first-order band at -520.7 cm^{-1} is evident, whose intensity is about an order of magnitude lower than that of the peak at 520.7 cm^{-1}. Although not shown in the figure, very weak higher-order Raman bands, corresponding to 3rd and 4th overtones of the TO phonon scattering, can be found correspondingly at ~1500 cm^{-1} and ~1900 cm^{-1} in the Stokes region of the Raman spectrum. The Raman band of 4th overtone is often used to test the sensitivity of a Raman instrument, as will be discussed in Chapter Three. However, the higher-order Raman bands are not detectable in the anti-Stokes region of Si at all. The example of Si demonstrates that, at ordinary temperatures, the measurement of Raman spectra in the Stokes region has the most practical importance. Indeed, the intensities of spectral bands and, thus, signal-to-noise ratios (S/N) in the Stokes region are much higher than those in the anti-Stokes as follows from (1.15).

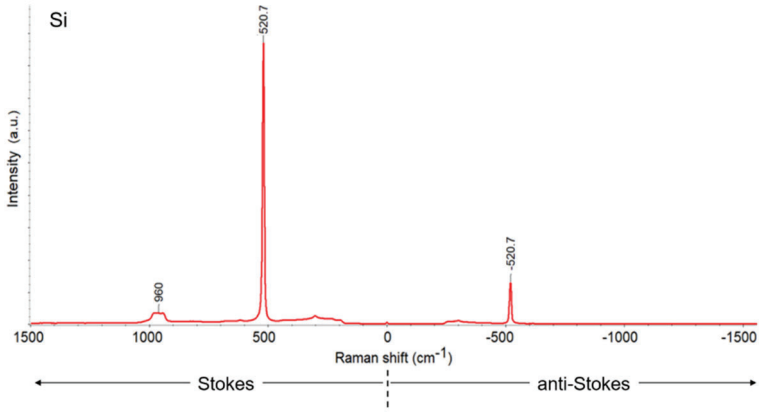

Figure 1-8. Raman spectrum of a Si wafer in Stokes and anti-Stokes regions.

In any spectral measurement under normal conditions, the vibrational bands of the small molecules considered above can be detected since the molecules of N_2, O_2, CO_2 and H_2O are the constituents of ambient air. As follows from equation (1.38), the frequency or the position of a vibrational band along the wavenumber axis increases with the increase of the force constant k, i.e., the strength of the chemical bond between the atoms and the decrease of the reduced mass M of the atoms participating in the vibration. Indeed, the stretching vibration of the hydroxyl group O-H of water containing light hydrogen strongly bonded to highly electronegative oxygen gives rise to the IR bands at 3756 and 3652 cm^{-1}, respectively, for asymmetric ν_{as}(OH) and symmetric ν_s(OH) types of the vibration (Fig. 1-9). Note that spectral bands of asymmetric stretching vibrations usually appear at higher wavenumbers than the symmetric ones. As a rule of thumb, stretching vibrations of chemical bonds that contain the light H atom always appear in the spectral region above 2000 cm^{-1}. The deformation or bending δ(HOH) vibration that alters the bond angle between the H atoms in the molecule of H_2O appears at 1595 cm^{-1}. Suppose an FTIR spectrometer with

a high enough spectral resolution is used for measurements. In that case, the considerable fine structure of the vibrational bands is observed in the IR spectra of small molecules in the vapour phase. The fine structure originates from transitions between quantized rotational energy levels that occur along with the vibrational transitions. The fine rotational structure can be quite complex, and the explanation of its manifestation is beyond the scope of this book. Thus, the band positions indicated by vertical lines correspond to pure vibrational transitions. As we know, only asymmetric stretching ν_{as}(CO) and bending vibrations δ(OCO) of carbon dioxide are IR-active, and the corresponding spectral bands appear at 2349 and 667 cm^{-1}, respectively. The vibrations of the diatomic homonuclear molecules of N_2 and O_2 are not IR-active and cannot be observed in IR spectra. However, these vibrations are Raman-active, and the peaks at 2229 and 1556 cm^{-1} are assigned to N_2 and O_2, respectively, in the Raman spectrum of ambient air shown in Figure 1-9. It should be noted that despite the fact that N_2 and O_2 are the dominant components of air (78% and 21% by volume, respectively), in practice, these bands can be observed when using sufficiently sensitive Raman spectrometers or under special measurement conditions. Nevertheless, the stable positions of these bands at normal conditions can sometimes be used to calibrate Raman spectrometers or as reference wavenumbers when tracking shifts of spectral bands in measured samples. Both stretching vibrations ν_{as}(OH) and ν_s(OH) of water, as well as the symmetric vibration ν_s(CO) of carbon dioxide, are Raman-active. The inset shows the spectral doublet associated with CO_2 as the result of Fermi resonance between Raman-active ν_s(CO) and the overtone of δ(OCO), which is forbidden in Raman but active in IR. The Fermi resonance occurs due to the fundamental ν_s(CO) transition expected at about 1330 cm^{-1} and the first overtone 2δ(OCO) at 2×667 $cm^{-1} = 1334$ cm^{-1} have approximately equal frequencies

and the same types of symmetry. The resonance interaction causes the 1330 cm^{-1} mode to shift to lower wavenumbers and the 1334 cm^{-1} one to shift to higher wavenumbers. The Fermi resonance leads to the manifestation of the two components at 1388 and 1285 cm^{-1} with an intensity ratio of about 2:1 as a result of the significant increase in the intensity of the weak overtone on account of the resonance coupling with the fundamental vibration. However, in practice, the concentrations of CO_2 should significantly exceed its normal content in ambient air for the Fermi doublet to be experimentally observed in the Raman spectrum. Note that, although the water vapour and CO_2 are the minor constituents of ambient air (only about 1% and 0.04% by volume, respectively), the intensities of the corresponding IR bands are significant, whereas the Raman-active bands are usually not experimentally observed as follows from Figure 1-9.

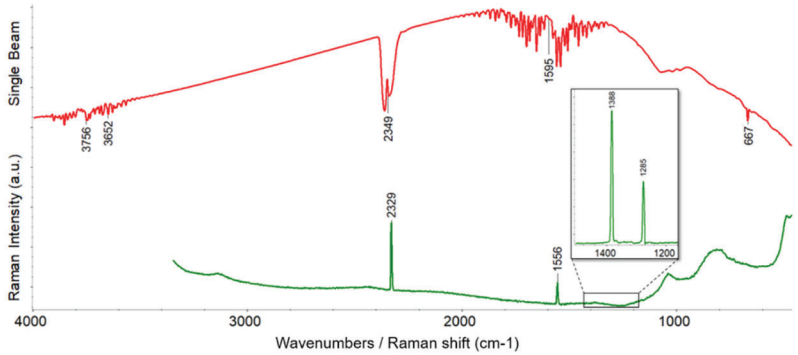

Figure 1-9. FTIR (red trace) and Raman (green trace) spectra of ambient air. The FTIR spectrum is the background scan (single beam) of an FTIR spectrometer. The FTIR and Raman spectra were measured with 4 cm^{-1} spectral resolution. The inset shows the Fermi doublet of CO_2, which could be observed in the Raman spectrum with an excessive concentration of this gas in the air. The broad bands below 1100 cm^{-1} arise from the silver coated glass slide used in the Raman measurement with 532 nm excitation.

To interpret the difference in the intensities of IR and Raman bands of H_2O, it can be helpful to conceive interrelation between incident light and the changes in dipole moments and polarizability of chemical bonds during molecular vibrations. The water molecule has a strong dipole moment, and it is said to be highly polarized. The electric field of excitation light cannot induce a large change in the dipole moment in such a polar molecule, and the polarizability, as defined above, of the water molecule is low. During vibrations, the magnitude of the dipole moment changes significantly, whereas the changes in the polarizability in view of its smallness turn out to be minor, and the polarizability derivative will be near zero. In accordance with (1.31–1.32) and (1.34–1.35), correspondingly, the intensities of vibrational bands of H_2O are high in IR and low in Raman spectra, and water is said to be a strong IR absorber but a weak Raman scatter. A similar consideration can be used to explain the strong intensity of the IR and the low intensity of the Raman bands originating from the vibrations of the highly polar C=O bonds in a nonpolar CO_2 molecule.

Accordingly, vibrations of the highly polar covalent bonds, such as O-H, C=O, C-O and N-O, in molecules result in a significant change of the magnitude of their dipole moment and, therefore, in the appearance of strong IR but rather weak Raman bands. In contrast, if a covalent bond is relatively neutral and does not carry a large dipole moment, then the bond is prone to polarization. As a result, the presence of covalent bonds, such as C-C, C=C and S-S, in molecules typically leads to strong Raman and weak IR bands in their vibrational spectra.

1.2.6. Principles of molecular symmetry

The simplest molecules, which consist of a small number of atoms, have relatively simple vibrational spectra. To predict the appearance of vibrational bands in the IR and Raman spectra of polyatomic molecules, one should consider the normal vibrations and symmetry of the molecules. Each ground state of the molecule is characterized, as is known, by its equilibrium configuration. The symmetry of molecules is related to the symmetry of their equilibrium configurations. The overall symmetry of the molecule is described by a set of operations that comprise a point group of symmetry. For a molecule, the equilibrium configuration of which belongs to a certain point group, there is a well-defined classification of normal vibrations according to the types of symmetry possible for this group. The classification of individual normal vibrations and molecules by their types of symmetry is performed in frames of group theory, which is a mathematical discipline that applies the symmetry concept to vibrational spectroscopy and provides the relationship between the molecular structure and the vibrational spectrum. Group theory is out of the scope of this chapter as there are already many reference materials on this subject in monographs and textbooks on spectroscopy. An introduction to molecular symmetry and point groups with an emphasis on their applications in vibrational spectroscopy can be found in sufficient detail in the book by Ogden (Ogden 2001), for example, and a summary of group theory applied to Raman spectroscopy was given by Tuschel (Tuschel 2014).

To illustrate the point groups and character tables, which make it possible to conclude whether the vibrations are IR- or Raman-active, we will limit ourselves here to only two examples—a water molecule H_2O and the simplest aromatic hydrocarbon, benzene C_6H_6.

To perform a symmetry operation, it is necessary to imagine a molecule rotated around an axis, reflected on the mirror's plane or inverted through a point located in the centre of the molecule. These axes, planes and points are called symmetry elements that form a designated point group. During the operations of symmetry for a given point group, the configuration of the molecule under consideration turns into itself, i.e., leaves it in a configuration that is indistinguishable from the original one.

For H_2O, the equilibrium configuration turns into itself when rotated by 180^0 about a second-order axis C_2 and reflected through the plane containing the molecule framework $\sigma_v'(yz)$ and the plane $\sigma_v(xz)$ perpendicular to it, as is shown in Figure 1-10(a). The axis of symmetry labelled C_2 and the mutually perpendicular mirror planes denoted by $\sigma_v(xz)$ and $\sigma_v'(yz)$ passing through the axis represent the elements of symmetry. The water molecule belongs to the point group of the symmetry designated by C_{2v}. Each point group has an associated character table, and the character table for H_2O is shown in Figure 1-10(b). The character table contains important information about a given point group in a compact form. It is used to classify molecular vibrations according to their symmetry and to predict whether a vibration is active or forbidden due to the symmetry motives. The character table starts with the point group indicated at the top left-hand corner. The symmetry elements possessed by the point group are given across the top row of the character table. The symmetry elements include identity operation, E, that does not change the symmetry of the molecule. The left-hand column lists the Mulliken symbols (or symmetry species) used to identify irreducible representations of the point group C_{2v}. The symbols *A* and *B* are given to one-dimensional representation and mean correspondingly symmetric and asymmetric states with respect to rotation

about a principal n[th]-order axis C_n by the angle of $\frac{360^0}{n}$, which for H_2O forms C_2. The subscripts *1* and *2* attached to *A* or *B* indicate, respectively, symmetric and asymmetric states with respect to the plane σ_v. The set of data elements held in the table represents the characters of the irreducible representations. The individual characters show how each irreducible representation transforms with each operation of symmetry. For example, for B_2, the rotation around C_2 and the reflection through σ_v results in inversion (the corresponding character values are equal to -1), while reflection through σ_v' and evidently the identity operation results in no change (the characters are equal to 1). The penultimate column of the character table consists of the symbols *x*, *y* and *z*, which represent the Cartesian coordinates, and the symbols R_x, R_y and R_z, which indicate the rotations about the three axes. Since a change in the dipole moment of a molecule, being a vector, occurs upon changing amplitude or orientation of the vector, the column provides the coordinate basis in which the vibrations may be IR-active. Thus, A_1, B_1 and B_2 constitute vibrational representations, while A_2, B_1 and B_2 correspond to rotational representations. The last column contains the squares x^2, y^2 and z^2, and binary products *xy*, *xz* and *yz*, i.e., the quadratic functions of the coordinates in which the polarizability ellipsoid is defined and thereby indicates the vibrations that may be Raman-active. Although the last two columns of the character table are particularly helpful to the spectroscopist, the entire procedure of prediction of the number of IR- and Raman-active vibration using the character table consists of the following general steps illustrated with H_2O: 1) generation of a reducible representation by considering every N atoms of the molecule in the Cartesian coordinates (for H_2O, $\Gamma_{3N} = \Gamma_9 = 9, -1, 1, 3$); 2) decomposition of the reducible representations into the sum of irreducible representation

($\Gamma_9 = 3A_1 + A_2 + 2B_1 + 3B_2$) using a special reduction formula; and 3) subtraction of rotational and translational representations from the reducible representation leaving only the vibrational symmetries ($\Gamma_{vib} = \Gamma_9 - \Gamma_{rot} - \Gamma_{trans} = 3A_1 + A_2 + 2B_1 + 3B_2 - A_2 - B_1 - B_2 - A_1 - B_1 - B_2 = 2A_1 + B_2$). Thus, the application of the reduction procedure to H_2O results in the three vibrations which are active in IR and Raman, as summarized in Figure 1-10(c).

It should be noted that the stretching vibrations of water in a condensed phase are shifted to lower wavenumbers at about 3400 cm^{-1} while the bending frequency increased to 1645 cm^{-1} due to the formation of strong hydrogen bond. The strong hydrogen bonding typically shifts the stretching vibrations to lower wavenumbers with greatly increased intensity in the IR spectrum due to the increased dipole moments.

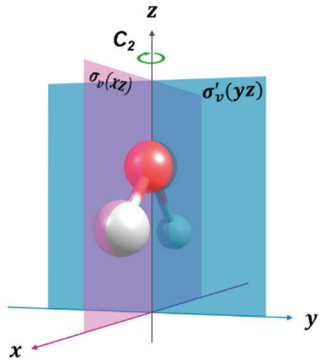

(a)

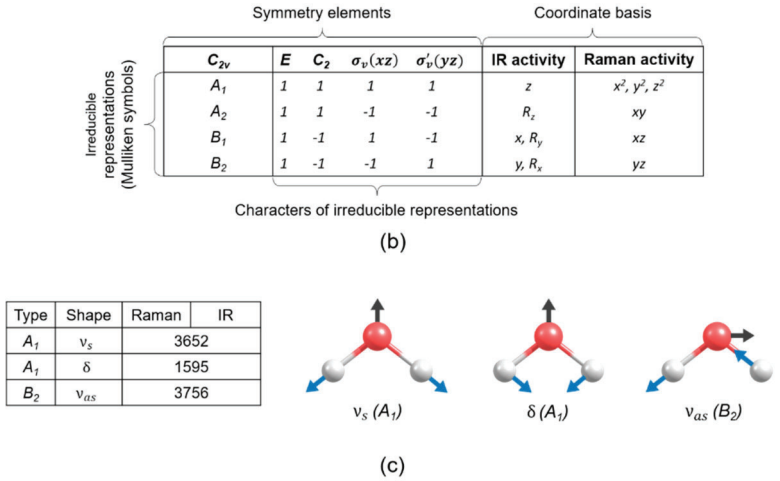

C_{2v}	E	C_2	$\sigma_v(xz)$	$\sigma'_v(yz)$	IR activity	Raman activity
A_1	1	1	1	1	z	x^2, y^2, z^2
A_2	1	1	-1	-1	R_z	xy
B_1	1	-1	1	-1	x, R_y	xz
B_2	1	-1	-1	1	y, R_x	yz

Type	Shape	Raman	IR
A_1	ν_s	3652	
A_1	δ	1595	
B_2	ν_{as}	3756	

Figure 1-10. Symmetry analysis for H_2O: (a) elements of symmetry, (b) character table, (c) normal vibrational modes, and the corresponding experimental vibrational frequencies observed for isolated H_2O molecules in the gas phase. The black and blue arrows indicate the directions of displacement of the O and H atoms, respectively, during the vibrations of H_2O.

With the increase in the number of atoms N in molecules, the number of vibrational modes increases threefold in accordance with 3N - 6(5). For example, the benzene molecule C_6H_6 has 30 vibrational modes (the number of atoms N = 12, $3 \times 12 - 6 = 30$), and its vibrational spectra may be expected to be quite complex. However, the benzene molecule possesses a centre of symmetry that constitutes a specific case in which the principle or rule of mutual exclusion applies. This rule states that there are no simultaneously active vibrational modes in Raman and IR spectra of the molecule with the centre of symmetry. In other words, for a centrosymmetric molecule, all vibrational modes that are Raman-active will

be inactive in the IR spectrum and vice versa. As shown in Figure 1-11, the equilibrium configuration of the benzene molecule has a much higher symmetry than the water molecule, and it belongs to the D_{6h} point group. Along with the axis of symmetry C_6 of the 6th-order, the molecule has a centre of symmetry *i*. During the operation of symmetry in this centre (inversion), the atoms symmetrically located at the same distances from the centre are interchanged in pairs. The molecule has a number of other symmetry elements, such as σ_h (the plane of the molecule itself), perpendicular to the axis C_6, six vertical planes of symmetry passing through this axis, and six horizontal axes of symmetry of the 2nd-order C_2 lying on the intersection of vertical planes with the plane of the molecule as shown in Figure 1-11(a). The superscripts prime ‘ and double prime “ denote the symmetric and antisymmetric operations with respect to the horizontal plane σ_h. For molecules like benzene that have an axis of symmetry of the order C_n where $n \geq 3$, along with singly degenerate representations *A* and *B*, there are doubly degenerate representations designated by *E* in the character table, which results in pairs of vibrations of different shapes with the same frequencies. Therefore, the number of different vibrational frequencies appears to be less than the number of vibrational modes. In the molecule that possesses the centre of inversion, all the normal modes of vibrations are either symmetric or asymmetric. The subscripts *g* and *u* are the symmetry notations that indicate, correspondingly, symmetric (“*gerade*” in German) and antisymmetric (“*ungerade*”) operations with respect to the inversion centre. For a polyatomic molecule of a certain symmetry, selection rules for vibrational transitions are different for IR and Raman spectra. These selection rules are determined by the symmetry of the combining vibrational states and the symmetry of the components of the dipole moment or the polarizability tensor, respectively. Totally symmetric

vibrations, which retain all of the symmetry of the molecule's equilibrium configuration, are always active in the Raman spectrum since the polarizability tensor always has components of a totally symmetric type. For molecules that do not possess a dipole moment due to symmetry, it is equal to zero not only for the equilibrium configuration but also for any configuration resulting from a fully symmetric vibration. Thus, in the vibrational spectrum of benzene C_6H_6, there are 14 in-plane and 6 out-of-plane vibrations. The symmetric vibrations (g) are active in Raman, and antisymmetric (u) are active in IR. The vibrations with the corresponding frequencies are summarized in the table in Figure 1-11(c). As an example, the vibrations that have the most intense experimentally observed Raman and IR peaks are shown in Figure 1-11(d), and their frequencies are emphasized in bold in the table. Indeed, the A_{1g} vibrations that maintain the centre of symmetry are Raman-active due to the change in the polarizability during the vibration but IR inactive since there is no change in the total dipole moment. On the contrary, the A_{2u} and E_{1u} vibrations that do not maintain the centre of symmetry are Raman inactive since there is no change in the polarizability; however, they are IR-active as the dipole moment arises due to the asymmetric change of the molecule with the vibrations.

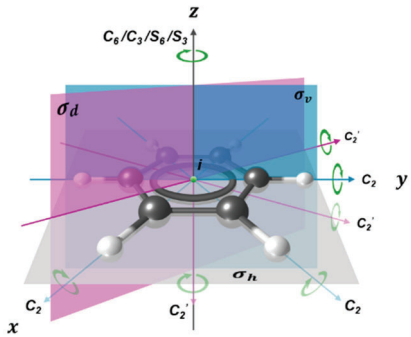

(a)

D_{6h}	E	$2C_6$	$2C_3$	$3C_2$	$3C_2'$	$3C_3''$	i	$2S_3$	$2S_6$	σ_h	$3\sigma_d$	$3\sigma_v$	IR activity	Raman activity
A_{1g}	1	1	1	1	1	1	1	1	1	1	1	1		x^2+y^2, z^2
A_{2g}	1	1	1	1	-1	-1	1	1	1	1	-1	-1	R_z	
B_{1g}	1	-1	1	-1	1	-1	1	-1	1	-1	1	-1		
B_{2g}	1	-1	1	-1	-1	1	1	-1	1	-1	-1	1		
E_{1g}	2	1	-1	-2	0	0	2	1	-1	-2	0	0	(R_x,R_y)	(xz, yz)
E_{2g}	2	-1	-1	2	0	0	2	-1	-1	2	0	0		$(x^2-y^2, 2xy)$
A_{1u}	1	1	1	1	1	1	-1	-1	-1	-1	-1	-1		
A_{2u}	1	1	1	1	-1	-1	-1	-1	-1	-1	1	1	z	z^3, $z(x^2+y^2)$
B_{1u}	1	-1	1	-1	1	-1	-1	1	-1	1	-1	1		$x(x^2-3y^2)$
B_{2u}	1	-1	1	-1	-1	1	-1	1	-1	1	1	-1		$y(3x^2-y^2)$
E_{1u}	2	1	-1	-2	0	0	-2	-1	1	2	0	0	(x,y)	(xz^2, yz^2) $[x(x^2-y^2), y(x^2-y^2)]$
E_{2u}	2	-1	-1	2	0	0	-2	1	1	-2	0	0		$[xyz, z(x^2-y^2)]$

(b)

Type	Shape	Raman	IR
A_{1g}	In-plane	**993**	
A_{1g}		**3062**	
A_{2g}		1326	
E_{2g}		608	
E_{2g}		1178	
E_{2g}		1596	
E_{2g}		3047	
B_{1u}			1010
B_{1u}			3060
B_{2u}			1110
B_{2u}			1648
E_{1u}			**1035**
E_{1u}			**1478**
E_{1u}			3070
B_{2g}	Out-of-plane	703	
B_{2g}		985	
E_{2g}		849	
A_{2u}			**673**
E_{2u}			405
E_{2u}			970

(c)

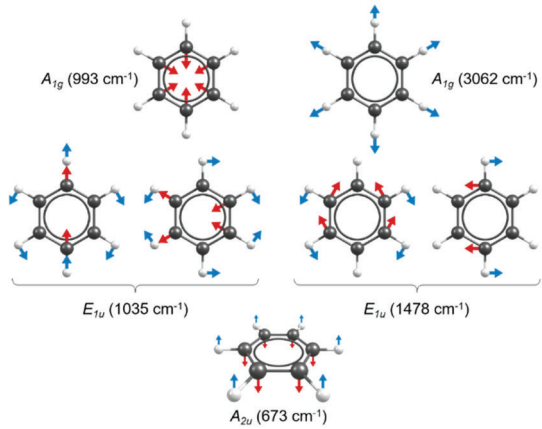

(d)

Figure 1-11. Symmetry analysis for the benzene molecule, C_6H_6: (a) elements of symmetry, (b) character table, (c) normal vibrational modes and the frequencies that can be observed experimentally, and (d) types of vibrations corresponding to the most intense peaks observed in the Raman and IR spectra. The red and blue arrows indicate the directions of displacement of the C and H atoms, respectively, during vibrations.

The IR and Raman spectra of benzene are shown in Figure 1-12. There is a handful of bands in the spectra since not all the bands which frequencies are listed in the table in Figure 1-11(c) can be experimentally detected due to their weak intensities. However, in the IR spectrum, there are noticeable peaks at 1960 and 1814 cm^{-1} not listed in the table that arise from overtones and combinations of lower wavenumber vibrations of the aromatic ring. As it follows from the rule of mutual exclusion explained above, there are no IR or Raman peaks that would have the same wavenumbers. In general, and as shown for benzene in Figure 1-11(d), symmetric and in-plane vibrations are the most prominent in the Raman spectrum, while asymmetric and out-of-plane vibrations are more pronounced in the IR one.

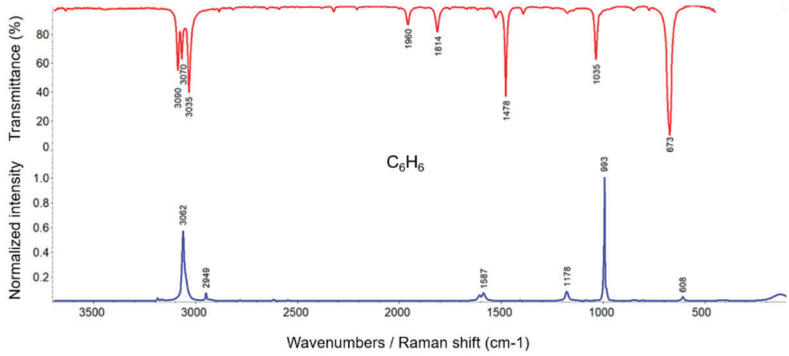

Figure 1-12. The IR (red) and Raman (blue) spectra of benzene C_6H_6.

Broadly speaking, the strong bands in the IR spectrum corresponds to the weak bands in the Raman spectrum and vice versa. Therefore, Raman and IR spectroscopies provide complementary information and, with the use of the two techniques, the active vibrational transitions can be found. Using

Raman and IR spectra, it is principally possible to describe a molecule completely, i.e., to establish the structure and symmetry of the molecule.

The application of group theory and the consideration of the selection rules becomes a progressively difficult problem as the size of the molecule increases and the symmetry diminishes. For example, in the vibrational spectra of molecules as large as cyclooctane C_8H_{16} (66 normal vibrational modes), many spectral bands overlap. In addition, a random coincidence of the spectral bands can be observed, whereas, in reality, they belong to different normal vibrations. Therefore, the unambiguous assignment of the vibrational frequencies in such cases will encounter significant difficulties.

1.2.7. Characteristic (group) frequencies

The prediction of a vibrational spectrum based on the knowledge of the structure and composition of a substance is known as a "direct" task of vibrational spectroscopy. The so-called "inverse" problem of spectroscopy is the determination of the characteristics of a substance (not directly observable in the spectrum) by its vibrational spectra. The "inverse" task of spectroscopy constitutes the primary goal of practical vibrational spectroscopy.

Since k and M in equation (1.38) are fairly reproducible for a specific type of chemical bond or a group of atoms composing a particular functional group, so-called characteristic or group frequencies can be established for vibrations of these moieties. The idea of the group frequencies is based on the assumption that vibrations of a specific bond or functional group are independent of the other vibrations in the molecule. Although molecules vibrate as a whole, complex motions can be treated in many instances as localized in the functional groups or well-defined structural units within the

molecule. The vast experimental material accumulated so far from the vibrational spectra of molecules confirms that the characteristic frequencies manifest at about the same wavenumbers regardless of the structure of the rest of the molecule. In other words, the observation of spectral bands in the spectra of different molecules in approximately the same relatively narrow spectral intervals is often indicative of a specific chemical functional group in the molecule. Thus, practical spectral analysis utilizes these characteristic group frequencies as molecular "fingerprints" to ascertain which functional groups are present in a sample. The IR and Raman characteristic group frequencies have been empirically accumulated and systemized in the correlation tables and charts over many years thanks to the hard work of many spectroscopists (Socrates 2004). The characteristic group frequencies have a principal practical value for the interpretation of Raman spectra of chemical compounds. These characteristic frequencies indicate the spectral interval where a particular vibrational band can be anticipated; however, as discussed above, the presence of a given band in vibrational spectra depends on the selection rules and the symmetry properties of the molecules. Some common characteristic Raman vibrational frequencies of functional groups in organic and inorganic compounds are provided in Appendix A.

As it follows from equation (1.38), the vibrational frequencies are expected to increase as the bond strength between the atoms participating in the vibration increases and the reduced mass of the atoms decreases. Stretching vibrations usually appear at higher frequencies than deformation vibrations. This trend takes place because the force constant for the stretching vibration typically has a higher value than that for the deformation vibration. Indeed, more energy is required to stretch the chemical bond than to deform it as the bonding force directly opposes the stretch. Inorganic compounds, such as

metal oxides, and organometallic compounds, which often contain heavy atoms or ions, usually have low vibrational frequencies. This tendency can be used to distinguish between vibrational frequencies of organic and inorganic compounds. Skeletal modes that involve the displacement of many atoms in a large molecule, such as polymers, usually appear at low frequencies.

Spectroscopists use Greek symbols and roman subscripts to describe the type of motion of a particular bond or a functional group associated with the frequencies in vibrational spectra. A list of vibrational mode symbols and their definitions is given in Table 1.2.

Table 1.2. The symbols used to assign specific spectral bands to the basic types of vibrations in chemical bonds and functional groups.

Symbol	Vibrational mode
ν_{as}	Asymmetric stretching
ν_{s}	Symmetric stretching
δ	Deformation (bending)
δ_{w}	Wagging
δ_{r}	Rocking
δ_{t}	Twisting

Thus, both IR and Raman spectroscopy are powerful and effective techniques for qualitative analysis, such as the identification of the molecular structure of chemical compounds based on their vibrational spectra. In practice, due to the higher likelihood of the manifestation of isolated bands in Raman spectra compared to their IR counterparts, Raman

spectra can be used to provide a more definitive identification of chemical compounds by searching the libraries of reference spectra.

1.3. Excitation wavelengths and fluorescence

As we know, vibrational spectra are observed as a result of transitions between quantized energy levels of molecules. Figure 1-13 shows the transitions in the cases of IR absorption, Raman scattering and fluorescence along with the approximate quantum yields (QY) of the corresponding processes. QY is defined as the number of times the acts of photon absorption, scattering or reemission occur divided by the number of incident photons in IR absorption, Raman scattering or fluorescence, respectively. For the sake of simplicity, only two vibrational levels, ground v_0 and the first excited v_1, are shown for the ground E_0 and the first excited E_1 electronic states. Respectively, only transitions between these levels are indicated by the arrows. The short-lived intermediate quantum state participating in Raman scattering is indicated by E_{virt}. The Raman transitions are shown for Stokes scattering only. Typical NIR-, Vis- and UV-laser excitation frequencies are marked in the energy (eV) and wavelength (nm) vertical axes.

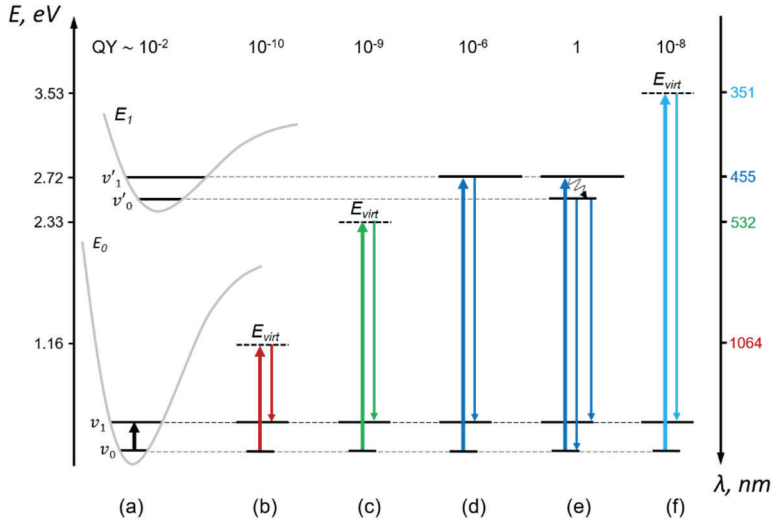

Figure 1-13. The transitions between the vibrational energy levels of a diatomic molecule in the form of Jablonski diagrams as the excitation energy increases from left to right and the approximate quantum yields (QY) of the corresponding processes: (a) IR absorption; (b) Raman with excitation in the near-infrared region (NIR-Raman); (c) Raman with excitation in the visible region (Vis-Raman); (d) resonance Raman; (e) fluorescence; and (f) Raman with excitation in the UV region (UV-Raman).

As mentioned above, the low quantum yield (QY) of the Raman effect is the major challenge in the practical detection of Raman scattering. Another challenge to Raman scattering comes from fluorescence emission that has a similar origin but much higher QY. Fluorescence may overwhelm or mask the relatively weak Raman signal, and the problem of circumventing fluorescence is of great importance in practical Raman spectroscopy.

Fluorescence and phosphorescence are special forms of a more general phenomenon known as photoluminescence (PL) – a light emission from a

matter after absorption of light. For the process of PL to arise, a molecule must first absorb a photon with enough energy (typically, in the visible or ultraviolet range of the optical spectrum) to excite it from the ground state to a higher electronic energy state. Then, the molecule quickly relaxes back down to the more stable ground state, releasing the excess energy. The release of the extra energy often occurs through a non-radial transition to a lower vibrational level of the same electronic state followed by the spontaneous reemission of a photon having less energy than the absorbed photon (see Stokes' rule above). The so-called non-radial decay is shown by the wavy arrow between v'_1 and v'_0 vibrational levels in Figure 1-13(e).

The major difference between fluorescence and phosphorescence is in the lifetime of the excited states of the fluorescent molecules. Fluorescence emission results from the transition between singlet electronic states, whereas photoluminescence occurs via the singlet-to-triplet transition, which is less probable than the singlet-to-singlet ones. Fluorescence has short lifetimes (fluorescence decay time) that typically range from 10^{-7} to 10^{-10} seconds; therefore, lasting as long as the matter is exposed to excitation light. The lifetime of the triplet state may be long enough to observe phosphorescence on a timescale up to minutes and even hours.

The term fluorescence was derived from the mineral fluorite or fluorspar (CaF_2). In 1852, G. Stokes noticed the colour-shifting effects in fluorspar and investigated the ability of the mineral to turn invisible ultraviolet into blue light. He gave this phenomenon the name fluorescence. The fluorescence spectrum appears at higher wavelengths (at lower energy) than the absorption spectrum because of the energy loss in the excited state due to vibrational relaxation, i.e., non-radiative dissipation of the excess vibrational energy through the heat transfer from the excited molecules to

the environment. As mentioned above, the shift between the wavelengths of excitation and emission in fluorescence is called the Stokes shift after its discoverer.

Figure 1-14 shows Raman spectra obtained from natural fluorite and pure grade CaF_2 of an optical window. The spectrum of natural fluorite exhibits a broad fluorescence "hump" that spreads from the anti-Stokes to the Stokes region. In naturally occurring fluorites, the fluorescence originates from traces of rear-earth elements which replace calcium in the crystal lattice or volatile hydrocarbons trapped in the lattice. In the spectrum of natural fluorite mined in England, fluorescence originates from divalent europium, which serves as the fluorescent centre (activator) to emit bright blue light from the mineral. In contrast to natural minerals, synthetically grown CaF_2 shows no signs of fluorescence due to its chemical purity.

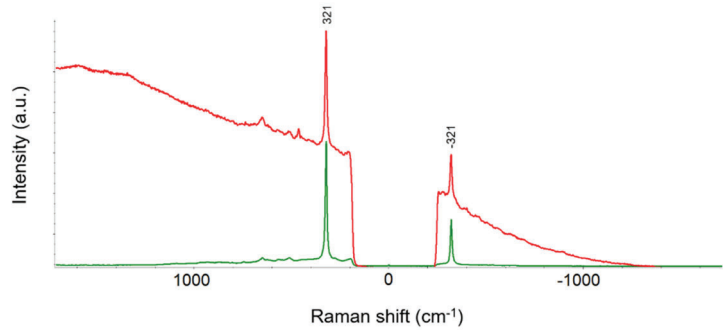

Figure 1-14. Raman spectra of natural fluorite from England (red) and pure grade CaF_2 optical window (green) in Stokes and anti-Stokes regions.

Fluorescence originates from fluorophores, the chemical compounds whose molecules typically contain several conjugated aromatic groups or heterocyclic systems with π-bonds. These parts of the molecules are called

chromophores, and they are responsible for the colours of the chemical compounds. Aromatic hydrocarbons, such as fluorescein, phenolphthalein, naphthalene, anthracene and perylene, generate a strong fluorescence upon excitation with visible light. The intrinsic fluorescence of biological tissues is often related to the presence of proteins, especially haemoglobin. In spectroscopy, this type of fluorescence is called autofluorescence. However, fluorescence may also originate from molecules of impurities of different nature and trace elements in the materials under study, as in the aforementioned natural fluorite.

In many practical cases, fluorescence background is a major problem when measuring Raman spectra. Indeed, the intensity of the fluorescence band is proportional to the amount of the absorbed light, and the maximum possible QY of fluorescence is 1.0 (100%) when each photon absorbed results in a photon emitted. Fluorophores that provide QY of 0.1 are considered to be strong fluorescent compounds. Thus, the fluorescence background can be up to 10^{10} times more intense than Raman scattering. Even weak fluorescence from the analyte or impurities in the sample is often much stronger than the Raman scattering and, therefore, can obscure the Raman bands.

There are mathematical, instrumental and sample preparation methods to reduce fluorescence in Raman spectra. These methods are based on the essential differences between the processes of fluorescence and Raman scattering. The differences and the corresponding methods are as follows:

1) Most fluorescent molecules and chromophores exhibit broad and usually structureless emission bands, while Raman peaks are narrow. This distinction allows various mathematical methods for baseline

correction to be utilized to remove the fluorescence background. One of the most frequently used methods for fluorescence correction in Raman spectra is based on polynomial fitting applied after or in real time with spectral measurements (Zhao, et al. 2007). Another so-called wavelet transform (WT) method (Chi, et al. 2019) provides a decomposition of the recorded spectrum into a low-frequency component (background) and the high-frequency components (Raman peaks and the spectral noise). The alternative instrumental approach is shifted-excitation Raman difference spectroscopy (SERDS). In this method, two Raman spectra are sequentially recorded using excitation laser lines slightly shifted by frequency (Gebrekidan, et al. 2016). The fluorescence emission, which is not as strongly frequency-dependent, does not change while the Raman spectrum shifts following the change of the excitation frequency. In this way, the fluorescence can be removed by mutual subtraction of the recorded Raman spectra followed by a spectral reconstruction procedure to recover the fluorescence-free Raman spectrum. However, once the intensity of the fluorescence background approaches the maximum of the detector's dynamic range and the shot noise becomes comparable with the intensities of Raman peaks, neither of these methods can be utilized effectively.

2) In contrast to Raman scattering, fluorescence only occurs if a molecule is excited up to a higher electronic state. Instrumental methods can reduce fluorescence by using longer excitation wavelengths, such as the visible 785 nm or near-infrared 830 and 1064 nm, where the photon does not have enough energy to excite most of molecules to higher electronic states. FT-Raman spectrometers that have been commercially available since 1986 and

recently developed dispersive instruments with 1064 nm excitation do not produce fluorescence and therefore are considered to provide truly fluorescence-free measurements. However, the drawback of the longer wavelength excitations is the significant decrease in Raman scattering efficiency as it follows from (1.34). Although dispersive instruments operating in the 780 - 830 nm excitation range improve detection limits on account of more sensitive silicon-based CCD detectors, their usage does not exclude fluorescence in all problematic cases.

3) The broad fluorescence band is independent of the wavelength of excitation light, while the position of a Raman peak in the wavelength scale depends on the excitation wavelength. With a UV laser excitation below 300 nm, fluorescence may be excited, but the fluorescence emission appears to be widely separated in the wavelength scale from the region of Raman scattering (Fig. 1-15(a)) so that the Raman spectrum can be recorded without the fluorescence interference (Asher and Johnson 1984). Moreover, for selected samples, the resonance Raman effect can increase the Raman intensities by several orders of magnitude. Meanwhile, one must use the UV excitations with great care as the high energy UV photons can cause damage to the sample and induce unwanted changes in biological samples, in particular.
4) Raman instruments offering multiple excitation wavelengths provide a great advantage in cases where samples show fluorescence in the visible range. The intensity of the Raman band can be significantly enhanced to overcome fluorescence when the frequency of the excitation wavelength gets close to the transition energy between two electronic states (Fig. 1-13(d)). This enhancement is the result

of the resonance Raman effect. This effect is achieved in resonance Raman spectroscopy (RRS) that selectively increases the Raman signal of chromophores in molecules. Ideally, tunable lasers for fine-tuning the excitation wavelength to the resonance with an electronic transition of the chromophores are required to enhance resonance Raman over possible resonance fluorescence effect.

5) The lifetime of fluorescence is of the order of nanoseconds. It is much longer than the Raman transition that is completed within a picosecond or less. Due to the lifetime differences, discrimination between Raman and fluorescence processes is possible (Fig. 1-15(b)). Complete or partial rejection of the fluorescence emission is achieved with time-resolved techniques in which ultrafast pulse lasers are used for excitation and time-gated devices (e.g., the intensified CCD detectors that are considered in Chapter Two) for detection (Everall, et al. 2001). However, only relatively recently, the cost and reliability of the time-gated technologies advanced sufficiently for the first commercial release of a Raman spectrometer by Timegate Instruments (Timegated Raman Technology n.d.) with picosecond pulsed excitation and time-resolved single-photon counting detection.
6) As mentioned above, fluorescence may originate from trace impurities or minor components of the sample. Photobleaching (sometimes termed “fading”) is a method of sample treatment that Raman spectroscopists often apply to decrease fluorescence originating from the contaminant samples. Photobleaching causes photolytic destruction of fluorescent impurities and, thus, can remove or partially quench fluorescence from the sample. Photobleaching is achieved by extended exposure of the sample to

intense laser radiation before measuring the Raman spectrum. The exposure time for adequate photobleaching can range from a few seconds to hours, depending on the nature and amount of the fluorescent impurities in the sample. Photobleaching should be used with care to ensure that the acquired Raman spectrum originates from the material under study rather than laser-induced photolysis products.

7) Another sample preparation technique is based on the physicochemical process of quenching that decreases the intensity of the emission from the fluorescing molecules. Processes, such as energy transfer or non-radiative decay by collisional exchange with surrounding molecules (Dong, et al. 2011), result in quenching, especially upon increasing pressure or the temperature. In the practice of Raman spectroscopy, the fluorescence background can be efficiently quenched, and the Raman signal can be significantly enhanced when a sample is placed in direct contact with metal nanoparticles (NPs) or deposited on a rough metal surface of predominantly Au or Ag. The fluorescence is quenched by energy transfer from the fluorescing molecules in the excited state to the metals. Taking advantage of the effect of surface-enhanced Raman scattering (SERS) that occurs when the sample molecules are situated in close proximity to the metals, it is possible to observe enhanced Raman bands over the reduced fluorescence (Campion and Kambhampati 1998). However, the improvements in Raman spectra significantly depend on the size of NPs or shapes and regularities of the metal substrate roughness.
8) If fluorescence originates from impurities in a sample or from the matrix surrounding a micro object of interest, the use of a confocal Raman microscope can mitigate the fluorescence background by

limiting the sampling volume from which the Raman signal is measured. This can be achieved by decreasing the size of the confocal diaphragm (pinhole aperture) that controls the sampling volume. The role of the confocal diaphragm will be considered in detail in Chapter Three.

A more detailed description of some of the above methods can be found in a review by Wie et al. (Wei, Chen and Liu 2015).

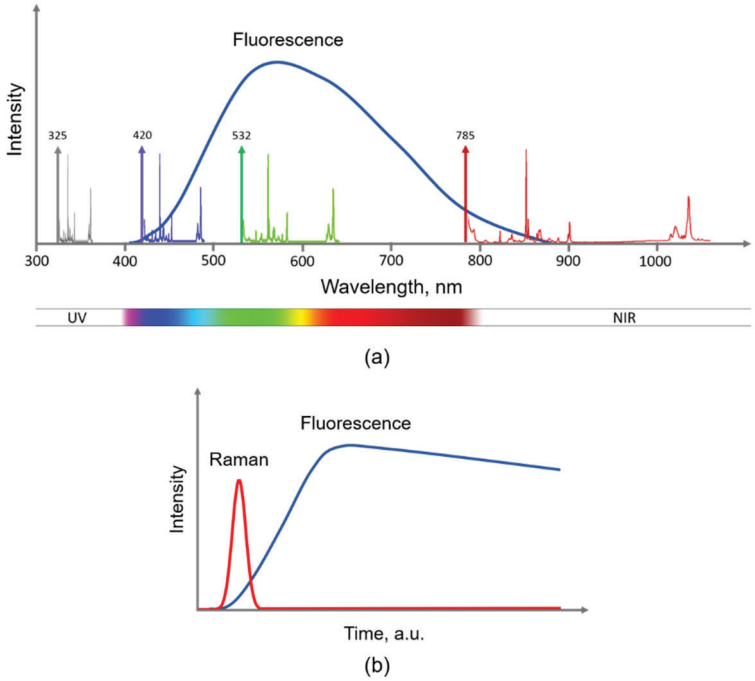

Figure 1-15. Raman scattering and fluorescence emission in (a) frequency (wavelength) and (b) time domains. The vertical coloured arrows in (a) indicate typical laser excitation wavelengths at 325 nm (invisible UV), 420 nm (blue), 532 nm (green) and 785 nm (dark red). To imagine how spectral background may be

altered by the superposition of the fluorescence emission, the Raman spectrum of polystyrene is shown at each excitation wavelength. The spectra of polystyrene are presented in an approximate Raman shift range of 50–3300 cm^{-1}. In the time domain (b), Raman scattering occurs quickly within the picosecond timescale and, thus, can be discriminated from fluorescence emission that has a much longer decay time.

It is worth mentioning that fluorescence is one of the most sensitive analytical techniques. Fluorescence can be detected even from a single molecule, and it is used in many chemical and biochemical applications. Efficient fluorescence detecting relies on the fact that spectrofluorometry measures the intensity of emitted fluorescence directly when filters or monochromators suppress the intense excitation light. In contrast, spectrophotometry is an absorption technique that measures the ratio of the intensities of the incident and transmitted light beams.

1.4. Polarization

Raman spectroscopy using a polarized excitation light provides useful information about molecular structure and the direction-dependent properties of samples, such as solid or liquid crystals, oriented polymer films and fibres, carbon nanostructures and other anisotropic materials. In modern Raman instruments, the lasers used for excitation are usually linearly polarized by design. Hence, Raman spectra measured using the naturally polarized light may not be well reproducible if the relative orientation of the ordered samples and direction of the laser polarization is not taken into consideration. For this reason, in general-purpose instruments, the laser excitation beam is purposely depolarized to assure consistent results regardless of the sample orientation. The Raman spectra obtained using the depolarized laser excitation are referred to as depolarized

Raman spectra. Advanced Raman instruments can be configured to perform both depolarized and polarized Raman measurements.

The polarization of the laser beam can be achieved using a polarizer or polarization filter. This optical device transmits a single state of polarization while deviating, reflecting or absorbing light with the orthogonal state of polarization. Classical quarter-wave plates constructed out of birefringent crystals, conventional interference thin-films, high-performance thin films composed of silver nanoparticles sandwiched between two glass substrates, etc., can be used for this purpose. The polarizer is oriented accordingly to obtain a required direction of polarization of the laser beam.

When a light beam passes through a polarization filter, the light becomes polarized such that the electric field vector of the light wave is oriented perpendicular to the light beam. This light is called linearly polarized, and it differs from the light wave with a freely rotating electric field vector of the depolarized light. When an ordered sample is exposed to the linearly polarized light, the sample may interact differently than it does for depolarized light, depending on how the sample is oriented relative to the direction of polarization. The scattered light may consist of the components with the directions of polarization parallel and perpendicular to the electric field vector in the incident light.

The detailed treatment of Raman intensities is based on a semiclassical theory of polarizability developed by Czech physicist George Placzek (Placzek 1931). One form of the expressions derived from Placzek's theorem for the intensities of parallel $I_{\parallel}$ and perpendicular $I_{\perp}$ components of scattered light is:

$$I_{\parallel} = \frac{16\pi^3 h(\bar{\nu}_0 - \bar{\nu})^4}{135c\bar{\nu}(1 - e^{-hc\bar{\nu}/kT})} N(45\alpha^2 + 4\gamma^2) I_0$$

and

$$I_{\perp} = \frac{16\pi^3 h(\bar{\nu}_0 - \bar{\nu})^4}{135c\bar{\nu}(1 - e^{-hc\bar{\nu}/kT})} 3N\gamma^2 I_0 \,,$$

where I_0 is the intensity of excitation light with the wavenumber $\bar{\nu}_0$, $\bar{\nu}$ is the wavenumber of a Raman spectral band, and N is the number of scattering molecules.

The ratio of the intensities of the perpendicular to the parallel component is called the depolarization ratio ρ:

$$\rho = \frac{I_{\perp}}{I_{\parallel}} = \frac{3\gamma^2}{45\alpha^2 + 4\gamma^2} \,.$$

This ratio represents an important value measured in Raman spectroscopy because it depends on the symmetry of the molecule and the normal vibrational mode. The factors α and γ are known as spherical or mean polarizability and anisotropy, respectively. The spherical polarizability is defined by the diagonal terms of the polarizability tensor (1.24) as

$$\alpha = \frac{1}{3}\left(\alpha_{xx} + \alpha_{yy} + \alpha_{zz}\right), \tag{1.39}$$

while the anisotropy is calculated from the off-diagonal terms using the equation

$$\gamma^2 = \frac{1}{2}\Big[\left(\alpha_{xx} - \alpha_{yy}\right)^2 + \left(\alpha_{yy} - \alpha_{zz}\right)^2 + (\alpha_{zz} - \alpha_{xx})^2 + 6\left(\alpha_{xy}^2 + \alpha_{yz}^2 + \alpha_{zx}^2\right)\Big]. \quad (1.40)$$

There are four fundamentally important values of the depolarization ratio ρ depending on the combination of the symmetry of the molecule and the normal vibration:

1) The molecule belongs to a spherical group of symmetry, such as tetrahedral T_d (e.g., carbon tetrachloride CCl_4, white phosphorous P_4, or methane CH_4), octahedral O_h (sulfur hexafluoride SF_6) or icosahedral I_h (buckminsterfullerene C_{60}), and the normal vibration is totally symmetrical. For example, if the molecule of CCl_4 is irradiated by the linearly polarized light, then the electric field vector of the induced dipole (1.8) oscillates in the same direction. For totally symmetric vibrations, such as the C-Cl stretching vibration corresponding to the band at 459 cm^{-1} in the Raman spectrum of carbon tetrachloride, the polarizability ellipsoid always has a shape of a sphere, and the molecule is polarized equally in every direction. Thus, the light emitted by the induced dipole retains the polarization of the incident light, and the component $I_\perp$ appears to be equal to zero. According to the equations (1.39) and (1.40), the spherical polarizability $\alpha^2 > 0$, but $\gamma^2 = 0$ as the result of $\alpha_{xx} = \alpha_{yy} = \alpha_{zz}$ and $\alpha_{xy} = \alpha_{yz} = \alpha_{zx} = 0$.

   Consequently, $\rho = 0$ and this vibration, as well as the corresponding Raman band, is called polarized.

2) The molecule possesses spherical symmetry, but the vibrational mode is asymmetric. Then, this vibration changes the polarizability shape from a sphere to an ellipsoid, and the dipole is mostly induced along the direction of the largest polarizability, namely, along one of the minor axes of the ellipsoid (Fig. 1-6). In the liquids and gases in which the molecules are randomly oriented, their ellipsoids of polarizability and the induced dipoles are also randomly oriented so that the anisotropy γ^2 will be nonzero while the spherical polarizability is $\alpha^2 = 0$ due to $\alpha_{xx} = \alpha_{yy} = \alpha_{zz} = 0$.

   Thus, $\rho = \frac{3}{4}$, and the band is said to be depolarized.

3) The vibrational mode is symmetric, but the molecule does not possess spherical symmetry. In this case, there may be both diagonal and off-diagonal terms in the polarizability tensor. Correspondingly, both the spherical polarizability α and the anisotropy γ will be nonzero. As a result, the values of the depolarization ratio ρ are in the range of $0 \leq \rho \leq \frac{3}{4}$.

4) For an asymmetric vibration in the molecule with lower than the spherical symmetry and, the vibration results in a depolarized Raman band with the depolarization ratio $\rho \geq \frac{3}{4}$.

It is worth mentioning that the depolarization ratio ρ quantitatively estimated from experimentally measured Raman spectra may differ from the theoretical values presented above. Namely, $\rho = 0$ for highly polarized bands is hard to reach in the experimental spectra. Indeed, the quality of

different optical components of the Raman spectrometer (diffraction gratings, polarizer and beamsplitter), elements of transferring and collecting optics (mirrors, prisms, lenses and objectives) and even sample cells influence the state of polarization of the light beam passing through them (Allemand 1970, Adar 2017). In practice, the depolarization ratios obtained for highly polarized bands in the ranges of values $0 < \rho \leq 0.1$ are considered to be satisfactory.

In a typical polarization experiment, a Raman spectrum is collected with the light linearly polarized in one direction, and then another spectrum is collected with the light polarized perpendicular to the first direction. Normally, the polarization experiment is performed without a polarization analyzer so that the scattered light of both polarizations is measured at its maximum intensity. However, polarizers and analyzers are the parts of Raman polarization optics in which the analyzer acts as a second polarizer. The main functional purpose of the analyzer is that it can be used to accurately check whether the polarization of the light has been changed after the interaction with a sample. The analyzer can be usually set to be either parallel or perpendicular to the polarization of the excitation light, but the intensity of Raman scattering decreases especially noticeably if the analyzer and polarizer are oriented orthogonally (crossed). Nevertheless, there are situations for which the use of the analyzer can be helpful in the characterization of solid-state structures and their band assignment.

When making polarization measurements, it is important to keep track of the directions of polarization, i.e., the orientation of the polarizer and analyzer, so that the results can be unambiguously interpreted. In polarization-dependent Raman spectroscopy, it is usual to designate the directions of incident and collected light and the directions of polarization

using Porto's notation introduced by and named after Brazilian physicist Sergio Porto. Porto's notation describes the position of a sample with respect to orientations of the polarizer and analyzer. The designation consists of four terms written in the form of

$$a(bc)d$$

and defined as follows:

a - direction of propagation of the incident laser beam
b - direction of polarization of the incident laser beam
c - direction of polarization of scattered light
d - direction of observations of scattered light

Thus, the outside terms a and d define the direction of the incident laser beam and the observation of scattered light, respectively. The terms b and c in the parentheses describe directions of polarization set by the polarizer and analyzer for the incident and scattered light, respectively.

In a Raman microscope, the so-called 180-degree backscattering sampling configuration is implemented by design. This means that the excitation laser beam coming from the microscope objective propagates along the vertical axis, and the Raman scattering is collected using the same microscope objective along the same axis but in the opposite direction. By convention, the Z-axis of the Cartesian coordinate system is chosen to be oriented the vertical way. The convention is also to use an overbar on the Z-axis notation to designate the opposite direction $\bar{Z}$. Thus, as follows from Figure 1-16, there are only four principal polarization orientations that can be analyzed with a Raman microscope:

Z(XX)$\bar{Z}$ - laser is polarized parallel to an *X*-axis; analyzer is set to pass the light polarized in *X*-axis;

Z(YY)$\bar{Z}$ - laser is polarized parallel to a *Y*-axis; analyzer is set to pass the light polarized in *Y*-axis;

Z(XY)$\bar{Z}$ - laser is polarized parallel to an *X*-axis; analyzer is set to pass the light polarized in *Y*-axis (polarized and analyzer are crossed);

Z(YX)$\bar{Z}$ - laser is polarized parallel to a *Y*-axis; analyzer is set to pass the light polarized in *X*-axis (polarized and analyzer are crossed).

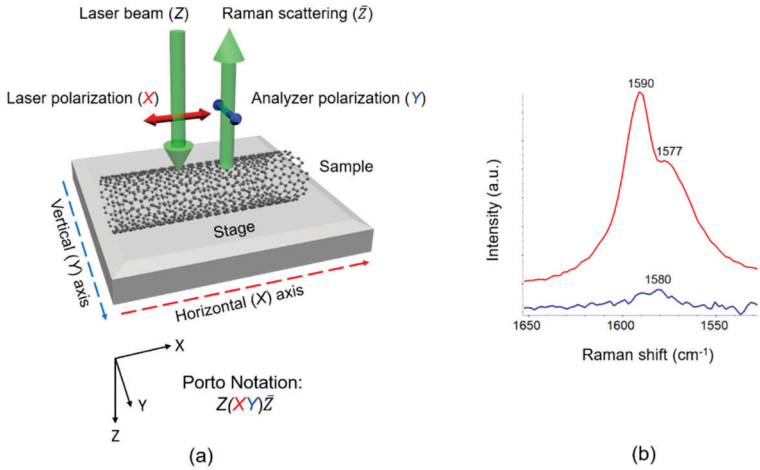

Figure 1-16. Raman polarization measurements: (a) the orientation of the directions of polarization (axes) in a typical Raman microscope and Porto notation (the paths of the laser beam and Raman scattering light are spaced apart for simplicity); (b) the change in the intensity of the G-band in the spectrum of an individual single-wall carbon nanotube (SWCNT) with polarization.

For an anisotropic sample, it is recommended to make measurements for all four positions of the polarizer and analyzer relative to the sample's orientation to describe the sample by means of polarization-dependent Raman spectroscopy. Polarized Raman with angle resolution, when the analyzer can be set to any angle between 0 and 90 degrees defined by a user, provides additional flexibility in Raman polarization experiments. It is also a good practice to measure the spectrum with the non-polarized incident laser beam to characterize the sample as completely as possible.

Historically, polarization-dependent Raman spectroscopy has helped to determine the symmetry of the vibrations and correctly assign the observed Raman bands. Classic examples of the polarized Raman spectra of cyclohexane and carbon tetrachloride can be found in many textbooks and original articles. In general, polarization-dependent Raman spectroscopy provides information about preferentially oriented molecules or materials since any nonrandom orientation may affect the depolarization ratio ρ of the Raman bands. Figure 1-16(b) illustrates the change in intensity of the G-band in the spectrum of an individual single-wall carbon nanotube (SWCNT) with polarization parallel and perpendicular to the direction of the nanotube axis. It has been observed experimentally (Duesberg, et al. 2000) that the intensity of the G-band is highest when the polarization of the incident light is parallel to the nanotube axis, and the band almost disappears when the polarization is perpendicular. The experimental observations were attributed to a strongly anisotropic optical property related to the one-dimensional shape of the nanotube. Polarized Raman spectroscopy is a powerful method to characterize the orientation and quality of alignment of SWCNT and multi-wall carbon nanotubes (MWCNT) in ordered films that have a significant practical role in modern

high-speed and low-powered semiconductor electronics (Cervini, et al. 2008, Wieboldt, et al. 2016).

A specific case of polarization is the use of circularly polarized light in the Raman Optical Activity (ROA) technique. The technique measures a difference in the intensity of Raman scattering from chiral molecules using the right- or left-circularly polarized incident laser beam. If the incident light is linearly polarized, the chiral molecules rotate the plane of polarization inducing a small circularly polarized component in Raman scattering. This component can be found experimentally by measuring the angle of rotation. The chiral molecules exist as two optical isomers or enantiomers that are mirror images of each other and are not identical, i.e., non-superposable. As an example, the chiral molecule of bromochlorofluoromethane and rotation of the plane of the linearly polarized incident light by a sample of one enantiomer of a chiral compound are shown in Figure 1-17. Enantiomers rotate the plane of polarization to equal extents but in opposite directions.

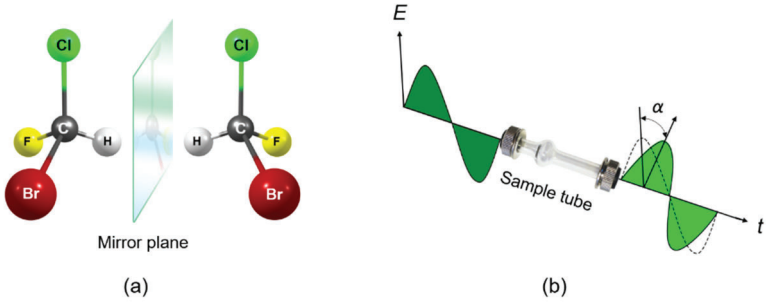

Figure 1-17: The chiral molecule of bromochlorofluoromethane with the mirror plane through which its enantiomers are reflected (a) and the plane of linearly polarized incident light *E* rotated through an angle α by a sample containing an enantiomer of a chiral compound (b).

Many biological and drug molecules are enantiomers. Sometimes the effect of two enantiomers on biological organisms or the physiological action of a pharmaceutical substance is markedly different. ROA provides detailed information about the configuration of the enantiomers and conformational dynamics. A comprehensive analysis of ROA techniques and applications can be found in the review by Barron (Barron 2015). Although ROA is still a somewhat specialized technique, the technical developments and experimental progress in recent years resulted in the commercialization and popularization of this technique by BioTools (www.btools.com n.d.).

1.5. Advantages of Raman spectroscopy

As mentioned above, Raman spectroscopy provides chemical and structural information complementary to FTIR. In general, chemical compounds manifest distinctive spectral bands in their Raman and FTIR spectra, but they may not coincide due to different selection rules. Moreover, no IR and Raman bands can be observed at the same wavenumbers in the spectra of centrosymmetric molecules, to which the rule of mutual exclusion applies. Which technique provides better results depends on the analyzed samples, the concentration of analytes, the surrounding matrix or solution, the presence of impurities, the desired sampling method and whether the sample is under temperature or pressure. For many applications, Raman spectroscopy offers indisputable advantages; the major ones are listed below:

1) No sample preparation is required, or the sample preparation is rather trivial. In contrast to FTIR, which often requires dissolution, diluting or pressing samples into pellets, no physical or chemical treatment of the sample is typically necessary for Raman

measurements. In principle, if a sample under study fits into the sample compartment of a Raman instrument, the Raman spectrum of the sample can be obtained.

2) The technique is nondestructive and saves the sample integrity provided that careful control of the laser radiation density is carried out to ensure that there is no laser-induced modification to the sample. Then, after the Raman measurements, the sample can be treated and analyzed by other methods. The nondestructive aspect is of paramount importance for forensic analyses where the samples collected during an investigation should be kept intact.
3) The non-contact method of examination of samples by light provides safe procedures for both samples and operators. On the one hand, the procedure ensures that no contamination is introduced into the sample. On the other, hazardous, toxic or unstable to air or moisture samples can be measured through a protective sampling insertion or placed in sealed glass containers. In FTIR spectroscopy, this is not possible because glass is a strong IR absorber.
4) Samples can be analyzed through transparent glass windows, cuvettes, vials, bottles or translucent polymer packaging due to the tightly focused laser beam in the Raman spectrometer. Recent developments and commercialization of Surface Offset Raman Spectroscopy (SORS) allow routine measurement and identification of materials in closed opaque containers.
5) Remote analysis can be conveniently realized in Raman spectrometers. Fiberoptic probes transmit laser light and collect Raman scattering over long distances, up to hundreds of meters away from the mainframe of the Raman instrument.

6) The nondestructive, noninvasive and non-contact nature of the Raman measurement makes it very suitable for *in situ*, *in vitro* and *in vivo* analysis. It can be used to monitor chemical reactions *in situ* within a reaction chamber, often at cryogenic or very high temperatures and pressures, including the identification and quantitation of combustion products in flames and plasmas. Raman spectroscopy can be used for *in vitro* and *in vivo* characterization of the chemical and morphologic structure of biological cells, tissue and microorganisms.
7) Since water is a weak Raman scatter and does not manifest much in Raman spectra, Raman spectroscopy is ideal for the study of analytes, e.g., biological compounds, in aqueous solutions. There is no need for time-consuming sample extraction or drying that may also alter the chemistry of the sample. This is a significant advantage over FTIR spectroscopy, which capabilities are limited by the strong absorption of water when the analysis of aqueous solutions is required.
8) Raman spectroscopy is applicable to a wide range of substances and materials. Raman spectra of liquids, solids, gases (even those composed of homonuclear molecules), vapours and aerosols can be obtained. The only exception is pure metals and alloys, which just reflect the light. However, metal oxides, carbides and nitrides are Raman-active. Samples can be in the form of a solution, slurry, gel, powder, chunk, crystal, wafer, film or fibre with various sizes, shapes and thicknesses.
9) During Raman spectral measurements, the full spectral region of fundamental vibrations typically from 50 to 3500 cm^{-1} can be recorded in a single exposure. Thus, Raman spectra are appropriate

for the characterization of organic and inorganic compounds, such as used in polymer composites. Indeed, in their spectra, the Raman bands of organic matrix and inorganic fillers can be simultaneously measured and analyzed. In contrast, FTIR instruments often require reconfiguration (a change of beamsplitters, detectors or sources) in order to cover the spectral region below 400 cm^{-1}.

10) Beyond general material characterization and identification, Raman spectroscopy also provides information on more subtle chemical effects, such as the extent of crystallinity, polymorphism, phase transformation, strain in materials and protein secondary structure.
11) Often, due to the higher likelihood of the presence of the Raman bands that are well resolved and do not overlap with their neighbours, Raman spectra are better suitable for material identification by a spectral library search.
12) Both Raman and FTIR methods can be used with the microscopic technique. However, combining a Raman spectrometer with a microscope results in one of the major advantages over FTIR: an order of magnitude better spatial resolution. Spatial resolution is improved because Raman spectroscopy uses an excitation wavelength in the visible region of the spectrum, whereas FTIR uses longer wavelengths in the infrared region. The shorter excitation wavelengths of the visible light result in a smaller diffraction limit and can, therefore, be focused onto a smaller spot on the sample than the longer wavelengths of infrared light. Raman microscopy is currently capable of probing objects as small as about 0.5 μm, whereas an FTIR microscope can resolve structures of 5–10 μm at best. Thus, individual particles, defects, trace

amounts of substances, biological cells and microorganisms can be analyzed by Raman microscopy on a sub-micron level.

13) A confocal analysis is another unique advantage of Raman microscopy. A confocal Raman microscope allows the measurement of a minuscule discrete volume in a transparent sample and, thus, can provide the analysis at different depths and even 3D spectrochemical rendering without physical slicing of the sample. The confocal capability is particularly useful for the nondestructive analysis of layered samples (e.g., multi-layered polymer films), volume inclusions and defects (in glass materials, plastics or minerals), semiconductor thin films and graphene layers.

In fairness, it should be noted that Raman spectroscopy also has known disadvantages. The major one is certainly the fluorescence interference that was considered in Section 1.3. Also, the laser power aimed at the sample needs to be thoroughly controlled to avoid local heating or photodecomposition, especially in resonance Raman experiments where the laser frequency is intentionally tuned into the absorption band of the compound under study. From an instrumental viewpoint, a research-grade Raman spectrometer, particularly a confocal Raman microscope with advanced options, costs noticeably more than its approximate FTIR equivalent, although more affordable desk-top and portable versions of Raman spectrometers have been manufactured in recent years.

Nevertheless, because of the significant advantages listed above, Raman spectroscopy plays an important role in both R&D and QA/QC in a variety of academic fields and industries, such as semiconductors, polymers, carbon

nanomaterials, pharmaceuticals, batteries, life sciences, art and archeology. Some of the applications will be illustrated in Chapter Four.

References

Adar, F. 2017. "Raman Polarization Measurements: Keeping Track of the Instrumental Components' Behavior." *Spectroscopy* 32 (2): 14–22.

Allemand, C.D. 1970. "Depolarization Ratio Measurements in Raman Spectroscopy." *Appl. Spectrosc.* 24 (3): 348–353.

Asher, S. A., and C. R. Johnson. 1984. "Raman spectroscopy of a coal liquid shows that fluorescence interference is minimized with ultraviolet excitation." *Science* 225(4659): 311–313.

Barron, L.D. 2015. "The development of biomolecular Raman optical activity spectroscopy." *Biomed. Spectrosc. Imaging* 4: 223-253. doi: 10.3233/BSI-150113.

Cabannes, J., and P. Daure. 1928. "Analyse spectroscopique de la lumiere obtenue par diffusion moleculaire d'une radiation monochromatique au sein d'un fluide." *Comptes rendus de l'Académie des Sciences* 186: 1533–1534.

Campion, A., and P. Kambhampati. 1998. "Surface-enhanced Raman scattering." *Chem. Soc. Rev.* 27 (4): 241–250.

Cervini, R., G.P. Simon, M. Ginic-Markovic, J.G. Matisons, C. Huynh, and S. Hawkins. 2008. "Aligned silane-treated MWCNT/liquid crystal polymer films." *Nanotechnology* (19): 175602.
https://doi.org/10.1088/0957-4484/19/17/175602.

Chi, M., X. Han, Y. Xu, Y. Wang, F. Shu, W. Zhou, and Y. Wu. 2019. "An Improved Background-Correction Algorithm for Raman Spectroscopy Based on Wavelet Transform." *Appl. Spectrosc.* 73 (1): 78–87.

Dirac, P.A.M,, and R.H. Fowler. 1927. "The quantum theory of dispersion." *Proceedings of the Royal Society of London, Series A* 114 (769): 710–728.

Dong, L., Ye, F., J. Hu, S. Popov, A.T. Friberg, and M. Muhammed. 2011. "Fluorescence quenching and photobleaching in Au/Rh6G nanoassemblies: Impact of competition between radiative and non-radiative decay." *J. Eur. Opt. Soc.* 6: 11019-1 - 11019-5.

Duesberg, G. S., I. Loa, M. Burghard, K. Syassen, and S. Roth. 2000. "Polarized Raman Spectroscopy on Isolated Single-Wall Carbon Nanotubes." *Phys. Rev. Lett.* 85 (25): 5436–5439.

Everall, N., T. Hahn, P. Matousek, A. W. Parker, and M. Towrie. 2001. "Picosecond Time-Resolved Raman Spectroscopy of Solids: Capabilities and Limitations for Fluorescence Rejection and the Influence of Diffuse Reflectance." *Appl. Spectrosc.* 55 (12): 1701–1708.

Fabelinskii, I.L. 1998. "Seventy years of combination (Raman) scattering." *Physics-Uspekhi* 41 (12): 1229–1247.

n.d. *Gaussian.* Accessed 4 23, 2019. http://gaussian.com/.

Gebrekidan, M.T., C. Knipfer, F. Stelzle, J. Popp, S. Will, and A. Braeuer. 2016. "A shifted-excitation Raman difference spectroscopy (SERDS) evaluation strategy for the efficient isolation of Raman spectra from extreme fluorescence interference." *J. Raman Spectrosc.* (47): 198-209. https://doi.org/10.1002/jrs.4775.

Griffiths, P.R., and J.A. de Haseth. 2007. *Fourier Transform Infrared Spectrometry.* Second. Hoboken, NJ: John Wiley & Sons, Inc. doi:10.1002/047010631X.

Kramers, H.A., and W. Heisenberg. 1925. "Über die Streuung von Strahlung durch Atome." *Zeitschrift für Physik* 31: 681–708.

Landsberg, G.S., and L.I. Mandelstam. 1928. "Eine neue Erscheinung bei der Lichtzerstreuung in Krystallen." *Die Naturwissenschaften* 16: 557–558.

Long, D.A. 2002. *The Raman Effect: A Unified Treatment of the Theory of Raman Scattering by Molecules.* John Wiley & Sons Ltd. doi:10.1002/0470845767.

Morse, Philip M. 1929. "Diatomic Molecules According to the Wave Mechanics. II. Vibrational Levels." *Phys. Rev.* 34 (1): 57-64. https://doi.org/10.1103/PhysRev.34.57.

Ogden, J.S. 2001. *Introduction to Molecular Symmetry.* Oxford University Press.

Placzek, G. 1931. "Intensität und Polarisation der Ramanschen Streustrahlung mehratomiger Moleküle." *Zeitschrift für Physik* 70 (1-2): 84–103. https://doi.org/10.1007/BF01391032.

Pushkarchuk, A.L. 2019. "Calculations performed for this book." Private communication.

Raman, C.V., and K.S. Krishnan. 1928. "A New Type of Secondary Radiation." *Nature* 121: 501–502.

Rocard, Y. 1928. "Les nouvelles radiations diffusées." *Comptes rendus de l'Académie des Sciences* 190: 1107–1109.

Singh, R. 2018. "Celebrating the 90th Anniversary of the Raman Effect." *Indian Journal of History of Science* 53 (1): 50–58.

Singh, R., and F. Reiss. 2001. "The 1930 Nobel Prize for Physics: A close decision?" *Notes and Records of The Royal Society of London* 55: 267–283.

Smekal, A. 1923. "Zur Quantentheorie der Dispersion." *Die Naturwissenschaften* 11 (43): 873–875.

Socrates, G. 2004. *Infrared and Raman Characteristic Group Frequencies: Tables and Charts.* Chichester: John Willey & Sons.

n.d. Timegated Raman Technology.

Tuschel, D. 2014. "Practical Group Theory and Raman Spectroscopy, Part I: Normal Vibrational Modes." *Spectroscopy* 29(2): 14–23.

Wei, D., S. Chen, and Q. Liu. 2015. "Review of Fluorescence Suppression Techniques in Raman Spectroscopy." *Appl. Spectrosc. Rev.* 50 (5): 387–406.

Wieboldt, D., K. Jinkins, A. Mashal, and M.S. Arnold. 2016. "Polarized Raman Spectroscopy of Aligned Semiconducting Single-Walled Carbon Nanotubes." *Spectroscopy* 31 (6): 36–44.

Wilson Jr., E. B., J. C. Decius, and P. C. Cross. 1955. *Molecular vibrations: the theory of infrared and Raman spectra.* New York: McGraw-Hill.

Wong, M.-L. 1994. "Polarizability and tensor ellipsoid in the Raman effect." *Vib. Spectrosc.* 7 (2): 197–199. https://doi.org/10.1016/0924-2031(94)85031-3.

n.d. *www.btools.com.*

Zhao, J., H. Lui, D. McLean, and H. Zeng. 2007. "Automated Autofluorescence Background Subtraction Algorithm for Biomedical Raman Spectroscopy." *Appl.Spectrosc.* 61 (11): 1225–1232.

CHAPTER TWO

RAMAN MICROSCOPY INSTRUMENTATION

2.1. Evolution of Raman Instrumentation

Since its discovery, Raman scattering of light has received wide scientific and practical applications. The discovery of this physical phenomenon led to the appearance of a method of Raman spectroscopy with corresponding instrumentation and the development of many critically important optical components and devices that make it possible to detect the inherently weak effect of Raman scattering.

The use of the first experimental equipment for detecting Raman scattering should naturally be attributed to the person who discovered it. In the publications (Raman 1928, Raman and K.S. 1928) that followed immediately after his pioneering experiment with sunlight and light filters (Chapter One, Fig. 1-1), C.V. Raman used a mercury arc lamp as the excitation source and a simple hand spectroscope to visually observe the scattered light. Soon after, he used a Hilger quartz spectrograph that allowed the first Raman spectra to be photographed. Simultaneously, in their work, G.S. Landsberg and L.I. Mandelstam assembled and used an experimental spectroscopic setup consisting of the Haereus mercury lamp for excitation, a Fuess Model B spectrograph with a large flint glass prism for spectral analysis and photographic plates for spectral registration.

After the discovery of Raman scattering, much work has been devoted to fundamental studies on its effect; however, progress in the development of instrumentation for Raman spectroscopy was rather slow. In the early years, the measurements of Raman spectra were performed using mercury sources with filters to provide nearly monochromatic radiation from the most intense mercury lines, prism spectrographs and photographic detection techniques. Due to weak light sources, poor sensitivity of the photographic materials and inherently weak Raman scattering from many materials, the accumulation of Raman spectra took hours or even days. Naturally, with Raman spectra photographed in such a way, the broad line of Rayleigh scattering always prevailed. The Raman spectral bands of the materials under study were observed as weak satellites. Nevertheless, Raman spectroscopy has been as commonly used in experimental practice as IR because of the relative ease of the Raman measurements over the IR during that period. However, about 1940, the development of high-quality and low-cost IR detectors and the launch of the first commercial IR spectrometers Model 21 by Perkin-Elmer and Model IR-2 by Beckman industrial companies allowed IR to surpass Raman in popularity. The interest in the Raman technique renewed in the late 1960s after the invention and commercialization of lasers as new monochromatic and powerful sources of light. Lasers entirely substituted the mercury lamps that had been used as light sources in the early days. The accompanying development of shot-noise-limited electronic detection systems dramatically improved the S/N in Raman spectra. Raman spectral measurements became relatively easy to carry out, and the number of commercially available Raman instruments has grown from year to year. Some milestones in the evolution of Raman instrumentation can be outlined as follows:

1928: Quartz spectrographs with a mercury arc lamp and photographic plates required long spectral registration times.

1939: Electrostatic-focusing Photomultiplier Tubes (PMTs), aka photomultipliers, were the first devices for the detection of light at the single-photon level in UV and visible spectral regions (Zworykin and Rajchman 1939). PMTs soon replaced the slow photographic registration in Raman instruments.

1955: Confocal microscopy pioneered by Marvin Minsky (Minsky 1988), who invented a point-by-point image construction by focusing a point of light sequentially across a sample and rejecting out-of-focus light.

1957: The commercial production of Cary Model 81 Raman spectrograph with an improved mercury vapour (low pressure) lamp called Toronto arc (435.8 nm excitation). It was first used by the Applied Physics Corporation (later known as Cary Instruments) and then spread throughout research laboratories.

1962: A pulsed ruby laser was first used (Porto and Wood 1962) as a new excitation source in Raman spectroscopy.

1964: Perkin-Elmer introduced the model LR-1 Raman spectrometer with a He-Ne laser (632.8 nm).

1965: Cary Model 81 Raman was re-designed to accommodate He-Ne laser (renamed Carry 81L or Carry 82), which established Raman as a research technique.

1976: Invented by a research group of the French National Center for Scientific Research (Delhaye and Dhamelincourt 1975), the first Raman

microspectrophotometer, a Raman instrument coupled with a conventional optical microscope, was commercially produced as the Molecular Optical Laser Examiner (MOLE) by Lirinord Instruments (then Dilor, now Horiba Scientific) in France.

1981: Spex Industries Inc. constructed a triple monochromator. In the instrument, the individual monochromators were successively arranged in additive and subtractive optical modes to effectively remove unwanted stray light in a narrow spectral range, e.g., Rayleigh scattering.

1984: A group of scientists from the University of Pittsburgh, under the supervision of S. Asher (Flaugh, O'Donnell and Asher 1984), first reported the use of a holographic Bragg diffraction filter to reject the dominant Rayleigh line while passing Raman scattering onto the spectrometer. More miniature spectrometers with a single monochromator and the holographic filter offered an optical throughput of about 50%. In contrast, the double and triple monochromators used in the previous dispersive Raman instruments and primarily applied in basic research provided a typical throughput of about 10% and less than 3%, correspondingly. The use of edge and notch holographic filters significantly facilitated the commercial production of compact Raman instruments oriented on analytical applications.

1986: T. Hirschfeld and B. Chase (Hirschfeld and Chase 1986) demonstrated the possibility of converting an FTIR spectrometer with NIR capability into an FT-Raman spectrometer that ensures that the Raman spectra in the NIR region are virtually free from fluorescence interference. Soon after, Digilab (then Varian, now Agilent), followed by Thermo

Scientific, Bruker and Perkin-Elmer, started mass producing FT-Raman spectrometers and modules.

1986: The charge-coupled devices (CCDs) invented in 1969 by W. S. Boyle and G. E. Smith at Bell Laboratories in the US rapidly became widely used as detectors in Raman instruments due to their high sensitivity after the successful demonstration (Murray and Dierker 1986) of their application for low light signal detection in Raman spectroscopy.

1993: The first true confocal Raman microscope, LabRam, was commercially launched by Horiba. In the following years, Renishaw, Thermo Scientific, Bruker Optics and Witec began the wide commercial production of various models of confocal Raman microscopes intended for research and analytical applications.

2001: Electron multiplying CCD (EMCCD) detectors were first introduced by Andor Technology to deliver both high sensitivity and speed. The detectors soon found applications in fast Raman imaging systems.

2008: The fully automated software-driven procedure for alignment and calibration of the Raman confocal microscope was patented by Thermo Scientific and implemented in its Almega and DXR models.

A comprehensive review of the evolution of Raman instrumentation over the past 80 years since the time of its discovery in 1928 can be found in (Adar, Delhaye and DaSilva 2007). The achievements in laser technology, the developments of interference filters for the rejection of Rayleigh scattering, CCD and EMCCD detectors, and the integration of a microscope within the Raman instrument made Raman spectroscopy a mainstream technique for a diverse range of applications in both research and analytical laboratories.

The interest in Raman microscopy has progressed since it was justified (Delhaye and Migeon 1966) that the intensity of Raman scattering did not significantly depend on the sample volume and remained constant with a diminishing sample size down to that determined by the diffraction limit of light, i.e., the wavelength of the laser excitation. With typical limits of detection in the nanogram range, confocal optical design and imaging capabilities, Raman microscopy has now become a powerful analytical tool for both the material and biological sciences.

A modern Raman microscope system is an integrated platform that generally combines a Raman spectrometer, an optical microscope and a controlling computer with the software for the acquisition and numerical processing of spectral data. The Raman microscope represents a scientific instrument capable of obtaining both traditional optical and spectrochemical images with a submicron spatial resolution. The common layout of the Raman microscope with all of its major parts and optical components is depicted in Figure 2-1.

An optical microscope (1) is used to observe a sample and focus the laser beam on it. In the Raman microscope, the excitation of the sample and the collection of the scattered light is performed in a so-called back-scattering or 180-degree configuration. The laser (3) emits excitation light (the green beam) that is focused by the microscope objective (4) onto the sample placed on the sample stage (5). The light is then scattered by the sample, collected by the same objective and directed through the plate beamsplitter (6) into the spectrograph (2). Thus, after being scattered by the sample and collected by the objective, the Raman and Rayleigh components of scattered light share a common path. These components are shown by the yellow and green dotted beams, respectively. The Rayleigh scattered component is then

blocked by the Rayleigh rejection filter (7). An optical interface (optical coupling) between the microscope and spectrometer (8) is used to transfer Raman scattering to the spectrograph. Raman scattering passes through the spectrograph's entrance aperture (a slit or a pinhole) (9) and is collected by the collimating mirror (10). The mirror directs the collimated beam onto the diffraction grating (11). The grating decomposes Raman scattering into its constituent spectral components, which are focused by a second mirror (12) onto the multi-element array detector (13).

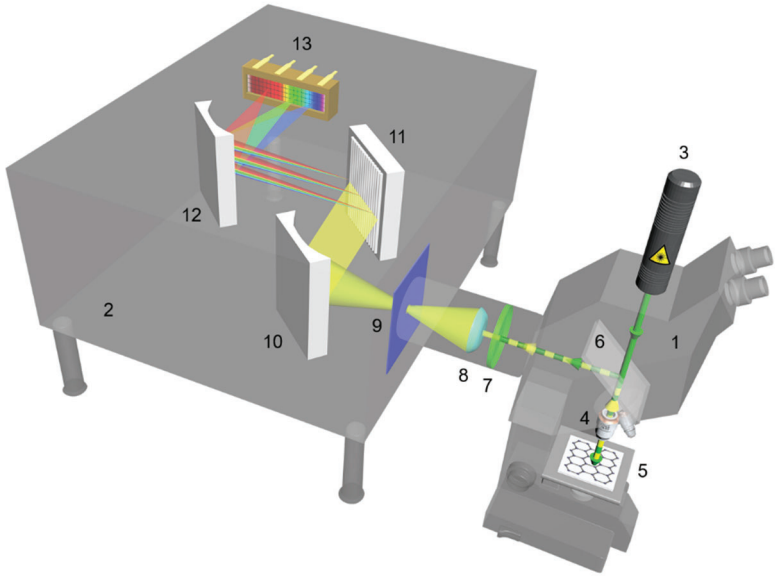

Figure 2-1: Schematic diagram of a Raman microscope: 1 – optical microscope; 2 – spectrograph; 3 – laser source; 4 – microscope objective; 5 – sampling stage with a sample; 6 – beamsplitter or dichroic mirror; 7 – Rayleigh filter; 8 – microscope-to-spectrograph coupling optics; 9 – spectrograph entrance aperture (circular diaphragm); 10 – collimating mirror; 11 – diffraction grating; 12 – focusing mirror; 13 – array detector.

The parts of the modern Raman microscope, their functions and major characteristics are outlined below.

2.2. Lasers

A light source is the starting point for spectroscopic experiments. A light source emits electromagnetic radiation by converting input energy into light. In a conventional light source, such as a lightbulb or a light-emitting diode (LED), the emitting medium excited by the electric current radiates photons randomly in all directions over a broad range of frequencies (wavelengths). This is called spontaneous emission. Since there is no correlation or coherence among the individual photons, the conventional light sources are incoherent.

In 1916, Albert Einstein wrote a revolutionary work in which he predicted an entirely new phenomenon in physics, a stimulated emission, and laid the foundations of the quantum-mechanical principle for lasers. He postulated that light could be emitted and absorbed not only spontaneously. There is also the possibility of stimulated emission, i.e., it is possible to “force” particles (atoms, molecules or ions) to emit light of a specific wavelength at the same time. The essence of this phenomenon is that an excited particle can emit a photon under the action of another photon without its absorption, provided that the energy of the photon is equal to the difference in the energy of the particle before and after the emission. In this case, the emitted photon is coherent with the photon that caused the radiation, i.e., these photons have identical properties: the direction of propagation, wavelength, phase and polarization. This process usually begins when an excited particle emits a spontaneous photon. When this photon interacts with another excited particle, the emission of the second photon is stimulated. These two

photons interact with two other excited particles, which leads to the emission of four photons and so on. The stimulated emission may result in the amplification of light. However, the amplification of light occurs if so-called population inversion can be achieved, i.e., there are more excited particles in the medium than unexcited, and the rate of stimulated emission exceeds the rate of absorption. This condition is not satisfied in the state of thermodynamic equilibrium and, therefore, various systems (electrical, optical and chemical) for pumping the active medium are used. Thus, the ability to "amplify" light in the presence of a sufficient number of excited particles leads to "optical amplification", which is the basis of the laser and justifies its acronym: "Light Amplification by Stimulated Emission of Radiation".

2.2.1. Types of lasers

Lasers can be classified according to various technological parameters: the most important of which are types of an active medium and duration of laser radiation at the output. All lasers are divided into three major categories based on the type of active medium: gas, solid-state and semiconductor. Formally, semiconductor lasers are also solid-state but traditionally stand as a separate group because they have a specific design and involve different physical processes. Lasers may operate in a continuous-wave (CW) or pulsed mode emission at the output. By definition, CW lasers emit a continuous beam of light with a stable output power on a long-time scale, whereas pulsed lasers generate very short pulses of power with a certain repetition rate.

While CW lasers with fixed wavelengths are commonly used for conventional Raman spectroscopy, advanced techniques, such as Stimulated Raman (SRS) and Time-Resolved Raman (TRRS) spectroscopies, typically

require high energy pulsed lasers to provide Raman scattering effectively. In the nonlinear Coherent Anti-Stokes Raman spectroscopy (CARS), pulsed excitation may also be advantageous.

Despite the variation in types, lasers consist of three common components: an optical resonator (laser cavity), an active medium and a pumping source (Fig. 2-2). The active laser medium is located between two mirrors placed at opposite sides of the optical resonator, with one of the mirrors being semi-transparent. The pumping source supplies external energy to the active medium. The two most common mechanisms of pumping are electrical and optical. Electrical pumping can be carried out by a direct current or an electrical discharge. For optical pumping, the energy source may be a lamp or another laser. Light photons generated in the active medium bounce back and forth between the resonator's mirrors, gaining light intensity with each pass through the active medium. Thus, the radiation from the active medium is amplified in the laser cavity. At the same time, a certain part of the radiation can exit the resonator through the semi-transparent mirror and form a laser output beam. The multiple reflections between the mirrors also ensure a narrowly focused beam because only photons travelling in the lengthwise direction of the cavity are reflected from both mirrors.

The population inversion in the active medium and the laser light generation occurs according to a four- or three-level energy scheme. In the former, the pumping energy excites the particles (atoms, molecules or ions) of the medium from the ground state level 0 into the upper temporary level 3. The particles then transfer by a fast radiative or non-radiative decay to a metastable level 2. The stimulated laser emission occurs from level 2 to level 1, which is above level 0, but quickly decays to the ground state. Thus, population inversion is achieved between levels 2 and 1 as the absorption from level 1 to

level 2 is very unlikely, and the population of level 2 is higher than that of level 1. The three-level scheme differs from the four-level one in that the particles from the ground state level 0 are excited into upper level 2, and the laser transition from level 1 ends on the ground state. It is much easier to achieve population inversion in a four-level active medium compared to a three-level one. Therefore, four-level active media are generally preferable and more common (e.g., Nd:YAG or He-Ne) than three-level ones (e.g., Ruby).

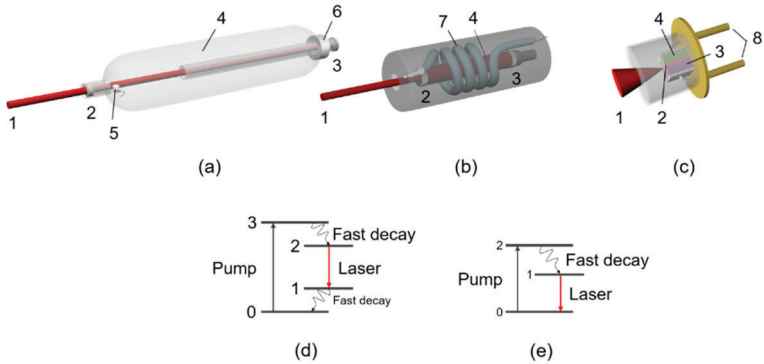

Figure 2-2: Major common and specific laser elements. (a) Gas laser: 1 – output laser beam; 2 and 3 – partially and totally reflecting mirrors of the laser resonator, respectively; 4 – active laser medium (e.g., He-Ne gas mixture in a glass envelope); 5 and 6 – cathode and anode for high-voltage electrical pump discharge, respectively. (b) Solid-state laser: 1 – output beam; 2 and 3 – partially and totally reflecting mirrors; 4 – active medium; 7 – flash lamp. (c) Semiconductor (diode) laser: 1 – divergent output beam; 2 and 3 – partially and mirror-polished totally reflecting surfaces of the semiconductor diode, respectively; 4 – active medium composed of P-I-N junction semiconductor structure (e.g., GaAs) with P-type material (green), N-type material (violet), and intrinsic active layer I consisting of quantum well (red layer); 8 – electrodes for electrical current pumping. (d) and (e) are the conceptual illustrations of, respectively, four- and three-level active laser media and their corresponding energy transitions.

For many years since the employment in Raman instruments, the laser was the most challenging component in terms of reliability and lifetime. In the early days, most Raman instruments were equipped with Ar-ion, Kr-ion, He-Ne or ruby lasers. An ion laser uses an intense electrical discharge (10–20 amperes) to create a plasma with a high density of noble gas ions. Therefore, it consumes a large amount of power. These lasers produce a lot of waste heat and thus require active cooling. Most lasers use a closed-circle water cooling system with a chiller, which further increases power consumption. The construction of the ion laser is complex and expensive. The advantage of ion lasers is their ability to generate radiation at several wavelengths. The wavelength selection is performed by rotating an angle-tuned quartz prism installed inside the laser cavity or slightly changing the slope of one of the resonator mirrors.

The He-Ne laser has been routinely used in early Raman instrumentations and measurements due to its ability to generate a light beam with a very stable frequency, a high spectral purity, superior spatial coherence and low divergence. However, the optical output power of He-Ne laser depends on the cavity length. To generate light powerful enough for Raman experiments, the laser tube needs to be particularly long (about 1 m to produce 35 mW of output power), making the laser generally large and inconvenient. The diffusion of small He atoms through the glass tube walls made the lifetime of the laser relatively short. A He-Ne laser requires a typically long warm-up time for stable generation. Nevertheless, ion and gas lasers were the first choices for Raman spectroscopy applications. Historically, plenty of Raman spectra were acquired using red 633 or 647 nm wavelength emitted, respectively, by He-Ne or a Kr-ion laser, as well as

blue 488 nm or green 514.5 nm excitation wavelength generated by an Ar-ion laser.

In recent years, the development in Raman instrumentation has evolved Raman spectroscopy into a standard analytical tool for many research and industrial applications. In comparison to gas and ion lasers, solid-state lasers offer a smaller size, require far less space and provide a more flexible arrangement, which allows for easy integration into desktop Raman instruments. Additionally, the energy consumption of solid-state lasers is lower than that of ion lasers in particular, which results in lower operating costs. The use of diode-pumped solid-state (DPSS) lasers guarantee compactness, reliability and a lifetime that allows users to run routine experiments for years without the need to service or replace the lasers. DPSS lasers are a modification of solid-state lasers. In DPSS lasers, a high-power IR laser diode provides optical pumping instead of an intense flash lamp used in traditional solid-state lasers. The pumping diode wavelength is selected to fit into the absorption band of the active medium. Because optical pumping is a resonant process, it is much more efficient than the broadband pumping provided by a xenon flash lamp. The most common active media in DPSS lasers are neodymium-doped glass (Nd:glass) or crystals such as yttrium aluminium garnet, $Y_3Al_5O_{12}$ (Nd:YAG), and yttrium orthovanadate, $YV0_4$ (Nd:$YV0_4$). The most frequently used Nd:YAG, which absorption band is located at about 800 nm, generates 1064 nm wavelength in the NIR region of the spectrum.

Since not all wavelengths of interest for Raman spectroscopy can be directly generated in accessible active laser media, there is a method for nonlinear optical frequency conversion. This method uses frequency multiplication to

produce the second harmonic (SHG or frequency doubling), the third harmonic (THG or frequency tripling) or the fourth harmonic (FHG or frequency quadrupling) by placing nonlinear crystals inside the laser cavity (this is called intracavity frequency multiplication). Frequency doubling can be achieved by passing the originally generated light beam through a nonlinear crystal that produces an output beam at twice its frequency and, respectively, half the original wavelength. The commonly used nonlinear crystals are lithium triborate (LBO), β-barium borate (BBO) and potassium titanyl phosphate (KTP). Frequency tripling is realized by placing two nonlinear crystals in a cascade manner: the first one for frequency doubling and the second to mix the original and doubled frequency. Frequency quadrupling requires the original beam to pass two nonlinear crystals sequentially. The frequency conversion method is used in both ion and solid-state lasers. For example, frequency doubling with BBO crystal was first used in Ar-ion laser to obtain excitation wavelengths in the UV region. DPSS lasers are specifically designed for the use of second, third and fourth harmonic generation to convert 1064 nm to shorter wavelengths. The SHG in Nd:YAG results in green light output at 532 nm wavelength, whereas THG and FHG provide the light radiation in UV at 355 and 266 nm wavelengths, respectively. Besides, by combining different laser-active dopants (Nd^{3+}, Yb^{3+}, Er^{3+}) in the active medium with frequency multiplication, it is possible to obtain laser sources with wavelengths from NIR to UV. While DPSS lasers generally cannot achieve the same maximum output power as their counterparts pumped by flash lamps, the usage of small pumping diodes accounts for their compactness and robustness; they also require less maintenance. Although the frequency conversion with the use of nonlinear crystals decreases the output power, DPSS lasers that are capable of maintaining several tens of mW of the power

in visible range replace legacy ion lasers and traditional solid-state lasers in many Raman instruments.

Another group of solid-state lasers, semiconductor lasers, also known as diode lasers, are very cost-effective, have a compact size and consume only a little electrical power. In semiconductor lasers, the p-n junction of a laser diode forms the active medium, and the optical gain is produced within the semiconductor material. Terminologically, a diode laser means a complete laser device that may contain other optical elements, while a laser diode refers directly to a semiconductor diode emitting a specific wavelength of light. Semiconductor lasers differ from solid-state lasers as their active media are based mostly on gallium mixtures with some other semiconductor materials, and they are pumped electrically with very high efficiency. However, the output beam of an individual laser diode is highly divergent and asymmetric, and its original wavelength characteristics are unstable. To correct the beam shape and decrease its divergence, diode lasers often include additional optics, such as a beam shaper and a beam collimator. The spectral emission of diode lasers is much broader than the fundamentally highly monochromatic emissions from gas or DPSS lasers. Since the spectral width and wavelength of diode lasers drifts with temperature, narrowing of spectral bandwidth and wavelength stabilization are required. To be suitable for Raman spectroscopy, the design of diode lasers includes a wavelength control element monolithically integrated or otherwise incorporated in an external cavity. Examples of the element are the distributed feedback (DFB) device, the distributed Bragg reflector (DBR) and the volume Bragg grating (VBG). VBG, also called volume holographic grating (VHG), is a diffraction grating produced by refractive index modulation in the volume of a photosensitive material. Careful thermal

control and optical alignment of diode lasers are required to ensure high stability of the wavelength and the narrow linewidth of the output emission, especially with varying ambient temperatures. Semiconductor lasers intended for Raman spectroscopy usually emit a single line in the red or NIR region depending on the specific composition of the active media. Blue wavelengths are available with semiconductor materials based on GaN. Implementation of nonlinear frequency conversion in the material inherently emitting in the red region can generate UV, as well as blue and green wavelengths. Nowadays, the supply and versatility of these lasers have permanently increased. Nevertheless, not all wavelengths of potential interest in Raman spectroscopy can be produced by electrically pumped diode lasers. Additionally, their relatively small structures often limit output power, especially when a narrow linewidth is desired.

More recently, optically pumped semiconductor (OPS) lasers that combine the diode pumping principle of DPSS lasers and the Ga-based active media of semiconductor lasers have emerged. OPS lasers have challenged the existing semiconductor lasers as they have overcome most of their limitations. The construction of OPS lasers is based on a semiconductor laser with a large-area emitting surface pumped by another laser diode. The use of optical pumping enables high power of the output radiation and a narrow linewidth. A wide range and variety of generated wavelengths can be achieved by altering the composition of the emitting semiconductor materials. This technological advantage allows the laser source to be precisely tailored to the requirements of almost any particular application, which makes it possible to efficiently conduct and optimize Raman spectroscopic experiments. OPS technologies enable highly reliable (over 50,000 hours), compact, high power and single-mode laser sources.

Modern solid-state lasers meet the most advanced optical performance requirements and are available in all wavelength ranges commonly used in Raman spectroscopy.

Table 2-1 summarizes the major laser sources used in Raman instruments and their important attributes.

Table 2-1: Laser sources commonly used for Raman spectroscopy and their major characteristics.

Laser	Active medium	Major operating wavelengths, nm	Pumping source	Applications and notes
He-Ne	Gas: a mixture of 75% helium and 25% neon	632.8	Electrical discharge	Still in use in high-end Raman microscopes
Ar^+-ion	Gas: ions of the noble gas argon	457.9, 488.0 and 514.5	Intense electrical discharge	Very stable output power, small air-cooled models still in use in high-end Raman microscopes
Frequency-doubled Ar^+-ion	Gas: ions of Argon + intra-cavity frequency-doubling crystal	228.9, 244.0 and 257.3	Intense electrical discharge	First excitation wavelengths available in the UV region
Kr^+-ion	Gas: ions of the noble gas krypton	468.0, 476.2, 482.5, 520.8, 530.9, 568.2, 647.1 and 676.4	Electrical discharge	Strong red emission at 647.1 nm, a broad selection of wavelengths potentially for resonance Raman, maintenance intensive, short operational lifetimes (< 2000 hours)

He-Cd	Gas: emitting metal cadmium evaporated into gas phase and mixed with buffer helium gas	325, 441.6	Electrical discharge	CW output in blue (441.6 nm) with high power (up to 150 mW) and ultraviolet (325 nm), short lifetime dictated by the amount of Cd in the laser tube reservoir
Ruby	Solid-state: chromium-doped sapphire Cr:Al_2O_3	694.3	Flash lamp	Used in the early days of Raman experiments, pulsed and quasi-CW modes of operation
Nd:YAG	Solid-state: neodymium-doped yttrium aluminum garnet Nd:$Y_3Al_5O_{12}$	1064	Flash lamp	Most widely used CW laser to provide up to 2 W power output for FT-Raman instruments, increasingly frequent deployment in dispersive systems
Frequency-converted Nd:YAG	Solid-sate: Nd:YAG + intra-cavity nonlinear crystals for frequency-doubling and sum frequency generation	266, 355 and 532	Flash lamp	Green (532 nm) and UV excitation (266, 355) wavelengths commonly used in Raman spectroscopy, possible intra-cavity nonlinear crystal degradation over time

Diode-pumped solid-state (DPSS)	Solid-state: Nd:YAG, neodymium-doped glass Nd:glass, ytterbium doped yttrium aluminum garnet Yb:YAG, or neodymium-doped orthovanadate Nd:YVO_4 and frequency-doubling $KTiOPO_4$ crystal	266, 355, 473, 532, 1064 and a few other wavelengths from NIR to UV as the result of doubled, tripled and quadrupled primary NIR wavelengths close to 1064 nm	Diode-pumped	Replace legacy ion- and solid-state lasers with flash lamp pumping in many Raman systems are limited to specific wavelengths inherent to the active media materials
Semiconductor (diode) lasers	GaN, InGaAs, GaAs, AlGaInP, AlGaAs	405, 455, 660, 780, 785, 808, 830, 905 and many other wavelengths from NIR to UV	Electrical current	Cost-effective, most compact size, low power consumption, yet relatively broad linewidth
Optically pumped semiconductor (OPS) lasers	InGaAs, other Ga-based mixtures	355, 458, 460, 488, 514, 532, 552, 561, 568, 577 and 639; already available with a variety of other wavelengths from UV to NIR	Diode-pumped	Reliable, compact, high power and high beam quality, still relatively expensive

2.2.2. Wavelength options

One of the main advantages of Raman spectroscopy is the independence of the appearance of the measured spectrum from the excitation wavelength. Nevertheless, the choice of laser wavelength requires consideration of various excitation wavelengths for obtaining the most informative Raman spectrum of a given sample.

As we know from Chapter One and equation (1.1), the scattering intensity is inversely proportional to the fourth power of the excitation wavelength $1/\lambda^4$. Therefore, Raman spectroscopists prefer shorter laser wavelengths, such as blue 488 nm, green 514 and 532 nm or red 633 nm, to obtain a stronger Raman signal and, respectively, a better signal-to-noise ratio (S/N) in the spectrum provided that all the other experimental conditions are equal. Blue and green wavelengths are typically reasonably suitable for transparent liquids and polymers, non-coloured inorganic materials and some resonance Raman experiments. However, as the Raman effect is an extremely weak phenomenon, a Raman signal in the visible optical range can easily be overwhelmed by autofluorescence from an analyte or even fluorescence from trace impurities in the sample under study.

For measurements of highly fluorescent materials, it is common to use NIR laser excitation with a 1064 nm wavelength. Although 1064 nm excitation ensures virtually fluorescence-free Raman spectra, it results in a theoretical decrease in scattering efficiency by a factor of 16 in comparison with the green 532 nm wavelength. Solid-state Nd:YAG 1064 nm lasers have traditionally been used in FT-Raman spectrometers with a single-element indium-gallium-arsenide (InGaAs) or a liquid nitrogen cooled germanium (Ge) detector. FT-Raman, however, is limited by long acquisition times and

the need for a high laser power to compensate for the decrease in scattering efficiency. In practice, high laser power may result in overheating the dark or coloured samples. Due to relatively less sensitive InGaAs detectors, the large diameter of the laser beam and other factors, the drop in the Raman intensity becomes even more significant than theoretically predicted.

Excitation in the UV spectral region is attractive for resonance Raman spectroscopy on biomolecules, such as proteins, DNA and RNA (S. Asher 1993). It also provides a unique opportunity to avoid both the fluorescence and interference of thermal emission at high temperatures in the study of catalysts and catalytic processes *in situ* (Rzhevskii, et al. 2001). Moreover, because of the $1/\lambda^4$ dependence, Raman scattering efficiency is higher in the UV region. Nevertheless, UV excitations in Raman spectroscopy need to be applied with care since thermal decomposition or other laser-induced modifications of samples are possible.

It is well recognized that the best trade-off between Raman scattering efficiency, fluorescence avoidance, laser-induced effects and compatibility with the detector's sensitivity can be achieved with the dark red 785 nm laser wavelength. It should be noted that 785 nm excitation causes a significant fluorescence in glass commonly used for laboratory glassware. A broad fluorescence band centred at about 1385 cm^{-1} originates from rare earth elements and certain impurities in the glass matrices. Therefore, it is recommended to avoid cuvettes, vials, microscope slides, coverslips and substrates made of glass when using 785 nm excitation as the fluorescence may significantly distort the measured spectrum.

Depending on the application and the material under investigation, the use of several excitation wavelengths and the ability to switch between different

wavelengths in a Raman instrument are considered to be a substantial advantage. Figure 2-3 provides examples of the application of different excitation wavelengths for the characterization of (a) the diameter distribution of SWCNT in a mixture based on the position and the intensity of radial breathing modes (RBMs) and (b) graphene on polycrystalline copper foil grown by the chemical vapour deposition (CVD) process.

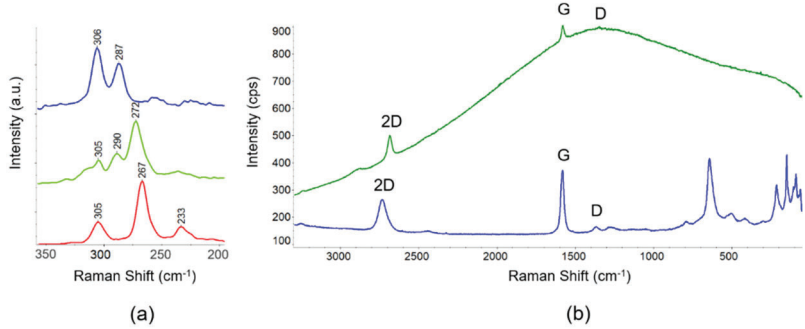

Figure 2-3: The influence of different excitation wavelengths on Raman spectra. (a) Raman spectra of a mixture of SWCNTs in the region of manifestation of RBMs measured with 455 (blue), 532 (green) and 633 (red) nm excitation wavelengths (the spectra are offset for clarity). (b) Raman spectra of multi-layered graphene on copper foil measured using 532 (green) and 455 (blue) nm wavelengths. The principal bands of graphene are marked as G, D and 2D. The bands in the region below 800 cm^{-1} belong to copper oxide.

Indeed, the RBM is a unique feature of SWCNT as it corresponds to coherent vibrations of the C atoms in the radial direction of the tube as if it is breathing. The related Raman peaks usually appear between 50 cm^{-1} and 400 cm^{-1} wavenumbers. An important attribute of this vibrational mode is the fact that its frequency is inversely proportional to the diameter d of the SWCNT so that $\nu_{RBM} \sim {}^{1}/_{d}$ (Costa, et al. 2008). Because the Raman

spectrum of SWCNT is essentially obtained due to a resonance phenomenon, a single excitation wavelength will only reveal the RBM peaks that correspond to the nanotubes being in resonance with the energy of this particular laser line. By measuring Raman spectra using other laser lines that provide appropriate resonance effects, a complete characterization of the diameter distribution in the mixture of SWCNTs is possible. Subsequently, the chirality and semiconducting/metallic behaviour of SWCNTs can be predicted (Dresselhaus, Dresselhaus and Jorio, et al. 2002).

One of the most scalable methods for producing high-quality graphene over large areas is its synthesis by the CVD process on copper foil, which features catalytic properties, low carbon solubility, low cost and ease of graphene transfer. It is highly desirable to characterize the graphene directly on the copper foil, thus significantly accelerating and simplifying graphene quality control in its originally grown state. In practice, 532 nm laser line is traditionally used for the graphene analysis on, for example, Si substrates. However, the green excitation wavelength leads to a noticeable fluorescence background from the copper metal foil. This background can make it difficult to quantify the graphene Raman bands' parameters accurately, resulting in the problematic spectroscopic assessment of graphene properties. Fortunately, laser excitations in the blue region, such as 455 nm, markedly reduce the background.

Important considerations relevant to choosing a laser excitation wavelength for Raman spectroscopy and microscopy can be found elsewhere (Tuschel 2016). In practice, when working with a variety of applications and materials, Raman spectroscopists always want to have access to as many excitation wavelengths as possible to perform Raman experiments in the most advantageous way. Flexibility and optimization of Raman experiments

are achieved in high-end Raman spectrometers and microscopes with multiple lasers, interchangeable Rayleigh filters and diffraction gratings.

In addition to the wavelength, there is a number of other laser performance parameters that should be considered when deciding on the best laser source for Raman microscopy. The parameters that have a key impact on a Raman microscope's technical capabilities include beam quality, power and brightness, spectral line width, and frequency and power stability.

2.2.3. Beam quality

The laser resonator design determines so-called transverse electromagnetic modes (TEMs), which describe the intensity distribution of the emitted light in the perpendicular plane (i.e., transverse) to the direction of propagation of the laser beam. These modes are designated as TEM_{mn} where the indexes *m* and *n* indicate the number of intensity nodes appearing in the horizontal and vertical direction in the intensity distribution pattern of the laser beam profile. The mode selection is typically controlled by inserting a circular diaphragm (pinhole) into the resonator. By adjusting the pinhole diameter to that of the desired mode, only this mode is allowed to pass through the pinhole and thus be amplified in the resonator, while all the other modes are blocked. The fundamental output transverse mode of the laser resonator is the lowest order TEM_{00} mode. The intensity profile of the TEM_{00} mode has a bell-shaped form well approximated by the Gaussian distribution. The intensity profile of the mode keeps the Gaussian distribution when the beam propagates in space and through any combination of optical elements, such as lenses and mirrors. The fundamental transverse mode TEM_{00} has the smallest diameter compared to higher-order modes (m, n > 0), which have a more substantial spatial expansion. The intensity distribution patterns of

the laser beam are shown in Figure 2-4. When a laser operates in several transverse modes, many modes are present at the same time, and the total intensity profile represents a superposition of all the transverse modes allowed in the laser resonator. Although the laser operating in higher-order modes (multi-mode regime) can produce higher output power, the beam profile has a larger divergence and lower brightness (radiance).

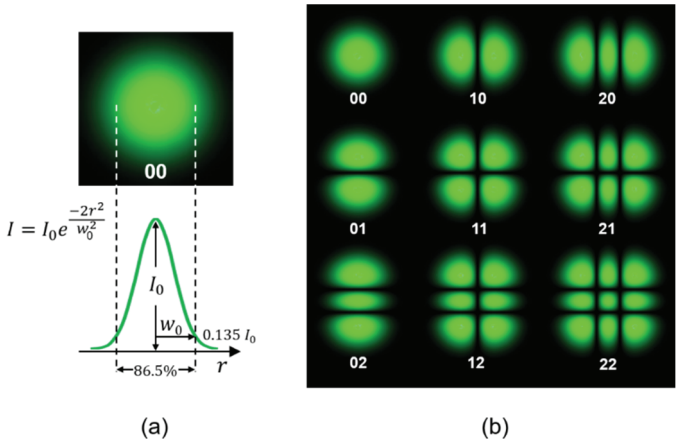

Figure 2-4: The transverse electromagnetic modes TEM_{mn} of a laser beam. (a) TEM_{00} and the radial distribution of its intensity approximated by Gaussian function. The diameter of the Gaussian beam $2w$ is defined as the distance between the two points at which the maximum beam intensity I_0 drops to I_0/e^2 $(0.135I_0)$. The fraction of the total intensity of the beam concentrated in the circle with a diameter of $2w$ is ~ 86.5%. (b) The intensity distribution patterns in the transverse electromagnetic modes TEM_{mn}.

The divergence of a laser beam is a measure of how much the beam expands over a propagation distance. The divergence is the result of diffraction, which is an inevitable effect of the wave nature of light. Diffraction exists in all optical systems and imposes the ultimate theoretical limit on their

performance. The diffraction effect makes a perfectly parallel laser beam physically impossible. Namely, diffraction causes the light beam to expand transversely as it propagates. The laser beam that keeps a nearly constant radius over a large distance and, thus, features a minimal divergence, is considered to be highly collimated. For the beam with an ideal Gaussian intensity profile corresponding to the TEM_{00} mode, the divergence half-angle is only defined by the minimum possible value stipulated by the laws of diffraction and is given by:

$$\theta_0 = \frac{\lambda}{\pi w_0}, \tag{2.1}$$

where λ is the laser wavelength, and w_0 is the radius of the beam at its narrowest point, which is called the beam waist. This Gaussian beam is considered to be a diffraction-limited beam. Actually, the laser profile deviates from an ideal Gaussian intensity distribution. In the laser industry, the degree of deviation is often specified using a beam quality factor or beam propagation factor called the M-square factor (M^2). The ISO Standard 11146-1 (2005) defines the M^2 factor as

$$M^2 = \frac{\pi w_0 \theta}{\lambda}. \tag{2.2}$$

For the ideal diffraction-limited Gaussian laser beam, M^2 is exactly equal to unity. Indeed, if we substitute θ in (2.2) with the θ_0 from (2.1), then

$$M^2 = \frac{\pi w_0}{\lambda} \times \frac{\lambda}{\pi w_0} = 1 .$$

M^2 is also specified as the ratio of a beam's actual divergence to the divergence of an ideal Gaussian beam with a single TEM_{00} mode. The divergence of an actual laser beam is then given by

$$\theta = M^2 \frac{\lambda}{\pi w}. \tag{2.3}$$

The divergence of the laser beam along the direction of its propagation is shown in Figure 2-5. For a real laser beam, M^2>1. He-Ne and ion lasers typically have M^2 <1.1 and 1.1 <M^2 <1.3, respectively, thus providing a beam quality very close to that of the ideal Gaussian beam. In contrast, even well-collimated beams of diode lasers operating in a single TEM_{00} mode regime usually offer an M^2 ranging from 1.2 to 1.8. It is generally difficult to obtain excellent beam quality and high output power at the same time, so it can be expected that M^2 increases if higher laser power is required. Therefore, for multi-mode lasers capable of generating high output power, the M^2 factor can be as high as 4 or 5.

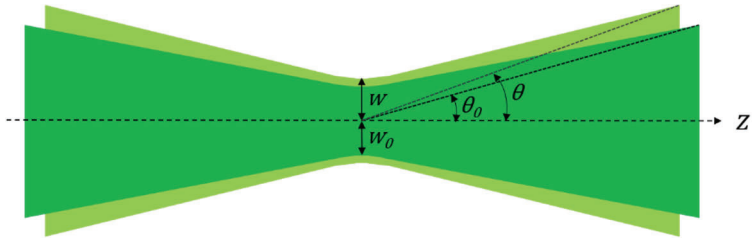

Figure 2-5: A cross-section of the laser beam along the direction of its propagation z illustrating the divergence of the ideal Gaussian (dark green) and real (light green) laser beams. Note that the divergence angle in this figure appears much larger than it actually is since the z scale is compressed to visualize the beam divergence better.

In Raman microscopy, it is necessary to focus the laser beam through a lens and other optical elements. If an aberration-free lens is used, the diffraction-

limited collimated Gaussian laser beam with M^2=1 can be focused into the smallest diffraction-limited spot d_{min} which, as it will be shown below and discussed in more detail in Chapter Three, is equal to approximately its light wavelength:

$$d_{min} = \frac{2.44\,\lambda\,f}{D}, \tag{2.4}$$

where f is the focal length of the lens, and D is the diameter of the laser beam.

The quality of the beam formed by a laser in a Raman microscope is critically important as the size of the focus spot is primarily responsible for the spatial resolution achievable in the microscope (see Chapter Three for more details). If the M^2 factor differs significantly from M^2=1, it affects the quality of the laser beam and cannot ensure a high spatial resolution and a high-power density in the focused spot.

2.2.4. Power and brightness

Power and brightness are two other important indicators of the suitability of lasers for Raman microscopy. Power is just a laser output, while brightness, as defined below, determines the power density obtained within a circular laser beam cross-section. There are various definitions of brightness within the laser and optical community. This term is often confused with radiance. Indeed, brightness is a somewhat subjective measure since it may depend on the visual perception of the radiation emitted by a light source and the position of an observer relative to the source. Radiance, on the other hand, can be considered as a strict quantitative measure for the brightness of a laser. Nevertheless, we will adhere to the term brightness because, among

Raman spectroscopists, radiance is often referred to as brightness, and it is traditionally used to evaluate the laser's capability to generate high optical intensity.

The brightness is defined as the power P emitted by a laser per unit surface area A and per unit of solid angle Ω and is usually expressed in Watts per square centimetre per steradian:

$$B = \frac{P}{A\,\Omega} \quad [W\ cm^{-2} sr^{-1}]\,. \tag{2.5}$$

Substituting the area of the circular beam $A=\pi w^2$ into this equation and taking into consideration that, for a sufficiently narrow cone, the solid angle subtended by the cone is $\Omega \approx \pi\theta^2$, we obtain

$$B = \frac{P}{\pi w^2 \pi\theta^2} = \frac{P}{(\pi w\theta)^2}\,.$$

Then, substituting $\pi w\theta$ with $M^2\lambda$ from (2.3), the brightness takes the form

$$B = \frac{P}{(M^2)^2\lambda^2}\,. \tag{2.6}$$

In this form, the brightness is a well-defined parameter that characterizes the laser beam, regardless of its position and direction. The brightness is directly proportional to the laser output power and essentially depends on the beam quality apart from the wavelength of the emitted radiation. This means that lasers with higher output power, especially multi-mode lasers, do not necessarily offer a higher brightness. On the contrary, so-called high-brightness lasers with a single TEM_{00} mode can produce a diffraction-limited focus spot with a higher density power at a sample that leads to an increase in Raman scattering intensity.

If the laser beam is focused, then its average local intensity at the focus (more correctly called light power density) is simply understood as power divided by the area of the focus spot:

$$I = \frac{P}{\pi w_f^2}. \tag{2.7}$$

By analogy with (2.5), the brightness at the spot takes the form

$$B = \frac{P}{\pi w_f^2 \, \varphi}, \tag{2.8}$$

where φ is the focusing angle. Combining (2.7) and (2.8), the intensity can be expressed as

$$I = B\varphi \, . \tag{2.9}$$

Thus, an optical system with a given focusing angle φ determines the local intensity proportional to the laser's brightness and then, the brightness (not just power) determines the achievable intensity. Substituting (2.6) in (2.9), the intensity appears to be inversely proportional to the square of M^2 factor:

$$I = \frac{P}{(M^2)^2 \lambda^2} \, \varphi \, .$$

M^2 relates the divergence of a collimated laser beam to a minimum focused spot size that can be achieved. The knowledge of M^2 allows Raman spectroscopists to modify theoretical formulae of beam diameter and focus spot size by simply introducing multiplication M^2 factor to account for the actual beam divergence. For example, a laser beam with M^2 =2 can at best be focused into a spot that is twice the size of a diffraction-limited beam

spot with M^2 =1. Respectively, the average local intensity of the laser beam with M^2=2 at the focus is proportional to $1/(M^2)^2$ and is 4 times lower.

2.2.5. Spectral linewidth

Even if a laser emits a single TEM_{00} mode, it may still generate multiple longitudinal (axial) modes with the same intensity profile but different wavelengths. These wavelengths are determined by the longitudinal modes of the resonator. The longitudinal modes occur as standing waves inside the resonator due to interference between the waves reflected back and forth off the resonator mirrors. Thus, the round-trip distance that the waves travel in a resonator of the length L must be equal to an integer number N of the wavelength λ:

$$2Ln = N\lambda\,,$$

where n is the index of refraction of the active medium. The integer N called a mode number is typically a very large quantity as the light wavelength is much smaller than the resonator length. In the frequency domain, the spacing between the longitudinal modes, which is often called the free spectral range, can be calculated as

$$\Delta\nu = \frac{c}{2Ln}. \qquad (2.10)$$

If the gain bandwidth is broader than the free spectral range, then there are multiple frequencies in the actual output beam of the laser, as shown in Figure 2-6. The gain bandwidth depends primarily on the properties of the active medium and the length of the resonator. In Raman spectroscopy, it is highly desirable that the laser generates only a single frequency corresponding to a single longitudinal mode of the resonator. Single-

frequency operation is realized when the gain bandwidth is smaller than the free spectral range of the resonator. For example, a He-Ne laser that has very narrow gain bandwidth can easily emit a single frequency, provided that its resonator is no longer than about 20 cm. However, for most solid-state lasers having a relatively large bandwidth, it is often impossible to make the resonator short enough to enlarge the free spectral range according to formula (2.10) to produce a single mode. A single-frequency operation can still be achieved using the line narrowing techniques. In practice, this is implemented by using intracavity optical filters, such as etalon (e.g., Fabry-Perot interferometer) or VBG (VHG) components, which suppress unwanted modes and pass one particular mode.

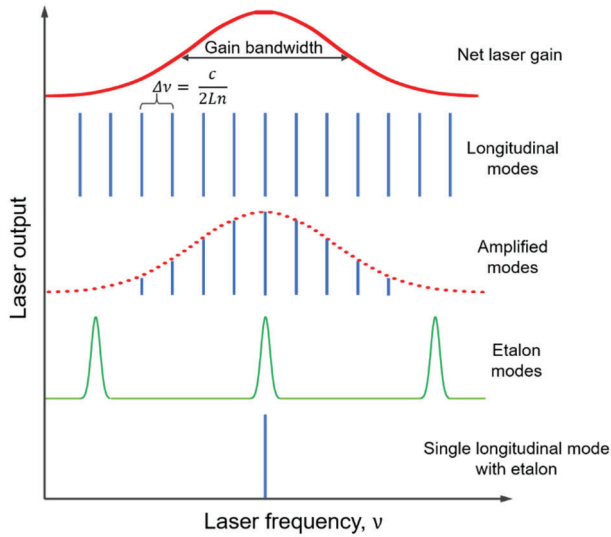

Figure 2-6. Longitudinal (axial) modes of a laser resonator and the single-frequency output of the laser obtained with Fabry-Perot etalon.

The narrow width of the laser line (high monochromaticity) is of direct importance for Raman spectroscopy since it should not significantly affect the spectral resolution, which is mainly determined by the monochromator used in a Raman instrument. In other words, the spectral width of the laser line should be noticeably narrower than the instrumental function of the monochromator.

Although the laser linewidth depends on the type of laser, a linewidth that does not exceed 1 cm^{-1} is suitable for most analytical Raman applications. Laser linewidths are often cited in terms of frequency rather than wavenumber or wavelength. Recalling the relation between wavelength and frequency for electromagnetic radiation (1.37) from Chapter One, wavenumbers can be converted to Hz and vice versa by simply multiplying or dividing the corresponding value by the speed of light, which is $2.99792458 \times 10^{10}$ cm/s:

$$\nu = \bar{\nu}\, c \quad [Hz], \qquad \bar{\nu} = \frac{\nu}{c} \quad [cm^{-1}]\,.$$

Thus, the laser linewidths of 1 cm^{-1} is equal to 29,979,245,800 Hz ≈ 30 GHz. To convert the linewidth $\delta\nu$ expressed in Hz to the linewidth $\delta\lambda$ in units of nm, the following formula can be derived:

$$\Delta\nu = \nu_1 - \nu_2 = \frac{c}{\lambda_1} - \frac{c}{\lambda_2} = \frac{c}{\lambda - \frac{\Delta\lambda}{2}} - \frac{c}{\lambda + \frac{\Delta\lambda}{2}} = \frac{c\left(\lambda + \frac{\Delta\lambda}{2}\right) - c\left(\lambda - \frac{\Delta\lambda}{2}\right)}{\left(\lambda - \frac{\Delta\lambda}{2}\right)\left(\lambda + \frac{\Delta\lambda}{2}\right)}$$

$$= \frac{2c\frac{\Delta\lambda}{2}}{\lambda^2 - \left(\frac{\Delta\lambda}{2}\right)^2} = \frac{c\Delta\lambda}{\lambda^2 - \frac{\Delta\lambda^2}{4}},$$

where Δv is the spectral interval in Hz, v_1 and v_2 are, respectively, the higher and the lower frequencies in Hz, λ_1 and λ_2 are the corresponding wavelengths in nm, and $\Delta\lambda$ is the spectral interval in nm. Since $\Delta\lambda$ is several orders of magnitude smaller than λ, then $\Delta\lambda^2/4$ is negligible and can be dropped. Therefore, it can be written as

$$\delta v \approx \frac{c\delta\lambda}{\lambda^2}$$

and, finally, as

$$\delta\lambda \approx \frac{\lambda^2\delta\nu}{c}.$$

Here, the linewidth $\delta\lambda$ depends on the laser wavelength λ so that $\delta\nu$ = 30 GHz is equivalent, for example, to $\delta\lambda \approx 0.03$ nm at the laser wavelength of 532 nm and $\delta\lambda \approx 0.06$ nm at the laser wavelength of 785 nm. As it was mentioned above, historically, the He-Ne laser was often the first choice for Raman spectroscopy due to its extraordinary stable output frequency and high beam quality. Indeed, the linewidth of a single-mode He-Ne laser is about 1.5 GHz without stabilization. Since the laser generates a 632.8 nm wavelength, the calculations using the above formulae result in the laser linewidth of 0.05 cm^{-1} in the wavenumbers and $\delta\lambda \approx 0.002$ nm in the wavelengths.

A single-frequency laser (sometimes called a single-wavelength laser) operating on a single fundamental longitudinal and a single transverse TEM_{00} resonator mode is the best option for Raman microscopy. Only this type of laser can provide the highest spectral and spatial resolutions, as well as the most effective Raman scattering from a diffraction-limited focused laser spot.

It should be borne in mind that single-frequency lasers may still emit light at frequencies other than that of the fundamental laser line. Gas lasers emit so-called plasma lines, while solid-state and, especially, diode lasers may produce much broader luminesce bands, both of which can interfere with Raman scattering. Unfiltered output beams of He-Ne and Ar^+-ion lasers contain numerous plasma lines. Although the extraneous plasma emission is typically a few percent of the laser's total power, the presence of the lines may result in spectral artefacts as the intensities of these lines are often comparable with those of Raman bands. To reject these unwanted emissions, “clean-up” bandpass filters are required. Note that although the plasma lines are normally filtered out, they can be potentially useful as internal standards for calibrating Raman spectrographs (Craig and Levin 1979) or when a precision measurement of band shifts in Raman spectra is required.

2.2.6. Frequency and power stability

The stability of the radiation frequency and output power of the laser is of fundamental importance. The former affects the accuracy of determining the positions of Raman bands and, therefore, is responsible for the possibility of performing a reliable qualitative analysis, i.e., the identification of substances. The latter directly influences the accuracy of determining the intensities of the Raman bands and, therefore, is accountable for consistent quantitative analysis.

While in practice the Raman shift axis is calibrated periodically, the laser frequency must remain stable not only between the calibrations but in the course of the spectral measurement. Small changes in the resonator length upon thermal expansion or contraction can result in the frequency drift and

affect the linewidth making these parameters reliant on the measurement time. Stable frequency generation is more difficult to achieve with a longer resonator and a resonator length control technique, e.g., measuring the transmission of a very stable reference cavity or a gas cell may be required.

Typical output power levels range from less than ten mW in UV lasers up to several hundred mW in NIR ones. The output power should not fluctuate for more than a few percent. Laser manufacturers often indicate power stability as part of their specifications. An optical feedback loop and thermoelectric stabilization of the cavity components is especially important for diode lasers to ensure their good power stability at varying ambient temperatures.

To control laser power and, respectively, the light power density at a sample, a set of neutral density filters (NDF) with discrete transmittances or an NDF with continuously variable transmittance is used at the laser output. The main function of the NDF is to protect the sensitive sample from any thermal or photochemical damage as a focused laser beam creates a very high density of power.

In the Raman microscope with its backscattering sampling geometry, the sample may reflect the laser beam backward into the laser cavity. The back reflection can cause power instability and the risk of permanent damage to the laser. It is recommended to have an optical back-reflection isolator integrated into the laser module or mounted externally.

To maintain a high output power and to ensure that a long measurement takes place under constant illumination conditions, active beam stabilization is often used in a Raman microscope to compensate for possible drift in the laser beam's position and alignment. The drift is caused by laser

instabilities, insecurely mounted optics, thermal fluctuations within the microscope itself, external vibrations, etc. Stabilization can be achieved via beam position control and correction. The control of the unintended beam deviations can be applied with, for example, a four-quadrant position sensor that monitors the displacement of the beam relative to the sensors' centre. Subsequent correction can be performed by kinematically mounted resonator mirrors using piezoelectric adjusters.

2.3. Microscope

The optical (light) microscope, or its principal components coupled with a Raman spectrometer, represents an essential integral part of a Raman microscope. This part allows the experimenter to visualize microscopic objects with high magnification, focus a sub-micron size laser spot on these objects and collect light scattered by them.

The microscope that uses a combination of optical objective and binocular (two eyepieces) is called the compound light microscope. It can produce a high total magnification calculated as the magnification power of the objective (typically up to 100×) multiplied by the power of the eyepieces (10× or 15×). A common compound microscope is equipped with a rotating turret known as a nosepiece that can accommodate from three to six objectives of different magnifications, thereby allowing the user to select an optimal one quickly. A compound microscope often enables various advanced illumination options, such as phase contrast, differential interference contrast (DIC), polarized light and fluorescence. The optical microscope integrated into a Raman microscope is normally equipped with a digital camera to capture a video image of the sample that can be analyzed, processed and correlated with the Raman spectral images acquired from the

sample. The video image can also be documented and saved along with the Raman images.

There are two major configurations of the light microscope to be integrated into the Raman microscope depending on the positions of the objective relative to the sample: upright and inverted. In the former, the objective is placed above the sampling stage, pointing down so that the samples are observed and measured from the top. In the latter, the objective is underneath the stage, pointing upward to analyze the samples from below. The inverted configuration is especially useful for examining living cells and organisms through the bottom of a cell culture vessel in liquid. The inverted microscope allows maintaining a more natural environment for the living specimen, thereby prolonging its life and enabling extended analysis time if required.

In either of the configurations, microscope objectives, which are often called objective lenses, are situated in the closest proximity to the sample being examined. The primary role of an objective in a light microscope is to magnify the details of the sample under study. The objective focuses the illumination light at the sample and collects the reflected light to capture the sample's details via the observer's eyes or video camera. In a Raman microscope, the objective has a dual function: in addition to observing the sample, it focuses the laser beam at a specific location on the sample and collects scattered light. This scattered light is then directed to a spectrometer to obtain a Raman spectrum of the sample. Thus, the objective of a microscope is an essential optical component from which sample analysis begins.

2.3.1. Microscope objectives

A microscope objective is composed of a complex set of lenses and other optical elements. Microscope manufacturers offer a great assortment of microscope objectives designed for a variety of applications and samples. Important parameters of a given objective and conditions for its use are specified in code by engravings made on its metal barrel (also called case or outer housing), as demonstrated in Figure 2-7. The illustration shows the typical markings for microscope objectives of two main categories. The first is a metallurgical or dry objective that works with an air gap between the front lens of the objective and the sample's top surface. The second is an immersion objective designed for working with a drop of an immersion fluid (water, oil or glycerin) between the front lens and the sample. Metallurgical objectives are used when contamination of the sample by immersion fluid is not acceptable or desired, or the Raman bands of a sample under study are so weak that residual Raman bands of the immersion fluid cannot be completely subtracted from the measured spectrum. The objectives of these two categories are distinctively marked on their barrels. The metallurgical objectives intended for both brightfield and darkfield illumination, which is a standard way of lighting a sample in reflected light microscopy, are marked by the code BD. In contrast, objectives that provide brightfield only illumination are usually unmarked. The BD type objectives normally have a wider diameter of the barrel to accommodate a hollow collar surrounding the lens elements and the additional light path. Consequently, these objectives require a larger diameter of a mounting thread in the microscope nosepiece. Brightfield only objectives require adaptors to fit the BD nosepiece.

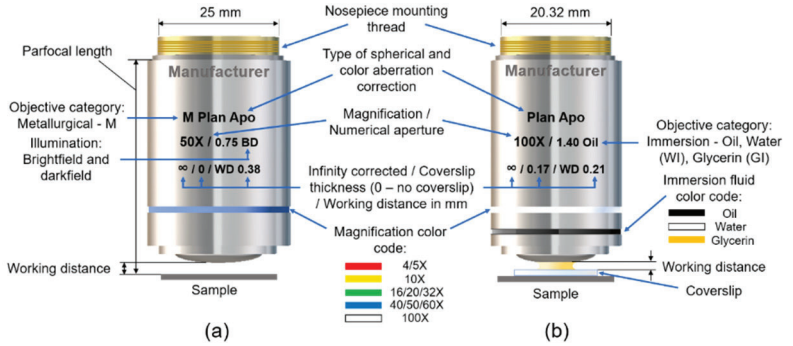

Figure 2-7. Metallurgical (a) and immersion (b) microscope objectives and designations of their characteristics.

As the light passes through the objective, it undergoes an axial (longitudinal) chromatic aberration that results in different colours (wavelengths) of light, which are focused at different distances from the objective's front lens (How Lenses Function 2016). Thus, in a Raman microscope that uses multiple lasers, the red, green and blue excitation wavelengths are focused on different points in the vertical axial direction. Namely, the shorter blue wavelength is focused above the focal plane, while the longer red wavelength is focused below the plane. The chromatic aberration is naturally caused by dispersion—the dependence of the refractive index of the lens on the wavelength of light.

The spherical surfaces of the lens cause a distortion known as spherical aberration. The spherical aberration occurs as a result of paraxial light rays that pass across the central region of the lens focus farther away than peripheral light rays that pass closer to the edges of the lens. When a collimated laser beam is focused by the lens, the spherical aberration leads to the beam distortions that expands the focused laser spot in the axial

direction and therefore worsen the axial spatial resolution. The curvature of the lens also results in the focus and contrast of the optical image fades out at the outer edges of the field of view.

Special objective designs are utilized to compensate for chromatic and spherical aberration to bring different colours to a common focal point and to produce a flat, sharp image within the field of view.

Correction for the focal points of blue and red wavelength is achieved by mounting convex and concave lenses made of different types of glass with dissimilar refractive indices inside the objective. Optical objectives constructed in this way are called achromats and are the most common types of objectives available for optical microscopes. Typically, achromatic objectives are not labelled with a special abbreviation.

In a Raman microscope with several excitation wavelengths, the application of microscope objectives with minimal chromatic aberrations is especially important. Such objectives should allow the focusing of different wavelengths and measuring spectra at the same point in a sample. A higher degree of correction for chromatic aberration is achieved in semi-apochromatic (also called fluorite) and apochromatic objectives, which are constructed using multiple combined lenses and special types of glass, such as fluorocrown, flint glasses or advanced synthetic substitutes. The former focuses the red and blue wavelengths at one point and brings the green one close to this point. The latter corrects the chromatic aberration, so that blue, green and red wavelengths are focused at the same point. For a given magnification, apochromatic objectives usually feature higher numerical apertures than achromats or semi-apochromats. However, semi-apochromats transmit UV light more efficiently since they are made of

synthetic CaF_2 crystals or special glass formulations. Although apochromats have the most sophisticated construction and are, therefore, the most expensive, they represent the best choice for high-end Raman microscopes with excitation wavelengths in a visible region. Semi-apochromats can be a good choice for a Raman microscope equipped with lasers emitting from near-UV to NIR, as they combine chromatic correction with high optical throughput and provide a reasonable balance between quality and cost.

All the three types of chromatically corrected objectives mentioned above produce a spherically aberrated image. An example of the effect of spherical aberration is an image blurred at the edges seen through a microscope. The planar (or plan) objective corrects the spherical aberration. The planar objective has a focal distance that is shorter for peripheral rays than for paraxial ones. The objective produces a flat image across the field of view and can also provide a much larger working distance. Plan-achromatic, plan-fluorite and plan-apochromatic objectives are corrected for both spherical and colour aberration.

In addition to the correction of optical aberrations, the most important criterion for choosing a microscope objective is its numerical aperture (*NA*). The value of the *NA* necessarily indicated on an objective barrel is a measure of its ability to resolve fine details in a sample under investigation. The *NA* of an objective is defined by

$$NA = n \sin\alpha , \qquad (2.11)$$

where n is the index of refraction of the medium that fills the space between the objective's front lens and the sample (for air, n = 1.00), and α is one-half the maximum angle of the cone of light that the objective's front lens can collect when the sample is in focus.

When the laser beam is focused by an objective on a sample, the laser spot is approximated by an Airy disk and its diameter in the XY focal plane in air is estimated using the equation

$$d_{xy} = \frac{1.22\,\lambda}{NA}, \tag{2.12}$$

where λ is a laser excitation wavelength, and *NA* is defined by (2.11). The Airy disk is the bright central region of the smallest diffraction-limited focused spot of light that a uniformly illuminated lens with a fully filled circular aperture can produce. For an aberration-free lens focused at infinity, the following approximation is valid:

$$NA = n\,sin\alpha = n\,sin\left[arctan\left(\frac{D}{2f}\right)\right] \approx n\,\frac{D}{2f}, \tag{2.13}$$

where *f* is the focal length of the lens, and *D* is the laser beam's diameter (see Fig. 2-8). Thus, the formula (2.13) can be derived from (2.4) by assuming the use of an objective in air (n = 1) and substituting $^{f}/_{D}$ with $^{1}/_{2NA}$ in (2.4):

$$d_{min} = \frac{2.44\,\lambda\,f}{D} = \frac{1.22\,\lambda}{NA} = d_{xy}\,.$$

Following the equation (2.12), the objective with *NA*=0.90 illuminated by 532 nm wavelength produces the spot diameter estimated as

$$d_{xy} = \frac{1.22\ \cdot 0.532\ \mu m}{0.9} = 0.72\ \mu m\,. \tag{2.14}$$

Hence, the higher *NA*, the smaller the spot that can be produced by the objective passing the light of a given wavelength (Fig. 2-8). The spot size is

directly related to the lateral spatial resolution in the Raman microscope since the incident light is focused in and the scattered light is collected from this spot. The lateral spatial resolution is generally defined as the shortest distance between two objects in the focal plane, which can be resolved. There is a certain criterion to quantify that two objects are resolved, which will be considered in Chapter Three. The spatial resolution is evidently better and is termed "higher" when the laser spot is smaller. A sub-micron lateral spatial resolution can be achieved for visible excitation wavelengths using objectives with a higher *NA*.

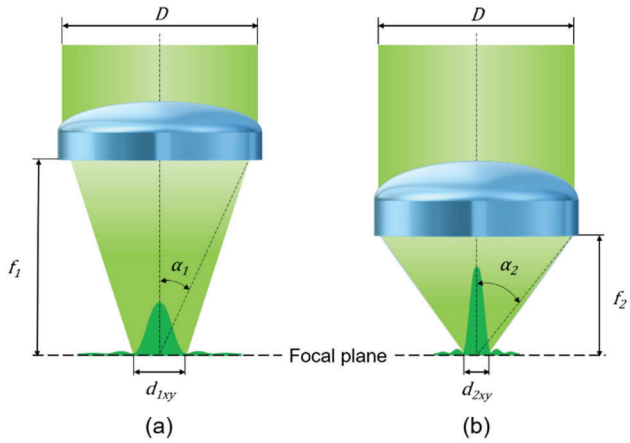

Figure 2-8. Diffraction-limited focused laser spot produced by objective lenses with low (a) and high (b) *NA*: *D* is the diameter of the laser beam that illuminates the lens; f_1 and f_2 – focal lengths; α_1 and α_2 – the half-angles of the cone of light that exits the lens; d_{1xy} and d_{2xy} – diameters of the laser spots for low and high *NA*, respectively. The diffraction pattern of focused light in the plane perpendicular to the focal plane with the central Airy disk and a few sidelobes is shown in dark green.

For a metallurgical objective designed to examine opaque samples using reflected light, *NA* can never be greater than 1 because α cannot exceed 90^0 and, as it follows from (2.11), $nsin\alpha \leq 1$ in air as $n = 1$. High-quality metallurgical objectives can have *NA* up to 0.95. However, one can increase *NA* by using an immersion objective and submerging both the objective's front lens and the sample in a transparent fluid with a higher refractive index, such as oil ($n = 1.52$) or water ($n = 1.33$). Therefore, the spatial resolution and the efficiency of the scattered light collection can be further improved. For the visible region's excitation wavelengths, colourless synthetic oils that are inert, remain stable over time and do not produce fluorescence are commonly used. In practice, most oil immersion objectives achieve a maximum *NA* value of 1.4. For UV excitation, glycerin immersion objectives are preferable. The water immersion objective is used in Raman microscopes in a manner similar to oil immersion objectives, but with water in place of the drop of oil. The water immersion objective is often employed in an upright microscope to dip directly into an aqueous biological buffer and analyze live biological cells and organisms. Additionally, the immersion fluids provide a heat dissipation effect, which may protect the sample from overheating and thermal degradation caused by laser radiation.

The correct magnification depends on what needs to be seen and examined. In simple terms, objective magnification is the degree to which an objective enlarges an object. The objective magnification power (M) is expressed as the ratio of the object's sizes in the image and focal planes. Recall that the total magnification in the observed image is the product of the magnification powers of the objective and an eyepiece. Low power objectives, sometimes called “scanning” objectives, provide observers with enough magnification for a good survey of a sample. One can examine, for example, a colony of

biological cells or a continuous large-area graphene film by way of visual scanning the sample. Higher power objectives allow smaller objects or sample details, such as individual organelles inside the cells or inhomogeneity of the graphene film, to be seen better. However, the objective magnification should not exceed a certain threshold, after which further magnification will not increase the optical resolution. Also, too high magnification may result in a dim image since the brightness of the image is proportional to NA^2/M^2.

The numerical aperture rather than a nominal magnification power is a major parameter of the microscope objective since objectives with the same magnification can have significantly different *NA* numbers. Namely, the numerical aperture is a property of the objective that determines how much fine detail one can see and how high resolution can be achieved in the image of a sample. Using an objective with the largest NA, the largest light power density at a focused laser spot, the highest collection efficiency and the best spatial resolution can be achieved for given experimental conditions.

Infinity corrected objectives, which were introduced about a decade ago and are ideally suitable for optical microscopes, are now common parts of Raman microscopes. After collecting light from a sample, the objectives create parallel light rays and, therefore, form a collimated beam of light that is focused at infinity. The collimated beam is brought into focus at the image plane by a tube lens, as shown in Figure 2-9. The infinity-corrected optics allow auxiliary analytical components (such as beamsplitters, illuminators, polarizers, DIC prisms and optical filters) to be placed into the space between the objectives and eyepieces so that no focus change or magnification correction is required in the observation path. When changing the infinity-corrected objectives, the location of the image plane remains the

same. Furthermore, the optical focus can be adjusted by moving the sample stage rather than the objective along the vertical axis. The infinity-corrected objectives can be interchangeable between the microscopes with different tube lengths, which typically range from 160 to 200 millimetres, depending on the microscope's manufacturer. These objectives are marked by the infinity symbol ∞ on their barrels.

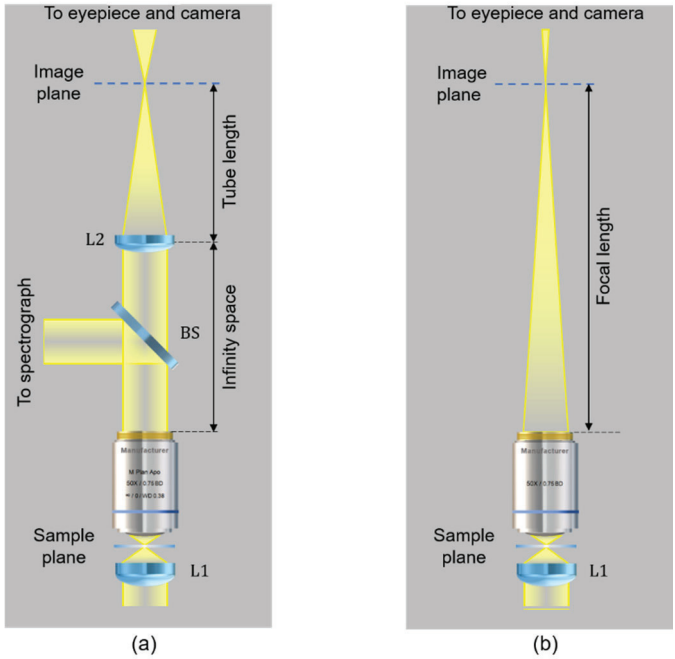

Figure 2-9. Principle diagrams of (a) infinity-corrected microscope and (b) an old type microscope with a fixed focal length: L1 – condenser lens, BS – beamsplitter, L2 – tube lens. The diagrams show the optical paths in transmission for simplicity.

Biological specimens, such as cells, microorganisms and tissues to be analyzed using a Raman microscope, often need to be prepared as a wet

mount. In the wet mount, a specimen contained in a liquid medium (water or buffer solution) is put on a standard microscope slide, and a thin glass coverslip (cover glass) is usually placed on top of the specimen. The coverslip serves two major purposes. First, it makes a flat surface and maintains the wet mount's uniform thickness for viewing and focusing the laser beam on the specimen. Second, it protects the front lens of the microscope objective from being contaminated by the specimen upon direct contact. The optimal thickness of the glass coverslip the objective is intended for is often engraved in millimetres on its barrel. For most objectives, the optimal thickness is 0.17 mm (the coverslip number or category is 1.5), although the thicknesses from 0.08 mm up to 0.64 mm are commercially available, which corresponds to the coverslip numbers from 0 to 4. If the objective is metallurgical and is not intended for being used with a coverslip, then it is indicated by 0 on its barrel.

A significant parameter, which is usually marked on the modern objective barrels, is its working distance (WD). The working distance is the distance between the objective front lens and the surface of a sample when the sample is in focus or between the objective front lens and the surface of the coverslip if the objective is designed to be used with the coverslip. Microscope objectives are usually designed with a short working distance. However, when the sample is placed at the bottom of a well or located in a reaction chamber with a thick observation window, objectives that have a longer working distance need to be used. The objectives designed to focus at long or extra-long working distances are labelled by the corresponding abbreviation LWD or ELWD. The objectives suitable for observing processes and samples inside chambers or ovens at high temperatures are marked as having ultra-long (ULWD) or super-long working distance

(SLWD). A larger working distance and thus a lower numerical aperture can be useful if the sample has a rough surface or complex topography that requires a larger clearance between the objective front lens and the sample in the axial direction. As a general rule, both the magnification and numerical aperture of a microscope objective is smaller if its working distance is greater. Immersion objectives are more restricted in the working distance lengths.

Another important parameter related to the objective size is its parfocal length. The parfocal length is the distance from the shoulder of the objective to the surface of a sample when the sample is in focus. When switching between microscope objectives with different magnifications but identical parfocal lengths by turning the nosepiece, only minimal sample refocusing may be required. Parfocal length varies between objective manufacturers, although the most widely used values are 45 and 60 mm. It is important to keep in mind that when using objectives from different manufacturers, the parfocal length should be the same.

When selecting a proper objective in a Raman microscope, one should consider the laser excitation wavelength. A common microscope objective that transmits about 90% of visible light at 532 nm wavelength may have less than 20% transmittance below 400 nm. For UV or deep UV excitations, specially designed objectives correspondingly made of fused silica or quartz are required. The microscope objective offering the maximum transmission in both the UV and NIR regions is still not available.

2.3.2. Sampling stages

All microscopes are equipped with a stage where the sample is positioned for examination. The microscope stage is usually flat, has a rectangular or

square shape and includes clips and holders to fix and hold the sample in place. The stage may contain specialized holders and adaptors for manipulating microscopic samples during their examination. The design and characteristics of the sampling stages for Raman microscopes are important as they determine the manner and the rate at which the sample can be scanned and the spectra at different points of the sample can be collected. For confocal Raman microscopy, the stages should provide precision motion in three degrees of freedom, i.e., in X (right and left), Y (back and forth) and Z (up and down) directions. Thus, the sample can be scanned under the objective in all these directions, and a 3D spectroscopic representation of the sample can be constructed.

There are two major types of mechanical XYZ translation sampling stages for both upright and inverted microscopes: manual and motorized (computer-automated). The manual stage has knobs (micrometre screws) that allow one to move the stage and position a sample finely under the objective alongside the X-, Y- and Z-axis by turning the corresponding knobs. The manual stage provides maximal travel distances of a few inches in all three directions. The precision and repeatability in sample positioning offered by manual stages are usually in the range of 5–10 microns, which makes these stages mostly suitable for single-point measurements. Raman confocal microscopes capable of analyzing samples of a variety of shapes and dimensions at the diffraction-limited spatial resolution require highly accurate focus control and, thus, high-precision motorized stages. Conventional Raman microscopes use stages driven by stepper motors, which are electric motors that convert digital pulses into mechanical shaft rotations. To achieve submicron precision and reproducibility of the sample positioning, the motorized stages often apply closed-loop control of the X-,

Y- and Z-axes by employing high-resolution encoders for the active positioning feedback. The stages driven by stepper motors scan the sample in a discrete mode of operation, which is often referred to as point-by-point or stop-and-go. In this mode, the sample is sequentially displaced in either direction by a preselected distance (step) and then measured. The array of Raman spectra obtained at predefined locations of a sample constitutes a Raman map. High-speed Raman imaging microscopes require the Raman maps to be acquired when the sample continuously moves along one of the axes and is shifted to the next line at a preselected distance when the end of the sweep is reached. The continuous raster scanning mode without stopping is a critical feature enabling ultrafast map acquisition and a real-time 2D or 3D Raman image rendering. Raman imaging requires sampling techniques that offer fast scanning speed and ensure high spatial resolution. The details of the techniques that deploy raster scanning piezo-actuated stages, Galvano scanners and the combinations of mechanical stages with the piezo or Galvano scanners are presented in Chapter Three.

2.3.3. Beamsplitters

In the back-scattering geometry implemented in all modern Raman microscopes, the laser illuminates the sample through the objective, and scattered light is collected with the same objective. Thus, the incident beam and the collected light beam before it is directed to the spectrograph share a common optical path. To separate the collected light beam from the laser beam, a special optical element or special arrangement of optical elements is usually employed. The simplest optical element used in the back-scattering configuration is a beamsplitter. The beamsplitter is a semitransparent mirror that both reflects and transmits a light beam. The most common laser beamsplitter is designed for an angle of incidence of 45^0

and provides 50/50 splitting ratios, which means that it reflects 50% of the power of the incident laser beam and transmits the remaining 50%. While this beamsplitter is easy to set up, much laser light power is lost. Indeed, since 50% of the power is lost on each passing through the beamsplitter, 75% of the light power is lost with two crossings.

To avoid such a loss of laser excitation efficiency, a metal mirror with a centred hole or a laser reflector can be used. The mirror is to be installed in the laser beam at an angle of 45° to it. A small hole is drilled in the centre of this mirror so that the collimated laser beam passes through it to the sample, and the back-scattered light collected with the objective is reflected from the mirror at an angle of 90° to the incident laser light. In another geometrical arrangement, the mirror is replaced with a laser reflector. The reflector is a glass plate with a mirror spot of a few millimetres in diameter in its centre, reflecting the laser beam aimed at the spot. It is mounted at 45° in the optical path of collected light so that the laser beam makes an angle of 90° to the collected light beam. The reflector directs the laser beam to the sample and then passes back-scattered light collected by the objective. Both the arrangements virtually allow a full laser output power to be focused on the sample. However, their realization with strictly orthogonal light beams leads to the appearance of a dark spot in the image plane corresponding to the hole in the metal mirror or the small mirror in the centre of the reflector. The dark spot then obscures the centre of the detector matrix in a spectrograph and distorts its illumination. Moving the dark spot away from the detector matrix requires introducing a small but carefully calibrated deviation from the light beams' orthogonality that may decrease the overall optical throughput of the Raman instrument.

Dichroic beamsplitters are rejection filters that reflect one specified spectral region while allows another to pass. They are commonly used at non-normal angles of incidence. Modern dichroic beamsplitters designed for Raman microscopes are available in a plate or cube form and offer various splitting ratios such as 70/30, 80/20 and even 90/10 for a specified spectral region. A good plate beamsplitter is slightly wedge-shaped to eliminate interference effects. A cube beamsplitter is composed of a pair of identical right-angle prisms adhered together on their hypotenuse faces with a metal or dielectric semitransparent layer deposited on one of the faces.

Effective collection of Raman scattered light in the back-scattering configuration can be achieved by combining a 90/10 beamsplitter with a Rayleigh filter. In one configuration, the beamsplitter and the filter are placed sequentially. The beamsplitter reflects 90% of the laser light of a certain excitation wavelength toward a sample. After the objective collects light scattered by the sample, the beamsplitter transmits only 10% of Rayleigh scattering but entire Raman scattering. The following Rayleigh filter blocks out residual Rayleigh scattering from getting into a spectrograph. This combination allows for approximately four times better efficiency that could be achieved with a conventional 50/50 broadband beamsplitter. Another configuration uses an advanced holographic optical element that integrates the functions of a beamsplitter and a Rayleigh filter. This element works in the so-called inject/reject mode, in which it injects 90% of the laser light to the sample and then transmits Raman scattering from the sample to a spectrograph while it rejects Rayleigh scattering. Both configurations shown in Figure 2-10 ensure high optical throughput and uniform illumination of the detector matrix. However, they require careful

tuning of the angles of the optical elements relative to the direction of the laser beam.

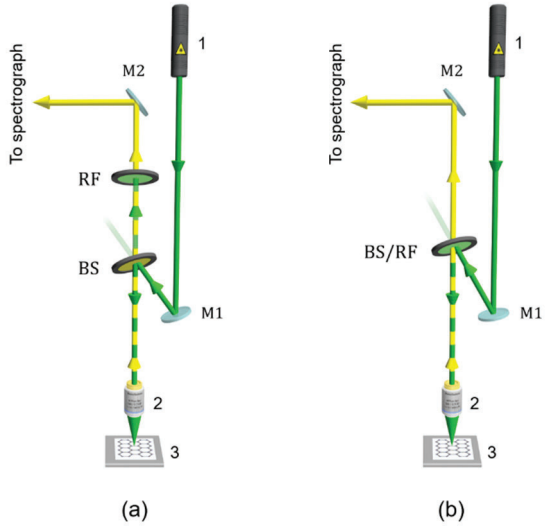

Figure 2-10. Combining a beamsplitter with a Rayleigh rejection filter in Raman microscope: (a) sequential configuration of the beamsplitter (BS) and the Rayleigh filter (RF) in the optical path; (b) holographic filter with combined functionality (BS/RF) in the inject/reject configuration. 1 – laser, 2 – objective, 3 – sample, and M1, M2 – mirrors. The green and yellow colours denote the laser beam and the beam formed by the objective after collecting scattered light from the sample.

2.3.4. Blocking Rayleigh scattered light

As mentioned in Chapter One, elastic Rayleigh scattering is light of the same wavelength that is used for excitation. Rayleigh scattering is very intense—at least a million times stronger than Raman scattering. Rayleigh scattered light is not of practical interest to Raman spectroscopists and, if this intense radiation passes into the spectrograph, it can mask the weaker

Raman spectrum from observation or even damage the Raman detector. Thus, it is necessary to block Rayleigh scattering (the Rayleigh line) from reaching the detector but pass Raman scattered light through to the detector. Sometimes this process is not very accurately referred to as blocking the laser line.

There are two main techniques for blocking Rayleigh scattering: 1) placing an optical blocking filter in the optical path of collected scattered light; 2) using a tunable filtering spectrometer to block an unwanted portion of scattered light.

The optical blocking filters used in Raman spectroscopy are divided into edge and notch filters in accordance with the shape of the frequency or wavelength response and into interference and holographic filters according to their designs. An edge filter, also known as a barrier filter, is a long pass optical filter that attenuates all wavelengths, including Rayleigh scattering, but transmits all wavelengths above a certain cut-off point. The edge filter allows measurements only to be made in the Stokes region of the Raman spectrum. A notch filter, often referred to as a band-stop or a band-rejection filter, rejects only a very narrow band of wavelengths which is chosen to coincide with Rayleigh scattering while transmitting both Stokes and anti-Stokes Raman scattering. Each specific laser excitation and, correspondingly, Rayleigh scattering wavelength requires an individual edge or notch filter.

An interference (often called dielectric) filter consists of multiple layers of thin dielectric films with different refractive indices deposited on a transparent polished inorganic glass or glass-ceramics substrate. The functionality of these filters is based on a reflection of an unwanted and

transmittance of the desired wavelengths due to the optical interference phenomenon that occurs between the incident, reflected and transmitted light wavelengths at the interfaces of the thin films. The number of layers and the difference in refractive index between the layers in the filter, i.e., the filter thickness and the profile of the refractive index modulation, determines the filter's optical density and spectral bandwidth. Optical density (OD) is a measure of an optical filter's blocking ability and is similar to (1.33) from Chapter One:

$$OD = log_{10}\frac{I_0}{I} = log_{10}\frac{1}{T},$$

where I_0 is the intensity of the incident light, I is the intensity of the light transmitted through the filter, and, thus, T is the transmittance of the filter.

Since Rayleigh scattering is a million times stronger than Raman, it has to be suppressed by at least six orders of magnitude to make the weak Raman scattering detectable. The filter that transmits only one-millionth of the incident light at a given wavelength has OD = 6 (often written as OD6). OD times ten is equal to the filter's transmittance, which is often specified in decibels (dB) so that the OD6 corresponds to a transmission loss of 60 dB.

The interference filters technology has improved over the years. The present filter manufacturers offer the number of dielectric layers that reach well over 100, ensuring OD > 6, and an adequate edge steepness, i.e., the sharpness of the transition profile from transmitted light to blocked light. These filters are available for use with lasers emitting in UV, visible and NIR spectral regions. They are environmentally stable, have a practically unlimited lifetime and a decent incident light power tolerance, although the damage may occur at high powers.

Despite the advancement of interference filters, the major technological impact on the development of compact analytical Raman instruments was made by VBG(VHG)-based holographic diffraction filters (Owen 2007). Volume Bragg holographic filters are composed of a relatively thick layer of a photosensitive material. In these filters, successive planes of high and low refractive indices are formed by means of laser holography and spatially modulated. The higher the number of planes that can be produced in the material, the narrower the bandwidth of the corresponding filter. These planes are separated by the distance $d=\lambda_0/2n$, where λ_0 is the wavelength of the recording laser light and n is the refractive index of the photosensitive material. When the light beam incidents upon the filter, the diffraction of light produces a selective reflection of the wavelength λ that fulfils the Bragg condition for the constructive interference

$$m\lambda = 2nd\,sin\theta\,,$$

where m is the order of diffraction, $d=\lambda_0/2n$ is the distance between the planes of high and low refractive indices, and θ is the glancing angle, i.e., the angle that complements the angle of incidence. All the other wavelengths that do not fulfil the Bragg diffraction condition are transmitted. If the angle of incidence is near normal so that $sin90^0 = 1$, then

$$m\lambda = 2nd\,. \tag{2.15}$$

Substituting $d=\lambda_0/2n$ into (2.15), the following equation can be obtained:

$$m\lambda = 2n\frac{\lambda_0}{2n} = \lambda_0\,.$$

Thus, in the first diffraction order, $m=1$, the filter reflects at the same wavelength as if the recording was performed at a normal incidence.

A group of scientists and engineers from EIC Laboratories and Physical Optics Corp. under the supervision of M. Carrabba (Carrabba, et al. 1990) first reported the observation of Raman spectra with a compact single-stage spectrograph using an edge holographic volume Bragg diffraction filter fabricated in a dichromated gelatin (DCG) emulsion. This holographic edge filter allowed a Raman spectrum in the Stokes region to be measured within less than 200 cm^{-1} of the Rayleigh line. Soon after, the notch holographic filters that maximized the edge steepness were developed to allow Raman spectra in both Stokes and anti-Stokes regions to be obtained within 50 cm^{-1} from the excitation wavelength (Schoen, et al. 1993). Since then, DCG has become a material of choice for the production of high-quality holographic filters and gratings. Despite proven advantages and affordable prices, gelatin filters have several drawbacks. First, DCG needs to be protected against moisture and properly sealed in a laminated filter assembly. Therefore, unlike the interference filters, the characteristics of gelatin-based holographic filters may degrade over time, and these filters are considered to have a finite lifetime. Second, the thickness of the filters is limited to a few tens of microns, which restricts the achievable minimum bandwidth to approximately 10 nm. Third, DCG absorbs sharply below 350 nm that excludes its use in filters for blocking UV wavelengths.

The requirements for narrow spectral bandwidth, robustness with respect to environmental factors and tolerance to any excitation wavelength led to the adoption of unique solid-state VBG-based optical filters fabricated in the bulk of photosensitive optical glasses (Moser, et al. 2008). The possibility of recording a three-dimensional hologram in the glass with a thickness of

several millimetres would allow the fabrication of VBG optical filters with bandwidths of orders of magnitude narrower than those achieved by gelatin-based technology. The ultra-narrow bandwidth of the notch filters enabled significant improvements in the Raman instruments for low-wavenumber measurements below less than 5 cm^{-1} in both Stokes and anti-Stokes regions. Furthermore, the notch filter allows the rejection band's position to be finely tuned to optimise the low-wavenumber cut-off. The so-called angle tuning is achieved by slightly altering the inclination of the notch filter relative to the incident light beam. The monolithic glass construction provides exceptional reliability and stable performance over an unlimited lifetime.

A photo-thermo-refractive (PTR) optical glass made of a Na_2O-ZnO-Al_2O_3-SiO_2 matrix doped with a silver (Ag), cerium (Ce) and fluorine (F) has the most successful applications in these filters due to superior environmental stability and high temperature damage threshold. The silicate glass matrix is not susceptible to humidity degradation. It can withstand noticeable temperature variations as the holographic image formed in PTR glass cannot be thermally distorted up to 400°C. In recent years, the exploitation of unique features of PTR glass has resulted in the development of novel volume multiplexed VBG filters with high rejection at multiple wavelengths (Glebov, et al. 2012). Such multi-band holographic optical filters are formed by recording a number of diffraction gratings in a single glass plate. This means that, for example, a 5 mm thick PTR glass plate can contain up to 5 diffraction gratings for a variety of wavelength combinations. Thus, a thick PTR glass plate can be used in a single VBG filter in a Raman spectrometer equipped with several laser sources.

VBG-based holographic filters provide significant advantages over typical interference ones due to their much narrower spectral bandwidths, higher edge steepness and independence of the optical transmission from the incident light's polarisation. Figure 2-11 depicts the typical responses of edge and notch filters as well as holographic and interference notch filters for comparison.

The only drawback of holographic notch filters fabricated in solid glasses is that their production with OD>4 is still difficult and expensive. To achieve OD with values of 6 and greater, it appears practically more reasonable to sequentially insert several filters with lower ODs in the optical pass of the scattered light.

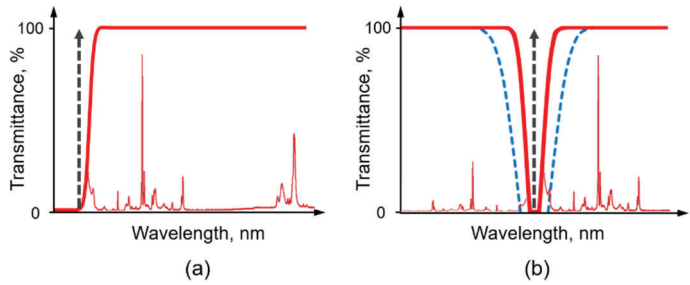

Figure 2-11. Principal plots of transmittance (solid red line) vs. wavelength for edge (a) and notch (b) filters. The blue dotted line in (b) shows the transmittance of a typical interference notch filter for comparison. The dotted vertical arrow indicates the wavelength of Rayleigh scattering (laser excitation). As an example, the Raman spectrum of polystyrene is shown in a full spectral range for Stokes shift in (a) and in half spectral range (the “fingerprint” region) for anti-Stokes (left) and Stokes (right) shifts in (b).

The second technique for blocking Rayleigh scattered light has been historically implemented with the use of multistage monochromator systems. In a triple monochromator, it is possible to configure the first two monochromators in a so-called subtractive mode. This premonochromator cascade separates Rayleigh from Raman scattered light and then blocks Rayleigh scattering from being transmitted to a third stage. The third stage acts as a regular single monochromator to disperse Raman scattered light and obtain the Raman spectrum. The triple monochromator system provides very high attenuation of Rayleigh scattering, while allowing the Raman spectrum to be measured closer than 5 cm^{-1} to the excitation wavelength. Moreover, the premonochromator cascade is tunable in the entire working spectral region of the instrument so that one system with a triple monochromator can accommodate any number of laser sources. However, such a system features a very poor optical throughput, is quite large and expensive. It usually requires rather more expertise to operate in comparison with a single monochromator system incorporating a Rayleigh blocking filter. All of these factors make multistage spectrometers with tunable filtering premonochromator mostly suitable for specific and non-routine Raman applications.

2.4. Spectrograph

An optical spectrometer performs a spectral (harmonic) analysis of the collected radiation. This analysis is most often carried out using a dispersing element (diffraction grating or prism), thereby deflecting the rays of different wavelengths at different angles. A spectrometer with a dispersing element is called dispersive, while a spectrometer that performs spectral analysis based on the principle of optical interferometry, such as the

Michelson interferometer in the FT-Raman instrument, is called non-dispersive.

Prism spectrometers have almost disappeared from use in recent years. Raman microscopes use spectrometers with a grating as the dispersing element. A typical dispersive spectrometer consists of five basic components: 1) an entrance aperture, 2) collimating optics, 3) a diffraction grating, 4) focusing optics, and 5) a detector.

The entrance aperture may be a slit, a pinhole or the output end of an optical fibre, as will be discussed below, and the spectrum can be essentially regarded as a discrete number of monochromatic images of the entrance aperture in the focal plane of the spectrometer. However, as Chapter Three will consider, the aperture confines an element of the sample from which the spectrum is measured. Thus, the aperture performs two main functions: it provides the necessary spectral and spatial resolution.

Collimating optics, which can be a mirror or a lens, collect the light diverging from the input aperture, form a collimated beam of light and direct it to the diffraction grating. The collimating optics ensure that the full area of the diffraction grating is properly illuminated, which is necessary for the optimal operation of the grating, as will be shown below.

The diffraction grating separates the light rays in space as a function of wavelength so that each constituent wavelength component is deflected under a certain angle, but all rays of the same wavelength travel under the same angle. The dispersed rays are then collected by the focusing optics, again represented by a mirror or a lens, which form an image of the entrance aperture by focusing the light rays of different wavelengths at the exit focal plane.

The detector placed in the exit focal plane generates an analogue electrical signal proportional to the intensity of the light that hits the detector. If the rays of different wavelengths are scanned over the detector through an exit slit sequentially by rotating the diffraction grating, then the instrument operates as a monochromator. The monochromator makes one measurement of the light intensity at a particular wavelength at a time. If a multichannel (array) detector is placed in the focal plane, then all the parallel rays of different wavelengths can be registered simultaneously, and the instrument works as a spectrograph. The spectrograph measures the light intensities at every wavelength and records the entire spectrum in a single snapshot.

There are two important merit figures that allow the evaluation and comparison of the spectrometers' performance: optical throughput and spectral resolution. The presence of an entrance aperture, which restricts the light flux passing through the spectrograph, results in a well-known trade-off between the spectral resolution and optical throughput of the dispersive spectrograph.

The basic components of the spectrograph are discussed in more detail below to provide a better insight into their influence on optical throughput and spectral resolution.

2.4.1. Diffraction gratings

The most important component of a dispersive spectrograph is the diffraction grating that provides angular dispersion of analyzed light, i.e., spatially separates its constituent wavelengths.

For over a hundred years, the prism has been the only apparatus to decompose analyzed light into its spectral components by mean of

dispersion. In 1786, the American astronomer David Rittenhouse first used the diffraction phenomenon to obtain a spectrum. The device he made consisted of hairs strung between two finely threaded screws. Later, in 1821, Bavarian physicist Joseph Ritter von Fraunhofer created diffraction grating formed by a string of thin wires stretched over a frame and developed the first theory of diffraction grating. Fraunhofer also proposed obtaining gratings with closely spaced narrow transparent and opaque parallel lines by mechanically ruling a glass plate's surface using a diamond point. He also proposed a method of obtaining a reflective grating by ruling grooves on the mirror surface of the metal. The use of diffraction gratings was limited by the difficulties in ruling the gratings of sufficient quality until the American physicist Henry Rowland constructed a dividing engine of extraordinary accuracy in 1882. The following production of high-quality gratings led to significant progress in spectroscopic instruments. The basic principles for manufacturing diffraction gratings proposed by Fraunhofer have remained the same until now, although the production techniques for spectroscopic diffraction gratings have improved significantly.

A typical diffraction grating consists of a substrate made of an optical material, with a large number of fine, equidistant, parallel lines (grooves) created on its surface. There are two types of diffraction gratings used in spectrographs:

1) Reflective grating, in which the grooves are created on a reflective surface of the usually metal-coated glass so that light reflects only between the grooves;
2) Transmissive grating, where the grooves are created on a transparent glass substrate so that light can pass between the grooves but not through them.

Regardless of the grating type, they both act on the same principle. An idealized transmissive diffraction grating can be imagined as consisting of a set of equidistant narrow slits. The action of the diffraction grating is based on the interference of light waves on these slits. The constructive and destructive interference of the light rays emanating from adjacent slits results in maxima and minima in the wave amplitude. The maxima are observed when the difference in the path of the rays $\Delta_2 - \Delta_1$ is equal to an integer number of the wavelengths (Fig. 2-12**)**. A simple geometric consideration allows the distribution of maxima to be defined by the equation

$$t(sin\varphi - sin\psi) = k\lambda\,, \tag{2.16}$$

where t is the spacing between the centres of the adjacent slits (the grating period), φ is the angle of diffraction, ψ is the angle of incidence, and the integer k is called the order of diffraction. A similar equation can be derived for reflective grating where light is reflected off the ruled surface at different angles φ corresponding to different orders k and wavelengths λ. Equation (2.16) is known as the grating equation.

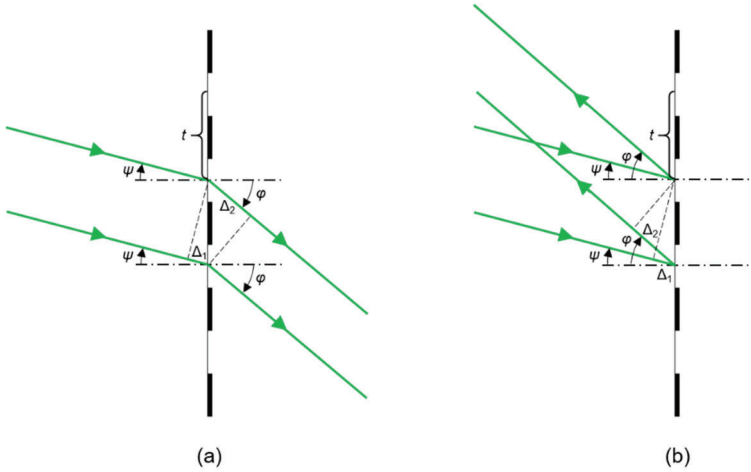

Figure 2-12. The principles of diffraction on transmissive (a) and reflective (b) gratings: ψ – the angle of incidence, φ – the angle of diffraction, t – grating period, and $\Delta_2 - \Delta_1$ – pathlength difference between incident and reflected rays.

A collimator plays an important role in forming a parallel light beam directed from the entrance aperture to the grating. Without a collimator, the diverging light rays from the aperture would incident onto the grating under variable angles. As follows from the grating equation, varying angle of incidence ψ results in changes to the angle of diffraction φ. Consequently, the same wavelengths of light in the same diffraction order are deflected at different angles, thereby blurring the resultant diffraction pattern. However, with a collimator, all angles of incidence are equal, and no blurring of the diffraction pattern will happen. When parallel rays of polychromatic light are incident on a grating, then light is dispersed so that each wavelength satisfies the grating equation. The grating equation allows the essential properties of the diffraction grating to be established.

The grating produces spectra corresponding to different values of k that can be positive or negative. For $k = 0$, a zero-order spectrum is obtained for which $sin\varphi = sin\psi$, regardless of the wavelength. Thus, there is no diffraction in the zero-order spectrum, and the rays of light follow the laws of geometrical optics.

For the higher orders of diffraction $k = \pm1, \pm2, \ldots$, equation (2.16) implies that the diffraction angle φ must increase as the wavelength λ increases. Thus, the grating reflects different wavelengths of light λ at different angles φ, making it possible to use the grating as a dispersing element. In the case of a white incident light, the grating produces a continuous, angle-dependent spectrum.

The maximum value of k_{max} is limited by the condition $|sin\varphi - sin\psi| \leq 2$. Then, from (2.16), it follows that

$$|k_{max}| \leq 2t/\lambda \ ,$$

and for the grating to produce a spectrum of at least the first order, the condition

$$t > \lambda/2 \qquad (2.17)$$

must be satisfied. Thus, the period t must be wider than the incident wavelength to cause diffraction. The number of grooves per unit length (grove density) usually given in mm (gr/mm) is called the grating constant. The grating constant is inversely proportional to its period so that gr/mm = $1/t$. For instance, as follows from (2.17), for $\lambda = 532$ nm, t should be more than 266 nm, i.e., the grating constant should be less than 3,759 gr/mm. The gratings used for applications in the visible spectral range typically have

from 600 to 2400 gr/mm. For longer wavelengths, the grating constant should be about 300 gr/mm or less.

The grating constant affects both the wavelength region in which the grating operates and the dispersion properties of the grating. The higher grating constant results in higher resolving power and greater dispersion of the grating. The resolving power R of the grating is defined in terms of wavelengths λ and the minimal difference $\delta\lambda$ between the wavelengths that can be resolved. The resolving power R is a dimensionless number. It can be theoretically shown that R is a product of the order of diffraction k in which the grating is used, and the number of grooves N illuminated on its surface by the incident light:

$$R = \frac{\lambda}{\delta\lambda} = kN. \tag{2.18}$$

Thus, in order to increase the resolving power of the grating, it is necessary to increase N. Accordingly, for the grating of a given width, the grating constant needs to be increased. It is important to note that the collimating mirror in the spectrometer (Fig.2-1) should be aligned to illuminate the grating's full width to provide the theoretically achievable resolving power.

Another factor that makes it necessary to increase the grating constant is the desire to increase the angular dispersion since the grating with a large angular dispersion ensures a proper resolution in a compact spectrometer. The angular dispersion D_φ defines the angular separation $d\varphi$ between light rays that the grating can resolve. The expression for angular dispersion D_φ can be obtained by differentiating (2.16) with respect to λ and keeping the angle of incidence ψ fixed:

$$D_{\varphi} = \frac{d\varphi}{d\lambda} = \frac{k}{t\ cos\varphi}. \tag{2.19}$$

The grating is also characterized by linear dispersion D_l, which is usually called simply the dispersion

$$D_l = \frac{dl}{d\lambda},$$

where dl is the linear separation between the resolved light rays measured on the exit focal plane of a spectrometer. The linear dispersion D_l depends on the exit focal length f. Thus, D_l is the product of the angular dispersion D_{φ} given in (2.19) and the focal length:

$$D_l = fD_{\varphi} = \frac{fk}{t\ cos\varphi}. \tag{2.20}$$

Hence, by using a diffraction grating with high angular dispersion, i.e., with a small period t or a high groove density, the output focal length f can be reduced, and the spectrometer could be made more compact. The dispersion at the exit focal plane of the spectrometer is often specified as reciprocal linear dispersion and given in nm/mm by

$$\frac{1}{D_l} = \frac{d\lambda}{dl} = \frac{t\ cos\varphi}{fk}.$$

The diffraction pattern produced by white light incident on a reflective diffraction grating is illustrated in Figure 2-13. The larger dispersion can be achieved in the higher orders in correspondence with the grating equation (2-16).

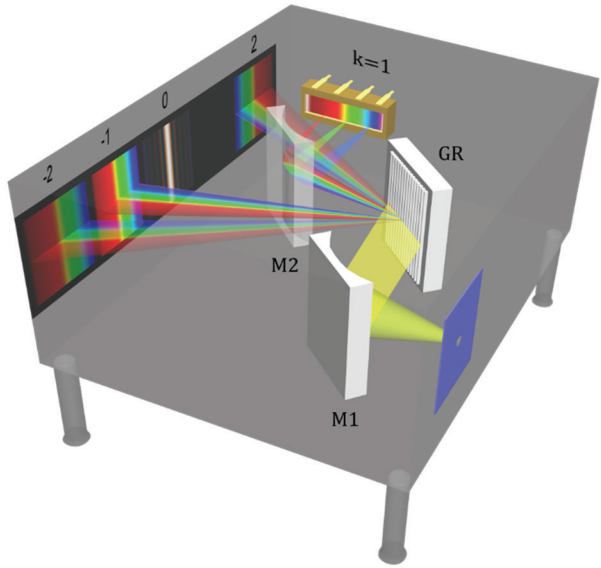

Figure 2-13. The diffraction pattern produced by a white light beam incident on a reflective diffraction grating (GR). The diffraction pattern is shown projected onto the inner wall of the spectrograph. The bright central line in the diffraction pattern corresponds to the zero-order spectrum, while the spectra of higher orders $k = \pm 1$ and ± 2 with increasing dispersion are produced on both sides of the bright line. M1 and M2 are collimating and focusing mirrors, respectively. The diffraction grating is usually positioned to project the first diffraction order k=1 on the focusing mirror M2, which then projects the first-order spectrum on the detector.

Multiplication of the reciprocal linear dispersion by the slit width results in the spectral resolution expressed in wavelength. A higher diffraction order can also be used to increase the resolving power and dispersion. However, an overlap of the high orders of diffraction can restrict the working spectral range of the grating. As follows from the grating equation (2.16), for a given angle of incidence ψ, the light of wavelength λ in the spectrum of the first

order is observed at exactly the same angle as the light of wavelength $\lambda/2$ in the second-order, as well as the light of wavelength $\lambda/3$ in the third-order, etc. The largest wavelength interval of a given diffraction order in which there is no overlap with an adjacent order is called the free spectral range of the grating, $\Delta\lambda$. Since the angles of incidence and diffraction for the adjacent overlapping orders are the same, then it follows from equation (2.16) that

$$k\lambda = (k+1)(\lambda - \Delta\lambda) ,$$

and the free spectral range is

$$\Delta\lambda = \frac{\lambda}{k+1} = \lambda_2 - \lambda_1 ,$$

where λ_1 is the shortest wavelength and λ_2 is the longest wavelength in the free spectral range. Obviously, the free spectral range decreases when the diffraction grating is used in higher orders. Thus, some measures have to be taken to separate the spectra of adjacent orders, for example, by using a bandpass filter. Meanwhile, in the first order, the free spectral range is $\lambda/2$, i.e., the grating can be used from λ_1 to $\lambda_2=2\lambda_1$ without overlapping with the second-order diffraction. For example, when using an excitation wavelength of 532 nm, the wavelengths up to 1064 nm can be observed in the first-order diffraction spectrum without overlapping. In Raman spectrometers, the diffraction grating is usually set to the first diffraction order because the grating efficiency decreases in higher orders.

The diffraction grating efficiency characterizes its optical throughput and can be specified as either absolute efficiency or relative efficiency. Absolute efficiency is defined by the ratio of the light power diffracted into the spectrum of a particular order to the light power incident onto the grating.

Relative efficiency is the fraction of the power diffracted into a particular order to the power that would be reflected by a plane mirror coated with the same material as the grating. The absolute diffraction efficiency is calculated by multiplying the relative diffraction efficiency by the reflectance of the coating material of the mirror:

Absolute efficiency = Relative efficiency × Reflectance of the mirror.

Because even the most effective mirrors do not provide 100% reflectance, the absolute efficiency always yields a lower numerical value than the relative efficiency of the same grating. Often, the manufacturers specify the grating efficiency in % of the absolute value. As a rule of thumb, the higher the grating constant, the more the grating's efficiency curve shifts towards shorter wavelengths.

The diffraction grating efficiency can be maximized for a particular wavelength such that most of the light power is concentrated into the first diffraction order at that wavelength and reduced at all other wavelengths. The efficiency optimization can be achieved by appropriate groove shaping, i.e., by making a sawtooth groove profile to form a step structure. The steps are sloped with respect to the grating surface at the so-called blaze angle, which determines the direction in which the maximum efficiency is reached. Therefore, the grating appears to "blaze" when viewed from that direction. The purpose of the slope of the steps is that the blaze angle θ_B can be chosen such a way that the light rays diffracted by the grating, and the rays reflected from the facets of the steps are both deflected in the same direction. Consequently, the angle of diffraction coincides with the angle of specular reflection that significantly increases the diffraction efficiency at a designated wavelength. The wavelength for which the blazed grating is

most efficient is therefore specified as the blaze wavelength. Absolute efficiency can reach over 80% for the specified wavelength. Figure 2-14 shows the reflective blazing grating principles and typical efficiency curves vs. wavelength for ruled and holographic blazed gratings.

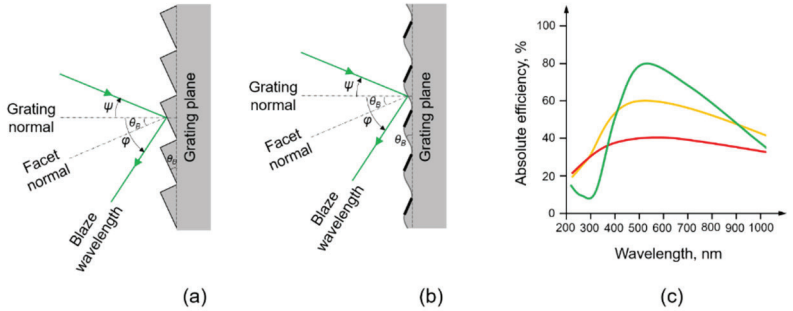

Figure 2-14. Simplified cross-sections of blazed ruled (a) and holographic (b) diffraction gratings and the typical efficiency curves (c) for ruled blazed at 500 nm (green), holographic blazed at 500 nm (orange) and ruled non-blazed (red) gratings.

Diffraction gratings can be manufactured using different technologies. According to traditional technology, equidistant grooves are mechanically ruled on a flat glass plate (transmissive grating) or a flat mirror (reflective grating) using a ruling machine with a diamond-tipped tool. These gratings are called ruled gratings. The mechanical ruling offers the robust creation of sawtooth groove profiles on a metallic surface and, thus, the fabrication of highly efficient blazed gratings. The principal disadvantages of using mechanically ruled gratings in spectrometers are as follows: 1) limited resolving power due to the difficulty of achieving a very high groove density; 2) the appearance of spectral “ghosts” (false spectral satellites) near the strong spectral lines resulted from periodic errors, which may be caused by the irregular operation of the ruling machine; and 3) diffuse stray light

originating from random groove irregularities or deviations from the ideal profile shape. Stray light is an important aspect of a spectral instrument with diffraction gratings. When a spectral instrument works at a limit of detection, the level of stray light from the grating and other optical elements sets the ultimate limit of detection. Modern interferometrically controlled ruling machines allow the intensity of the spectral ghosts and the stray light to be reduced to a very low level.

Optical holographic technology is used to produce diffraction gratings by recording a fine laser interference pattern in a photoresist film deposited on a substrate. Patterns can be created on a wide range of hard materials, such as glass, quartz and different semiconductors. In contrast to ruled gratings, holographic gratings are free of both periodic and random ruling imperfections due to the very precise spacing between grooves which is achieved in the optical interference pattern. As a result, they produce no spectral ghosts and ensure very low stray light. They can be made with a groove density as high as 6000 gr/mm, which gives them a high resolving power. Standard holographic gratings have symmetric sinusoidal groove profiles. They are generally less efficient than mechanically ruled gratings, and their efficiency curves are generally smoother, flatter and broader than for ruled gratings. Holographic gratings can be used over a spectral range from deep-UV to NIR; nevertheless, their efficiency can be optimized for a specific spectral region by altering their groove depth or making asymmetric groove profiles. In the optimized region, the absolute efficiency can reach well over 50%, especially for gratings with high groove density. Moreover, holographic gratings are easy to manufacture in cases where it is difficult to apply traditional mechanical ruling, for example, when the ruled areas must be large or curved.

Therefore, ruled gratings tend to be used in applications that require high efficiency, while the holographic gratings are more suitable for measurements in a wide spectral range with minimal stray light.

When polarized light incident a grating, the grating efficiency depends on the orientation of the plane of polarization relative to the direction of the grooves. For maximum efficiency, the grating should be oriented such that the plane of polarization is oriented perpendicular to the grooves.

Even though reflective gratings are most widely used in modern Raman spectrometers, transmissive grating makes possible a more compact spectrometer design with collimating and focusing lenses instead of mirrors.

Nowadays, most diffraction gratings are replicated from master gratings, also known as original gratings. Numerous replicas can be made of a master grating manufactured according to one of the technologies mentioned above. Modern replicating processes allow the batch production of diffraction gratings and ensure the replicas have the same properties and quality as the master grating for a significantly reduced production cost.

2.4.2. Detectors

Focusing optics ultimately collect the light diffracted by the grating onto a detector mounted in the focal plane of the spectrograph. A charge-coupled device (CCD) is now one of the most commonly used detectors in Raman spectroscopy. The CCD's major advantage is its high sensitivity to light, which makes it very suitable for the detection of the inherently weak Raman scattering and a multichannel principle of operation, which allows the full Raman spectrum to be obtained by the simultaneous measurement of its spectral components. By the full Raman spectrum, we mean the spectrum

in the range of wavenumbers corresponding to the fundamental vibrations of the main chemical groups.

The concept for CCD was invented in 1969 by Willard Boyle and George Smith of Bell Laboratories, who were awarded the Nobel Prize for Physics in 2009. Basically, a CCD is an integrated circuit formed on a silicon substrate. The electronic band structure of crystalline silicon is such that the energies of the top of its valence band and the bottom of the conduction band are equal to 1.14 eV and 3.3 eV, respectively. The bandgap specifies the energy required to produce an electron-hole pair with conduction or free electron, which moves within the silicon's crystal lattice and serves as a charge carrier. The light photons with energies from 1088 nm to 376 nm corresponding to the silicon bandgap impinging on the silicon surface can be absorbed by the material and create free electrons due to the photoelectric effect. Thus, light photons from NIR to UV can generate a charge in silicon that is then collected, transferred, read out and converted by electronics into digital data corresponding to the intensities of the wavelengths incident on the detector.

A CCD detector consists of a large number of photosensitive elements arranged in a two-dimensional array on the silicon substrate. The discrete elements of the array are called pixels, which is a word that is derived from “PICture ELement”. The pixels are defined in the silicon matrix by a grid of current-conducting polysilicon pads called gates. Electrical electrodes are connected to the gates. The entire structure is composed of the gates, metal electrodes, an insulating silicon oxide layer and a silicon semiconductor. This structure is known as a metal-oxide-semiconductor (MOS) capacitor, which is operated both as a photodiode and storage device, and it is the principal component of the pixel.

The pixels are arranged in rows and columns. The matrices of CCD detectors for Raman spectrographs have a rectangular shape and typically comprise 1024, 2048 or 4086 vertical columns and from 128 to 512 horizontal rows with a pixel size ranging from 13.5 μm to 26 μm. In a typical dispersive Raman spectrograph, constituent wavelength components of analyzed light are projected onto the CCD array's long axis. Thus, the longer horizontal direction along the rows is ascribed to the dispersion or spectral axis and the vertical direction along the columns - to the spatial axis (Fig. 2-15).

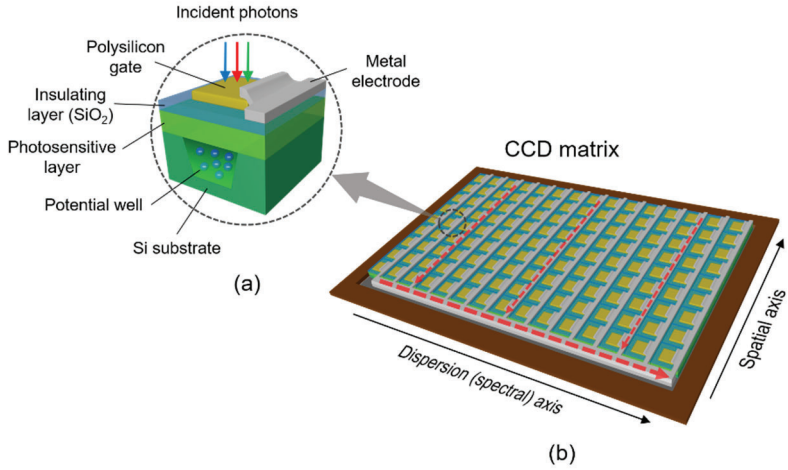

Figure 2-15. A single CCD detector pixel (a) and the CCD matrix (b). The vertical red dotted lines in (b) indicate the directions of the charge transfer in columns (only the three lines are shown for simplicity), while the horizontal line points out the charge shift in the readout register of the CCD matrix.

Once light photons fall on the CCD, the negatively charged electrons are generated in a photosensitive layer often referred to as the depletion (charge-free) region. This region is composed of epitaxially grown silicon

with a doping level that differs from that of the silicon substrate. The positively charged gate electrodes make the photoelectrons migrate to the areas underneath the gates called potential wells. Because of the insulating layer made of SiO_2, the electrons cannot penetrate through this layer to the gate and, instead, are accumulated into electrically positive potential wells associated with each pixel.

In principle, each absorbed light photon can generate one free electron so that the resulting charge accumulated in each pixel is proportional to the number of incident photons. CCD accumulates the charge during a specified time interval, which is referred to as the exposure time. Since the detector is mounted in the focal plane in such a way that the constituent wavelength components are distributed horizontally across the long axis of the CCD, each pixel of the same vertical column receives light photons of the same wavelength. The resulting charge in each column must be quantified to determine the intensity of the corresponding spectral components.

The process of reading the charge is carried out electronically using an electrode grid on the CCD matrix. The grid performs the function of a shift register for charge transfer. During the readout, the stored charge is shifted along transfer channels under the influence of voltages applied to the electrode grid. The frequency of the charge transfer, i.e., how frequently per second the transfer channel is capable of transporting the charge by one pixel, is called the pixel clock. The transfer of charge is directly coupled to a clocked voltage pattern assigned to the grid, thereby justifying the term “charge-coupled” device. The frequencies at which CCD detectors run today are approximately between 25 and 50 MHz.

In CCD detectors, the charge is moved by a series of parallel shifts sequentially transferring charge from one pixel to the next. The charges in adjacent pixels may be combined, and this process is called pixel binning. The charge is finally collected in a readout (horizontal shift) register, which is situated down the long side of the detector matrix parallel to the dispersion axis of the CCD. In the CCD detector operating in so-called spectroscopic mode, a full vertical binning (FVB) readout sequence is implemented. During FVB readout, the charge from each complete column of pixels is simultaneously moved down and summed into the corresponding pixel of the readout register to increase the resulting charge. The FVB readout reduces the total number of charge transfer operations required to read out the whole CCD and results in a decrease in both the readout noise and the readout time. However, it increases the probability of cosmic ray spikes appearing in the Raman spectrum. The resulting charge in each pixel of the readout register represents the light intensity distribution along the dispersion axis. The charge is then read out by being shifted horizontally one pixel at a time from the readout register to a single point at the input of a preamplifier.

After the resulting charge is converted into a proportional voltage by the preamplifier, the signal is transmitted to an analog-to-digital converter (ADC), which converts the analogue voltage value into a digital number corresponding to the magnitude of the voltage. The digital numbers at the ADC output are represented in a binary form, i.e., the number of discrete values of power of two, 2^n, that can be electronically read out and interpreted by a computer. The resolution of ADC is determined by its bit length n. The ADC commonly used in conjunction with CCDs for Raman spectroscopy has a resolution of 16 bits and cannot output a number larger than $2^{16} =$

65536 discrete levels of spectral intensity. In practice, to avoid detector saturation but allow further increase in signal-to-noise ratio (S/N), one can use multiple exposures to integrate the charge collected during a single exposure and then average it. We will refer to the overall time of measurement using the multiple exposures as the integration time. The use of multiple exposures allows cosmic ray spikes to be identified and eliminated from the Raman spectrum using a simple algorithm for comparing the Raman spectra obtained in each exposure.

An important characteristic of the CCD detector is its dynamic range that specifies the maximum signal magnitude that the detector can quantify. The maximum dynamic range of the CCD detector is determined by the resolution of ADC. The practical dynamic range is defined as the ratio of the maximum measurable signal to the minimum one. At each pixel, there is a minimum amount of noise which is associated with the physical properties and operational conditions of the CCD. The noise is determined by dark current, readout noise and shot noise. In practice, the minimum noise in the CCDs is reduced to several electrons per pixel.

Dark current or thermal noise in CCD detectors is due to the charge that primarily originates from the thermal emission at defect surface sites in Si. This process creates extraneous electrons which cannot be distinguished from the actual photoelectrons generated in the pixels. However, the level of dark current is strongly dependent on the temperature of CCD. At room temperature (~ 22^{o}C), the noise associated with the dark current can be as great as thousands of electrons per pixel per second. As a result, the dynamic range will be reached in several seconds, and the detector will be saturated. The dark current can be greatly reduced by cooling. In most CCD detectors, the dark current drops by a factor of two for every 5–8^{o}C decrease in

temperature. In the high-end Raman spectrometers and, especially, microscopes, CCD detectors are cooled thermoelectrically with Peltier junctions or cryogenically with liquid nitrogen (LN). Peltier or thermoelectric (TE) coolers can lower the temperature to about -100°C. At these temperatures, the dark current may be between one and a few electrons per pixel per second. By cooling the CCD cryogenically down to temperatures below -120°C, the noise associated with the dark current can be virtually eliminated as its level reduces to less than one electron per pixel per second. Although a CCD could be further cooled down to exclude the dark current from the occurrence entirely, it results in a detrimental effect on other detector parameters, such as efficiency and charge transfer rate. Most modern Raman instruments use detectors with a built-in TE cooler, although LN-cooled detectors provide noticeable advantages for certain low-light applications. Cooling the CCD to temperatures well below 0°C requires the CCD matrix to be isolated from its environment and, therefore, be embedded in a hermetic evacuated enclosure to avoid moisture condensation.

Readout noise is the noise of the electronics that amplify and digitize the signal from the detector; it is consequently attributed to the preamplifier and the ADC. Readout noise is independent of signal magnitude, although it increases to some extent with temperature. When the signal magnitude is high, readout noise is negligible, but the S/N ratio can be limited by the readout noise when the signal magnitude is low. The readout noise can never be eliminated completely; however, it essentially depends on the readout rate. The faster the readout rate, the higher the readout noise. The readout rate of most scientific-grade CCD detectors is adjustable in accordance with experiments for which they are used. For example, an

experiment that tracks rapid kinetic processes requires a fast readout to achieve adequate time resolution.

Signal shot noise (also known as photon noise in the context of photon detection by CCDs) is a noise that is intrinsic to the light intensity measurement process. Shot noise originates from the particle nature of the light photon, and its magnitude is proportional to the square root of the total signal intensity. In the Raman spectrum, shot noise can arise from the sample, background, fluorescence sources and stray light. Strictly speaking, the dark current and readout noise constitute the detector noise floor that defines the detection limit that the signal must overcome.

Quantum efficiency (QE), also known as the spectral response, is an essential characteristic of the sensitivity of CCD detectors and a critical factor in deciding whether a detector is suitable for a given experiment. QE is a measure of the probability of an incident photon with a particular wavelength to generate a photoelectron in the active region of the CCD detector. No photoelectron is generated if the photon never reaches the photosensitive layer or passes completely through the layer. Thus, the signal generated by the CCD detector is the product of the number of light photons impinging on the detector and its QE. If the noise floor is assumed to be constant, CCD detectors with a higher QE produce Raman spectra with higher S/N values. QE is normally expressed as a percentage so that QE of 100% assumes total certainty that an incident photon generates a photoelectron, although, in practice, no one CCD offers QE of 100%. As the wavelength of the incident photons changes, the QE also changes. The configuration, the grid architecture and the detector's physical composition determines how it responds to photons having different wavelengths.

The major configurations of the CCD detectors for Raman spectroscopy include front-illuminated, back-illuminated and deep-depletion CCDs. The principal cross-sections of these CCDs and their typical QE characteristics are illustrated in Figures 2-16 and 2-17, respectively.

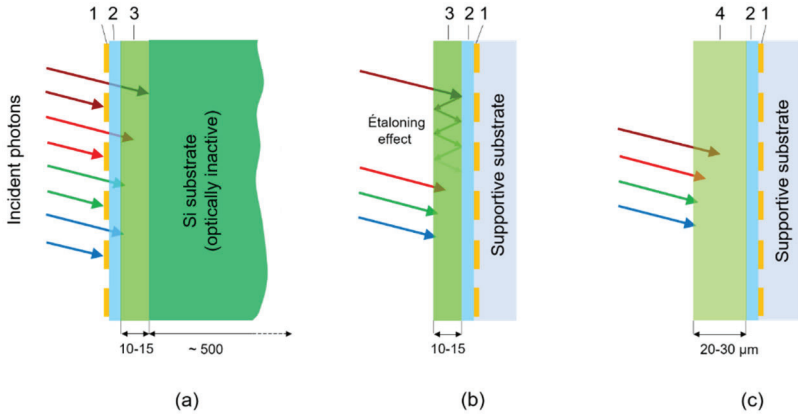

Figure 2-16. Simplified cross-sections of front-illuminated (a), back-illuminated (b), and deep-depletion (c) CCD detectors: 1 - gates and electrodes, 2 –insulating layer made of SiO_2, 3 - photosensitive region, 4 - the photosensitive region with a higher resistivity Si. The incident photons of different wavelengths and their depths of penetration are indicated by the corresponding colours' arrows. Typical thicknesses of the photosensitive layers and bulk Si are indicated in microns. The étaloning effect in back-illuminated CCD (b) created by deep penetration of long light wavelengths (dark red) through the photosensitive region is shown as multiple reflections from the boundaries of the region.

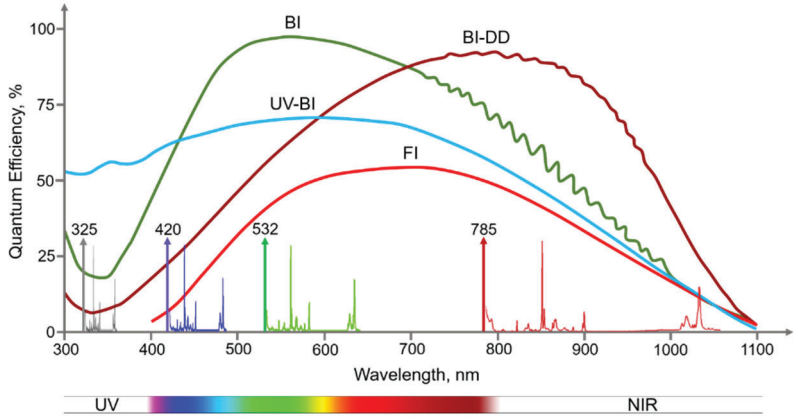

Figure 2-17. Typical QE characteristics of back-illuminated (BI), back-illuminated deep-depletion (BI-DD), UV-enhanced back-illuminated (UV-BI) and front-illuminated (FI) CCD detectors. To illustrate how the variation of QE curves with wavelength would modulate the intensities of Raman bands, the spectra of polystyrene in the range of approximately 50–3300 cm^{-1} for the Stokes region are shown for the typical excitation wavelengths of 325, 420, 532 and 785 nm.

In a front-illuminated (FI) CCD, light photons impinge on the detector's front surface, which, as mentioned above, is overlaid with a grid of metalized and polysilicon electrodes. Obviously, metalized electrodes completely block the light photons from penetrating into the photosensitive region, thereby reducing the light-sensitive area of the detector. In contrast, the polysilicon electrodes transmit some of the incident photons to the photosensitive layer, although they reflect and absorb the rest of the photons, depending on the thickness of the electrodes. The electrode grid makes it difficult to apply an anti-reflective coating which could reduce reflection losses. With any grid architecture, the maximum QE achievable in the FI CCD is about 50% at a wavelength of around 700 nm. As the polysilicon electrodes become opaque for wavelengths below 400 nm, a

standard FI CCD provides poor QE in blue and UV regions. An enhanced UV version of FI CCD in which its matrix is coated with luminescent material to convert high energy UV photons to lower energy green photons extends the response to 200 nm with a QE of 10–15%. The FI CCD detectors are the best choice for Raman applications that require multiple excitation wavelengths from blue to NIR.

A back-illuminated (BI) CCD can be imagined much like a FI CCD, but with the CCD matrix mounted upside down so that photons impinge upon the back side of the matrix. Since the back of the CCD matrix has no electrodes on it, the surface is clear of any obstacles for the photons to enter the photosensitive region. However, in order to make this design work effectively, it is necessary to remove some layer of the silicon substrate via chemical etching to provide the photons with access to the depletion region. This is why these types of detectors are also known as back-thinned (BT) CCDs. Thinning also makes the silicon wafer more fragile, and another blank silicon wafer is normally used as a supportive substrate. The back of the CCD matrix can be coated with an anti-reflection coating (for example, layers of MgF_2 and HfO_2) to reduce surface reflection losses and make them more sensitive, especially in the UV region. These factors result in BI CCDs with a dramatically increased QE that attains 95–98% at about 550 nm, which means that almost all light photons can be detected.

At first glance, the high QE of BI CCDs provides a clear advantage. However, there is a drawback. In contrast to the shorter light wavelengths, which are absorbed close to the silicon surface, the longer wavelengths penetrate much deeper into the silicon before being absorbed. This deeper penetration can result in the longer wavelength of light passing all the way through the thinned region and cause constructive and destructive

interference by multiple internal reflections at the boundaries of the photosensitive region. This effect is an analogue to one that occurs in a Fabry-Pérot étalon consisting of a thin, transparent optical medium with two flat, highly parallel and reflective surfaces. Thus, the reflected light creates the étaloning effect, that is, it generates an interference fringe pattern. The light intensity modulation produces the corresponding charge modulation in the photosensitive region. As a result, the oscillations in the spectral response particularly noticeable in the red and NIR regions occur. The amplitude of the oscillations depends on the parallelism of the reflective surfaces and the incident light intensity. The étaloning leads to the interference fringes superimposed on Raman spectra producing spectral artefacts, masking the real spectral bands and therefore making characterization and identification of samples problematic. Figure 2-18 illustrates the manifestation of the étaloning effect in Raman spectra obtained using a 785 nm laser when the fluorescence from the samples cannot be completely suppressed.

Methods, such as absolute intensity (radiometric) calibrating, averaging the interference pattern by binning in vertical (spatial) columns and roughening the rear surface of the depletion region, can be used to reduce étaloning effect in BI CCDs. The latter method introduces irregularities to the reflective surfaces to impair their parallelism in a controlled manner to prevent the light from reflecting back and forth into the depletion region. This method is the most effective as it can reduce the amplitude of fringes by a factor of 5. Nevertheless, the interference pattern cannot be totally suppressed, and BI CCDs are not recommended for use with 785 nm or longer wavelengths excitations in Raman spectrometers. BI CCDs are ideally suited for detecting extremely low signals, such as those originating

from weak Raman scatters or very low concentrations of target analytes in samples. BI CCDs are usually more expensive than FI CCDs as they require extra processing during production.

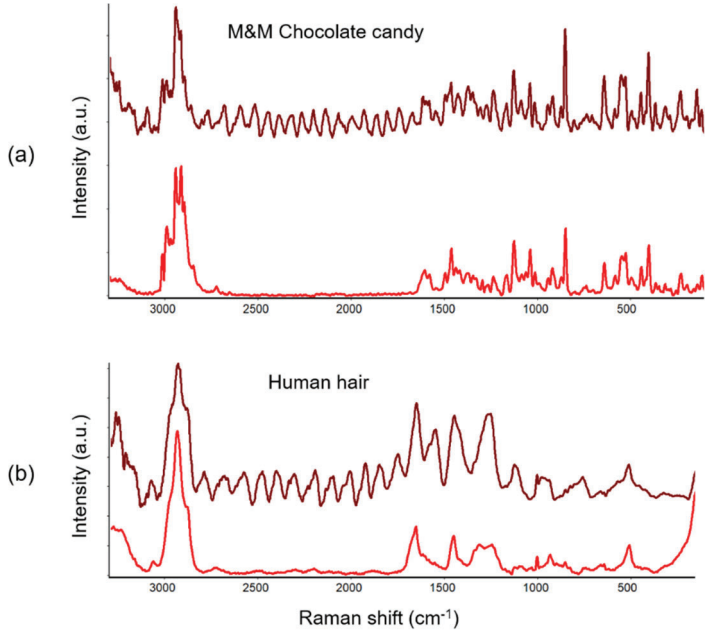

Figure 2-18. Comparison of Raman spectra of M&M's chocolate candy (a) and a human hair (b) obtained using a 785 nm laser in a Raman microscope equipped with a BI (brown) or a FI (red) CCD detector. The interference fringes caused by the étaloning effect in BI CCD detector noticeably distort the Raman spectra: the fringes interfere with the Raman bands in the region of about 3300–1200 cm^{-1} in (a), while almost all the Raman bands are masked by the strong fringes in (b). In contrast, the Raman spectra measured with the FI CCD detector show no spectral artefacts. The spectra are corrected by removing the baseline caused by fluorescence, normalized and then offset for clarity.

As mentioned above, the depth over which light photons can generate photoelectrons in the silicon increases with an increasing wavelength. As silicon starts to become transparent to the wavelengths longer than 800 nm, i.e., the NIR photons pass through the photosensitive region without generating photoelectrons, the QE of standard BI CCD quickly decreases. To improve QE, especially in the NIR region, deep depletion (DD) CCDs can be employed. This configuration of CCD has a thicker photosensitive region, which is referred to as a deep depletion region made of high resistivity silicon. The thicker photosensitive region provides a longer absorption path to longer wavelength photons and subsequently increases the probability of these photons being absorbed and generating photoelectrons. The higher resistivity silicon allows the electric field created by electrodes to penetrate the entire depth of the thicker depletion region and, therefore, more effectively capture and collect the photoelectrons.

The DD CCDs can be manufactured in both the front-illuminated and back-illuminated variants. Both variants benefit from an improved response in NIR. Advanced back-illuminated deep-depletion (BI-DD) CCDs can provide maximum QE up to 95% and up to 40% QE at 1000 nm. It should be mentioned that BI-DD CCDs manifest an extremely weak étaloning effect, typically reduced by a factor of > 10 in comparison with a conventional BI CCD. The high sensitivity combined with the low étaloning makes them the detectors of choice for Raman spectroscopy applications that require 785 nm or longer excitation wavelengths. A disadvantage of DD CCDs is their higher dark current, so it is often recommended that they are cryogenically cooled when used to detect weak Raman bands.

As mentioned above, readout noise dramatically increases with higher readout speeds of the CCDs. Thus, these detectors are mainly used at low

readout frequencies and, correspondingly, are suitable for relatively slow rates of acquisition of spectral data. Meanwhile, there is a great demand for scanning large areas and conducting confocal three-dimensional analysis, especially when studying spatially heterogeneous samples or rapidly changing systems within a reasonable time of the experiment. Another need is to minimize the potentially harmful effects of laser radiation on photosensitive samples. In order to meet these needs, a Raman microscope is often equipped with an electron-multiplying CCD (EMCCD). These detectors offer the fastest acquisition rates with the high S/N in every spectrum.

A key technological difference between EMCCD and CCD detectors is that the former employs a charge amplification stage, the electron-multiplying (EM) or gain register, which boosts the photoelectron charge before digitization. The EM register is placed between the shift register and the output preamplifier. The gain register consists of a large number of stages where a much higher than normal clocking voltage (usually, 40–50 V vs. 10 V in CCD) is applied to supply the electrons with additional energy. As the charge is being transferred for readout, it passes through the EM register. In each stage of the register, when the electrons have enough energy, they are multiplied by impact ionization, which is a type of avalanche effect. The multiplication probability at every stage of the register is usually no higher than 2%. Nevertheless, as the number of stages is large (typically > 500), the resulting charge can be very high so that a single input photoelectron producing thousands of output electrons. This technology is called electron-multiplying. Its fundamental advantage is that the gain applied to the signal in the EM register before readout is sufficient to consider the readout noise negligible compared to the signal at any readout rate. At fast readout rates,

a conventional CCD would yield a readout noise equal to or greater than the input signal. In practice, it is important to eliminate dark current in the EMCCD since even a single electron thermally generated in silicon will be amplified in the EM register. Thus, it is critical to use a high-end EMCCD detector equipped with a TE- or LN-cooling system. EMCCD detectors used in Raman microscopy are typically cooled down to at least -70^0C with TE coolers and employ the maximum gain of 1000 for optimal performance.

As a result of the effective suppression of readout noise and dark current, EMCCD detectors are considered to be limited only by shot noise. However, there is an additional noise source in EMCCD detectors as the electron multiplication mechanism required to reduce the readout noise also induces an additional noise called multiplicative noise. This noise increases the signal's shot noise by a factor of 1.4. It is manifested as a diminished S/N ratio and an increase in the pixel to pixel variation in the signals obtained under low-light conditions. Since a detector's sensitivity is determined by the two principal parameters, QE and the noise floor, EMCCD detectors can deliver higher S/N values in Raman spectra obtained in low-light conditions than conventional CCDs with substantially the same QE. Nevertheless, when an experiment does not require fast acquisition speed or high temporal resolution and a longer exposure time is suitable, it can still be more beneficial to use a conventional high-end CCD. For convenience, most of the modern EMCCDs for Raman spectroscopy allow the EM gain to be turned off and on to enable switching between advanced EMCCD and regular CCD modes of operation.

Because of the lower costs, higher QE and better resolution, EMCCDs replaced intensified CCD (ICCD) detectors which have been used in applications that required fast spectral acquisition speeds. In an ICCD, an

image intensifier is placed in front of the CCD matrix to enhance its light detection capability. The intensifier typically consists of three main components: a photocathode, a micro-channel plate (MCP) and a phosphorescent screen. In a spectrograph equipped with ICCD, after the different light wavelengths are being separated by a diffraction grating and projected to the detector, the corresponding light photons incident on the photocathode. The photocathode has a rather moderate QE. Typically, it does not exceed 50% in the blue-green region of the optical spectrum. The corresponding fraction of the photons that fall onto the photocathode is converted into electrons. The electrons are then accelerated towards the MCP due to a high electric voltage (usually, 600–900V) applied between the photocathode and the MCP. The electrons are multiplied inside the MCP channels, and the cascade of electrons then strikes the phosphorescent screen. It causes this screen to emit far more photons than were incident on the photocathode. The phosphorescent screen is usually coupled to the CCD matrix by a fibre optic bundle or high numerical aperture lenses. Although the screen emits all photons at the same (green) wavelength, the locations on the CCD matrix which the photons impinge against corresponds to the positions of the wavelengths that were initially projected on the photocathode. Thus, the Raman spectrum can be read out from the CCD matrix. The resolution of an ICCD is limited by the geometry of its MCP and is usually ¾ times lower than can be achieved in the CCD matrix itself.

The intensifier enables a shutter functionality, i.e., it can be used as a detector gate since the voltage applied between the photocathode and the MCP can be switched on and off. Thus, the gate can be open and closed at a very fast rate. The highest performing ICCD detectors enable shutter times as short as 200 picoseconds. The ICCDs, in combination with pulsed laser

excitation, still have an advantage over EMCCDs in applications that require extremely fast detection, such as in the time-resolved Raman spectroscopy that minimizes fluorescence interference mentioned in Chapter One.

While today CCD and EMCCD are mainstream detectors for high-end Raman spectrometers and microscopes, scientific complementary metal–oxide–semiconductor (sCMOS) detectors are rapidly gaining in popularity. Early CMOS detectors have suffered from inferior light sensitivity and quality issues, but continuous improvements in their design and process technology have mostly eliminated these shortcomings. sCMOS detectors perform a basic function similar to that of the CCDs. The relative strengths and weaknesses of the two technologies are manifested in the way they read the signal accumulated in the pixel. In contrast to a CCD, the sCMOS detector has pixels composed of a photodiode-amplifier pair that converts the charge into a voltage. The conversion occurs instantaneously instead of sequentially, as in the CCD detector, and the data of each horizontal or vertical pixel line is digitized by an ADC placed at the end of the corresponding pixel line. As a result, very fast readout rates can be achieved in sCMOS detectors. The optimized architecture of the new generation of sCMOS detectors combines fast readout rates with low noise that eliminates the multiplicative noise introduced in EMCCDs. sCMOS detectors have lower power consumption and allow a matrix of a smaller size to be designed or more pixels to be arranged in the matrix. Due to a higher response in the UV regions, sCMOS detectors are considered to be universal for Raman applications requiring multiple excitation wavelengths ranging from UV to NIR. The incorporation of amplifiers and ADCs in a single matrix lowers the cost for these detectors since they contain all of the

necessary electronics to produce an output digital signal. Until recently, sCMOS detectors implemented front-illuminated technology that could not yet provide a QE to correspond to the most sensitive EMCCDs. The latest developments in back-illuminated technology for sCMOS detectors largely address the high sensitivity requirements of Raman spectroscopy for ultra-low light measurements. sCMOS detectors currently find uses in high-speed Raman imaging and applications that require a high temporal resolution.

A comprehensive description of the fundamental and operational principles of Si-based detectors can be found elsewhere (Durini, D. 2019, Janesick and Putnam 2003).`

As mentioned in Chapter One, Raman spectra obtained with the use of excitation sources emitting in the visible region are frequently obscured by fluorescence originating from the sample. The likelihood of fluorescence can be reduced by moving away from the visible region by using NIR or infrared excitations so that insufficient energy transferred to the sample could not cause the fluorescence. However, Si-based CCD detectors cannot be used at wavelengths longer than about 1100 nm because the photon energy is less than the silicon bandgap, and silicon becomes transparent to the incident photons.

Multichannel array detectors based on indium-gallium-arsenide (InGaAs) compound semiconductors were developed to extend the sensitivity of detection in NIR and short-wavelength IR (SWIR) regions from 800 nm up to 2000 nm depending on the composition of the semiconductor. InGaAs detectors are linear photodiode arrays with as many as 512 elements. This size still imposes a limit on the wavelength range that can be simultaneously acquired. Recently, 1024-element arrays have been manufactured. The

length of the 1024-element array is ideal for Raman spectrographs as they allow for a broad spectral range to be covered. The standard pixel height of 500 μm is well suited for mounting the detector in the spectrograph focal plane. Overall, InGaAs detectors are not as efficient as Si-based CCDs since their QE is lower (about 75%), as illustrated in Figure 2-19. Moreover, their read noise is higher, they require cooling similar to that used in CCDs, and their cost is quite high. A specific feature of InGaAs detectors is that their long-wavelength cutoff in the SWIR region is reduced when they are cooled. Typically, the cutoff shifts by 8 nm for every 10°C of the change in temperature. Despite these disadvantages, InGaAs detectors allow dispersive spectrographs to be combined with longer wavelength laser excitations, such as 1064 nm, generated by the Nd:YAG laser traditionally used in FT-Raman instruments. Being more sensitive and compact than FT-Raman instruments, dispersive spectrographs and the 1064 nm lasers employed in Raman microscopes offer promising results for applications where fluorescence avoidance and nondestructive levels of laser power are crucial factors. Examples of these applications include the identification of highly coloured microplastics and fibres, the characterization of artworks and forensic pieces of evidence and examination of biological samples.

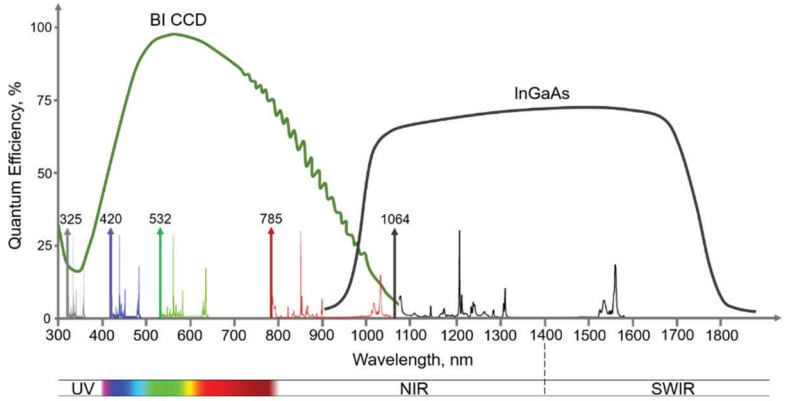

Figure 2-19. Typical QE characteristics of Si-based BI CCD and InGaAs detectors for comparison. The spectrum of polystyrene in the range of approximately 50–3300 cm^{-1} in the Stokes region is shown for the excitation wavelengths of 1064 nm (black). Note that InGaAs detector provides more linear response than Si-based CCD.

2.4.3. Types of spectrograph configurations

The most widely used spectrograph configuration for Raman spectroscopy is based on the Czerny–Turner design. The Czerny–Turner spectrograph employs concave collimating and focusing mirrors and a planar reflective diffraction grating. The Czerny–Turner design offers flexible and easy configurable setups to fit specific instrument and application requirements. This design provides a flat focal plane suitable for array detectors. However, the primary issue for a classical Czerny–Turner spectrograph with collecting and focusing mirrors placed symmetrically relative to the grating is astigmatism that results in the spectral resolution varying across the spectrum and depending on the excitation wavelength. Multiple modifications and optimizations (Shafer, Megill and Droppleman 1964,

Xue, Wang and Lu 2009, Sze and Wei 2018) resulted in a successful reduction of the aberrations in Czerny–Turner spectrographs.

Figure 2-20 exemplifies an asymmetric and crossed configuration of the Czerny–Turner spectrographs, a triplet mirrors spectrograph and an alternative spectrograph with a transmissive grating. These configurations are most often used in modern Raman microscopes. The asymmetrical configuration improves optical performance by reducing aberrations. The crossed configuration provides a more compact layout of the optical components and the geometry of the optical paths. The triplet mirrors spectrograph employs an additional focusing parabolic mirror to minimize aberrations. The focusing optics with two mirrors also make the spectral resolution less dependent on the excitation wavelength, resulting in a configuration that is superior to the Czerny-Turner spectrograph with a single focusing mirror. Transmissive gratings simplify the optical designs and are beneficial in fixed grating spectrographs.

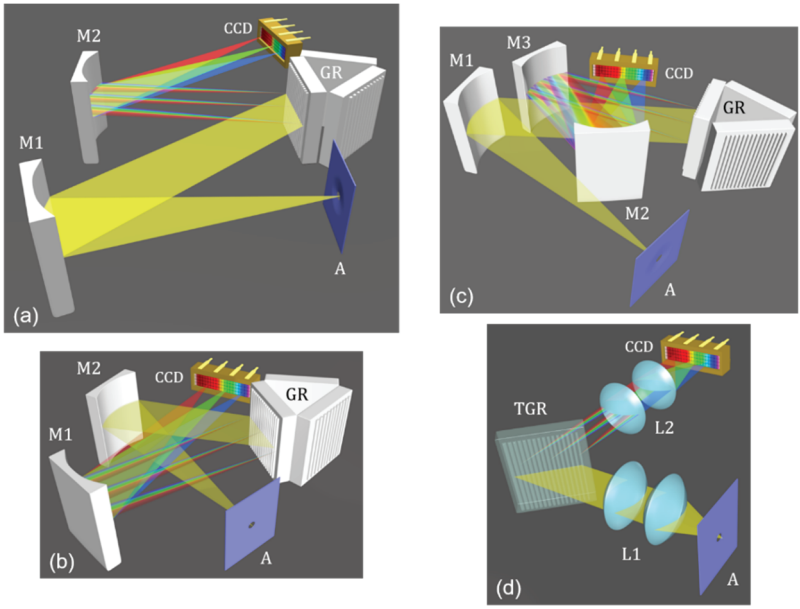

Figure 2-20. Asymmetric Czerny-Turner (a), crossed Czerny-Turner (b), triplet (c), and transmissive grating (d) spectrographs: A – pinhole aperture, M1 – collimating mirror, M2 – focusing mirror, M3 – parabolic mirror for aberration correction, GR – rotational turret with diffraction gratings, L1 – collimating lenses, L2 – focusing lenses and TGR – transmissive grating.

Several diffraction gratings, often with different groove density and, consequently, spectral dispersion, is usually mounted on a rotational turret. A triple-grating turret is a standard option available in many Raman spectrographs. The turret operation is normally computer-controlled to reduce the risk of handling these delicate optical components. The drive mechanism rotates the turret to select a grating and turns the selected grating around its pivot axis to set an operational wavelength. As an example, Figures 2-21 (a) and (b) illustrate the process of acquisition of a Raman spectrum of polystyrene by sequentially projecting two halves of the

spectrum onto CCD by turning a diffraction grating GR1. When the turret rotates and replaces the grating GR1 by GR2 with half the dispersion, the full spectrum is projected onto the CCD and acquired in one pass, but with half the spectral resolution (c).

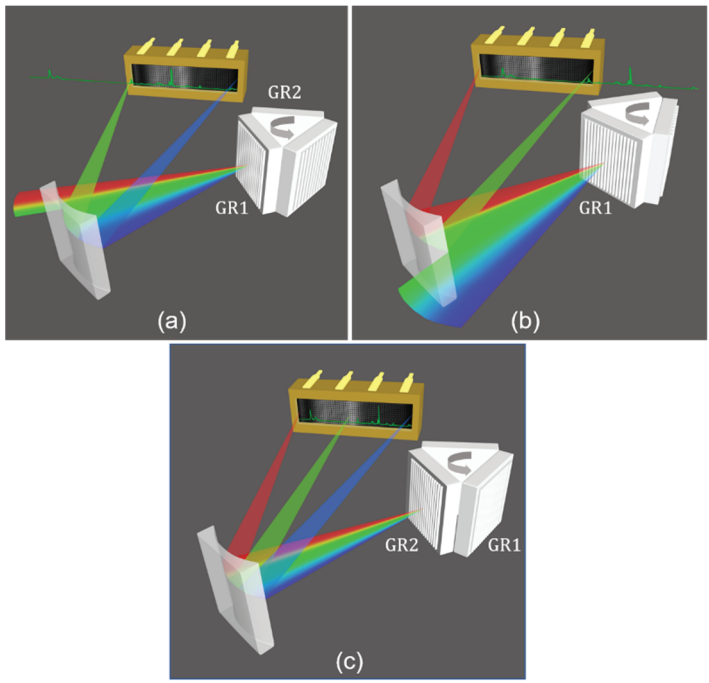

Figure 2-21. Acquisition of a Raman spectrum using diffraction gratings on a rotational turret. In (a) and (b), two halves of a spectrum are sequentially projected onto CCD and acquired using the diffracting grating GR1. In (c), the full spectrum is projected and acquired using GR2 grating with half the dispersion and, respectively, half the spectral resolution. The Raman spectrum of polystyrene is shown as an example.

This practice of turning the grating, acquiring the spectrum in multiple spectral regions and stitching the regions together using spectroscopic

software is often applied in Raman spectrographs. Despite the significant advantages of multi-grating turrets, moving the gratings has a few shortcomings. First, it takes time to move between grating positions and, if a broad spectral coverage is required, collecting multiple regions may be too time-consuming for fast spectral imaging or reaction monitoring applications. Second, as the different regions of the spectrum are acquired at different times, continuous reaction kinetics measurements appear to be problematic. Third, the grating mechanical drive inevitably yields errors in the accuracy and repeatability of the grating position when turning the grating that, correspondingly, introduces inaccuracies in optical performance and the Raman spectra. These shortcomings are addressed by using a fixed position grating that directs the full spectral range of most interest in Raman spectroscopy (for example, from 100 to 3500 cm^{-1}) to the array detector while maintaining adequate spectral resolution.

The important conditions to consider when positioning the spectrograph in a Raman microscope are temperature and vibration. The effects of temperature and vibration on the mirrors, gratings, lenses, windows, laser sources and detectors can cause them to shift over time. These may result in misalignment of the optical components and, consequently, in the deterioration of the spectrograph's performance.

There are two fundamental design requirements that must be met to maintain the robustness and stability of Raman spectrographs. First, any optical component in the spectrographs must be firmly secured in position, and displacement of its centre with respect to the optical axis is precluded. Second, the optical components must be installed in such a way that the forces of gravity acting on them do not cause shifting due to their weight. Therefore, optical components should be installed horizontally to minimize

their displacement that can be increased by gravity upon thermal changes or vibrations. As such, the horizontal positioning of the spectrograph in a Raman microscope is a preferred orientation. The spectrograph needs to be placed away from any sources that may generate excessive heat, such as a light illuminator, and positioned low enough with respect to the entire Raman microscope's centre of gravity to minimize vibrations' effect. If the spectrograph is mounted vertically to provide a more compact configuration of the Raman microscope, all the optical components should be clamped securely against a rigid surface on the mounts or spacers designed to hold the components. Any non-permanent fixing, such as with adhesives, should be avoided.

There are two important merit figures that allow the evaluation and comparison of the spectrometers' performance: the spectral resolution and the optical throughput.

2.4.4. Resolving power of a spectrograph

The resolving power or spectral resolution characterizes the ability of an instrument to separate two closely spaced spectral lines. The theoretical resolution of the dispersive spectrometer is determined by the size and angular dispersion of the diffraction grating that was considered above. The practical (also known as effective) resolution is always less than the theoretical limit.

The practical resolution is determined by the instrumental function, also known as the apparatus function or instrumental profile. It is a measure of the intensity distribution in the exit focal plane of the spectrometer, assuming that there is an ideal monochromatic spectral line at the entrance of the spectrometer. If the instrument did not introduce distortions in the

intensity distribution of this ideal monochromatic line, then a series of infinitely narrow spectral lines would be obtained at the exit of the instrument. In fact, the lines formed in the exit focal plane of the spectrometer, even if they correspond to monochromatic radiation, always have a finite width. The following factors mostly contribute to the broadening of the spectral lines by a spectrometer: 1) the spectral line is an image of the entrance aperture (typically, a slit), which always has a finite width in a real instrument; 2) diffraction phenomena and aberrations of the optical components of the spectrometer; 3) a finite detector (pixel) size. Thus, the spectrometer, when measuring a monochromatic spectral line, records a spectral profile of finite width. The instrumental function determines the shape and width of the profile. The instrumental function's width cannot be less than the width of the geometric image of the slit.

From a spectroscopist perspective, the practical resolution is a more important characteristic than dispersion. Indeed, if the instrumental function is wider than the distance between monochromatic lines, then they will be poorly resolved, even if they are far apart from each other. The resolution of the spectrograph determines the smallest wavelength interval for which two spectral lines are still observed separately. The Rayleigh and Sparrow criteria are the two quantitative measures most often mentioned in spectroscopy, which establish when two spectral lines are regarded as resolved. The Rayleigh criterion was originally accepted for a diffraction profile in astronomical observations and usually applied to a circular aperture. According to the Rayleigh criterion, two point sources of equal intensity are regarded as resolved when the main diffraction maximum of one intensity distribution profile coincides with the first minimum of the other. As a result, the intensity at the midpoint between the two profiles is

about 80% of the maximum intensity, and a clear dip is observed. In the Sparrow criterion, a more rigorous condition is applied. According to this criterion, two point sources are considered resolved when the resultant intensity at the midpoint between the diffraction profiles shows only a minimum beginning to appear. Figure 2-22(a) illustrates the intensity distributions satisfying the Raleigh and Sparrow criteria.

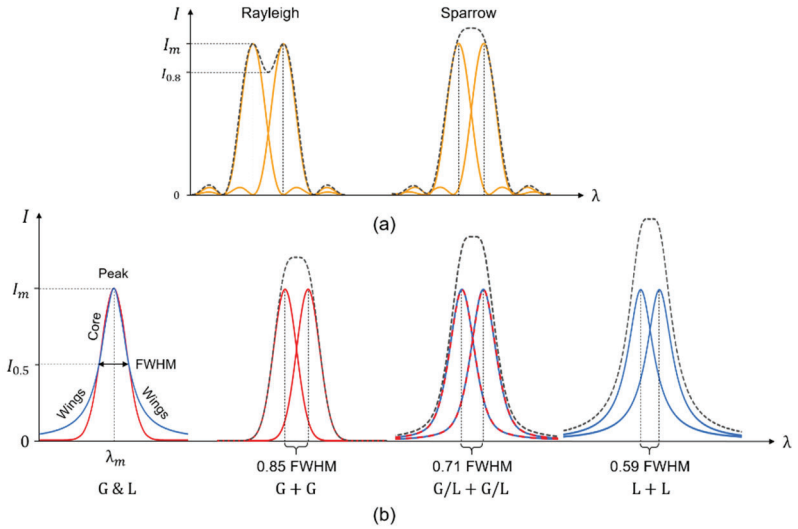

Figure 2-22. Spectral profiles and resolution criteria: (a) two diffraction profiles matching Rayleigh and Sparrow resolution criteria; (b) Gaussian (red) and Lorentzian (blue) spectral profiles with equivalent FWHM overlaid for comparison (G&L), and the Sparrow resolution limits for two pure Gaussian (G+G), a mixture of Gaussian and Lorentzian (G/L+G/L) and two pure Lorentzian (L+L) profiles. The separations between the peaks at the Sparrow resolution limit are indicated in terms of the FWHM values of the profiles. $I_{0.8}$ and $I_{0.5}$ correspond to 80% and 50% of the maximum intensity I_m distribution.

In optical spectroscopy, the functions that describe the spectral lines have a bell-shaped profile that asymptotically tends to zero on both sides of its maximum (peak). Therefore, the wavelength interval, in which the function decreases to half of its maximum value, is usually taken as the width of the spectral line. This interval is called the full-width at half-maximum (FWHM) of the spectral line, often shortened to the halfwidth or linewidth. In practice, the bell-shaped spectral profiles are best approximated by a mixture of Gaussian and Lorentzian functions expressed, respectively, by the formulae

$$I_G(\lambda) = I_m exp\left[-\frac{ln_2(\lambda_m - \lambda_i)^2}{(FWHM)^2}\right] \tag{2.21}$$

and

$$I_L(\lambda) = I_m / \left[1 + \frac{(\lambda_m - \lambda_i)^2}{(FWHM)^2}\right], \tag{2.22}$$

where I_m is the maximum intensity corresponding to the position λ_m of the peak of the spectral line. The simplest mixture of Gaussian and Lorentzian profiles are represented by their linear combination A×G + (1-A)×L with A (a variable parameter often called the coefficient of shape) being the fraction of Gaussian profile ($0 \leq A \leq 1$). Many individual bands observed in Raman spectra are well approximated by this linear combination when the coefficient of shape A equals about 0.5. The central part of the profiles around the peak is called the core or kernel, while the side parts asymptotically approaching zero are called the wings. The Gaussian and Lorentzian profiles with an equivalent FWHM mostly coincide in their cores but differ markedly on the wings. The intensity of the maximum of the spectral line (the peak height) is usually measured from the spectral

baseline. The Gaussian and Lorentzian profiles and their superpositions are shown in Figure 2-22(b).

The Rayleigh and Sparrow criteria are traditionally applied to the bell-shaped spectral lines observed in optical spectroscopy. From a practical viewpoint, the Sparrow criterion is more justified since it is based on the implementation of the second derivative, which turns into zero at the midpoint of the resultant intensity profile. Figure 2-22(b) illustrates the Sparrow criterion applied to Gaussian, Lorentzian line shapes and their linear combination with A=0.5. Respectively, the Sparrow criterion establishes that these spectral lines can be resolved when their maxima are separated by about 0.85, 0.59 and 0.71 of their FWHM. In contrast, the Rayleigh criterion underestimates the practically achievable spectral resolution.

When considering the spectrometer's instrumental function, it was assumed that its slit was illuminated by monochromatic radiation. In fact, every spectral line resulting from a vibrational transition occupies a specific interval of the wavelengths. Each energy level is characterized by a specific interval of energies—the width of the level. Consequently, the linewidth is determined by the sum of the widths of the energy levels involved in the transition. Various factors contribute to the broadening of the energy levels and, therefore, the linewidth. The natural linewidth arises from Heisenberg's uncertainty principle, which implies uncertainty in a quantum system's energy state due to uncertainty in the state's lifetime. The natural linewidth is very small and can be neglected when considering vibrational spectral lines. In a gas phase, the energy levels are broadened due to collisions between the atoms or molecules and differences in their travelling speeds relative to the detector (the Doppler effect). The spectral lines of

gases are very narrow and are often regarded as quasi-monochromatic. The vibrational spectral lines of materials in a condensed phase (liquids and solids) are broadened significantly due to different mechanisms of interactions between the neighbouring chemical groups and molecules and their strength (for example, the Van der Waals mechanism or hydrogen bonding). As a result, the typical vibrational spectra of substances in a condensed state consist of individual spectral lines or closely spaced overlapped lines that form spectral bands with the bandwidths ranging from several to a few hundreds of cm^{-1}. All of the mentioned broadening mechanisms form the so-called intrinsic line shape. These mechanisms are divided into homogeneous and inhomogeneous ones and are fairly well described by the Lorentzian and Gaussian functions, respectively. When both broadening mechanisms are presented simultaneously, which often occurs, the line shape can be given by a convolution of the Lorentzian and Gaussian functions resulting in a Voigt profile (Demtröder 2008).

Similar to the formation of the intrinsic line shape, it is reasonable to assume that the line broadening at the spectrometer's exit can also be represented by the convolution of the line profile itself with the spectrometer's instrumental function. Thus, designating the intrinsic line shape by *L(x)* and the instrumental function by *I(x)*, the shape of the line *R(x)* registered by the spectrometer results from the convolution denoted by the symbol ⊗:

$$R(x) = L(x) \otimes I(x) = \int_{-\infty}^{+\infty} L(x')\, I(x - x')dx'. \qquad (2.23)$$

The convolution operation can be thought of as an overlap of the two functions as one function slides over the other. Mathematically, this operation is expressed by the integral of the product of these functions.

Suppose that the width of the spectral line is large compared to the width of the instrumental function. If *I(x)* is nonzero only inside a small interval *Δx*, then convolution (2.23) is defined by

$$R(x) = \int_{x-\Delta x/2}^{x+\Delta x/2} L(x')\, I(x - x')dx'. \qquad (2.24)$$

Using the mean value theorem for definite integrals, formula (2.24) can be rewritten as

$$R(x) = L(\bar{x}) \int_{x-\Delta x/2}^{x+\Delta x/2} I(x - x')\, dx', \qquad (2.25)$$

where $\bar{x}$ is a value inside the interval $x-\Delta x/2 < \bar{x} < x+\Delta x/2$. Given that

$$\int_{x-\Delta x/2}^{x+\Delta x/2} I(x - x')\, dx' = 1\,,$$

the formula (2.25) reduces to the equality

$$R(x) = L(\bar{x})\,.$$

Since *L(x)* varies little within the small interval *Δx*, it can be assumed that

$$R(x) = L(x)\,.$$

Thus, if the width of the intrinsic spectral line significantly exceeds that of the instrumental function, then the shape and width of the line recorded by the spectrometer practically coincide with the parameters of the intrinsic line. If the FWHM of the instrument function constitutes no more than ¼ of the FWHM of the intrinsic spectral line, then the broadening of the FWHM

of the experimentally registered line over that of the intrinsic line is about 5%. If the FWHMs of the intrinsic spectral line and the instrument function are the same, then the FWHM of the registered line will increase by about 40%. From the other side, the intrinsic spectral line is considered to be quasi-monochromatic if its FWHM is small enough compared to that of the instrumental function. In this case, the registered FWHM will be mostly determined by the instrumental function.

A stringent theoretical consideration of all factors influencing the effective resolution is usually not possible; however, it can be empirically estimated. In practice, finding two adjacent spectral lines of the same intensity and halfwidth in a vibrational spectrum to comply with the resolution criteria is very problematic. Instead, the FWHM of a single quasi-monochromatic line registered by the spectrograph provides a good estimate of the instrumental function directly related to the practical resolution. The quasi-monochromatic spectral lines can be best approximated by the emission lines of gases. The emission sources (for example, Hg, Ar, Ne, Kr, and Xe lamps) are readily available and can be easily mounted like a regular sample. Then the spectrum of an emission source is recorded using the measurement parameters set for a given configuration of the spectrometer and required for the sample under study. As an example, Figure 2-23 shows the emission spectrum of Ne lamp along with the Raman line of a diamond and the empirically obtained resolving power of the spectrograph configured with 532 nm laser.

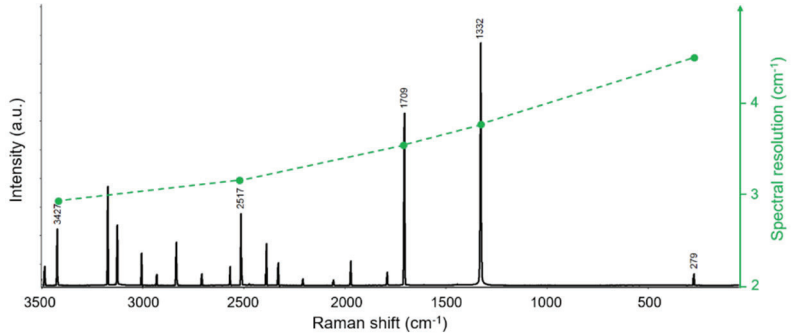

Figure 2-23. The emission lines of Ne lamp in the region of 50-3500 cm^{-1} and the Raman peak of a diamond at 1332 cm^{-1} measured using 532 nm laser. The green dotted curve shows the spectral resolution of the spectrograph at different wavelengths.

The FWHMs of several emission lines estimated by the best curve-fitting using the linear combination of Gaussian and Lorentzian profiles and the coefficient of shape A ≈ 0.5 were found to be 4.3, 4.5, 5.1 and 6.4 cm^{-1}, respectively, for the lines at 3427, 2517, 1709 and 279 cm^{-1} wavenumbers. This method proposes an objective evaluation of the instrumental function since it provides a direct measurement of the instrument's response to the Dirac delta function represented by the atomic emission lines. As it is known, the intrinsic width of the Raman line of the diamond at 1332.4 cm^{-1} is equal to 1.2 cm^{-1} (Prawer and Nemanich 2004). The FWHM of the experimentally registered spectral line of the diamond was estimated to be 5.3 cm^{-1}. This is in good agreement with the FWHM values of the emission lines, which makes the diamond line also suitable for evaluating the instrumental function of a Raman spectrometer with a moderate spectral resolution. To assess the resolving power of the spectrograph used for these measurements, its instrumental function should be multiplied by a factor of

0.71. This factor corresponds to the Sparrow resolution criterion for the combination of Gaussian and Lorentzian profiles with the coefficient of shape A = 0.5 (see Fig. 2-22) used in the best curve-fit. Thus, the spectral resolution values were estimated to be 3.0, 3.2, 3.6, 3.8 and 4.5 cm^{-1}, respectively, at 3427, 2517, 1709, 1332 and 279 cm^{-1} wavenumbers. Note that the spectral resolution varies slightly and nonlinearly across the spectrum, as previously mentioned.

In general, spectrographs introduce distortion into the intrinsic spectral profiles. To register an intrinsic linewidth of about 5 cm^{-1} with negligible distortion, the spectrograph must have a practical spectral resolution better than 1 cm^{-1}. A spectrograph with a practical resolution of about 3.5 cm^{-1} is capable of registering an intrinsic linewidth of at least 20 cm^{-1} without distortion.

Spectrograph manufacturers often prefer to specify the resolution in cm^{-1} per pixel of the CCD detector. This parameter is termed the digital or pixel resolution and usually corresponds to the point spacing in the digitized spectrogram. The digital resolution is related to the Nyquist-Shannon sampling theorem that states that the sampling frequency should be greater than twice the highest frequency in the spectrum. The highest frequency that can be detected by the spectrograph is determined by its spectral resolution. Consequently, at least two CCD pixels must fall within the spectral resolution value. Otherwise, the size of the pixels will limit the resolution of the spectrograph. Therefore, the digital resolution is two times higher than the spectral resolution.

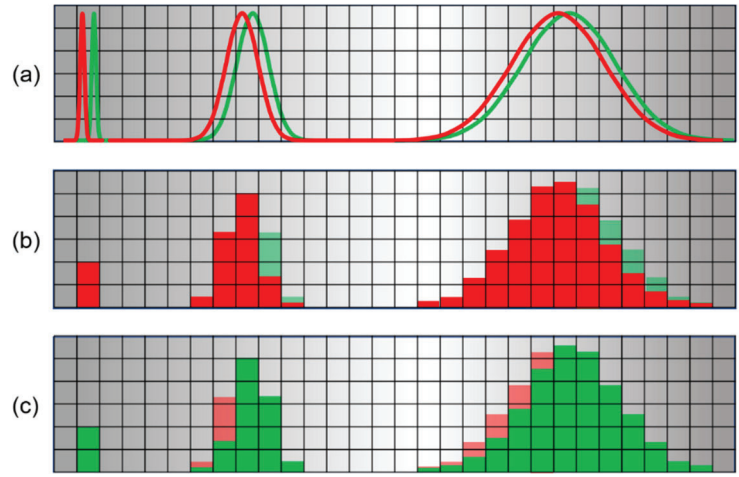

Figure 2-24. Two closely spaced spectral lines (red and green) projected onto the detector array in analogue form (a) and converted to digital form (b and c). The position of the maxima of the lines differs by less than one pixel. The pixel filling histograms shown in (b) and (c) for the red and green lines, correspondingly, demonstrate the coincidence of the histograms for the lines fitting a single vertical pixel column (left) and their mismatch as the lines become broader (middle and right).

Figure 2-24 illustrates how two closely spaced spectral lines are projected onto the detector array in analogue form (a) and conversed to digital form (b–c). The position of the maxima of the lines differs within one pixel. Suppose both the lines are so narrow that they fit entirely in one vertical column of pixels. In that case, such lines cannot be resolved because, regardless of the exact position of the line's maximum within the pixel, the total charge is only accumulated and read out from this column of pixels. If the FWHMs of these lines span two pixels, as required by the Nyquist-Shannon theorem, these spectral lines are resolved. Indeed, the digital

projections of these lines on the detector, as shown by pixel filling histograms in the columns, do not coincide. When the spectral lines get broader so that their FWHMs occupy several pixels, their maxima's position can nevertheless be determined with adequate accuracy, as long as the corresponding histograms do not completely coincide with each other. Thus, in contrast to the often-repeated misleading statement, determining an accurate position of the band and its shift in the wavenumbers scale does not require spectral resolution equal to or better than the value of the assumed shift. The position of a spectral band can be found quite accurately by calculating the so-called centre of gravity of the band or from a curve-fitting procedure.

2.4.5. Optical throughput of a spectrograph

The light collecting efficiency of a spectrograph is usually expressed in terms of the f/number (called f-number)

$$f\# = f/\# = \frac{f}{D},$$

where f is the focal length measured as the distance inside the spectrograph from its entrance aperture to a collimating mirror, and D is the diameter of the diffraction grating projection to the collimating mirror (effective diameter). As historically accepted in photography and astronomy, it is written as $f\#$ or $f/\#$, where # is the f-number. In accordance with (2.13), and because the spectrometer optics are in air (n = 1), an approximate relation between the spectrograph's numerical aperture and the f/number is given by

$$NA \approx \frac{1}{2\ (f/\#)}. \tag{2.26}$$

Thus, the smaller the number, the more light is collected by the spectrograph.

The ratio of the light flux passing through the entrance aperture of the spectrograph to the corresponding flux incident on the detector is called the optical throughput (often referred to as luminosity in old articles and textbooks) of the spectrograph. The practical optical throughput is determined by the losses of light energy during absorption, reflection and scattering by the optical elements of the spectrograph.

Optical materials used in Raman spectrographs in the wavelength range for which they are intended usually have low absorption coefficients, so that the absorption losses, for example, in lenses, do not exceed a few %.

Reflection losses are mainly associated with the reflection from the surface of optical mirrors used in the spectrographs. An optical mirror is a thin layer of commonly aluminium (Al), silver (Ag) or gold (Au) deposited on a substrate, which is often made of glass or copper. These metal-coated mirrors have different reflectivity at different wavelengths. The Al- and Ag-coated mirrors provide high reflectivity in the visible range of wavelengths. The Ag-coated mirrors are the most effective across the visible range reflecting about 95% of the incident light, while Al-coated mirrors reflect about 90%. In the UV range, the reflectivity of silver drops down significantly, whereas aluminium keeps high reflectivity. The reflectivity of aluminium decreases well below 90% in the region from about 700 to 1000 nm. In the NIR region, Au-coated mirrors allow the reflectance as high as 98% to be achieved. However, Au-coated mirrors cannot be used for

wavelengths shorter than 600 nm. Typical spectral reflectance curves of the bare metals are shown in Figure 2-25.

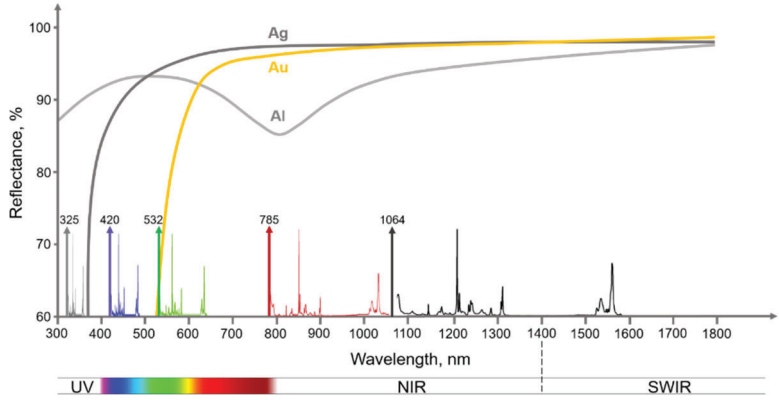

Figure 2-25. Typical reflectance (%) vs. wavelength curves of bare Ag, Au and Al metal layers on mirrors. To illustrate how the reflectance of the mirrors would affect the intensities of Raman bands in the regions from UV to SWIR, the Raman spectra of polystyrene in the range of approximately 50-3300 cm^{-1} are shown for the excitation wavelengths of 325, 420, 532, 785 and 1064 nm.

Aluminium and gold are corrosion-resistant metals, but silver darkens quickly unless used in a dry, uncontaminated environment. Stable and durable metal-coated mirrors are made by overcoating the metal layer with a protective dielectric layer that is harder than the metal surface (e.g., silicon monoxide SiO or silicon dioxide SiO_2). A metal-coated mirror with the dielectric layer is called the protected metal mirror. A more complex dielectric coating is used to fabricate the so-called enhanced metal mirror having its reflectance increased by several % over a specific spectral region. The spectral reflectance curves of the protected and enhanced mirrors may

differ to some extent from the curves for the corresponding uncoated metals in Figure 2-25.

In contrast to reflective gratings, transmissive gratings are typically etched directly into a pure fused silica substrate and often coated with an anti-reflection (AR) layer on the surface opposite to the ruled surface. Since there is no reflection from the metal coating in the transmissive gratings, a proper AR coating can provide close to 100% transmittance of the gratings. In general, transmissive gratings are considered to be more efficient than reflective ones.

The amount of light that is reflected from a surface of a transparent dielectric material is characterized by its reflection coefficient $\mathcal{R}$ and is calculated by the well-known Fresnel formula of small incidence angles in air:

$$\mathcal{R} = \left(\frac{n-1}{n+1}\right)^2, \tag{2.27}$$

where n is the refractive index of the material. Optical glass materials used to fabricate lenses typically have a refractive index ranging from 1.5 to 1.7. Thus, the reflection losses in a lens made of a common glass material ($n \approx 1.5$) are about 4% and 8% taking both sides of the lens into account. However, similar to AR-coated gratings, a suitable AR-coating on the lens ensures losses that do not exceed a few %. Therefore, as a rule, a lens is more efficient than a mirror.

When calculating the total transmission of a dispersive spectrometer, it is necessary to consider all its optical components' efficiency. In the dispersive spectrometers, the total number of surfaces on which reflection or transmission occurs often reaches 14. If we consider the loss on one surface to be 5% on average, then the total transmission will be

$$\tau = (1 - 0.05)^{14} \approx 0.5 .$$

Obviously, when evaluating the final optical throughput of a Raman spectrometer, it is essential to take the detector efficiency into account that was discussed above.

The amount of light energy incident on the detector depends on the spectrometer's entrance aperture and its lighting conditions. In the Raman microscope, the light scattered by a sample and collected by an objective is transmitted via coupling optics to the spectrometer. It is the coupling optics that substantially determines the optimal lighting conditions for the entrance aperture of the spectrometer.

2.5. Microscope-to-spectrometer coupling optics

Attaching an optical microscope to a spectrometer, optical coupling, is not as trivial as it might seem at first glance. Implementation of appropriate coupling optics for transferring light from a microscope to a spectrometer is extremely important. It should ensure optimal optical throughput, spectral and spatial resolution are achieved.

Numerical aperture is an essential parameter to consider when selecting appropriate coupling optics. In order to fill the diffraction grating, the *NA* of the lens that focuses light on the spectrometer aperture must match the *NA* of the spectrometer. Such a condition stipulates the maximal spectral resolution achievable in the spectrometer. However, a "direct" coupling illustrated in Figure 2-26(a) is unlikely to be practicable. The *NA* of the focusing lens is determined by the diameter of the lens and the focal length according to (2.13). This lens is installed in the optical path of the scattered light collected from the sample by an infinity-corrected objective. Assuming

that the focal length corresponds to a typical tube length of 200 mm in an infinity-corrected microscope (see Fig.2-9) and the diameter of the tube lens is equal to the diameter of a microscope objective of about 20 mm, we obtain the NA = 0.05. For a typical spectrometer with f/4, the NA = 0.125, as follows from (2.26). Thus, an additional intermediate magnification of 2.5 is required to match the numerical aperture of the focusing lens to the entrance aperture of the spectrometer; otherwise, the grating will be only partially illuminated.

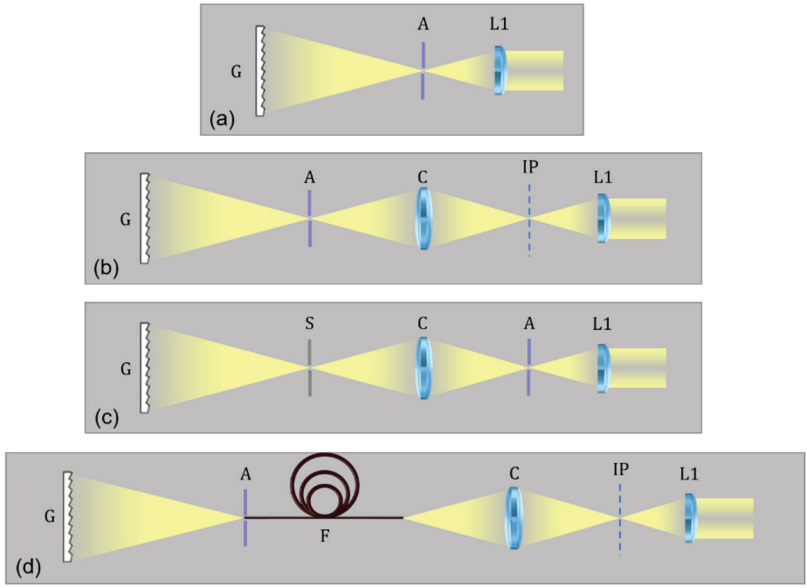

Figure 2-26. Principle configurations of microscope-to-spectrometer coupling optics: (a) "direct" coupling; (b) coupling with magnifying optics; (c) coupling with magnifying optics and a separate pinhole and slit; (d) coupling with optical fibre. G – diffraction grating in the spectrometer, A – pinhole aperture, L1 – focusing lens, C – coupling optics, IP – image plane, S – slit aperture, and F – optical fibre.

In practice, it is important to estimate the diameter of the light spot produced in the image plane, considering the diameter of the focused laser spot on a sample assessed by equation (2.12) and the magnification of the microscope objective. As follows from (2.14), for an objective with the high $NA = 0.9$ typical for 100× magnification (often denoted as 0.9/100× objective) and the 532 nm excitation wavelength, the spot size on the sample is estimated to be 0.72 μm. Thus, the light spot produced in the image plane is 0.72 μm × 100 = 72 μm. Similarly, for the 0.75/50× objective and the same 532 nm excitation, the diameter of the light spot in the image plane brings 0.87 μm × 50 = 43.5 μm. Knowledge of the size of the light spot in the image plane is essential for the correct choice of the spectrometer entrance aperture's shape and size.

Figure 2-26(b)–(d) illustrates the three principal configurations of the coupling optics used in modern Raman microscopes. The coupling optics denoted by lens C in Figure 2-26(b) allows the image of the laser spot produced in the image plane to be magnified and projected onto the spectrometer entrance aperture. In this configuration, the entrance of the spectrometer can be a round aperture (confocal pinhole) or a slit. The confocal pinhole enables the confocal mode of operation while its diameter influences both the extent of confocality and spectral resolution. The slit allows more light to be collected by the spectrometer in a non-confocal mode while its width controls the spectral resolution. The pinhole must be chosen to match the size of the light spot in the image plane. For a light spot of 72 μm and the confocal pinhole diameter set to, for example, 50 μm, the pinhole provides a high enough extent of confocality and sufficient collection efficiency. The actual size of the light spot projected onto the spectrometer entrance depends on the magnification of the coupling optics.

Manufacturers of commercial Raman microscopes often do not disclose the magnification factor, which means that in such systems, the diameter of the pinhole or the width of the slit is adjusted accordingly to the magnification factor by default. Thus, for the light spot of 72 μm in the image plane and the confocal pinhole diameter of 50 μm, the coupling optics with, for example, 2.5 magnification produces a 72 μm × 2.5 = 180 μm light spot and the pinhole is increased by the same factor of 2.5 resulting in 50 μm × 2.5 = 125 μm opening at the spectrometer entrance. The choice of a confocal pinhole or slit at the spectrometer entrance offers the advantage of easy switching between confocal and non-confocal modes of operation, as well as optimizing optical throughput.

In the configuration shown in Figure 2-26(c), the confocal pinhole is set at the image plane while the slit is installed at the spectrometer entrance. In contrast to the previous configuration, the separation of the pinhole and the slit permits an independent setting of the extent of confocality and tuning the spectral resolution. This configuration allows the diameter of the confocal pinhole to be chosen directly to match that of the light spot produced in the image plane.

The optical system that consists of lenses and transfers light over an air gap in both these configurations is called a free-space one. The free-space coupling offers potentially the least loss of light upon its transfer from the microscope to the spectrometer. However, using the free-space optics with a fixed magnification in combinations with many interchangeable microscope objectives results in inevitable underfilling or overfilling the spectrometer entrance aperture for some of the objectives. The underfilling occurs when the diameter of the light spot is smaller than the diameter of the confocal pinhole or the width of the slit that, respectively, decreases the

extent of confocality or allows more stray light to enter the spectrometer. The overfilling means the diameter of the light spot is larger than the diameter of the confocal pinhole or the width of the slit. In this case, less light enters the spectrometer, and the optical throughput of the system with a particular objective decreases. For confocal Raman microscopy, the coupling optics are usually designed with a magnification factor optimized for objectives with high *NA*.

An alternative design of the optical transfer system that contains an optical fibre is illustrated in Figure 2-26(d). The optical fibre consists of an optically transparent core most often made of silica glass surrounded by a cladding layer. The fibre transmits light as a waveguide due to the phenomenon of total internal reflection on the core-cladding interface when the core has a higher index of refraction than the cladding. The numerical aperture of the optical fibre is determined by the maximum angle for which the total internal reflection is possible. The *NA* value is calculated from the difference between the refractive indices of the core and the cladding. For typical core diameters of multimode fibres between 50 and 100 μm, the values of *NA* may range from 0.1 to 0.2 which is close to the *NA* = 0.125 of the spectrometer with f/4 as in the example above. Thus, the output end of the fibre may be placed directly at the entrance of the spectrometer so that the core of the fibre represents the confocal pinhole with a fixed diameter between 50 and 100 μm. While the output end of the optical fibre attaches fairly easily to the spectrometer, accurate positioning of the light beam at the collecting end is required to achieve the best light injection efficiency. This is often accomplished using another microscope objective and a precise positioning mechanism. It worth mentioning that lasers can also be coupled to the microscope using optical fibres.

The undisputable advantage of the coupling by means of fibres is the flexibility of the Raman microscope setup that allows the light microscope, spectrometer and lasers to be arranged in the most compact and optimal way in the analytical laboratory. The drawback of fibre coupling is that it brings higher losses of light than a free-space configuration. The attenuation of light upon its propagation in an optical fibre occurs due to reflection losses at the two ends of the fibre and scattering and absorption in the fibre material. According to Fresnel formula (2.27), for a typical fibre core with $n \approx 1.5$, the optical losses at the two ends consists of 8%. The scattering and absorption result in an exponential decay of light with increasing fibre length. Additional attenuation may be induced by bending the fibre too tightly, as the excessive bending may result in a light leak through the cladding. The optical losses in a fibre with a length of just a few meters may exceed 30%. Autofluorescence within the fibre material generated at particular laser wavelengths must be filtered out; otherwise, it can add unnecessary background to Raman spectra. Thus, the optical fibres used in Raman microscopy should be made of high-quality materials, minimized in terms of their length and be handled with care.

2.6. Optical components maintenance and cleaning

The optical components of Raman spectrometers and microscopes should be maintained with proper care to ensure their performance and usable lifetime. Even very small irregularities, such as microscopic scratches or dents, may cause unwanted scattering of light, which seriously degrades the performance of the optical components in critical spectral measurements.

As mentioned above, the surfaces of lenses are often coated with an anti-reflection layer to prevent loss of light due to reflection. Mirrors and

gratings have highly reflecting coatings to achieve the maximum reflection of light. Filters have coatings to cut off undesired wavelengths. These coatings are usually very delicate and can be damaged by improper handling and cleaning.

The particles of dust, small stains or organic films that can be accumulated on the surfaces of lenses, mirrors, filters and gratings increase light scattering and, therefore, decrease the overall optical throughput of the instrument over time. These contaminants may also lead to unnecessary absorption, unexpected fluorescence and diffraction effects.

The methods used for cleaning optical components depend on both the materials of optical components and the nature of contaminants to be removed. There are several basic rules to follow when cleaning the optical components:

1) Do not clean an optical component if it is not necessary. Inspect the component for dust stains and organic films by holding it near a bright visible light source. Looking at the component under different angles reveals scattering from dust and stains or interference pattern from a thin film;
2) Consult the manufacturer if there is any doubt as to the ability of an optical component to withstand a particular cleaning solvent or tool;
3) A qualified specialist should only clean the laser optics;
4) Never touch the delicate surface of coated optical components since human sweat is one of the most corrosive liquids for dielectric reflective and anti-reflective coatings. Fingerprints accidentally left on a coated optical surface should be cleaned as soon as possible to avoid staining or damaging the coating. Handle optics in a clean,

dust-free environment while wearing gloves or finger coats made of a powder-free latex;

5) Never use sharp or metal tools near optical surfaces. Instead, use wooden or plastic implements;
6) As a first step in the cleaning process, always use a dust blower, canned compressed air duster or a cylinder of dry air or nitrogen to remove the contaminants off sensitive optical components to avoid physical contact.

Dust can be removed from the surface of most optical surfaces, including dielectric reflective and anti-reflective coatings, by brushing with a soft camel-hair brush, which is often attached to a regular dust blower. If the lenses or mirrors are still not clean after blowing and brushing the dust off, then proper optical cleaning solvents and tools can be used to remove the residual contaminants. Lenses and mirrors should be cleaned with reagent-grade (spectroscopically pure grades are the best) solvents and a lint-free lens tissue intended for cleaning optics. The lens tissue should be soaked with the solvent because dry lens tissue can scratch optical surfaces. Several solvents are suitable for cleaning procedures, such as acetone, methanol and isopropyl alcohol and their mixtures. Acetone dries too quickly and does not always have time to dissolve all impurities. The mixture of 60% acetone and 40% methanol is a good solvent to be used. The methanol slows down the evaporation time and dissolves the contaminants that acetone alone would not be able to clean. Isopropyl alcohol is safe and effective, but its relatively slow evaporation can sometimes leave dried streaks on the surface of the lens and mirrors.

If the lens or mirror is still dirty, then a mild soap solution in distilled water can be used to gently wash the components. The optical components should be rinsed with isopropyl alcohol or acetone to remove the soap residue. However, mirrors with a bare metal coating are too delicate to be cleaned by a contact method using a lens tissue. Even a bare Al-coated mirror cannot withstand cleaning with anything but the gentlest camel-hair brush. It is very difficult to clean Ag- or Au-coated mirrors that are not overcoated with a hard protective layer, such as SiO. They can only be cleaned by repeatedly non-contact washing and rinsing using optical cleaning solvents.

Filters can be cleaned using the same methods as lenses or mirrors. However, the preferred method is to use an air blower or compressed air to remove contaminants.

During cleaning, an optical component should be placed on a soft surface to avoid scratches. It is recommended that the component is wiped slowly and evenly. Slow wiping allows the solvent to evaporate without streaking. The component's edges should be cleaned before cleaning its central part in order to prevent contaminants from being smeared to the centre. Then, for round shape components, the tissue should be moved in a circular path starting from the centre and then spiralling in an outward direction to pull contaminants off the components. For a rectangular component, the tissue should be moved in a single direction across the component repeatedly until the whole surface of the component is wiped. It is highly recommended to just wipe the tissue once and then discard it. A lens tissue must never be reused.

Due to the construction of diffraction gratings, they should be cleaned with special care. It is usually safe to remove surface dust from them using an air

blower or compressed air. However, cleaning the diffraction gratings by any contact means must be avoided since there is a risk of damaging them permanently.

Repeated cleaning will inevitably wear out the surface of the optical components, and their performance may degrade significantly. Therefore, a good practice is to use the manufacturer's suggested preventive maintenance for protecting optical components from dust and other contaminants.

2.7. Some key aspects to consider when choosing a Raman microscope

Obviously, the choice of the Raman microscope configuration and its main components is dictated by its application. No one instrument can cover all spectroscopic applications and needs. However, a user who prudently evaluates the requirements of the applications can assess the tradeoffs related to choosing between configurations of microscopes, spectrographs, lasers, detectors, filters, other optical components and features. For example, biological applications, especially related to the study of live biological cells, may require an inverted microscope with a water immersion objective.

Since the half-widths of the bands in the spectra of solids rarely appear to be narrower than 10 cm^{-1} and, in the spectra of liquids, mostly exceed 20 cm^{-1}, spectrographs that provide spectral resolution in the range of 2–5 cm^{-1} are generally well suited for analyzing samples in a condensed phase. As a rule, compact Raman microscopes equipped with spectrographs having a focal length between 0.2 m and 0.3 m contain fewer reflective and refractive optical components, increasing their optical throughput. The cost

of spectrographs rises with their size and improving spectral resolution. The choice of high spectral resolution is justified for specialized applications or the analysis of gas samples, which is a rather rare task for Raman microscopy.

If the Raman microscope is expected to operate in harsh environments, then the design of the instrument must ensure that all optical components are securely mounted to minimize the effects of vibration and temperature fluctuations. Often, Raman microscopes structurally integrated with high-resolution spectrographs require installation on optical tables with vibration damping.

The optimization of Raman experiments for a variety of applications and materials require multiple laser sources. The Raman microscope should be equipped with the optical components most suitable for the laser being used. Changing the excitation wavelength requires installing a diffraction grating that operates at a corresponding blazing angle to maintain a high optical throughput. While a 785 nm laser can minimize fluorescence from many materials and samples, its use in combination with a BI CCD detector can lead to a noticeable étaloning effect in the recorded spectra. The use of a BI-DD CCD significantly reduces the possible étaloning and increases the S/N in the spectra obtained with this laser. However, using the same detector with the lasers that emit in the shorter wavelength region will decrease the spectral sensitivity. The use of 1064 nm radiation to suppress fluorescence requires that the spectrograph be equipped with an InGaAs detector. Thus, a spectrograph supplied with optical ports for multiple detectors is an undeniable advantage of high-end Raman microscopes. Optics and coatings appropriate for specific excitation wavelength and spectral range should also be taken into consideration, especially when UV lasers need to be used.

By selecting the excitation wavelength, especially in the UV or blue spectral regions, different resonance Raman spectra of the same molecule can be obtained. If the excitation wavelength matches the absorption band of a specific part of the molecule, then the Raman spectrum associated with this part of the molecule is selectively enhanced. The UV wavelengths help avoid fluorescence in some biological samples, CVD diamond, soil, used crankcase oil, etc. It also allows measurements to be made away from the black body emission in studies of catalytic reactions *in situ* at elevated temperatures. The shallow penetration depth of UV light is used for selective analysis of a thin top surface layer in complex semiconductor heterostructures.

Although measurements of Raman spectra are usually performed in the Stokes region using edge Rayleigh filters, notch filters allow measurements to be made in both the Stokes and anti-Stokes regions. The measurements in the anti-Stokes Raman region may be required for certain specialized applications, Raman thermometry and *in situ* investigation of materials at high temperatures.

As will be considered in more detail in the following chapters, fast sample scanning mechanisms and methods, along with EM CCD detectors, constitute a technical base for obtaining 2D and 3D Raman spectral images in a variety of applications in material and biological sciences.

References

Adar, F., M. Delhaye, and E. DaSilva. 2007. "Evolution of Instrumentation for Detection of the Raman Effect as Driven by Available Technologies and by Developing Applications." *J. Chem. Educ.* 84 (1): 50–60.

Asher, S.A. 1993. "UV Resonance Raman Spectroscopy for Analytical, Physical, and Biophysical Chemistry." *Anal. Chem.* 65 (4): 201A-210A. https://doi.org/10.1021/ac00052a715.

Carrabba, M.M., K.M. Spencer, C. Rich, and D. Rauh. 1990. "The Utilization of a Holographic Bragg Diffraction Filter for Rayleigh Line Rejection in Raman Spectroscopy." *Appl. Spectrosc.* 44 (9): 1558–1561.

Costa, S., E. Borowiak-Palen, M. Kruszynska, A. Bachmatiuk, and R.J. Kalenczuk. 2008. "Characterization of carbon nanotubes by Raman spectroscopy." *Materials Science-Poland* 26 (2): 443–441.

Craig, N.S., and I.W. Levin. 1979. "Calibrating Raman Spectrometers with Plasma Lines from the Argon Ion Laser." *Appl. Spectrosc.* 33 (5): 475–476.

Delhaye, M., and M. Migeon. 1966. "Interкt de la concentration d'un faisceau laser pour l'excitation de l'effect Raman." *C. R. Acad. Sc. Paris* 262: 1513–1516.

Delhaye, M., and P. Dhamelincourt. 1975. "Raman microprobe and microscope with laser excitation." *J. Raman Spectrosc.* 3 (1): 33-43. https://doi.org/10.1002/jrs.1250030105.

Demtröder, W. 2008. *Widths and Profiles of Spectral Lines.* In: *Laser Spectroscopy*, 61-98. Springer-Verlag, Berlin, Heidelberg. https://doi.org/10.1007/978-3-540-73418-5_3.

Dresselhaus, M.S., G. Dresselhaus, A. Jorio, A.G. Souza Filho, M.A. Pimenta, and R. Saito. 2002. "Single Nanotube Raman Spectroscopy." *Acc. Chem. Res.* 35 (12): 1070–1078. https://doi.org/10.1021/ar0101537

Durini, D. 2019. *High Performance Silicon Imaging: Fundamentals and Applications of CMOS and CCD Sensors.* 2nd. Edited by D. Durini. Woodhead Publishing.

Everall, N., T. Hahn, P. Matousek, A. W. Parker, and M. Towrie. 2001. "Picosecond Time-Resolved Raman Spectroscopy of Solids: Capabilities and Limitations for Fluorescence Rejection and the Influence of Diffuse Reflectance." *Appl. Spectrosc.* 55 (12): 1701–1708.

Flaugh, P.L., S.E. O'Donnell, and S.A. Asher. 1984. "Development of a New Optical Wavelength Rejection Filter: Demonstration of Its Utility in Raman Spectroscopy." *Appl. Spectrosc.* 38 (6): 847–850.

Glebov, A., O. Mokhuna, A. Rapaport, S. Vergnole, V. Smirnov, and L.B. Glebov. 2012. "Volume Bragg Gratings as Ultra-Narrow and Multiband Optical Filters." *Proc. of SPIE* 8428: 84280C-1 - 84280C-11. https://doi.org/10.1117/12.923575.

Hirschfeld, T., and B. Chase. 1986. "FT-Raman Spectroscopy: Development and Justification." *Appl. Spectrosc.* 40 (2): 133–137.

2016. "How Lenses Function." Cannon Asia, November 13. Accessed April 4, 2020. https://www.youtube.com/watch?v=EL9J3Km6wxI.

Janesick, J., and G. Putnam. 2003. "Developments and applications of high-performance CCD and CMOS imaging arrays." *Annu. Rev. Nucl. Part. Sci.* 53: 263–300. https://doi.org/10.1146/annurev.nucl.53.041002.110431.

2005. "Lasers and laser-related equipment — Test methods for laser beam widths, divergence angles and beam propagation ratios. Part 1: Stigmatic and simple astigmatic beams." International Organization for Standardization,

Litwiller, D. 2001. "CCD vs. CMOS: facts and fiction." *Photonics Spectra* 35 (1): 154–158.

Minsky, M. 1988. "Memoir on inventing the confocal scanning microscope." *Scanning* 10 (4): 128-138. https://doi.org/10.1002/sca.4950100403.

Moser, C., L. Ho, E. Maye, and F. Havermeyer. 2008. "Fabrication and applications of volume holographic optical filters in glass." *J. Phys. D: Appl. Phys.* 41 (22): 224003-224010. http://dx.doi.org/10.1088/0022-3727/41/22/224003.

Murray, C.A., and S.B. Dierker. 1986. "Use of an unintensified charge-coupled device detector for low-light-level Raman spectroscopy." *J. Opt. Soc. Am. A* 3 (12): 2151–2159. https://doi.org/10.1364/JOSAA.3.002151.

Owen, H. 2007. "The Impact of Volume Phase Holographic Filters and Gratings on the Development of Raman Instrumentation." *J. Chem. Educ.* 84 (1): 61–66.

Porto, S. P. S., and D. L. Wood. 1962. "Ruby Optical Maser as a Raman Source." *J. Opt. Soc. Am.* 52: 251–52.

Prawer, S., and R.J. Nemanich. 2004. "Raman Spectroscopy of Diamond and Doped Diamond." *Math. Phys. Eng. Sci.* (362): 2537–2565.

Raman, C.V. 1928. "A Change of Wave-laugh in Light scattering." *Nature* 121: 619.

Raman, C.V., and Krishnan K.S. 1928. "The Negative Absorption of Radiation." *Nature* 122: 12.

Rzhevskii, A.M., P. Choi, F.H. F.H. Ribeiro, R.J. Gulotty Jr, and M.M. Olken. 2001. "Monitoring of molybdenum H-ZSM5 catalyst preparation by in situ ultraviolet Raman spectroscopy." *Catal. Lett.* 73 (2-4): 187–191.

Schoen, C.L., S.K. Sharma, C.E. Helsley, and H. Owen. 1993. "Performance of a Holographic Supernotch Filter." *Appl. Spectrosc.* 47 (3): 305–308.

Shafer, A.B., L.R. Megill, and L. Droppleman. 1964. "Optimization of the Czerny–Turner Spectrometer." *J. Opt. Soc. Am.* 54 (7): 879–887. https://doi.org/10.1364/JOSA.54.000879.

Sze, J-R., and A-C. Wei. 2018. "Crossed Czerny–Turner Spectrometer with Extended Spectrum Using Movable Planar Mirrors." *Appl. Spectrosc.* 72 (5): 776–786. https://doi.org/10.1177/0003702817752486.

Tuschel, D. 2016. "Selecting an Excitation Wavelength for Raman Spectroscopy." *Spectroscopy* 31 (3): 14–23.

Xue, Q., S. Wang, and F. Lu. 2009. "Aberration-corrected Czerny–Turner imaging spectrometer with a wide spectral region." *Appl. Opt.* 48 (1): 11–16. https://doi.org/10.1364/AO.48.000011.

Zworykin, V. K., and J. A. Rajchman. 1939. "The electrostatic electron multiplier." *Proc. I.R.E.* 27: 558.

CHAPTER THREE

CONFOCAL RAMAN MICROSCOPY AND IMAGING

3.1. Basic principles of confocal Raman microscopy

Raman microscopy is now well established as one of the most powerful analytical techniques for a diverse range of applications in physical (material) and biological sciences in both research and analytical laboratories. In the Raman microscope, a research-grade optical microscope is coupled to a laser excitation source and spectrometer, thereby constituting a scientific instrument capable of obtaining both traditional optical and spectrochemical images with a spatial resolution at the diffraction limit of light (<1 micron). Although this spatial resolution is lower than that achievable in scanning electron (SEM) or atomic force (AFM) microscopy, it enables the measurement of chemically and spatially inhomogeneous samples to reveal their chemical composition, morphology, molecular orientation, conformation, polymorphism, crystallinity, material deformation, local temperature, etc. Spectrochemical imaging creates a 3D dataset with the Raman spectrum at each point of a 2D spectral image of a given sample area. This dataset is often referred to as a "hyperspectral" cube. More correctly, this data set should be called 4-dimensional because, at each point in the 2-dimensional area, the Raman spectrum is represented by two coordinates: the Raman shift and the intensity. A 3D spectrochemical representation of the sample can be constructed by acquiring 2D area

images at different depths in a confocal mode by sequentially shifting the laser focus inside of a transparent or translucent sample. This method of 3D spectrochemical imaging preserves the sample integrity and avoids possible artefacts that may result from physically cutting or sectioning the sample. No other microscopic technique offers such a combination of spatial resolution and “information-reach” spectral content within a workable acquisition time.

Despite advances in automation and usability, Raman microscopes continue to be sophisticated analytical tools. The lack of a clear understanding of the instrument’s optimal configuration and the interaction between its components can lead to unsatisfactory results.

A handful of parameters such as excitation wavelength, objective magnification, aperture setting and sampling step are needed to operate a Raman microscope and control data collection. Even so, it is essential to understand the relationships between the parameters and their limitations. A successful Raman microscopic experiment is about setting clear research goals, fully understanding specimen details, and adjusting the measurement parameters to achieve the maximum quality of spectral data for the reasonable time of the experiment.

3.1.1. The role of confocal aperture (pinhole)

When operating a confocal microscope or discussing the instrument’s characteristics, terms like confocal aperture or pinhole are inevitably mentioned. As microscopists know, confocal means "having a common focus". In light microscopy, the definition means that the light is only collected from a focal plane in a sample that allows slices of the sample to be optically separated and observed.

In Raman microscopy, when a laser is used for illumination and an optically conjugated spectrometer is employed for measurement, it is imperative to have the laser light beam focused and the spectrometer aligned to collect the scattered light from the exact same point.

The paths of the light rays in the Raman microscope and the function of a confocal aperture are illustrated in Figure 3-1. Similar schematic diagrams of the light rays may be found in many tutorials and publications dedicated to confocal light microscopy. The light rays from the laser and the rays collected by the microscope objective from the focused laser beam are denoted in green, while the rays entering the spectrometer are yellow. As the circular aperture (pinhole) is placed in the image plane of the microscope, the pinhole is confocal with the focal point. The principal role of the confocal pinhole is to spatially filter the light rays collected by the microscope objective and to pass the selected rays through the pinhole to the spectrometer.

A closer look at the operation of the pinhole is given in Figure 3-1(a)–(c). The laser beam focused by the objective converges in the form of a cone in the focal plane and then diverges in the same way. The volume illuminated by the focused laser beam can be depicted as a green hourglass shape (Fig. 3-1[c]). The objective collects the light scattered from this hourglass shape; it is then magnified and projected onto the image plane. The light rays emanating from the converging and diverging cones above and below the focal plane are combined to form a converging green cone in the image plane. When a pinhole is placed in the image plane, it blocks all the rays emanating from the out of focus regions and allows only the rays from a small volume around the focal point to pass through. The small volume can be represented by the prolate spheroid "spread" out along the optical axis

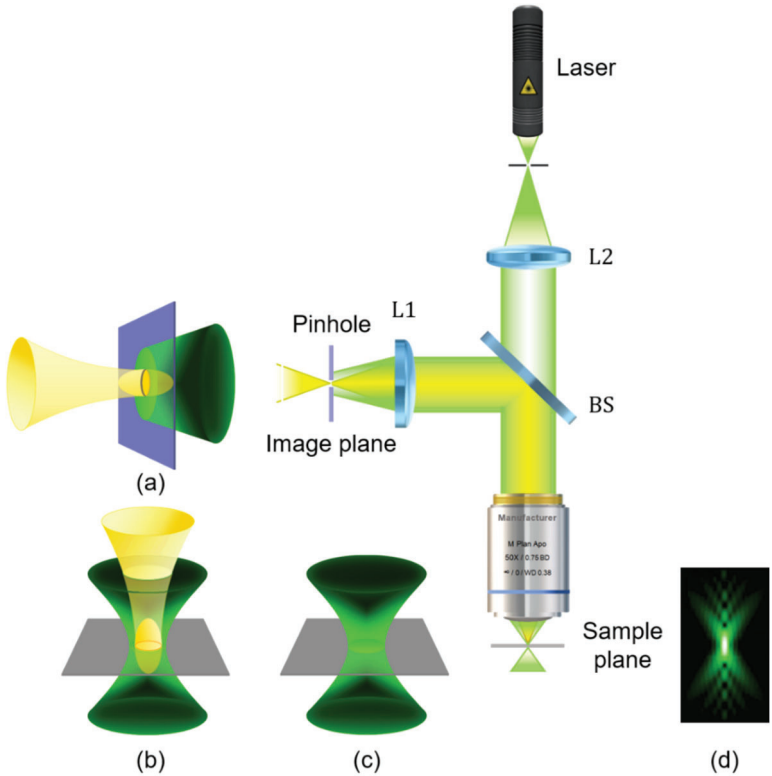

Figure 3-1. The basics of a confocal Raman microscope. The paths of light rays emitted by the laser and collected by microscope objective (green) and the rays "observed" by the spectrograph through a confocal pinhole (yellow) are shown in the centre, where BS is a beamsplitter, and L1 and L2 denote the focusing lens and the laser beam expander lens system, respectively. The pinhole placed in the image plane cuts the rays from the laser beam projected onto the image plane and makes the rays from the small volume enclosed by the prolate spheroid shown in yellow pass through (a). The volume illuminated by a focused laser beam in the sample plane is shown by the green hourglass shape (c). The spheroid back-projected onto the sample plane visualizes the volume element shown in yellow, which is measured through the confocal pinhole (b). The diffraction pattern of light in the focused laser beam is shown in the section perpendicular to the sample plane (d).

(Wallace, Schaefer and Swedlow 2012). This prolate spheroid is highlighted in yellow in Figure 3-1(a). Since the image and sample plane are conjugated, the spheroid can then be projected back onto the sample plane to visualize the small volume element from which the spectrograph measures the scattered light. Thus, the confocal aperture ensures that only the light emanating from the spatially discriminated volume depicted by the yellow spheroid inside the green hourglass shape (Fig. 3-1[b]) passes from the laser focus to the spectrometer.

The effect of the attenuation of the out-of-focus regions represents spatial filtering and is described in terms of the point spread function (PSF) (Lichtman 2013). The volume element measured in the confocal mode is determined by the so-called effective optical PSF. This is a product of the hourglass shape illuminated by the laser and the volume of the spheroid "observed" by the spectrograph through the pinhole. An effective PSF constitutes one of the essential properties of the confocal Raman microscope.

In a non-confocal mode of operation provided using a slit aperture, the Raman spectrum measured by the spectrometer represents Raman signals that emanate from the entire hourglass shape. Suppose this shape comprises chemically different and spatially separated microdomains. In that case, the recorded Raman spectrum is the superposition of Raman spectra of all these microdomains, and they are not discriminated spatially. A significant improvement in the spatial discrimination is obtained in both the lateral (perpendicular to the optical axis of the objective, i.e., in the horizontal XY plane) and axial (along the optical axis, i.e., in the vertical Z-axis) directions in the confocal mode of operation.

By varying the diameter of the confocal aperture, operators of Raman microscopes can select the volume element to measure at a given objective magnification and optimize the intensity in the Raman spectra of the materials under study. A confocal aperture with the ability to continuously vary its size is often called a confocal diaphragm. The confocal diaphragm is advantageous for precise confocal Raman microscopy.

A description of the confocal pinhole physically placed in the image plane of the microscope objective in terms of simple geometrical optics can be found elsewhere (Puppels, et al. 1991, Tabaksblat, Mieer and Kip 1992).

An alternative approach to the confocal configuration of a Raman microscope with a virtual (electronic) pinhole, formed by active pixels in the central part of the CCD detector, was first demonstrated by Williams (Williams, et al. 1994). To implement the virtual pinhole, only a narrow central section of the CCD matrix along its spectral dispersion axis (see Chapter Two, "2.4.2. Detectors") is read out. The pixels in the spatial direction outside that central section are made inactive and do not contribute to the intensity of the measured Raman signal. Confocal mode of measurement can be ensured if the narrow central part of the CCD matrix is well aligned with the small volume illuminated by the focused laser beam in the sample. Although the number of active central pixels in the spatial axis of the matrix can be conveniently controlled by software, this arrangement requires that all optical aberrations in the spectrograph and, especially, in the diffraction grating, are thoroughly corrected. This arrangement still includes a slit as a primary aperture and may necessitate aberration-corrected concave diffraction grating. The size of the virtual pinhole can be varied by changing the number of vertical pixels in the active part of the CCD matrix.

The intensity distributions on a CCD matrix in configuration with the physical and virtual confocal pinhole are illustrated in Figure 3-2.

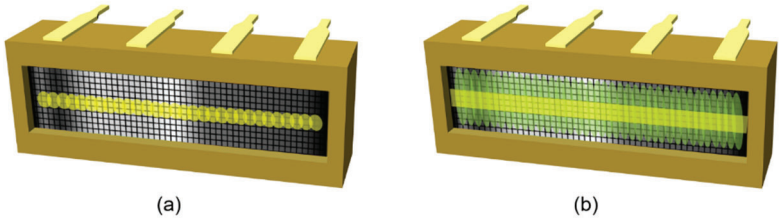

Figure 3-2. The illumination pattern of the CCD matrix: the illuminated pixels corresponding to the constituent wavelengths of analyzed light dispersed along the spectral (horizontal) axis of the CCD matrix are determined by the aperture projected on the matrix. In the configuration with a physical pinhole (a), the number of illuminated pixels shown in yellow in the spatial (vertical) axis is determined by the projected diameter of the pinhole. In the configuration with a virtual pinhole (b), the matrix is illuminated through the slit (green area), but the intensity of the wavelength components are read out only from a narrow central part composed of several active vertical pixels (yellow area). The number of active pixels along the vertical axis of the matrix sets the size of the virtual pinhole.

The confocal configuration can also be achieved by placing an optical fibre in the image plane (Schrum, Ko and Ben-Amotz 1996, Kimura and Wilson 1991).

Regardless of how the confocal configuration is implemented in the Raman microscope, if the optical paths of the laser and spectrometer are not properly aligned, the hourglass figure and spheroid may turn out to be spatially offset at the sample. Hence, the intensity of the Raman scattering received by the spectrometer may be significantly reduced, and spatial

discrimination is adversely affected, disabling the Raman microscope to operate in the confocal mode.

3.1.2. Optical alignment and calibration

Optical alignment and calibration are two important but different processes, which must be routinely executed for the optimal performance of any high-end Raman microscope.

In the course of time, all Raman microscopes are subject to alignment and calibration drifts. These drifts may be caused by laboratory temperature fluctuations, external disturbances of the instrument, normal wear of system components occurring during regular operation, and many other factors. Misalignments must be corrected by periodic maintenance procedures provided by the Raman microscope's manufacturer.

A proper confocal configuration of a Raman microscope means the spheroid is well centred within the hourglass shape, as illustrated above. The process of bringing the laser focus and the volume element “observed” by the spectrometer into a perfect coincidence is known as alignment. Looking through binocular eyepieces at a sample and viewing the laser spot positioned in the middle of the crosshairs in the centre of the field of view in no way ensures that the spectrometer is “seeing” the same spot. The alignment procedure usually implies maximizing the intensity of the measured Raman signal, thereby, aligning the optical paths of laser light focused on the sample and scattered light collected from the sample and transmitted to the spectrometer. The regular alignment compensates for variations caused by the inevitable drift over time. A correctly aligned confocal Raman microscope provides the best spatial discrimination at a high intensity of the Raman spectrum.

Calibration is another procedure that ensures the accuracy of the experimentally measured Raman spectrum, with the correct Raman shift and spectral intensity. Unlike FT-IR instruments with a built-in "internal standard," a laser that monitors the optical path difference in the interferometer and provides accurate wavenumber measurements, dispersive Raman instruments must use samples or standards that have spectral peaks with known Raman shifts for calibration. Raman spectra obtained with different lasers may have significant variations in the relative peak intensities, mainly as a result of wavelength-dependent differences in the quantum efficiency of the CCD. The intensity difference can be adjusted using the so-called white-light correction technique. The white-light correction is an intensity normalization procedure that utilizes either a broadband white-light radiation standard applicable to multiple excitation wavelengths or wavelength-specific intensity correction standards. The procedure establishes a scaling factor to correct the intensities depending on the wavelength along the Raman shift axis.

Manually performed alignment and calibration procedures usually require a certain level of qualification for the maintenance personnel and additional materials and sources; it also often increases the downtime of the instrument during the operation. If offered by the Raman microscope manufacturer, automated procedures significantly simplify the alignment and calibration processes and exclude errors or user subjectivity.

The optimal performance and operational readiness of Raman microscopes can be achieved by a regular alignment and calibration of all involved optical components. Thermo Scientific pioneered a fully automated alignment and calibration procedure (see Chapter Two, "2.1. Evolution of Raman Instrumentation"). This procedure is performed in a software-

controllable manner using a dedicated matchbox-sized tool placed on the microscope stage. The user handles this tool as a sample and focuses on a small pinhole in the centre of the box (Fig. 3-3). Inside the box, there is a set of miniature parts: a photodiode, a neon (Ne) lamp, a small piece of polystyrene and a broadband white-light lamp. During the automated alignment and calibration procedure, a precision micromotor sequentially moves the parts in and out under the pinhole so that each part or their combination participates in essential steps in the procedure. Namely, the photodiode and the polystyrene are used to align the

(a) (b)

Figure 3-3. The alignment and calibration tool to be placed on the microscope stage (a), and the bright pinhole of the tool in the optical focus centred on the microscope eyepiece crosshair (b).

optical path of the spectrometer and the laser beam, respectively, by maximizing the spectral response from both parts. The correction for the possible wavelength nonlinearity of the spectrograph employs multiple precisely characterized lines in the emission spectrum of the Ne lamp. The polystyrene standard is used to calibrate the excitation laser frequency and the Raman shift axis using several well-defined spectral peaks in the Raman spectrum of polystyrene. The multipoint calibration corrects the spectral

distortion in the spectrograph and, thus, permits spectrograph-to-spectrograph data transfer. The intensity correction uses a standardized white-light lamp to compensate for the decline in the CCD detector efficiency at shorter and longer wavelengths.

Since the introduction of this procedure in 2008, major Raman microscope producers have implemented automated protocols for the alignment and calibration of their instruments or computerized their existing ones; however, these protocols can differ markedly in their implementation methods and involved components. For example, cyclohexane, naphthalene, or benzonitrile can be used as Raman shift standards besides polystyrene (ASTM International 2014). The emission lines from low-pressure discharge lamps containing mercury or argon can be used instead of the Ne lamp.

Bruker developed and patented the SureCal® technique for the calibration of the Raman shift in real time. This technique is employed in the Bruker SENTERRA Raman microscope, which will be described in Section 3.6.1. According to the technique, the Raman spectrum of a sample and the emission spectrum of the Ne lamp embedded in the optical configuration of the microscope are measured simultaneously. The spectrum of the sample and the peaks of Ne are collected by different areas of the CCD detector, as shown in Figure 3-4(a). By tracking the positions of Ne emission peaks, the positions of the Raman bands can be instantaneously corrected to remove instabilities. This method, however, does not exclude a possible shift in the positions of the Raman bands caused by the instability of the laser frequency. In order to take the fluctuations of the frequency caused, for example, by a change of the temperature of the laser, into account, it is necessary to project an attenuated Rayleigh scattering line onto the detector

along with several nearest Ne lines, as shown in Figure 3-4(b). Such an implementation will make it possible to track the change in the laser frequency by the position of the Rayleigh line relative to the Ne peaks and, accordingly, to correct the positions of the bands in the Raman spectrum. However, this implementation requires a significantly more complex optical design.

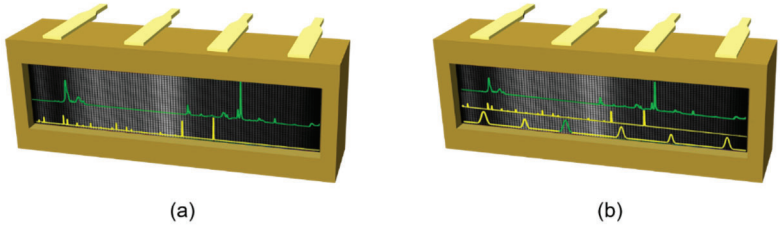

Figure 3-4. Real-time calibration of the Raman shift: (a) The CCD matrix is subdivided into two spectral (horizontal) segments for simultaneous collection of a Raman spectrum and the emission spectrum of the Ne lamp; (b) The third lower segment is used to collect the attenuated Rayleigh line (green contour) and a few emission lines of Ne (yellow contours) with a higher spectral resolution to track the shift of the laser excitation line. As an example, the spectrum of polystyrene obtained with 532 nm laser (green) is projected on the upper segment of the CCD, while the spectrum of Ne (yellow) is shown in the lower segments in (a) and (b).

White light sources with a well-defined spectral output of intensity versus wavelengths, such as tungsten or tungsten-halogen lamps, can be used to calibrate the spectral response of Raman spectrometers. However, due to their geometric dimensions, these light sources are difficult to mount on the sampling stages used in Raman microscopes. In collaboration with ASTM International, the National Institute of Standards and Technology (NIST) developed and certified a set of standard reference materials (SRMs). These

standards are luminescent glass materials with the size of a regular sample. The SRMs were calibrated to provide a source of known emission for the correction of the relative intensity of Raman spectra obtained with instruments using the laser excitation wavelengths of 488/514, 532 or 785 nm (Choquette, et al. 2007). The relative intensities of the measured Raman bands of a sample can be corrected for the instrument-specific response by a computational procedure that uses a correction curve. As an example, the curve generated using a certified SRM 2241 chromium-doped sodium borosilicate matrix glass for 785 nm laser excitation (NIST 2018) is illustrated in Figure 3-5. This curve, together with a standard's luminescence spectrum measured experimentally, can be used to determine the scaling factor for the relative intensity correction unique to each Raman instrument. The resulting intensity correction is used to obtain Raman spectra that are independent of instrument-specific spectral responses, which is essential when comparing the measured spectra with reference ones or transferring quantitative analysis methods between Raman instruments.

Despite the differences in the practical implementation of the protocols, all of them lead to a considerable simplification of the alignment and calibration procedure and an improvement in its reliability.

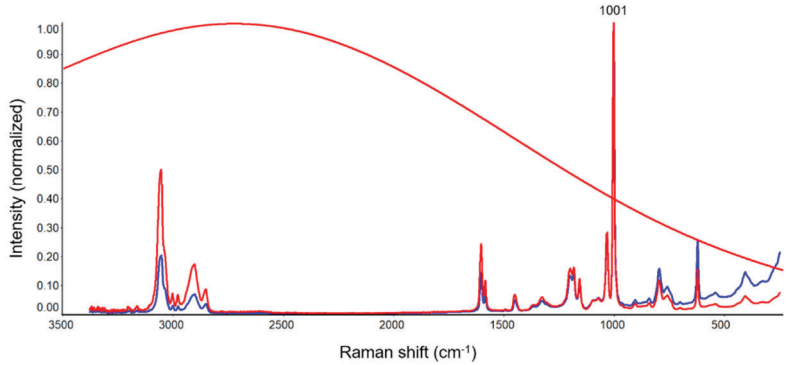

Figure 3-5. The fifth-order polynomial curve of SRM 2241 standard (red) and the uncorrected (blue) and corrected (red) Raman spectra of polystyrene measured using a 785 nm laser. The spectra are normalized to the peak at 1001 cm^{-1}.

3.1.3. Raman maps and images

Confocal Raman microscopy is widely used to measure and image chemical and physical properties of samples in one, two and three dimensions. There are two approaches to obtaining Raman spectral images: global illumination and sequential scanning of a sample. In the former, a certain area of the sample is illuminated, and a narrow spectral interval is measured over the entire area. Usually, a specific Raman band is filtered by a tunable optical filter (TOF). Global illumination is still a developing technology for Raman spectral imaging and is beyond the scope of this book. In the latter, a sample is placed on an automated XYZ mapping stage and moved under the microscope objective to measure Raman spectra sequentially at different points in the sample. Alternatively, the laser beam can scan the sample in a raster mode. Either way, Raman spectra can be obtained in a wide spectral range with a high spectral resolution and spatial discrimination throughout the entire sample.

Raman spectral image acquisition is essentially a two-step process. The first step is mapping, which is the process of measuring Raman spectra at predetermined locations at a sample. The mapping is carried out by means of a laser beam focused at a point or along a line and sequentially scanned across the selected area. The area and the measurement locations are determined by the operator of a Raman microscope and controlled by proper software.

One of the most attractive features of confocal Raman microscopy is the ability to perform nondestructive analysis of a transparent or translucent sample at different depths. Assuming the confocal Raman microscope is properly aligned, the focused laser beam may be stepped through the sample perpendicular to its surface, while Raman spectra are recorded in so-called depth profiling mode. By collecting a Raman area (XY) map in a plane parallel to the sample surface at a distance Z below the surface of the sample (probing distance), a spectrochemical image deep within the sample can be obtained by analogy with the image produced by optical sectioning microscopy. This technique is referred to as Raman optical sectioning because it does not require the physical cutting or sectioning of the sample. By measuring Raman spectra or acquiring Raman maps successively at different probing distances with typically a regular interval along the vertical Z-axis, a depth profile or 3D representation of the sample may be, respectively, constructed. In general, the maps may be collected along a line in horizontal X and Y or the axial Z direction, from an area in horizontal (XY) or vertical (YZ or XZ) plane, or a sequence of XY areas along the vertical Z-axis to render a volume (XYZ) of the sample.

The second step is the spectrochemical image generation. The image is constructed by processing the array of spectral data in the corresponding

map in a variety of ways as individual spectral peak parameters, the ratio of peak intensities, correlation with a reference spectrum or based on more complex chemometric and statistical methods of the analysis (Mark and Workman Jr. 2018) commonly used in optical spectroscopy. A meaningful number of Raman spectral images generated from a map is determined by the distinguishable spectral features associated with the different sample constituents or properties. Theoretically, the maximal number of spectrochemical images that may be generated from a single map is equal to the number of resolved spectral elements. Since humans can easily recognize visual targets based on colours, the processed data outcomes are usually visualized in pseudo-coloured Raman images with different colour schemes or patterns. In the most commonly used pattern designed around the three primary colours and categorized as warm and cool, the red and blue colours are designated, respectively, to the highest and lowest values of the outcomes.

Thus, depending on the map's geometry, Raman spectrochemical images can be represented by colour-coded lines, areas or volume structures in which the colours indicate the spatial distribution of chemical components or sample properties. As an example, Figure 3-6(a–e) shows a 3D Raman spectral image acquired within a rectangular box of a sample composed of 10 μm polystyrene beads embedded in a glass matrix. The 3D Raman image and the isosurface shown in Figure 3-6(g) are generated as the integrated intensity of the spectral band of polystyrene at 1001 cm^{-1}. The depth profile of an individual particle from the cluster is represented in Figure 3-6(f).

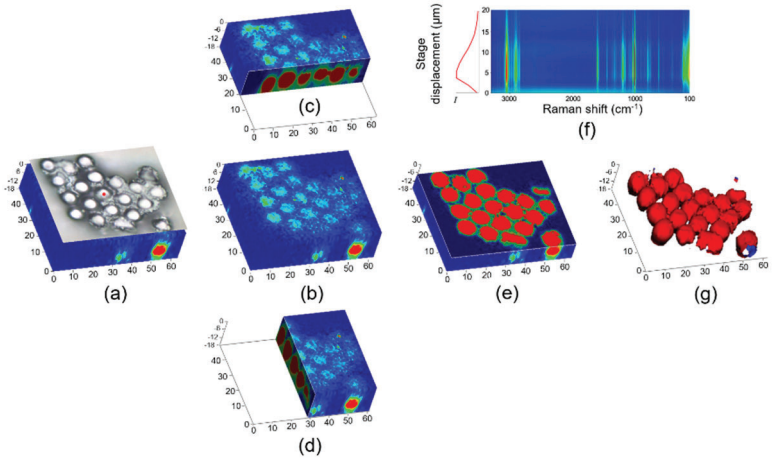

Figure 3-6. Rendering the Raman spectral image obtained from a cluster of polystyrene spherical particles with the diameters of about 10 μm embedded in a glass matrix: (a) optical image of the sample surface superimposed on the 3D Raman image; (b) the 3D Raman image shown without the optical image; (c) an XZ section of the 3D image; (d) a YZ section of the 3D image; (e) the XY section at a probing distance of 8 μm. The red colour shows the highest intensity of the band at 1001 cm^{-1} in the Raman spectrum of polystyrene and, consequently, highlights the polystyrene particles, while the blue colour corresponds to the glass matrix. The isosurface (g) visualizes the locations and shape of the polystyrene particles. The depth profiles of an individual particle from the cluster measured at the point indicated by the red dot in (a) are shown in (f). In the depth profiles, the integrated intensity *I* of the polystyrene band at 1001 cm^{-1} (the left inset) and the intensities of the Raman bands of polystyrene in the spectral range of 100-3200 cm^{-1} (the right inset) are shown as a function of the sample stage displacement by Z-axis.

3.1.4. Focused laser beam and sampling volume element

When a microscope objective focuses the laser beam, the illuminated volume can be determined by the space enclosed by an hourglass shape

shown above in Figure 3-1(c). This volume is characterized by its "waist" or the diameter of the laser spot in the XY focal plane approximated by the Airy disk as expressed in Chapter Two by (2.12)

$$d_{xy} = \frac{1.22\,\lambda}{NA}, \tag{3.1}$$

where λ is a laser excitation wavelength, and *NA* is a numerical aperture of the microscope objective.

Consider an example of the diffraction-limited illumination of the sample with a 532 nm excitation light using an objective with *NA*= 0.9 and 100× magnification (100×/0.9). According to equation (3.1), the diameter of the focused laser spot will be 0.72 μm at the sample plane. The spot will be projected onto the image plane with magnification by a factor of 100. Assuming that the image plane coincides with the spectrograph entrance, the beam diameter will be 72 μm at the spectrograph entrance. If a confocal pinhole with a diameter of 50 μm is set at the entrance of the spectrograph, then only part of the light from the 72 μm beam spot can pass through the pinhole and reach out to the detector. Thus, a pinhole size that is less than the diameter of the laser spot projected onto the image plane will improve the lateral spatial discrimination by a factor of about 1.4. However, the improvement in the lateral spatial discrimination is accompanied by a significant loss in the intensity of the Raman signal and factor 1.4 is considered to be an optimally achievable improvement in practice.

Various expressions for the height of the hourglass shape can be found in the literature. For example, the height can be defined as the distance between the converging beam above the focal plane and the diverging beam below the focal plane where the brightness is taken to be equal to one half

of the maximal brightness of the beam at its focus. Thus, the height is determined by the distance $z = \pm z_R$ (Rayleigh range) between the two planes at each side of the focused spot where the width d of the beam is a factor of $\sqrt{2}$ larger than it is at the focus (as shown in Fig. 3-7) and, consequently, the area of the beam cross-section is doubled.

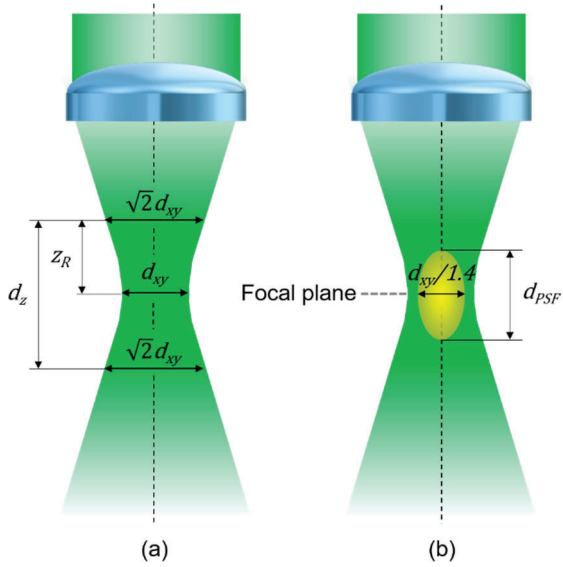

Figure 3-7. Diameter d_{xy} and depth of focus d_z of the focused laser beam (a) and the confocal depth d_{PSF} (b).

The distance between the two points is often referred to as the depth of focus. The following equation may be used to estimate the depth of the region illuminated by a laser in the Z direction:

$$d_z = \frac{2.53\,\lambda}{NA^2}. \tag{3.2}$$

Actually, there is no such strict cut-off distance from the focus so that appreciable scattering may occur along the direction of the laser beam propagation outside the Rayleigh ranges. A less rigorous approximation for the depth of focus can be given by

$$d_z = \frac{4\,\lambda}{NA^2}. \tag{3.3}$$

Given that d_z is inversely proportional to the square of *NA*, the numerical aperture of the microscope objective has a greater effect on the depth of focus than the excitation wavelength.

Dividing (3.2) or (3.3) by (3.1), the ratio of d_z to d_{xy} is derived, respectively, as

$$\frac{d_z}{d_{xy}} = \frac{2}{NA} \quad or \quad \frac{d_z}{d_{xy}} = \frac{3.3}{NA}. \tag{3.4}$$

Formulae (3.4) can be combined in the following relation:

$$\frac{d_z}{d_{xy}} > \frac{2}{NA}. \tag{3.5}$$

When the laser beam is focused in air, the depth of focus is more than twice the size of the laser spot, since the maximum *NA* of an objective operating in the air does not exceed 0.95.

However, the illuminated volume from which the Raman spectrum is collected in a condense-phase sample expands as equations (3.3)–(3.5) have to include the refractive index of the sample *n*. The formula (3.3), for example, should be presented as

$$d_z = \frac{4\,n\lambda}{NA^2}.$$

Thus, the depth of focus is a function of the instrument parameters (λ, NA) and the sample's characteristics (n).

In the confocal arrangement, the height of the sampling volume element, which is called the confocal depth, can be estimated with the use of a PSF. Practical calculation of an effective PSF is a quite complicated task that requires taking the details of the optical design of a given confocal Raman microscope, the quality of its optical components, the characteristics of the laser beam and many other factors into account. Nevertheless, the confocal depth determined by the major axis of the prolate spheroid shown in Figure 3-1(b) and Figure 3-7 (b) may be approximated by the following equation:

$$d_{PSF} = \sqrt{\left(\frac{0.88\lambda}{n - \sqrt{n^2 - (NA)^2}}\right)^2 + \left(\frac{\sqrt{2}\,nD_{PH}}{NA}\right)^2}, \qquad (3.6)$$

where D_{PH} represents the diameter of the pinhole projected back onto the sample plane, which, in general, can be calculated in micrometres if one knows the total magnification factor of the microscope with a given objective (Carl Zeiss n.d.).

As it follows from equation (3.6), for the excitation wavelength λ and the objective with a given NA, the first term under the root is constant, and the confocal depth is influenced exclusively by the pinhole diameter in the second term. The dependences of the confocal depth on the excitation wavelengths calculated in accordance with equation (3.6) for different

apertures in the air (n = 1) and for the sample with n = 1.5, which is typical for the majority of polymers, are shown in Figure 3-8.

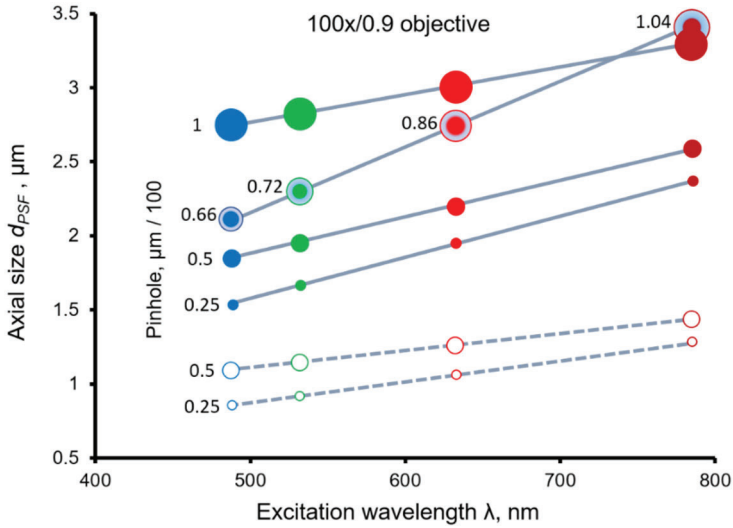

Figure 3-8. The confocal depth d_{PSF} as a function of the excitation wavelength and the diameter of the confocal pinhole. The colours of the circles codify the wavelengths: 488 nm (blue), 532 nm (green), 633 nm (red) and 785 nm (dark red). The diameters of the circles are proportional to the 100, 50 and 25 µm pinholes. The filled circles (solid lines) correspond to the refractive index n = 1.5, and the clear circles (dashed lines) correspond to n = 1. The confocal depths calculated for the pinholes equal to the Airy disk diameters for each excitation wavelength are shown by circles with the dots inside.

The calculations were made for the 100×/0.9 objective assuming that the total magnification factor of the microscope is equal to the magnification of the objective. Thus, the numbers at the lines and next to the dots denote the confocal pinhole diameter in micrometres (µm) divided by the magnification factor of 100. The depth discrimination improves (the

confocal depth decreases) as the excitation wavelength shortens and the pinhole diameter reduces. It is logical to assume that making the pinhole as small as possible is the best option for depth discrimination. However, as the pinhole size reduces, the amount of light collected from the sample and reaching the detector also decreases. It is often considered that setting the pinhole equivalent to the Airy disk for a given λ is a good balance between Raman signal intensity, spectral resolution and spatial discrimination. The 50-μm pinhole provides a good approximation to the Airy disk for blue and green wavelengths, whereas the 100-μm pinhole works well for red and dark red excitations. Because the Raman scattering is intrinsically weak, pinhole apertures with diameters smaller than 25 μm are rarely used and are only practical for the materials with strong Raman cross-sections. The dashed lines calculated for $n = 1$ define the smallest achievable axial sizes and, thus, the best axial discriminations. It is clear that the axial discrimination worsens as the refractive index of the sample increases.

Thus, using the confocal pinhole improves both the lateral and axial spatial discrimination and particularly accounts for the ability of the confocal Raman microscope to provide optical sectioning of a sample. To achieve the higher spatial discrimination, a shorter excitation wavelength, an objective with higher *NA* and a smaller confocal pinhole should be used. Optical objectives with higher *NA* provide the highest power density of the excitation light and have the highest collection efficiency. However, a lower *NA* may be necessary if the sample's topography requires a broader stage movement in a vertical direction or requires sampling through a coverslip or a sample cell window.

It needs to be emphasized that, in practice, the confocal aperture does not restrict the sampling volume element to a prolate spheroid with a sharp

boundary depicted in Figures 3-1(b) and 3-7(b). The measured Raman intensities may fall off fairly slowly on either side of the focal plane in the axial direction. Bridges demonstrated that, in a confocal configuration with a virtual pinhole, the depth profile follows a Lorentzian function (Bridges, Houlne and Harris 2004). The relatively slow decay in the Z-axis is in marked contrast to the relative tight confinement in the XY plane. This slow decay means that one can, in certain circumstances, detect significant out-of-focus Raman signals a long way above and below the nominal focal plane, which are well outside the calculated confocal depths presented in Figure 3-8.

An essential consequence of the confocal mode of operation is the fact that it can be used to better discriminate the Raman signal from the fluorescence background. In the case of superimposed Raman and fluorescence signals from a sample, one should increase the power density of the laser light at the sample and decrease the size of the pinhole. At first glance, the need to increase the power density may appear surprising. Indeed, at moderate levels of excitation power, the intensities of both Raman scattering and fluorescence are proportional to the excitation power. However, the increased excitation power quickly quenches the fluorescence background so that the fluorescent intensity no longer increases with the increasing power density. In contrast, the intensity of Raman scattering increases in line with the power density. Provided that the fluorescence is quenched and, thus, is emitted evenly from the illuminated volume, decreasing the pinhole results in a drop in the intensity of the fluorescence that surpasses the decrease in the intensity of the Raman signal. The relative increase of the Raman signal takes place because most of the excitation light intensity

(~84%) is concentrated in the central Airy disk. This effect is demonstrated for polyurethane in Figure 3-9.

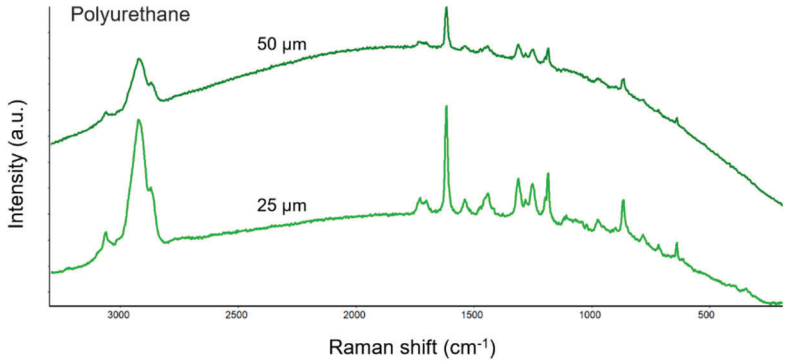

Figure 3-9. Raman spectra of polyurethane obtained using 532 nm laser and 50×/0.75 objective. The spectra were measured with 50 or 25 µm confocal pinhole as indicated. The spectrum measured with a 25 µm pinhole manifests the decrease in the fluorescence background relative to the Raman bands and a better signal-to-noise ratio.

It should be emphasized that when performing spectral measurements using a metallurgical ("dry") objective (the most common commercial choice) beneath the surface of a sample with a refractive index *n*, the effect of refraction at the air/sample interface shifts the point of focus much deeper into the sample than the sample displacement in the vertical Z direction designates. As a result, the depth scale appears to be falsely compressed, typically by a factor roughly equal to the refractive index *n* of the sample. At the same time, the confocal depth spreads further in comparison with the measurements in air that causes a decrease of spatial discrimination in the axial direction. This effect escalates when increasing the probing distance. Also, the efficiency of the collection of scattered light decreases noticeably

with the probing distance. The optical effects within a condense-phase sample have been discussed at length in the literature and are summarized in Figure 3-10. Everall first pointed out the data misinterpretation that can result from neglecting the refraction effect when measuring the depth profile of a sample using the metallurgical objective. He detailed the common artefacts and errors in confocal Raman microscopy (Everall 2000, Everall 2009, Everall 2010). Further contributions to the thorough description of the problem that accounts for the effects of dispersion and spherical aberration have been carried out by other experimenters (Tomba, Arzondo and Pastor 2007, Baia, et al. 2002, Sourisseau and Maraval 2003).

Dry corrected objectives or immersion objectives with a fluid that matches the refractive index of the sample may be used to minimize the problem of laser beam refraction at the air/sample interface (Everall, et al. 2007). Filling the gap between the objective's lens and sample with an index matching fluid removes the bending of the light at the surface of the sample caused by refraction. An oil immersion objective can be used for confocal Raman measurements within polymers, since the refractive index of oil (n = 1.52) is close to that of many polymer materials. The use of oil instead of air between the objective and the sample restores the spatial discrimination, eliminates the depth scale compression and increases the amount of scattered light collected at the probing depth. However, the use of oil with the immersion objective may cause contamination of the sample. As such, this method can scarcely be considered nondestructive, and it is not generally applicable when the sample needs to be kept intact.

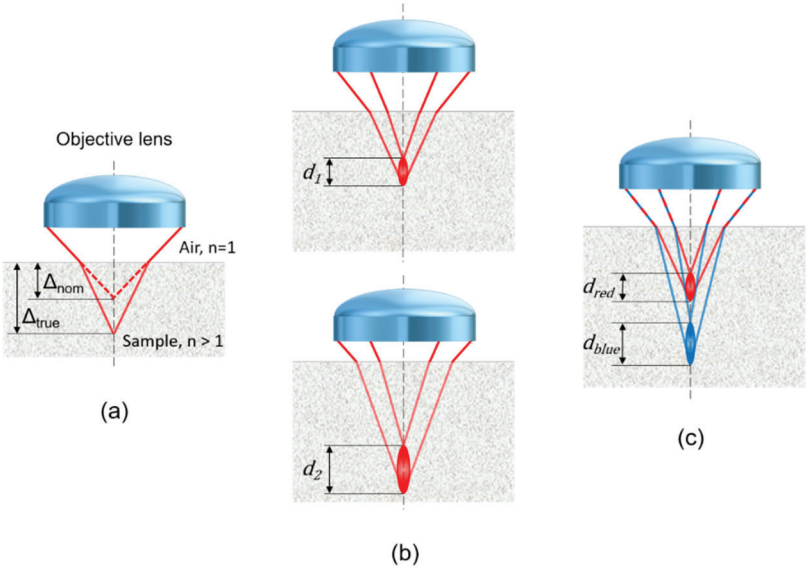

Figure 3-10. The optical effects in a solid sample when a metallurgical objective is used to focus the laser beam and make spectral measurements below the sample surface. (a) Due to the refraction at the interface between the sample (refractive index n > 1) and air (n = 1), the point of focus is shifted into the sample by distance Δ_{true}, which is deeper than the sample displacement Δ_{nom} designates. (b) As a result of spherical aberrations, the marginal and near-axial rays are refracted and focused at different depths so that the depth of focus elongates in the vertical direction from d_1 to d_2 as the laser beam is focused deeper in the sample. (c) The effect of dispersion changes the angle of refraction at the air/sample interface for different excitations wavelengths so that the blue wavelengths are focused deeper in the sample than the red ones. The depth of focus d_{blue} is more elongated for the blue wavelengths than for the red ones d_{red}.

The examples of the application of dry and oil immersion objectives for the confocal measurements of multi-layered polymer films will be presented in Chapter Four.

3.2. Mechanisms and conditions of sample mapping

The design and characteristics of the sample scanning mechanisms and techniques are important as they determine the way and the rate at which the Raman map is collected. Conventional instruments are equipped with mechanical stages driven by stepper motors, while high-speed imaging systems use sampling mechanisms based on the raster scanning principle. The main difference is that the former scans the samples in a discrete point-by-point, also called stop-and-go mode, while the latter allows scanning continuously without stopping, which is a critical feature for fast mapping.

During the map acquisition, the mechanical stage accelerates after each stop, moves at a constant speed, decelerates, and then stops and settles to allow a Raman spectrum at the next point to be measured. This sequence of actions explains the terms "point-by-point" and "stop-and-go" when describing the operating mode of the mechanical stage. This mode offers the same size of the laser spot at each point and the adequate precision of their positioning on the map. However, the motion of the mechanical stages in the intermittent stop-and-go regime results in a longer acquisition time in comparison with other mapping techniques.

In a line scanning mode, a cylindrical lens focuses laser light into a line segment on a sample instead of a spot, as a regular microscope objective would. Special collecting and coupling optics project the line segment onto the entrance slit of the spectrograph so that the segment length fits the slit height. The CCD readout electronics partition the detector matrix into

several areas, each of which includes all horizontal and a certain number of vertical pixels, equal for each area as illustrated in Figure 3-11. Since the slit is then projected onto the spatial axis of the CCD matrix in the spectrograph, each area of the matrix collects the Raman spectrum from a fraction of the line segment focused on the sample. Thus, the number of

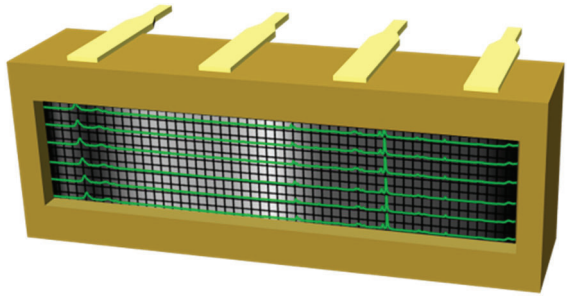

Figure 3-11. Schematic illustration of the partition of CCD matrix for simultaneous measuring Raman spectra of multiple locations on a sample. The spectrum of polystyrene collected in each of the six segments of the matrix, occupying a full raw of horizontal and two vertical pixels, is shown as an example. In reality, the matrix is usually partitioned into 25 or 50 segments in the spatial axis.

vertical pixels in the area determines the spatial discrimination within the focused line. To some extent, this spatial discrimination is comparable with that achievable by par-sampling in point-by-point mapping considered below. The line scanning mode offers a faster speed than point-by-point mapping because multiple sample locations in the line are measured simultaneously. To map an XY area, the sample is moved perpendicular to the line segment in the X direction and then shifted parallel in the Y direction by the distance equal to the line segment length. The

mapping is usually performed in a zigzag manner. The line scanning mode provides better protection of the sample from overheating and possible thermal degradation compared to point-by-point mapping. Indeed, the laser beam is spread over the illuminated line segment rather than being tightly focused in a single point. However, line scanning has a major disadvantage; namely, it cannot be used for actual confocal measurements as it does not employ a confocal pinhole. In addition, line scanning is subject to non-uniform illumination between the centre and the edges of the line segment.

The highest scanning speed and precise positioning throughout the scanning area can be achieved with the employment of piezoelectric or galvanometer scanners. Piezoelectric scanners are available in the form of sample stages or microscope objective positioners. Servo-controlled galvanometer scanners use movable mirrors to raster the laser beam over the scanning area. However, both mechanisms are designed to scan relatively small areas, usually limited to a few hundred microns in either direction. Besides, when scanning with the use of a galvanometer scanner, the shape of the focused laser beam deviates from the ideal round spot as the laser beam moves away from the centre of the scanned area, thereby reducing spatial discrimination in the off-centre parts of the sample. The combination of mechanical stages with piezo or galvanometer scanners can increase the scanned area, although this arrangement requires careful alignment.

Recently, a magnetic linear motor stage with closed-loop optical encoders became available. In contrast to the mechanisms of raster scanning by a laser beam, this stage moves continuously, while the CCD is read out at certain intervals determined by the sampling step and exposure time. The stage moves relative to a fixed objective to keep the incident laser beam perpendicular to the sample surface. In contrast to galvanometer scanners,

it preserves the circular spot of the focused laser beam throughout the entire scanned area. The movement usually occurs in a zigzag manner. The spectrum accumulates while the stage is moving so that the resultant Raman spectrum is obtained from a linear segment of the sample rather than a discrete point. The area of the segment is determined by the laser spot size multiplied by the sampling step: that is, the distance that the stage passes for a predetermined exposure time. The speed of the stage movement v_{stage} is usually controlled by software based on the sampling step equal to the linear segment l_s divided by the exposure time t_{exp} defined by the operator:

$$v_{stage} = \frac{l_s}{t_{exp}}.$$

This method allows the map of a relatively large sample area to be acquired with high spatial precision and a fast speed. The measurement of the linear segment results in a better opportunity to detect Raman scattering from a small object; however, it also results in worse spatial discrimination compared to a measurement at a discrete point.

In Raman microscopy, the smallest object that can be captured and measured is determined by the focused laser spot size and the distance between the points of the mapping grid, usually referred to as the sampling step. There are three principal mapping conditions that set the relationship between the laser spot and the sampling step:

1) Par-sampling: the laser spot is equal to the step size;
2) Under-sampling: the laser spot is smaller than the step size;
3) Over-sampling: the laser spot is larger than the step size.

Sometimes, these conditions are expressed in terms of the ratio of the measured area to the total area of the map

$$N \times \pi \left(\frac{d_{xy}}{2}\right)^2 / L \times W \,,$$

where N is the number of measured points, and L and W are, correspondingly, the length and width of the area. The ratio is called the sampling ratio and results in ~ 1, <1, and >1 for par-sampling, under-sampling and over-sampling, respectively. Under-sampling is generally employed when a sample needs to be evaluated, especially at a preliminary phase of the spectroscopic experiment. If there is enough *a priori* knowledge about the sample composition, as well as the distribution of its components and their sizes and shapes, then par-sampling or properly selected under-sampling conditions can be used. Over-sampling can improve the precision and contrast in Raman images, but it requires longer acquisition times and does not improve spatial resolution.

Figure 3-12(a)–(c) schematically illustrates the relationship between the laser spot and step size in an area map when the laser spot size and dimensions of the object are comparable. Obviously, under-sampling may result in skipping the microscopic object (red circle) present in the sample, while par-sampling and over-sampling ensure the object is captured.

The examples of mapping an individual polystyrene (PS) bead and a PS bead adjacent to a polymethyl methacrylate (PMMA) bead using different sampling steps are shown in Figure 3-12(d) and (e), respectively. Polymer beads of 1 μm nominal diameters were deposited on a glass slide, and the maps were acquired using a 532 nm excitation wavelength, a 100×/0.9 objective and a continuously moving XY stage. According to equation (3.1),

the laser spot of about 0.7 μm was close to the diameter of the polymer beads. The Raman images in Figure 3-11(d) and (e) were generated using a multivariate curve resolution (MCR) method that extracts spectral components corresponding to PS, PMMS and glass. These compounds are indicated, respectively, by red, yellow and black, visualizing the shape of the polymer beads in Raman images. Clearly, under-sampling at a 1.2 μm step causes image blurring and does not display the actual shape of the beads, although it still allows the PS and PMMS parts to be discriminated. Par-sampling with the step of 0.6 μm approximately matching the size of the laser spot provides a satisfactory representation of the shape of the individual PS bead, as well as the adjacent PS and PMMA beads. Over-sampling at the 0.3 μm step results in the Raman image that more accurately depicts the shape of the polymer beads. Mapping the adjacent PS and PMMA beads at a 0.3 μm step means approximately three sampling points per the diameter of the beads. As a rule of thumb, three sampling points per object's aspects are recommended if the shape and dimensions of closely situated objects need to be well discriminated against and accurately represented in the Raman image. Over-sampling by further reducing the step size leads to a minor improvement of the contrast in the Raman images but longer acquisition time. Obviously, this recommendation applies to both the lateral and axial measurements. Note that the Raman images in Figure 3-12(d) and (e) slightly overestimate the sizes of the beads because the images are formed as a convolution of the original object with a laser spot of a similar size. The larger the object, the lesser the effect of the size of the laser spot on the object size estimated from the Raman spectral image.

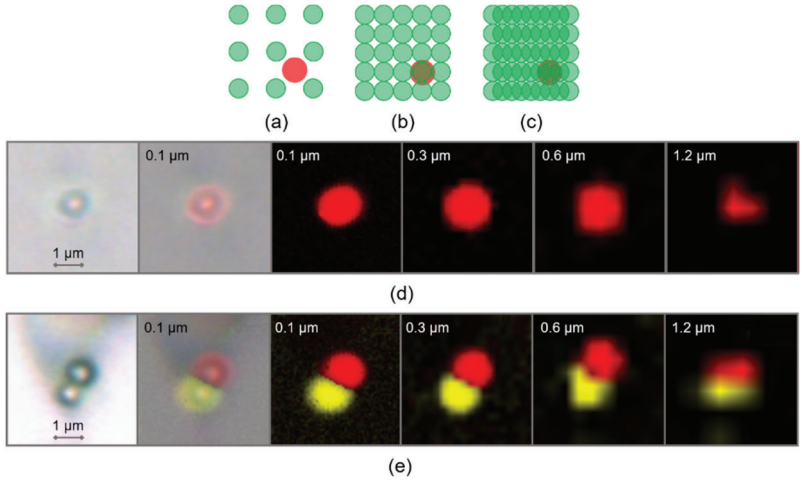

Figure 3-12. The relationship between the sizes of the sample, laser spot and the sampling step. The green and red circles represent the laser spot and a small sample, respectively, in the schematic of the conditions of under-sampling (a), par-sampling (b) and over-sampling (c). The Raman images of individual polystyrene (PS) bead (d) and the adjacent PS and polymethyl methacrylate (PMMA) beads (e) are constructed from the maps acquired using a 532 nm laser for excitation, 100×/0.9 objective and different sampling steps. The Raman images are generated as spectral components extracted by the MCR method with the red and yellow colour highlighting PS and PMMA, respectively. From left to right: optical images of the beads observed using 100×/0.9 objective, semitransparent Raman images (0.1 µm mapping step) superimposed on the optical images of the beads and Raman images constructed from the map collected at 0.1, 0.3, 0.6 and 1.2 µm steps.

The analysis of a large heterogeneous sample using Raman imaging requires optimising the sampling conditions based on the sizes, shapes and spatial distribution of spectroscopically distinguishable constituents of the sample. An example of choosing different sampling steps and representative

mapping areas for the spectrochemical characterization of a pharmaceutical dosage form is presented in Figure 3-13.

A solid bead with a diameter of about 1 mm from a multi-particulate pharmaceutical dosage form was used for the experiment. The bead was cleaved in halves, and one half of the bead was analyzed to expose the multi-layered structure of the bead, render the distributions of an active pharmaceutical ingredient (API) and excipients and assess the dimensions and shapes of the microparticles in the core unit of the bead.

The spectral measurements were performed with a 780 nm laser to minimize fluorescence that might originate from pharmaceutical excipients under shorter wavelengths excitations. The maps were acquired using the mechanical XY stage in the discrete point-by-point mode. The small red dots in the optical images shown in Figure 3-13 correspond to the points of measurements on the map grid. The Raman images were constructed as correlations with the reference spectra of pure ingredients of the dosage form.

The map comprising the whole circular cross-section of the bead was collected with a metallurgical 20×/0.40 objective from the grid of 2500 points at 20 μm equidistant spacing in both X and Y directions. As the laser spot size was estimated to be a bit over 2 μm according to equation (3.1), the mapping of the whole area of the bead with 20 μm steps resulted in obvious under-sampling.

Despite the under-sampling, the Raman image analysis of the whole cross-section of the bead established the circular layered distribution of the ethylcellulose, API, talc and the core unit's composition as a mixture of sugar and starch. The thickness of the layers and the size of the core unit

can also be readily determined, as demonstrated in Figure 3-13(a). It was found that the core of the bead was covered by an intermediate layer of a mixture of the API and talc, followed by the outer layer composed of primarily the pure API. From the outside, the bead was coated with a thin layer of ethylcellulose. Although the Raman spectral images confirmed the content uniformity within the layers, they did not provide any fine details on the dimensions and shapes of the particles or the agglomerates that these ingredients may form.

The full-area visual inspection was then performed to select the areas of interest for mapping with finer sampling steps.

The map from an area about 70 × 300 μm^2 of the bead shown in Figure 3-13(b) was acquired using the 50×/0.50 objective and 5 μm sampling step. The laser spot size focused by the objective was about 1.9 μm that still resulted in under-sampling. Nevertheless, the Raman images evidence a sharp boundary between the core composed of the sugar and starch mixture and the intermediate layer of API and talc around the core unit. The agglomeration of talc in discrete domains, some of which reach up over 20 μm in size, is seen in the intermediate API layer and the outer one to a smaller extent.

The Raman image of the 18 × 21 μm^2 area shown in Figure 3-13(c) illustrates the ability to identify the small particles in the bead core. The image discloses that the round shape microparticles with diameters of about 10 μm in the mixture of sugar and starch are composed of starch. The map was acquired using the 100×/0.90 objective, which produced about a 1.1 μm laser spot at the 1 μm sampling step that corresponds to par-sampling conditions.

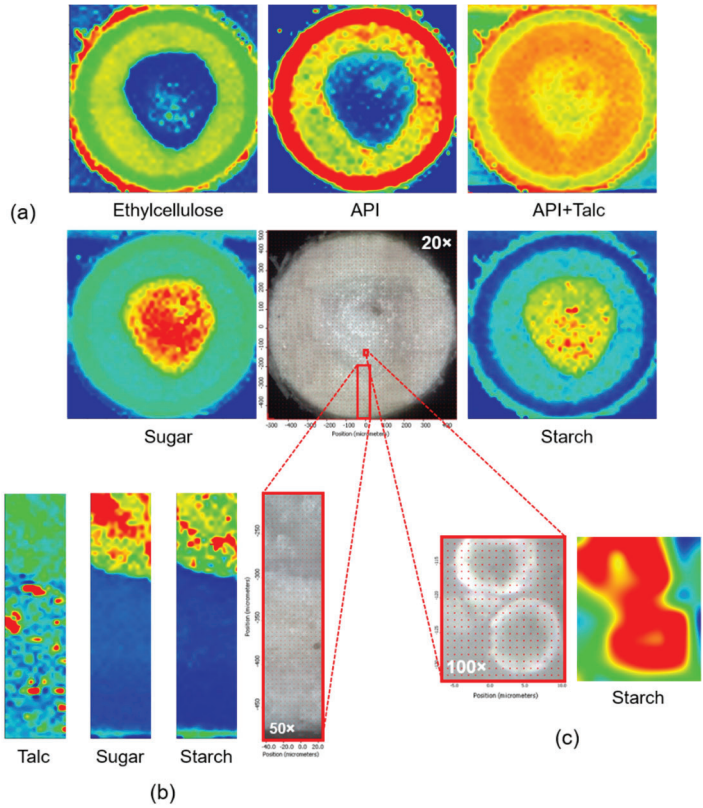

Figure 3-13. The optical and Raman images obtained from a cross-section of a pharmaceutical bead: (a) The Raman images constructed from the map of the whole cross-section show the distribution of the API and excipients in the bead; (b) The Raman images of the smaller area allow the talc particles to be identified in the API layers; (c) The spherical particles observed in the optical image were found to be composed of starch. The magnification of the microscope objectives used for obtaining the optical and Raman spectral images is indicated on the optical images. The Raman images were generated as spectral correlations with the reference spectra of the corresponding ingredients so that the red colour shows the areas with the highest correlation and, thus, the distribution and concentration of the ingredients.

Depending on the size of the mapped area and the sampling conditions, the total map acquisition times in this example lasted from half an hour to several hours.

Although under-sampling can lead to the loss of some information about the sample composition and structure, it is often tempting to apply under-sampling because it may radically reduce the time spent on the map acquisition compared to par-sampling. Before choosing under-sampling, the best approach is to evaluate the acquisition time and decide if it is practically acceptable. In this example, reducing the sampling step to implement the par-sampling conditions did not reveal any additional data on the layered structure of the bead but made the time for mapping the entire area impractically long.

Par-sampling offers an adequate characterization of the sample, although it often requires long acquisition times since the laser spot diameters do not exceed 5 μm even at longer excitation wavelengths and for microscope objectives with a low NA. Finding statistically significant, but not large areas of the sample and acquiring maps in par-sampling conditions maintain a rational balance between the information content of the Raman spectral image and the time of its acquisition.

In practice, the intensities of Raman spectra, which may vary by several orders of magnitude depending on the Raman cross-section of the materials under study, must be taking into account. Thus, the time of the map acquisition is determined not only by the sampling conditions but also the adequate integration time to obtain the Raman spectrum of a constituent with the lowest Raman cross-section in the heterogeneous sample. A thorough consideration of the relations between the laser spot size, mapping

area, sampling mode and Raman intensities can be found elsewhere (E. Lee 2012).

The essential characteristic of a Raman microscope with the mapping capability is the speed of map acquisition determined by the construction of the sample scanning mechanism and the readout rate of the detector. Synchronization of continuously moving XYZ stages or other fast scanning devices with the high readout rates of EMCCD detectors offers a prompt spectrochemical characterization of relatively large samples. To demonstrate the difference in the effectiveness of the analysis, Figure 3-14 represents another example of a pharmaceutical application where the Raman spectral images were obtained from a tablet containing a low dose of zolpidem tartrate. The maps were acquired using Raman microscopes with similar optical design and spectrographs but different sampling stages and detectors. Both the instruments were configured with a 785 nm laser for excitation, a 10×/0.25 objective and a 50 μm pinhole aperture. The mapping grid was also selected to be similar: a 25 μm sampling step over a sample area of about 4 x 2 mm^2 that yielded about 11000 Raman spectra in total. However, one map was acquired on a conventional Raman microscope equipped with a mechanical XYZ stage and a standard CCD detector, while the other one was obtained on a Raman system that employed the continuously moving magnetic motor stage mentioned above and an EMCCD. Significantly faster speed of measurements of individual Raman spectra achievable in the latter resulted in more than an order of magnitude reduction in the map acquisition time, namely, 25 min. vs. 9 hours for the conventional one. Despite the significantly different total acquisition times, the individual Raman spectra obtained at the equidistant locations of the mapping grid—the discrete points in the experiment performed on the

conventional Raman microscope, and the linear segment (also called pixels) carried out on the fast scanning instrument—demonstrate a comparable level of S/N ratio.

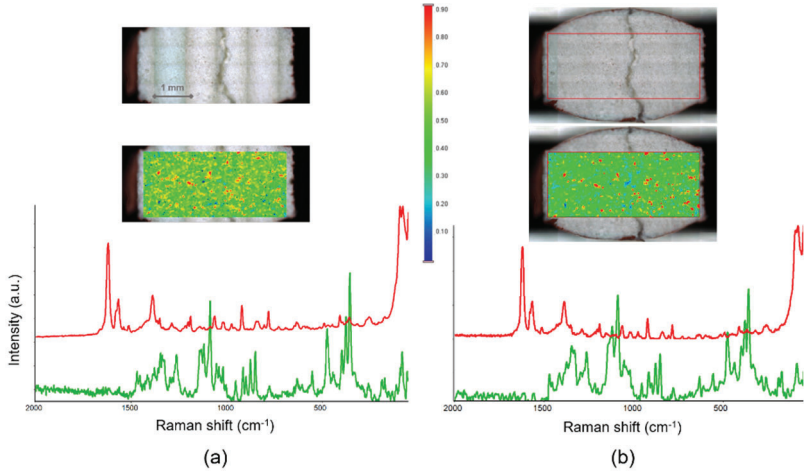

Figure 3-14. Raman images and spectra of a tablet with a low dose of zolpidem tartrate obtained on conventional (a) and fast scanning (b) Raman microscopes. From top to bottom: light images of the tablet; Raman images generated as correlation with a reference spectrum of zolpidem tartrate superimposed on the light images; representative mean spectra of zolpidem tartrate (red) and lactose (green), the major excipient of the tablet, retrieved from the red spots and green areas, respectively. The spectra are shown after baseline correction and offset for clarity. The inset in the middle shows the colour-coded correlation scale for the Raman images. Both the spectral images demonstrate the distribution of the zolpidem tartrate in the tablet, exposing some spotted domains in which the API is concentrated in almost pure form.

Mapping via the continuously moving stage ensures a higher probability that small objects will be detected than with stop-and-go movement, where spectra are measured only when the sample stage stops. For a comparison,

Raman spectral images of a polished ceramic sample obtained using a Raman microscope that enables the sample stage to operate in either continuous or stop-and-go mapping mode are presented in Figure 3-15. The mapping of the same area of the sample was performed with a 633 nm laser for excitation, a 10×/0.25 objective, a 50 μm pinhole aperture and a 20 μm sampling step over the area of about 3.3 x 1.6 mm^2 that yielded about 13000 Raman spectra. The Raman images were generated as the spectral correlation with a Raman spectrum of the diamond. Apart from essentially different acquisition time and severe under-sampling conditions (the sampling ratio <<1), the Raman spectral image obtained with the continuously moving stage discloses the presence of diamond particles in the sample. The particles probably remained on the surface of the sample after processing the ceramic with a diamond tool. In contrast, the Raman image generated from the map acquired with the stage operated in stop-and-go mode failed to reveal the presence of the diamond particles on the surface of the sample.

The Raman microscopes equipped with fast scanning mechanisms and usually EMCCD detectors are often called imaging Raman microscopes. Manufacturers of Raman microscopes use this term for marketing purposes to emphasize speed and other advantages over conventional stop-and-go mode systems, which are accordingly called mapping Raman microscopes. The imaging microscopes allow the composition and morphology of a sample to be measured and visualized in a detailed Raman spectral image in real time. They principally bring new analytical capabilities in the spectrochemical characterization of large samples on a microscopic scale and can be really used to "find a needle in a haystack" as in the example above. These instruments offer extraordinary productivity combined with

information-reach spectral and spatial content. Due to the high scanning speed and, as a consequence, the rapid dissipation of heat, imaging Raman microscopes also ensure less laser-induced damage to sensitive samples, especially biological ones.

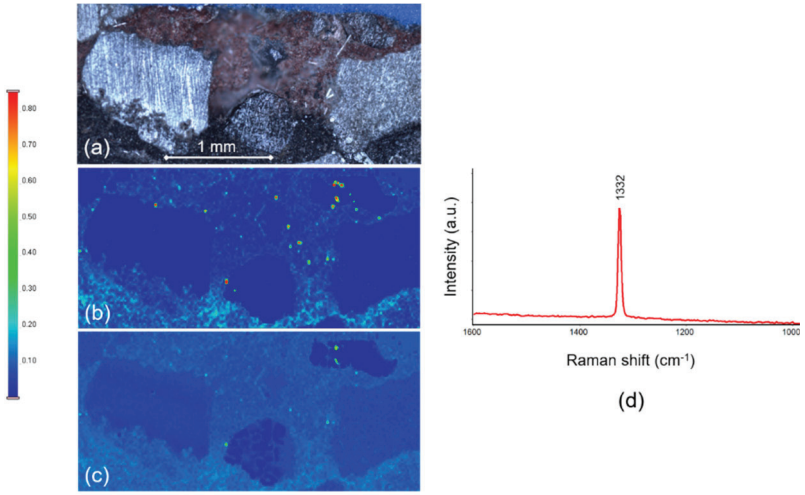

Figure 3-15. The optical image of the surface of a polished ceramic sample (a) and the Raman spectral images obtained with the sample stage moving continuously (b) and in the stop-and-go mode (c). The Raman images were generated as the correlation with the reference spectrum of the diamond. The red spots in the Raman image (b) correspond to the diamond particles on the surface of the sample. A strong peak of the diamond at 1332 cm^{-1} is observed in the mean spectra retrieved from the red spots shown for a typical particle (d). The diamond particles are skipped when mapped in the stop-and-go mode as no corresponding spots are exposed in the Raman image (c). The inset on the left shows the colour-coded correlation scale for the Raman images.

Imaging Raman microscopes offer more opportunity for par-sampling and over-sampling, which are generally beneficial for detailed Raman images

with high contrast. In general, in the Raman image composed of numerous spectra, the requirements to S/N ratio in the spectra in individual pixels can be somewhat lowered than that to Raman spectra measured at the corresponding single point. Indeed, statistically averaged spectra in the adjacent pixels of the Raman image with improved S/N can be provided both in real time and by post-processing.

Although the advances in technology and elegance in instrument design can improve the utility of Raman microscopy as an analytical tool, there is still a need for the experimenter to understand the process and parameters involved and make informed decisions for generating scientifically meaningful Raman spectral images. The experimenter has the privilege to set the objectives of the analysis and decide which parameters are the most and the least significant for the sample. The instrument performance, that is, its appropriate alignment, is the top priority for any high-precision experiment. A rational balance between the sampling method and the time of the measurements ensures an optimal experiment design.

3.3. Evaluation of spatial resolution and sensitivity of confocal Raman microscopes

The ability to discriminate the Raman signals of closely spaced microscopic objects or a microscopic object from a surrounding matrix, and hence to chemically identify the objects, is determined by lateral and axial spatial resolutions achieved in a confocal Raman microscope. The definition of the resolution was originally derived from the ability to resolve two point light sources, such as distant stars observed with an optical telescope in astronomy. This definition was adopted for imaging systems, including optical and Raman microscopes.

Spatial resolution is defined as the shortest distance between two objects such that their presence can be distinguished in the image. The smaller the distance between the two objects, the higher the resolution. The measure of spatial resolution depends on the criterion selected to determine this distance. Following the original astronomical interpretation, the generally accepted standard to quantify that two objects are resolved is the Rayleigh criterion. By this criterion, as mentioned in Chapter Two, two light point sources of the same intensity are considered resolved when the central diffraction maximum of one intensity distribution profile coincides with the first minimum of the other. For the Airy function in equation (3.1), this criterion results in the lateral resolution given by the radius of the Airy disk

$$R_{xy} = \frac{0.61\,\lambda}{NA}, \tag{3.7}$$

that is, by merely dividing d_{xy} in (3.1) by the factor of 2.

In principle, a similar approach can be applied for the theoretical estimate of the axial resolution based on the confocal depth defined by equation (3.6). Thus, by selecting the shorter wavelength of the excitation light and the microscope objective with a higher *NA*, two objects can be resolved at a smaller distance and the spatial resolution can be improved.

It is worth emphasizing that equation (3.1) is generally valid for a microscope objective with a high *NA* if the laser beam fills the entire input pupil of the objective. Under-filling leads to stray light reflections inside the objective and makes the actual *NA* less than its nominal value. Thus, the real focused spot appears to be larger than the diffraction-limited one. However, over-filling of the objective's aperture partially cuts off the laser beam that results in the decrease of light intensity and, more importantly, disrupts the

Gaussian shape of the laser beam. Over-filling leads to divergence of the laser beam and an increase in the size of the focused spot. When designing Raman microscopes, a slight under-filling of the input pupil of the objective is often practised, although at the expense of a somewhat larger focused spot. Consequently, the numbers obtained from equation (3.7) and other formulae that offer even smaller numbers should be considered some of the limit values which practically achievable results can only approach to.

The determination of the spatial resolution of a confocal Raman microscope strictly following the Rayleigh criterion is hampered because it is practically impossible to find or fabricate suitable targets. Indeed, the objects in such targets should not only be much smaller than the Airy disk but spaced at distances that could be varied to satisfy the Rayleigh criterion.

The recent technological developments in confocal Raman microscopy and imaging for the characterization of two- and three-dimensional spatial distributions of materials on a submicrometer scale dictate the need for reference standards that could be used to test the confocality of Raman microscopes in order to evaluate their capabilities and objectively compare with each other. Although there has been progressing in the fabrication of sophisticated polymer resolution targets (Kauffman, Gilliam and Martin 2008), most work to date has been performed with much simpler test systems.

The right way to predict the spatial resolution of a confocal Raman microscope is to estimate its spatial instrumental function, that is, the lateral and axial dimensions of the effective PSF produced by the instrument. Because the spatial representation of an object obtained from the measurements is a convolution between the object and the effective PSF, a

practical way to evaluate the effective PSF is to scan a laser spot over an object, the size of which, mathematically speaking, approaches the δ-function. Next, depending on the scanning direction, the lateral or axial intensity profile is generated. The small objects from which the Raman scattering is collected contain a limited amount of substance. Therefore, this substance must have a sufficiently high Raman scattering cross-section to ensure reliable and reproducible measurement.

Historically, a polished Si or Ge wafer has been used for measuring the intensity profiles in both the lateral and axial directions. Polished wafers or slices of the Si substrates are readily available from semiconductor vendors. The lateral resolution target, such as a piece of severed Si, is often referred to as a knife edge. The target is scanned perpendicular to the cut edge, and an intensity profile of the Si band at 520 cm^{-1} is generated along the line. This test provides a satisfactory estimate for the laser spot size and helps to identify performance issues (e.g., a malfunctioning sampling stage or poor optical alignment). As the laser beam penetrates into Si or Ge by very shallow distances, the wafer surface can be assumed to be a layer of infinitesimal thickness. A simple experiment that evaluates the confocal depth consists of mapping a Si wafer in the Z direction. However, as pointed out by Adar (Adar 2010), if the visible, especially, longer wavelengths such as 785 nm are used for the excitation, then the depth of penetration into the Si is not negligible. As a result, the confocal depth may appear significantly overestimated if the objects comparable to the size of the diffraction-limited laser spot need to be characterized.

A single CNT and a layer of graphene represent practically ideal structures to test lateral and axial resolutions correspondingly. CNTs range from a subnanometer to a few nanometers in diameter and may be up to several

micrometres long. Since a typical carbon atom has a diameter of about 0.3 nm, the thickness of a single graphene layer is close to the same value. While having infinitesimal dimensions in comparison with the corresponding lateral and axial dimensions of the PSF, these materials provide a high enough Raman signal to allow reliable measurements.

The results of the experiments with these test structures are illustrated in Figure 3-16.

To test the lateral resolution, a single individual CNT on Si substrate was used, and its location was tracked by SEM. The beam of a 532 nm laser was focused on the surface of Si using a 100×/0.9 objective, and an area map of about 2×2 μm^2 was acquired in a confocal mode (the pinhole diameter was set to 50 or 25 μm) with a 0.1 μm step to ensure a high contrast Raman image. The Raman image in Figure 3-16(a) was obtained using a 50 μm confocal pinhole and generated as the integrated intensity of the G band at about 1600 cm^{-1}. Then, a set of profiles was generated, that is, graphs showing the change in the integrated intensity perpendicular to the axis of the CNT, and an average FWHM of these profiles was calculated to estimate the lateral diameter of the PSF. The FWHM numbers of 0.36 and 0.29 μm, where the subscript indicates the diameter of the confocal pinhole in microns, show that the size of the confocal spot decreases and, consequently, the lateral resolution improves with the reduction of the diameter of the pinhole, respectively, from 50 to 25 μm.

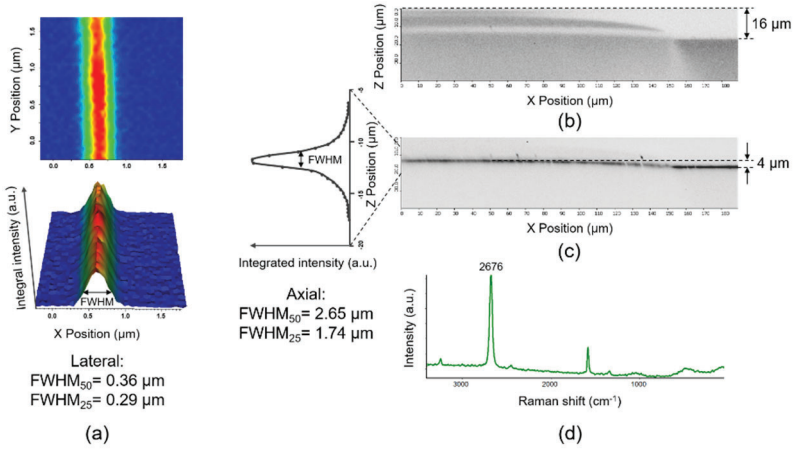

Figure 3-16. Test structures based on CNT and graphene for confocal lateral spot size and axial depth estimation: (a) The Raman spectral image of a small area containing CNT on the Si substrate generated as the integrated intensity of the G peak at 1600 cm^{-1} (top) and the corresponding pseudo-cube (bottom) showing the profile of the intensity perpendicular to the CNT. (b) The grey-scale Raman optical section of the test structure containing graphene showing a flank of the thin layer of glass on top of the glass substrate. (c) The grey-scale Raman optical section of the same structure displaying the layer of graphene partly "sandwiched" between two layers of glass and on the glass substrate. An effect of the depth compression is observed in both the images in the area where the graphene is "sandwiched" between two layers of glass. The inset on the left shows the depth profile of graphene generated as the integrated intensity of the 2D (G') band at 2676 cm^{-1}. A representative Raman spectrum of the single layer of graphene in glass is shown in (d). The FWHMs of the lateral and axial profiles are given for 50 and 25 μm confocal pinholes as denoted by the subscripts.

To test the confocal depth, a layer of graphene "sandwiched" between two layers of glass was prepared as a test structure. The structure was fabricated by placing a drop of sodium silicate (41% solution, Loudwolf Inc., Dublin,

CA) on a single layer of graphene synthesized on a microscope glass slide using a CVD process (CVD Equipment Corp., Central Islip, NY). The sodium silicate (aka "liquid glass") was then dried to form a glass layer about 16 μm thick over graphene. The Raman map was acquired using 532 nm laser for excitation with a metallurgical 100×/0.9 objective from an XZ area of about 190 × 40 μm^2 with 0.2 μm sampling step in a confocal mode (50 or 25 μm pinhole diameter). The XZ area was chosen so that it enclosed the flank of the upper layer of glass. Thus, graphene inside the glass and graphene on top of the glass microscope slide not coated by sodium silicate were included in this area. The grey-scale Raman image shown in Figure 3-16(b) was generated as the integrated intensity of the glass bands below 1000 cm^{-1}. The image shows that the thickness of the upper layer of glass is gradually decreasing, and it ends at the horizontal position with coordinate X at about 150 μm.

The Raman image in Figure 3-16(c) was obtained with 25 μm confocal pinhole and generated as the integrated intensity of 2D (G') band of Graphene at 2676 cm^{-1}. It worth mentioning that the Raman image explicitly demonstrates the depth compression when the confocal analysis is performed using a metallurgical objective from a material with $n > 1$. It is clearly seen that at the X position of about 150 μm, the graphene layer bends. The "sandwiched" layer shifts closer to the glass surface by approximately 4 μm relative to its actual position on top of the surface of the glass slide. The axial compression factor is easily calculated since "sandwiched" graphene is observed at the Z position of 12 μm (16 μm - 4 μm = 12 μm), and the thickness of the upper layer of glass is 16 μm. Thus, this factor is equal to 16 μm /12 μm = 1.33. The compression factor appears to be close enough to $n = 1.5$ for ordinary glass and, as mentioned above, is

roughly defined by the sample's refractive index. The inset on the left shows the depth profile constructed as the integrated intensity of the 2D (G') band of graphene. The Lorentzian function well approximates the shape of the profile, and a mean FWHM of several profiles taken at different X positions between 0 and 50 μm and obtained with the confocal pinhole of 50 and 25 μm was found to be 2.65 and 1.74 μm, respectively. The gradual decrease of the intensity of the 2D (G') band above and below its maximal value in accordance with the Lorentzian distribution indicates that the confocal pinhole does not cut the Raman signal abruptly, although the smaller pinhole noticeably decreases the confocal depth and, thus, improves the axial resolution. A representative mean Raman spectrum of "sandwiched" graphene is shown in Figure 3-16(d).

The experimentally demonstrated confocal depth is in good agreement with the theoretical prediction. In this example, with a 532 nm excitation wavelength, a metallurgical 100×/0.9 objective and a 25 μm confocal pinhole, the confocal depths obtained experimentally and calculated from equation (3.6) result in 1.74 and 1.60 μm, respectively. Well-designed and properly aligned confocal Raman microscopes ensure that the confocal depths differ from the calculated D_{PSF} by no more than 30%.

The results of the Raman optical sectioning of the graphene layer buried inside the glass demonstrate that this test structure can be used to predict confocal depths achievable under practical conditions. As the refractive index of glass is close to the refractive indices of the majority of polymers, the confocal depth and axial compression factors derived from the analysis of this structure may help to more accurately retrieve the Raman images obtained from within multi-layered and composite polymers. These results also suggest that test structures fabricated with CNT and a layer of graphene

can be used for a comprehensive examination of the confocal capabilities of high-end Raman microscopes and to perform a comparison of these instruments.

The sensitivity of Raman microscopes is usually tested using a piece of crystalline (c-Si) silicon. The c-Si is a strong Raman scatter so that its vibrational overtones, more correctly called the transverse optical (TO) modes of different orders, can be observed in the Raman spectra. However, the so-called fourth-order TO mode, which appears at about 1950 cm^{-1} (indeed, the first-order mode located at 520 cm^{-1} is multiplied by 4, and the resulting Raman shift slightly decreases due to the anharmonicity coefficient mentioned in Chapter One), has a very weak Raman band. For this reason, the ability of a Raman microscope of a given configuration to detect the 4^{th}-order TO mode of c-Si demonstrates the sensitivity of the instrument. It is considered to be a proper test to compare instruments with each other. Typically, manufacturers of Raman microscopes quote spectral data obtained on instruments configured to provide maximum absolute sensitivity, that is, using excitation wavelengths that correspond to the regions of the detectors' maximum sensitivity.

As an example, a Raman band of 4^{th}-order TO mode of c-Si wafer measured on a Raman microscope equipped with a 532 nm laser for excitation, a FI CCD and a 100×/0.9 metallurgical objective is shown in Figure 3-17(a). In the confocal setting with a pinhole aperture, the instrument demonstrates high enough sensitivity as the 4^{th}-order band is detected within 1 min. of integration time and 10 mW of laser power at the sample. Obviously, a longer integration time noticeably improves S/N in the Raman spectrum so that the peak of gaseous N_2 in the ambient atmosphere can be observed at 2329 cm^{-1}. If the instrument operates in the non-confocal mode (the aperture

is a slit instead of a pinhole), the intensity of the N_2 peak significantly increases relative to the height of the Raman band of the 4th-order mode of c-Si, and the peak of O_2 at 1556 cm^{-1} can also be well observed.

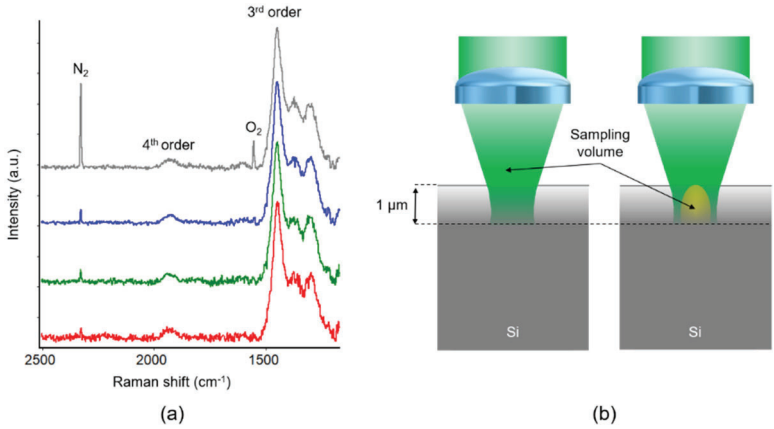

Figure 3-17. The measurements of the 4th-order TO mode of c-Si. (a) The Raman spectra obtained in a confocal setting for 1 min. (red), 5 min. (green), 15 min. (blue), and the Raman spectrum measured in a non-confocal setting for 15 min. (grey). The spectra are baseline-corrected and offset for clarity. (b) The sampling volume from which the Raman scattering is collected is indicated by the yellow spheroid in the confocal and by the green hourglass shape in the non-confocal setting.

Indeed, as illustrated in Figure 3-17(b), in the confocal setting, the sampling volume element is represented by a spheroid plunged into the c-Si wafer. In a non-confocal setting, the Raman scattering is collected from within the volume of the focused laser beam, which has the shape of an hourglass, as discussed in paragraph 3.1.1 above. Since the depth of penetration of the 532 nm wavelength into c-Si is about 1 µm, it limits the amount of c-Si material from which the Raman scattering is collected to a very shallow depth. Thus, the amount of c-Si in the sampling volume does not differ much

between the confocal and non-confocal settings. At the same time, in a non-confocal setting, the scattering from the atmospheric N_2 and O_2 molecules contained in an hourglass shape above the surface of the c-Si wafer makes the corresponding Raman peaks more intense than the 4^{th}-order TO band of c-Si.

The results of these measurements may also be used to check the extent of a Raman microscope's confocality. In the Raman spectrum obtained on a microscope with high confocality, the N_2 peak should be about the same height as the 4^{th}-order band of c-Si. The increase of the relative intensity of the N_2 peak may evidence of the instrument's insufficient confocality or its poor alignment.

3.4. Confocal Raman measurements of samples with irregular surfaces

As follows from the above considerations and Figure 3-17, it is essential to focus well on the sample surface if confocal measurements are to be taken. Often, the sample's surface requires special preparation, such as fine cutting, pressing or polishing to make it flat and suitable for mapping an XY area or a line along the surface in the confocal mode. The preparation, if possible, needs to be done with caution as it can, to some extent, modify the surface of the sample and, respectively, may lead to the appearance of spectral artefacts. Appropriate levelling of the sample is also required to keep its surface horizontal within the area that needs to be mapped. However, many samples have complex surface topography and must remain intact or cannot be flattened. Such samples are natural stones and minerals, medicinal tablets and capsules, semiconductor devices or those composed of powders or microparticles of different sizes, just to name a few. If the

sample tilt or its surface roughness exceeds the confocal depth required for the measurements, then at least part of the sample may go entirely out of focus, and no meaningful spectral data will be obtained from this part. As a result, the obtained spectral data may appear insufficient or not representative of the sample.

In order to adjust the position of the laser focus to the complex surface topography, various methods and technologies are used. They can be divided into two major categories: single-pass and two-pass techniques.

In the single-pass techniques, the surface of the sample is kept in focus during the map acquisition with the use of a compensation mechanism based on closed-loop feedback. In a mode often referred to as Raman autofocus, the sampling stage moves up and down along the Z direction in small increments at each predetermined point on the surface to maximize the detected Raman signal. It is assumed that the maximum signal is achieved when the sample is correctly positioned in focus, and the corresponding Raman spectrum is then measured. Obviously, this mode of operation is very slow and suitable for relatively small mapping areas or large sampling steps. In faster single-pass techniques, the surface irregularities are measured based on the principles of optical profilometry, such as white light interferometry and optical triangulation. These methods require the installation of additional light sources, sensors and other optical components in the microscope. Nevertheless, these technologies make it possible to track changes in the profile of the sample in the range from hundreds of nanometers to few millimetres, thereby maintaining the surface in focus in real time when acquiring Raman maps.

In the two-pass techniques, the topography of the surface is first recorded. It may be performed using the so-called visual autofocus by increasing contrast within the field of view (frame) of the microscope. The position of the sample in focus can be adjusted until the maximal contrast in the optical image is achieved. Then, a Raman map is acquired from the sample maintained in this position. If the area of the sample that needs to be mapped exceeds the size of the single frame, then the sample is scanned horizontally and sequentially at different Z positions. The multiple frames at different focal planes are stitched together to montage a multi-focus optical image of the sample. The individual frames with maximal contrast are then extracted to synthesize the topographical image in which the sample surface appears in the best focus, and the Z positions of the well-focused frames are recorded. In the second step, the Raman spectra are measured at the predefined positions of the mapping grid while the Z position of the best-focused frames is retrieved from the recorded surface topography, and the vertical position of the stage is dynamically adjusted to that Z during the measurements. The two-pass techniques are more time consuming than single-pass ones. The two-pass methods are usually not suitable for a sample whose surface topography changes, for example, as a result of drying or thermal expansion or contraction during the map acquisition.

Figure 3-18 shows an example of the confocal analysis of API distribution in an uncoated medicinal tablet with an identification mark that has been embossed on its surface. When mapping the tablet at a fixed Z position, the API distribution is adequately tracked in that part of the tablet that is well in focus. In the area of embossing, the depth of which significantly exceeds the depth of focus of a given objective, the surface goes out of focus. Accordingly, the loss of confocality results in the deterioration of the quality

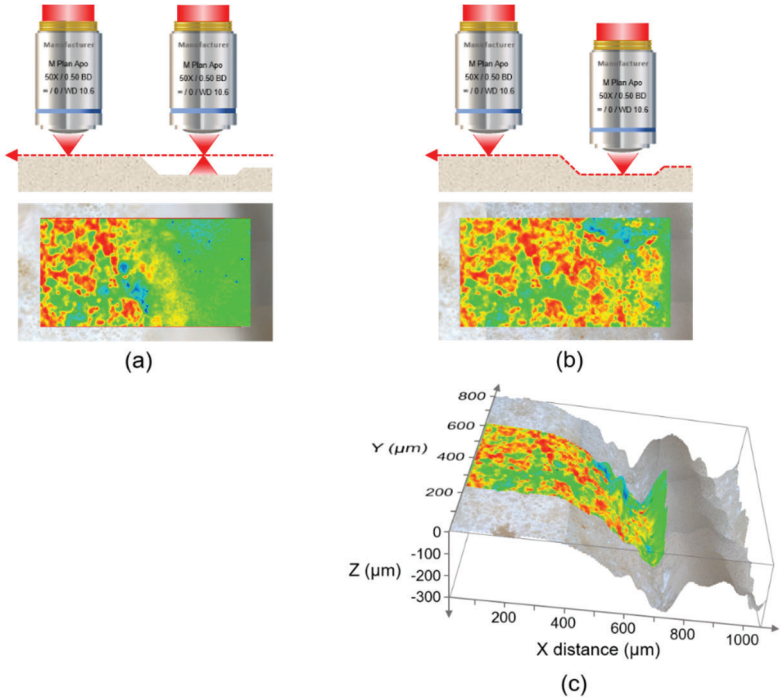

Figure 3-18. Mapping a part of a medicinal tablet with an uneven surface: (a) scanning the tablet at a fixed Z-position of the stage; (b) scanning in Z positions dynamically adjusted to the surface profile of the tablet; (c) the recorded topography of the tablet surface. The maps were acquired using a 50×/0.50 metallurgical objective and a 785 nm laser. The Raman images were generated as a correlation with an API's reference spectrum and superimposed on the corresponding optical images. The Raman image generated from the map obtained when the stage Z position matched the surface topography demonstrates that the API highlighted in red is distributed over the entire mapped area. In contrast, in the Raman image generated from the map obtained at a fixed Z position, the API is not recognized in the out-of-focus area.

of the measured spectra, so that the API cannot be distinguished from excipients (a). Raman mapping, performed by dynamically changing the Z position of the sample stage to adjust focus to the tablet surface profile, provides confocal measurements on the uneven surface and, accordingly, adequate API tracking throughout the analyzed area, as illustrated in (b) and (c).

It worth mentioning that, if a sample does not manifest optical disparities and, thus, produces a low-contrast image in brightfield illumination, then the optical autofocus technique may not correctly work unless special methods that generate the contrast are employed. The methods of optical contrast enhancement that are most often used in Raman microscopy include darkfield illumination, polarized illumination light and differential interference contrast (DIC). If a sample is too dark, i.e., it strongly absorbs the visible light, it is difficult to measure its topography using light interferometry techniques accurately. Therefore, the right choice of technique for mapping rough or irregular surfaces depends on the sample's optical properties. The line scanning mode with a cylindrical lens mentioned above cannot be effectively used with either of these techniques as only part of the line is guaranteed to be maintained in focus on the irregular surface.

3.5. Raman measurements beyond the diffraction limit of light

As shown above, a well-designed and properly aligned confocal microscope can discriminate objects on a submicron scale that is confined only by the diffraction limit of light. However, in the rapidly advancing field of engineered nanomaterials, such as CNT, carbon nanofibers, graphene,

quantum dots, nanodiamonds, ultra-thin films and a diversity of other nanostructures, a resolution beyond the diffraction limit is desirable.

The development and understanding of nano-engineered materials have been positively impacted by a variety of techniques which includes scanning electron microscopy (SEM), transmission electron microscopy (TEM), scanning tunneling microscopy (STM), X-ray photoelectron spectroscopy (XPS), scanning near-field optical microscopy (SNOM) and atomic force microscopy (AFM). SNOM and AFM, which do not provide direct information about the chemical nature of a material, have recently been coupled with confocal Raman microscopy. The basic idea of coupling both the SNOM and AFM with Raman microscopy is to confine the focussed laser spot to nanometric dimensions to overcome the diffraction limit of light and, thus, combine the higher spatial resolution with detailed chemical information.

The scanning near-field optical microscope was invented by Dieter Pohl (IBM Laboratory, Zurich, Switzerland) in 1982. The principle of operation of this instrument is based on the phenomenon of light passing through an aperture of a subwavelength size, which is often realized in the form of a hollow tip with an internal diameter <100 nm. The so-called near-field region is located directly behind the aperture within a distance much less than the wavelength of the light. In this region, the electromagnetic field is in the form of a localized evanescent (not propagating) wave. In 1995, Catherine Jahncke, Michael Paesler and Hans Hallen first combined Raman microscopy with SNOM (Jahncke, Paesler and Hallen 1995). In a Raman microscope equipped with a subwavelength SNOM aperture tip, the laser light is focused through the aperture, and the sample is placed in the near-field region, as illustrated in Figure 3-19(a). The near-field Raman image is

formed by scanning the sample beneath the SNOM aperture tip and recording the intensity of Raman scattering as a function of the tip position. During the scan, it is necessary to keep the tip in the immediate vicinity (<10 nm) of the sample surface. The probe tip movement is monitored and controlled by a feedback system and usually a piezoelectric XYZ scanner to keep the tip within the near field. The topographic and Raman images providing high spatial resolution can be generated simultaneously. The lateral resolution achievable in a Raman-SNOM instrument, which is determined by the diameter of the aperture and the distance between the probe tip and the sample, can be ~ 50 nm.

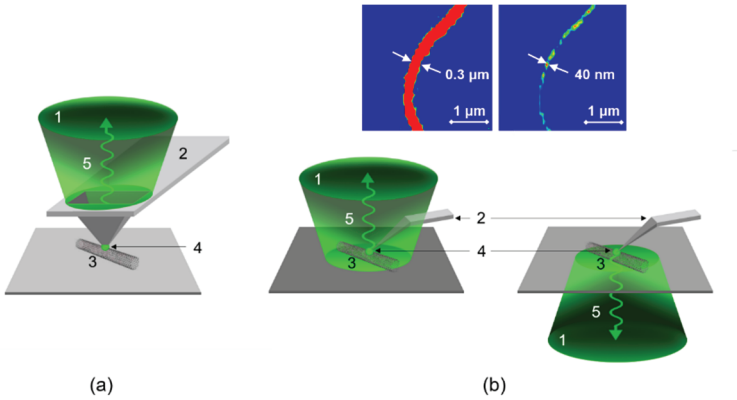

Figure 3-19. Schematic diagram of Raman-SNOM (a) and Raman-TERS (b) coupling: 1 – focused laser beam (green truncated cone), 2 – cantilever, 3 – sample (SWCNT), 4 – hot spot, 5 – the light scattered from the hot spot (squiggly arrow). The Raman-TERS is shown in the two most commonly used configurations: top (left) and bottom (right) illumination setups. The colour insets show the conventional Raman (left) and TERS (right) images of an SWCNT generated as the peak intensity of the G band at about 1600 cm^{-1}. The lateral spatial discrimination improves from ~ 0.3 μm in the conventional confocal Raman image to ~ 40 nm in the image obtained using TERS.

Obviously, the optical throughput of the Raman-SNOM setup is limited by the very small aperture. Furthermore, compensating such a low throughput by increasing the power of the excitation light above approximately 10 mW can destroy the tip, which is usually made of SiO_2 coated with aluminium. In practice, the intensity of the Raman signal is typically reduced by five orders of magnitude in comparison with that achieved in confocal Raman microscopy without SNOM, which severely limits the S/N ratio in the spectra obtained in Raman-SNOM experiments. Therefore, materials with high Raman cross-section are only suitable for analysis with Raman-SNOM. The reviews of the key technical issues of Raman-SNOM can be found elsewhere (Zhang, Zheyu Fang and Zhu 2017, Hallen and Jahncke 2003).

The atomic force microscope was invented by Gerd Binnig, Calvin Quate and Christopher Herber in 1986. The AFM working principle is the measurement of the interactive forces between the sample surface and a sharp tip at the end of an elastic cantilever. The force applied to the tip by the surface results in the bending of the cantilever. It is possible to characterize the sample's topographical, mechanical and electromagnetic properties by measuring its cantilever deflection. The combination of AFM with Raman microscopy enables these properties to correlate with the chemical information about the sample. However, the combined measurement, commonly referred to as co-localized Raman-AFM, suffers from the same limitations that apply to conventional confocal Raman microscopy, that is, intrinsically weak Raman signal and diffraction-limited spatial resolution.

In order to perform measurements with a spatial resolution beyond the diffraction limit, tip-enhanced Raman spectroscopy (TERS) is employed. In

2000, Mark Anderson (Anderson 2000) and Raoul Stockle (Stockle, et al. 2000) were the first to use a metalized tip to produce Raman spectra and images. TERS is based on the amplification of the Raman signal in accordance with the principle of surface-enhanced Raman scattering (SERS). The illumination of noble metal nanostructures with laser light causes collective electron oscillations on the metal surface, known as localized surface plasmon resonance. This resonance induces intense local electromagnetic fields, resulting in a dramatic enhancement of the Raman signals emanating from the molecules located in close proximity to the metal nanostructures. While the focused laser beam illuminates the AFM tip, the amplification only occurs from the so-called hot spot near the sharp tip inside the diffraction-limited laser spot, as shown in Figure 3-19(b). The size of the hot spot constitutes several tens of nanometers and is mostly determined by the diameter of the tip apex. Thus, the spatial resolution is limited by the confinement of the electromagnetic field rather than the excitation light wavelength. The colour insets in Fig.3-19(b) show the conventional Raman (left) and TERS (right) images of a single CNT on Si substrate obtained using 532 nm excitation and generated as the peak intensity of the G band at about 1600 cm^{-1}. The CNT widths were estimated to be about 0.3 μm and 40 nm in Raman and TERS images, respectively. While the wavelength of light limits the lateral resolution in the conventional confocal Raman image, TERS can provide about an order of magnitude better spatial resolution.

The tip coated with SERS active metal (typically Au, Ag or sometimes Pt) and aligned with the focused laser beam is used as a Raman signal enhancer while scanning over the sample surface. Similar to Raman-SNOM, TERS employs an accurate closed-loop positioning system provided by the

piezoelectric XYZ scanner in AFM. In contrast to Raman-SNOM, due to the Raman signal amplification, the sensitivity of TERS is highly increased, which makes this technique suitable for the spectroscopic characterization of a variety of materials and biological systems in diverse environments, such as ultrahigh vacuum, electrochemical surroundings and liquids. Single-molecule imaging with TERS has been reported (Zrimsek, et al. 2017).

The main problem of the practical use of TERS remains steadiness in the face of external vibrations when scanning a sample and the reliability of the tip itself. The questions about reproducibility and standardization of TERS measurements are also still important.

Since the first reports issued in 2000, a vast amount of literature has been dedicated to the technical and practical aspects of TERS. Because the scope of this book is not intended for a detailed overview of TERS, the interested reader is referred to a few recent surveys of TERS (Langer, et al. 2020, Verma 2017, Jiang, et al. 2016, Kumar, et al. 2015, Kurouski 2018), as well as the theory and practice of SERS (Haynes, McFarland and Van Duyne 2005, Pilot, et al. 2019, Pérez-Jiménez, et al. 2020, Ou, et al. 2011).

3.6. Designers and producers of Raman microscopes

This paragraph contains a list of companies designing and producing Raman microscopes for scientific research and analytical applications. Even though there are a number of manufacturers of Raman microscopes with long-standing reputations, the popularity of these instruments and the power of the analytical capabilities they provide encourage new companies to offer their designs and solutions. All these companies are listed in alphabetic order. The links to the companies' web pages contain information about

Raman instruments and the technologies they offer. A brief description of the Raman microscopes produced by these companies and their main characteristics and specific features are given below.

3.6.1. Bruker

Bruker Corporation develops and delivers high-performance scientific, analytical and process analysis instruments and solutions for a wide range of applications. Bruker is one of the world's leaders in the instrumentation and technologies for molecular spectroscopy designed, manufactured and developed in Germany.

Bruker supports the SENTERRA platform inherited from the Chromex model since Bruker Optics acquired the Chromex spectroscopy business from the Japanese optical company Hoya in 2004. Bruker offers a SENTERRA II (Bruker Raman Microscopes SENTERRA II n.d.), a confocal Raman microscope that provides mapping and fast imaging functionality. The SENTERRA II is based on the Olympus BX series optical microscope with all the necessary tools for sample visualization and contrast enhancements, such as Koehler brightfield illumination, polarized light, DIC, darkfield and fluorescence illumination. In the instrument, the spectrograph and lasers are mounted on top of the Olympus BX microscope frame allowing optical and Raman microscopy capabilities within a compact design. The microscope is placed on a heavy base plate for guaranteed support and stability. In the standard configuration, the instrument is equipped with 532 and 785 nm lasers. There are optional 514 and 633 nm excitation wavelengths. The instrument covers the full Raman spectrum in a single scan with 4 cm^{-1} spectral resolution. Diffraction gratings providing a higher resolution are available as an option.

The SENTERRA II features the patented SureCal™ continuous wavelength calibration method that conducts the calibration automatically with better than 0.2 cm^{-1} accuracy. This method eliminates regular calibrations with external standards. As previously mentioned in this chapter, SureCal™ utilizes the reference emission from a Ne lamp that impinges onto the detector along with collected Raman scattering to provide accurate and reproducible positions for the Raman bands in the measured spectrum.

A patented automatic fluorescence rejection method based on the shifted-excitation Raman difference spectroscopy (SERDS) principle is used for rejecting fluorescence from many samples. In this method, the excitation laser (typically, a diode laser emitting at 785 nm) is operated at two different temperatures controlled by electrical current. The different operational temperatures result in small change in the excitation wavelength, and two spectra slightly offset in the Raman shift scale are recorded. These two spectra are then subtracted from one another to generate the differential spectrum, in which the broad fluorescence is deducted (somehow similar to the action of a first derivative). The differential spectrum is then integrated, thereby yielding the desired Raman spectrum without the fluorescence. For ultimate fluorescence suppression, the SENTERRA II can be combined with an FT-Raman module in the RamanScope III system, which provides NIR excitation with a wavelength of 1064 nm.

The SENTERRA II may be configured as an upright or inverted Raman microscope. The inverted configuration of the optical microscope provides convenient access from the top required for many biological applications.

For larger objects, which exceed the dimensions of the sample stage, the SENTERRA II can be placed on a heavy-duty motorized Z-support that lifts

the instrument. This configuration is typically used in arts and archaeology for the Raman analysis of paintings and statues, as well as ancient manuscripts and documents.

An integrated design of the Bruker's benchtop AFM and the SENTERRA II confocal Raman microscope is available.

All measurement parameters and essential functions of the SENTERRA II instrument are controlled by OPUS software. The SENTERRA Raman wizard guides the user step-by-step through the measurement procedure to Raman mapping, depth profiling and 3D image generation.

3.6.2. CRAIC Technologies

CRAIC Technologies is an American manufacture of UV, visible and NIR spectrophotometers for scientific and industrial applications.

CRAIC offers an Apollo II Raman microspectrometer (Apollo Raman Microspectrometer n.d.), which features a modular and flexible design. The instrument is based on a solid-state Lightblades™ Raman spectrometer that can be mounted on top of an optical microscope. Up to three lasers may be incorporated into the system. The offered excitation wavelength include 405, 532, 638, 785 and 830 nm. The instrument can be supplied with hardware and software for automated spectral analysis and 3D Raman imaging.

The Apollo II Raman microspectrometer is a Class IIIB laser system. It is intended for general purpose laboratories performing routine research, quality control and failure analysis. The Apollo II can be combined with other CRAIC microspectrometers to deliver analytical capabilities ranging

from UV-visible-NIR microspectroscopy to film thickness measurements and more.

3.6.3. Edinburgh Instruments

Edinburgh Instruments Ltd. is a UK-based company, who has been designing and manufacturing spectroscopic instrumentation for almost fifty years.

In 2019, the company diversified its portfolio by introducing a compact and highly automated RM5 Raman microscope for analytical and research purposes (Edinburgh Instruments - Raman microscopes n.d.). The RM5 is based on the Olympus BX53 optical microscopes with corresponding sample visualization and contrast-enhancing techniques, including brightfield, darkfield, polarized light, DIC and fluorescence illumination. The instrument incorporates a 225 mm focal length asymmetric Czerny-Turner spectrometer with a 5-position grating turret providing the spectral resolution of 1.4 cm^{-1} and the spectral coverage from 50 to up to 4000 cm^{-1}. The spectrometer has two ports that can accommodate CCD, EMCCD and InGaAs detectors. The RM5 Raman microscope can be integrated with up to three computer-controlled lasers, typically 532, 785 and 1064 nm. The confocality of the Raman microscope is ensured by an adjustable pinhole. The instrument allows simultaneous observation of the sample and laser focus. The RM5 can be configured with a manual or motorized XYZ sample stage. The RM5 enables an automated alignment and calibration procedure with integrated Raman standards.

In 2020, the company designed a research-grade confocal Raman microscope RMS1000 with an open architecture. The instrument can be equipped with up to 5 internal computer-controlled lasers, such as 325, 532,

638, 785 and 1064 nm. It has two spectrograph options (standard compact spectrograph and a long focal length one for high resolution, sensitivity and stray light rejection). The RMS1000 can be configured with five-position grating turret and up to 4 detectors, including CCD, EMCCD and InGaAs. The versatile capabilities of the instrument extend its applications to time-resolved fluorescence microscopy and fluorescence lifetime imaging.

The Ramacle™ software package is used for complete instrument control, automated acquisition of Raman maps and spectral data handling.

3.6.4. Horiba Scientific

Horiba Scientific is a division of Horiba Ltd, a Japanese manufacturer of precision instruments for measurements and material analysis. Horiba Scientific (Horiba Scientific n.d.) is the recognized leader in Raman spectroscopy, with a long history of innovations in this field. The company pioneered the confocal Raman microscope and designed and manufactured these instruments for over four decades.

The current line of Raman microscopes contains LabRAM and XploRA models. The LabRAM Soleil is a highly automated system that can be easily adapted for the most challenging applications in both academic and industrial laboratories. The system can be configured with up to four internal and two external lasers for excitation from UV to NIR (the typically offered lasers are 325, 405, 473, 532, 638 and 785 nm). In a basic configuration, it provides a low-frequency cut-off at 30 cm^{-1} of the Raman shift. The excitation wavelength with the corresponding Rayleigh filters and diffraction gratings are selected through software. The instrument offers auto-alignment procedure, ultra-fast QScan™ mapping capabilities for 3D Raman imaging and 2D topography. The patented QScan™ confocal

imaging mode allows one to scan a focused laser beam over a multi-layered sample without moving the sample and measure Raman spectra while directly observing the sample in the video image. The LabRAM Soleil can be coupled with TERS and SEM.

The LabRAM HR Evolution is a confocal Raman microscope providing high spatial and spectral resolutions. The system can be mounted with up to three internal lasers and up to three detectors enabling spectral measurements in the wavelength range from deep-UV to SWIR. The instrument allows for access to low frequencies down to 5 cm^{-1} using the VBG filters. The LabRAM HR Evolution includes advanced SWIFT™ and DuoScan™ fast Raman imaging technologies. SWIFT ™ allows continuous movement of sample stages and Raman spectra measurement through high-speed coordination between the stage and the EMCCD detector. In DuoScan™ mode, two orthogonally rotating mirrors driven by piezoelectric scanners raster the laser beam within the field of view of a given microscope objective. The raster pattern is defined and adjusted by the user. DuoScan™ allows for quick integration of the Raman signal over the scanned area to provide a spectrum equivalent to all spectra of the same area measured in a point-by-point mode of operation and then averaged. As a result, DuoScan™ ensures maps are acquired for a time that is several orders of magnitude faster than in the point-by-point mode, albeit the loss of lateral resolution. The LabRAM HR Evolution is compatible with AFM and TERS. The instrument can be equipped with a transmission Raman accessory for bulk analysis of semi-opaque and turbid materials. This accessory is often used for the quantitative analysis of pharmaceutical tablets. CaptuR, a laser trapping solution based on the laser tweezers principle, is available for fine control of the particle's position during the spectral measurements.

The XploRA and XploRA Plus are confocal Raman microscopes intended for multi-user facilities. The standard configuration of the instrument includes up to three lasers with the 532, 638 and 785 nm excitation wavelengths. The XploRA can be configured as an entry-level Raman microscope with a manual stage, while the XploRA Plus offers the option of fast mapping with SWIFT™ and EMCCD detectors, Raman polarization and upgradability to AFM.

All of the instruments have 8 levels of attenuating laser power control from 0.01 to 100%. The instruments are operated by a modular and easy configurable LabSpec 6 software. The software provides advanced multivariate analysis of spectral data and the particle finder capability to automatically find, locate, measure and classify particles by morphology and chemical composition.

3.6.5. JASCO

The Japan Spectroscopic Company (JASCO) was founded in 1958 to provide the scientific community with optical spectroscopy products. Over many years, JASCO's spectroscopy product line has expanded to incorporate virtually every type of optical spectroscopy, including Raman microscopes.

JASCO offers the NRS series of confocal Raman imaging microscopes (JASCO n.d.), which consists of three models: NRS-4500, NRS-5000 and NRS-7000.

The NRS-4500 is an entry-level confocal Raman microscope incorporating an aberration-corrected Czerny-Turner monochromator with a 200 mm focal distance and a single detector. The instrument offers several standard

configurations with a single 633 nm laser or a 532/785 nm laser combination and the option for a third laser that can be mounted internally or externally. The instrument can be used with either a manual or a motorized XYZ mapping stage.

The NRS-5000 and NRS-7000 are research-grade confocal Raman microscopes with 300 and 500 mm spectrographs, respectively, which provide a high spectral resolution. The instruments can accommodate two detectors and up to six laser sources from deep-UV to NIR: 244, 266, 325, 355, 442, 488, 514, 532, 633, 660, 785 and 1064 nm. For the blue and green excitation wavelength, the measurable spectral range can cover the Raman shift from 50 to 8000 cm^{-1}. Available detectors include CCD, EMCCD and InGaAs array (in combination with 1064 nm laser). The instruments feature Dual Spatial Filtration (DSF) technology which optimizes confocal focusing, reduces the effects of fluorescence and improves spatial resolution, especially in the axial direction. The patented Spatial Resolution Image (SRI™) function allows for simultaneous observation of the sample, the laser spot (including the one produced by a 1064 nm laser) and the aperture image. The optical alignment and the Raman shift axis calibration using an internal Ne lamp are performed in a software-controlled mode. The options and accessories include measurements of low wavenumber down to 10 cm^{-1}, the units for obtaining Raman spectra in transmission mode, and measurement of large liquid and solid samples.

The Spectra Manager™ software suite offers measurement control and confocal multi-area mapping with real-time display of spectrum, current measurement point, sample identification, Raman image analysis and autofocus based on both optical contrast and Raman signal optimization. The Surface Scan Imaging (SSI) procedure assesses the surface shape of the

sample prior to spectral measurement. Then, the Raman spectra are measured at the axial positions adjusted in accordance with the surface shape. Using SSI, it is possible to measure a sample with an uneven surface and obtain Raman spectra with adequate S/N ratio at all data points. The proprietary Sample Search function analyzes the optical image of the sample and automatically selects measurement positions based on the size, contrast and colour of the microscopic objects specified by the user.

All the NRS models include a Class 1 laser safety sample chamber with a laser interlock. A rigid honeycomb optical base is the foundation of the instruments ensuring high vibration resistance. The instruments are compact enough to fit on a laboratory bench.

3.6.6. Nanophoton

Nanophoton Corp. is a Japanese producer of innovative Raman microscopes, which was established in 2003. Nanophoton Corp. offers several models of confocal Raman microscopes and specialized systems (Nanophoton n.d.).

The RAMANwalk is a compact Raman microscope that can be equipped with one or two lasers (the offered excitation wavelengths are 488, 532, 671 and 785 nm), a manual or motorized XY stage and an additional ability to scan a sample by the laser beam. The instrument enables a random point-scanning mode by moving the laser beam along the most appropriate paths, which have been predetermined with the sample observation method based on the theory of stochastic processes. Using “ingenious” scanning, the RAMANwalk allows the acquisition of Raman maps to be performed faster than in the conventional point-by-point mode.

The confocal Raman microscope RAMANtouch/RAMANforce is equipped with a spectrograph that has a 550 mm focal length and a 3-position grating turret. The instrument can be configured with multiple lasers emitting in UV and visible spectral ranges: 325, 355, 405, 457, 488, 532, 633, 671 and 785 nm. In addition to the point illumination mode and the galvanometer scanner, the instrument offers a dedicated line illumination of the sample. The patented method of line illumination enables simultaneous recording of 400 Raman spectra that significantly increases the speed of Raman map acquisition. The RAMANtouch/RAMANforce provides a ZTrack measurement function that tracks irregularities of a sample surface from its video image and collects a Raman map of the uneven surface. The video image of the sample is also used to detect particles, followed by the measurement of Raman spectra of these particles automatically and with quick autofocus. The instrument can be configured as an upright or inverted microscope.

The RAMANtouch vioLa modification is a dedicated Raman microscope for use in the UV region. The instrument features a Schwarzschild reflective (mirror-based) objective that provides both a high NA and high optical throughput in a wide wavelength range, including deep UV. High-speed mapping can be performed using lasers emitting in the wavelength range from deep-UV to visible: 257, 266, 325, 355, 405, 457, 488 and 532 nm.

The RAMANdrive is a specialized Raman microscope for Si wafer analysis equipped with a 300 mm stage to accommodate whole wafers.

The RAMANview is a fast screening Raman system that expands the field of view and extends the depth of focus to observe and analyze large samples with sloped and curved surfaces without moving them. The instrument is

equipped with a 350 mm spectrograph and 532 and 671 nm lasers. It ensures a safe distance between microscope objectives and samples; it also allows measurements to be made in deep containers, vessels and reaction chambers.

Nanophoton offers a TERS-ready Raman microscope, TERSsense, with a spatial resolution beyond the diffraction limit of light.

3.6.7. Renishaw

Renishaw Plc is a British engineering company specialising in the precision measurement industry for over 40 years. The company (Renishaw n.d.) is one of the world leaders in Raman spectroscopy that offers high-performance Raman microscopes for a broad range of applications.

Since the introduction of the RM Raman microscope in 1992, Renishaw has designed, developed and refined a research-grade inVia confocal Raman microscope for more than two decades. The inVia Raman system incorporates a Leica light microscope. The system supports a multiple optical path design that enables UV lasers to be used along with any visible or NIR lasers. The system can be configured with one or two detectors and three or more laser sources ranging from deep-UV (229 nm) to NIR (1064 nm), which are kinematically mounted on an integral baseplate to ensure high mechanical stability of the system. The excitation wavelength options also include 244, 325, 442, 457, 488, 514, 532, 633, 785 and 830 nm. The laser attenuation to 16 different power levels from 0.00005 to 100% is controlled through software. The instrument allows simultaneous laser and white light sample illumination with the observation of the location of the focused laser spot on a sample using an internal video camera. The near-

excitation tunable filter (NExT) option provides access to wavenumbers as low as about 10 cm^{-1}. Currently, the inVia is available in four models.

The inVia Basis represents an entry-level confocal Raman microscope with semi-automatic changing of lasers and optical components. Although the laser and spectrograph alignment is completed in an automated mode, the instrument calibration is performed using manual control. The inVia Basis can be upgraded to a highly automated inVia Reflex Raman microscope.

The inVia Reflex enables software-controlled switching between lasers and optimization of their optical alignment. It contains internal standards (Si, Ne and white light sources) for the automated alignment, calibration and performance monitoring.

The flagship inVia Qontor confocal Raman microscope is a flexible research-grade instrument with the capability to track the position of the laser focus on irregular sample surfaces in real time. The focus tracking technology, LiveTrack™, works in both white-light video viewing and Raman acquisition modes, offering the advantage of the single-pass mode that does not require a pre-scan of the sample. To rapidly survey large areas of a sample, TrueImaging™ option is available in the instrument. In this mode of operation, the laser light illuminates a circular area of the sample and a tunable filter is used to transmit light from a selected Raman or photoluminescence band directly onto the detector in a single step. The high speed of this mode makes it particularly suited for rapid surveying large areas in applications such as contaminant detection. The ultra-fast Raman imaging is realized using StreamLine™ technology, which combines illumination of a line on the sample with a continuous sample stage motion.

The advanced Raman imaging technologies are implemented with a proprietary Centrus detector. The matrix of the detector is easily reconfigured to support the imaging modes with circular, line and point focus illumination. The Centrus detector has a high quantum efficiency across a broad range of wavelengths from 229 to 830 nm. The detector supports SynchroScan™ technology that enables collecting a full Raman or broad photoluminescence spectrum with high spectral resolution in a single measurement.

The inVia InSpect model is a dedicated Raman microscope optimized for trace analysis and intended for use in forensic laboratories. The instrument is configured with 532 and 785 nm lasers; it uses image recognition algorithms and measurement control for particle analysis.

Renishaw offers the RA802 Pharmaceutical Analyzer and the RA816 Biological Analyzer—compact benchtop Raman imaging systems designed for the pharmaceutical industry and biological or clinical research, respectively. Both the analyzers combine LiveTrack™ and StreamLine™ technologies to generate Raman images of uneven or curved surfaces of tablets, capsules, granules, powders and biological tissues. These instruments can analyze various samples without the need for user intervention.

Renishaw's Windows-based Raman Environment WiRE™ software provides a communication interface between the user and the Raman instrument. It controls the acquisition of Raman data and offers dedicated data processing and analysis options, including 3D Raman image rendering.

The InVia Raman microscopes can be coupled with AFM and SEM systems available from different vendors.

It worth mentioning a specific feature of Renishaw's confocal microscopes––the proprietary EasyConfocal™ method. It uses a combination of two apertures—one physical (the spectrograph entrance slit) and one virtual (the central segment of the CCD matrix) to spatially filter Raman scattering collected from the sample and provide the required depth resolution. Also, in all inVia instruments, the spectrophotometer is mounted vertically enabling quick access to its optical components through an easy opening lid. However, this arrangement requires reliable securing of the optical components and their steadiness.

3.6.8. SOL Instruments

SOL Instruments Ltd. is a Belarusian manufacturer of lasers and technologically advanced instruments for spectroscopy, microscopy and elemental analysis with over two decades of history of innovations. SOL Instruments (SOL Instruments n.d.) offers Confotec series of confocal Raman microscopes.

The Confotec MR200 is a compact entry-level confocal Raman microscope equipped with a single CCD detector and one to three lasers.

The Confotec MR350, Confotec MR520 and Confotec MR750 confocal Raman microscopes are designed for measurements with high spatial and spectral resolutions. The instruments are equipped with an aberration-corrected Czerny-Turner spectrograph with a focal length of 350, 520 or 750 mm corresponding to the model number and automated 4-position grating turret. The instruments can be configured with two lasers: a built-in laser (473 or 532 nm) and an external one (633 or 785 nm). The instruments offer 2D and 3D Raman spectral imaging using XY galvanometric scanner combined with a piezo-driven focus positioner that moves the microscope

objective in the Z direction. The microscopes are equipped with a laser beam expander module to form the desired shape of the beam on the sample. The microscopes feature high-speed ultra-wide panoramic spectral imaging (Raman and Rayleigh scattering) with a high spatial resolution achievable using a combination of XY galvanometric scanner with the motorized microscope stage and a PMT detector. The instruments have a compact rigid design and enable automated spectral calibration**.**

All the Confotec MR Raman systems are based on the research-grade upright Nikon Eclipse Ni-U microscope with the standard tools and modules for transmission illumination, polarization, phase contrast, DIC and epi-fluorescence.

The Confotec NR500 is a high-precision, highly automated 3D laser scanning confocal Raman microscope with a 520 mm spectrometer and two detectors. The spectrograph is mounted in a vertical position with a modular rigid rod design for long-term temperature stability. The microscope can be used with five simultaneously installed lasers, and the excitation wavelength can be selected by switching the optical components within the instrument. Typically offered are 325 nm He-Cd, 473 nm DPPS, 532 nm DPSS, 633 nm He-Ne and 785 nm DPSS lasers. The Raman microscope features multifunctional analytical capabilities that include 3D confocal Raman imaging, photoluminescence, Raman transmission and 3D high-contrast measurements in reflected light. The optimal extent of confocality is achieved with the use of a continuously variable pinhole. The Confotec NR500 can be configured with an upright Nikon Eclipse Ni-U or inverted Nikon Eclipse Ti2 optical microscope.

To the best of the author's knowledge, the Confotec CARS is the only commercially available multichannel 3D scanning coherent anti-Stokes Raman scattering (CARS) microscope designed and provided by SOL Instruments. Although CARS technology is outside the scope of this book, it should be noted that one of the main advantages of CARS is that this method generates a more intense signal than spontaneous Raman scattering. In addition, the anti-Stokes signal is recorded in the spectral region free from the autofluorescence occurring in the Stokes region. As a result, due to its high-speed scanning and high sensitivity, the system allows noninvasive analysis of biological samples with high spatial resolution without the need to apply fluorescent markers.

3.6.9. Thermo Fisher Scientific

Thermo Fisher Scientific is an American provider of scientific instrumentation, laboratory equipment, chemicals, consumables, software and services to academia, government and industry. The company is a recognized world leader in FTIR instrumentation and techniques.

Thermo Fisher Scientific (Thermo Fisher Scientific n.d.) offers a family of DXR desktop confocal Raman microscopes built on the principle of open configuration. This design allows users to select the correct excitation wavelength, spectral range and resolution to immediately configure the instrument in the laboratory in accordance with the requirements of a scientific experiment or analytical measurement. This capability is ensured by the employment of Smart™ technology that enables pre-aligned optical components (lasers, Rayleigh filters and gratings) to be easily installed by the user. There are no principle limitations imposed on the number of excitation wavelengths: the lasers supplied by users can be added to 455,

532, 633 and 785 nm lasers offered by the manufacturer. The excitation wavelength is selected by manually installing and replacing the corresponding laser and the associated optical components. The wideband spectrograph with a fixed grating mount integrated into the DXR microscopes allows the Raman spectrum to be obtained in the 50-3500cm^{-1} spectral range in a single exposure. The DXR models are equipped with a single detector. All the diffraction gratings used in the spectrograph are blazed-angle gratings that ensure high optical throughput and spectral sensitivity for all offered excitation wavelengths. Optimal performance and operational readiness of the DXR microscopes are ensured by a fully automated procedure of alignment and calibration of all the optical components using a patented calibration tool. The DXR instruments provide a fine laser power control by 0.1 mW increments at the sample. Raman polarization option offers a stepping position variation between a polarizer and analyzer with an increment of one degree. All the DXR instruments are class I laser safety systems. The standard trinocular viewing head allows users to safely see the sample via the colour video camera on the monitor screen and through the binoculars. The operator's safety is ensured by a laser light interlock triggered when the doors to the sample compartment are opened. The clam-type doors allow different accessories to be mounted in the sample compartment and connected to external controllers using wires and hoses. The DXR microscopes can be equipped with an extended reach adapter for measuring samples that do not fit into the sample compartment. A rigid cast base made of a metal alloy and put on rubber dampening pads ensures the instrument's stability during spectral measurements.

The DXR Raman microscope is a research-grade confocal Raman microscope with a CCD detector and an XYZ motorized mechanical

mapping stage. The instrument can be interfaced with rheometers, AFM and SEM systems. It operates under OMNIC™ Atlus software for image analysis, particle identification and classification, and comprehensive chemometrics.

The DXRxi Raman imaging microscope is a highly automated system equipped with an EMCCD detector and a proprietary magnetic linear motor XYZ stage with closed-loop optical encoders. The sample mapping is performed by moving the stage in a zigzag manner, with the laser beam being always orthogonal to the sample surface. Combining the speed of the EMCCD detector with the fast, continuous movement of the stage allows for scanning sample areas up to 4 x 3 inches. The Raman shift can be automatically calibrated at predetermined time intervals during lengthy map acquisitions to maintain the accurate positions of the measured spectral bands. The OMNICxi controlling and processing software employed in DXRxi provides real-time optimization of the measurement parameter (laser power, exposure time, pixel size, number of scans, etc.) and real-time Raman image generation. Multiple areas of the sample may be selected for the analysis, and the measurement parameters for each area can be set individually. The software offers a terrain mapping mode that allows users to keep the area of interest in focus over the sloped, rough or irregular sample's surface. Terrain mapping is performed by first determining the topography of the sample's surface using the video camera. Then, the map acquisition follows this measured topography maintaining focus throughout the area of interest. OMNICxi software provides topographical and dynamical 3D visualization and manipulation tools.

The DXR Raman microscope and DXRxi Raman imaging microscope have been designed with a focus on multi-user and multitasking laboratories in

research institutions, industrial enterprises and contractor services with varying user skills.

3.4.10. WITec

WITec is a leading German manufacturer of high-quality, flexible and innovative nano-analytical Raman, AFM and SNOM systems. WITec (WITec n.d.) offers a series of confocal Raman microscopes Alpha represented by four models: Access, 300R, 300RI and Apyron.

The Alpha Access is an entry-level system that enables single-spot measurements or Raman mapping while delivering quality spectral data and the extent of confocality achievable in all instruments of the Alpha family. It offers upgradeability to 3D Raman imaging, AFM or SNOM, along with modularity for quick adaptation to new experiments and applications.

The Alpha 300R is the confocal Raman imaging system offering 2D (in a basic configuration) and 3D (with advanced options) Raman spectral imaging. The basic configuration requires manual sample positioning in the Z direction, while the advanced options include TrueSurface^{TM} technology for confocal Raman imaging guided by surface topography and ultrafast Raman imaging. The instrument with the TrueSurface^{TM} option is equipped with a sensor for optical profilometry. The topographic coordinates from the profilometer measurement are used to follow the sample surface in mapping mode so that even rough or inclined samples always stay in focus. The mapping is performed using a piezoelectric scanner with the scanned area typically within 200 × 200 μm^2. Available illumination options include phase contrast, DIC and epi-fluorescence measurements. The system can be equipped with one out of two spectrometers: UHTS-300 or the SpectraPro-300i. The lens-based UHTS-300 spectrometer supplied with a single

detector features high optical throughput and can be configured with one to three diffraction gratings on a turret. The mirror-based SpectraPror-300i provides a wide spectral range for multiple excitation wavelengths from UV to NIR. Typically offered excitation wavelengths include 325, 405, 442, 457, 488, 514, 532, 633 and 785 nm. The SpectraPror-300i spectrometer can accommodate a combination of two detectors, including the BI DD CCD recommended for 785 nm excitation, the EMCCD for ultrafast Raman imaging and the avalanche photodiode detector for applications involving extremely low light levels, such as single-molecule fluorescence detection. The focal length for both spectrometers is 300 mm, as indicated in the model number. The calibration of the spectrometer in the Alpha 300R Raman microscope is performed in a manual mode using a Hg-Ar spectral lamp connected directly to the spectrometer.

The Alpha 300RI is an inverted Raman microscope with all the functionality of the upright Alpha 300R model. The ability to view and investigate samples from below provides an advantage when working with aqueous solutions and oversized samples. The Alpha 300RI is intended for applications in life sciences, biomedicine and geosciences.

The Alpha 300 Apyron is a top of the line Raman imaging system in the WITec microscope series. It offers a highly automated flexible configuration for a variety of Raman applications and experiments. The instrument provides automated alignment and calibration of spectrometer and microscope components, including filters, gratings and video camera. The mapping can be performed using a multi-stage arrangement that combines the piezoelectrical scanner and a motorized stage, enlarging the scanned area. The TruePower^{TM} method automatically controls the laser output power with an accuracy of 0.1 mW. The instrument can be equipped

with the UHTS-300, UHTS-400 or UHTS-600 spectrometers having focal lengths of 300, 400 and 600 mm, respectively, and the spectral resolution increasing in accordance with the focal length. Since the UHTS spectrometer has a single detector port, in order to use lasers with, for example, 514 and 785 nm wavelengths, two spectrometers with different detectors may be required to provide the highest measurement sensitivity for both the lasers.

In the Alpha series of instruments, the optical coupling between the microscope, spectrometers and lasers is enabled by optical fibres.

For incorporating AFM and SNOM capabilities, the Alpha microscopes are equipped with a special objective that consists of a standard microscope objective (typically 10×/0.25 or 20×/0.4) and an inertial drive assembly that magnetically holds the cantilever. The objective is used to focus the beam of the excitation laser on the sample and the beam of the deflection laser of a different wavelength onto the cantilever. This setup allows simultaneous observation of the cantilever and the sample.

An active vibration isolation system is typically used for enhancing the stability of the Alpha series instruments, especially, for measurements in Raman-AFM and Raman-SNOM modes.

The Suite FIVE is a software environment for data acquisition, evaluation and processing in all WITec Raman microscopes. The integrated wizard guides the user through the entire experiment, from the initial settings to spectral data and Raman image post-processing. The software architecture supports integrated functionality for Raman, Raman-AFM, Raman-SNOM, Raman-SEM and fluorescence modes of operation.

WITec Raman microscopes are focused on research and industrial laboratories with advanced imaging requirements. The instruments are oriented on users with practical skills in Raman microscopy.

3.7. Some practical aspects of working with confocal Raman imaging microscopes

First of all, appropriate alignment and calibration are the top priority when conducting high-precision confocal Raman experiments. To keep the high instrument performance, alignment and calibration should be performed on a regular basis in strict accordance with the manufacturer's recommendations.

Maintaining the correct calibration of microscope objectives, video camera, sampling stage and scanning mechanisms is necessary for the precise superposition of optical and Raman spectral images. Individual spectra can be retrieved from any point or pixel in the Raman image to allow an appropriate correlation of the spectral data with the detailed optical image of the sample. Often, after replacing an objective or inserting a new one, its calibration using special optical targets or other procedures established by the manufacturers of Raman microscopes is required.

When the lasers are turned on, they should be given enough time to warm up in order to emit a stable excitation frequency. The time this takes depends on the type of laser, and it usually requires several minutes, although, for a He-Ne laser, it may take longer. EMCCD detectors commonly used for the acquisition of Raman images are capable of measuring single spectra within milliseconds, that is, 1000 spectra per second. A massive array of spectral data is commonly generated as a result of the Raman image acquisition. If, for example, an image comprises 1000 × 1000 points, and each spectrum is measured in the spectral range from 100 to 3500 cm^{-1} with a digital

resolution of 2 cm^{-1} per pixel of the detector matrix and 2^{16} discrete levels of spectral intensity, which correspond to 2 bytes, then the computer memory required for storing the corresponding data file needs to be

$$1000 \times 1000 \times (3500 - 100) / 2 \times 2 \text{ bytes} \approx 3.4 \text{ gigabytes (GB)}.$$

Assuming a 0.5 μm diameter of the laser spot, which is achievable in confocal mode using 100× objectives with a high *N.A.*, and par-sampling conditions of mapping, the area of a sample measured in this example is only about 0.5×0.5 mm^2. The storage space increases significantly if larger areas or 3D structures are to be mapped as the arrays of the data may consist of millions of spectra.

The data stream generated during fast Raman image acquisition requires computers with high-performance processors and extended memory capacity. The computers should support advanced graphic capabilities to visualise and analyse Raman images and, especially, 3D image datasets. The workstation computers that manufacturers of Raman microscopes usually offer with their systems are the most optimal options.

Since in confocal Raman imaging experiments, millions of spectra may be acquired in par-sampling or over-sampling conditions, the accumulation time per spectrum must be kept reasonably short. As a result, the requirement for S/N ratio in individual Raman spectra is not as stringent as for slower mapping experiments usually performed in under-sampling. The software for Raman imaging should offer an instant averaging of spectra by the adjacent pixels in order to ensure the S/N adequate for analysis of the mean spectra, even if single spectra in these points manifest barely detectable Raman bands.

In contrast to the conventional measurement of Raman spectra, where the problem of removing spectral spikes caused by cosmic rays is successfully solved using various mathematical algorithms, the software for Raman imaging should be able to detect and filter out these spikes with a single exposure if a sample map is to be collected in a single run. Since the problem of removing cosmic ray spikes in Raman imaging software remains relevant, it is important to evaluate the reliability of the solutions offered by different providers for this purpose.

The Raman imaging software should offer comprehensive chemometrics and statistical processing for the Raman datasets and generate graphic images that can be easily documented, shared and adapted for presentations, reports and scientific publications.

References

Adar, F. 2010. "Depth Resolution of the Raman Microscope: Optical Limitations and Sample Characteristics." *Spectroscopy-US* 1–7. Accessed May 24, 2020. http://www.spectroscopyonline.com/depth-resolution-raman-microscope-optical-limitations-and-sample-characteristics.

Anderson, M.S. 2000. "Locally enhanced Raman spectroscopy with an atomic force microscope." *Appl. Phys. Lett.* 76: 3130–3132. https://doi.org/10.1063/1.126546.

n.d. *Apollo Raman Microspectrometer.* Accessed June 13, 2020. http://www.microspectra.com/products/apollo.

ASTM International. 2014. *Standard Guide for Raman Shift Standards for Spectrometer Calibration.* doi:10.1520/E1840-96R14.

Baia, L., K. Gigant, U. Posset, G. Schotinger, W. Kiefer, and J. Popp. 2002. "Confocal Micro-Raman Spectroscopy: Theory and Application to a Hybrid Polymer Coating." *Appl. Spectrosc.* 56 (4): 536–539.

Bridges, T.E., M.P. Houlne, and J.M. Harris. 2004. "Spatially Resolved Analysis of Small Particles by Confocal Raman Microscopy: Depth Profiling and Optical Trapping." *Anal. Chem.* 76 (3): 576–584.

n.d. *Bruker Raman Microscopes SENTERRA II.* Accessed June 11, 2020. https://www.bruker.com/products/infrared-near-infrared-and-raman-spectroscopy/raman/raman-microscope-senterra-ii.html.

Carl Zeiss. n.d. "Confocal Laser Scanning Microscopy. Principles." *Education in Microscopy and Digital Imaging.* Accessed May 9, 2020. http://zeiss-campus.magnet.fsu.edu/referencelibrary/pdfs/ZeissConfocalPrinciples.pdf.

Choquette, S.J., E.S. Etz, W.S. Hurst, D.H. Blackburn, and S.D. Leigh. 2007. "Relative Intensity Correction of Raman Spectrometers: NIST SRMs 2241 Through 2243 for 785 nm, 532 nm, and 488 nm/514.5 nm Excitation." *Appl. Spectrosc.* 61 (2): 117–129.

n.d. *Edinburgh Instruments - Raman microscopes.* Accessed November 19, 2020. https://www.edinst.com/types/raman-microscopes/.

Everall, N., J. Lapham, F. Adar, A. Whitley, E. Lee, and S. Mamedov. 2007. "Optimizing Depth Resolution in Confocal Raman Microscopy: A Comparison of Metallurgical, Dry Corrected, and Oil Immersion Objectives." *Appl. Spectrosc.* 61 (3): 251–259.

Everall, N.J. 2010. "Confocal Raman microscopy: common errors and artefacts." *Analyst* 135: 2512–2522.

Everall, N.J. 2009. "Confocal Raman Microscopy: Performance, Pitfalls, and Best Practice." *Appl. Spectrosc.* 245A–262A.

Everall, N.J. 2000. "Modeling and Measuring the Effect of Refraction on the Depth Resolution of Confocal Raman Microscopy." *Appl. Spectrosc.* 54 (6): 773–782.

Hallen, H.D., and C.L. Jahncke. 2003. "The electric field at the apex of a near-field probe: implications for nano-Raman spectroscopy." *J. Raman Spec.* 34 (9): 655–662. https://doi.org/10.1002/jrs.1048.

Haynes, C.L., A.D. McFarland, and R.P. Van Duyne. 2005. "Surface-Enhanced Raman Spectroscopy." *Anal. Chem.* 77 (17): 338A-346A. https://doi.org/10.1021/ac053456d.

n.d. *Horiba Scientific.* Accessed June 6, 2020. https://www.horiba.com/en_en/products/by-technique/molecular-spectroscopy/raman-imaging-and-spectroscopy/.

Jahncke, C.L., M.A. Paesler, and H.D. Hallen. 1995. "Raman imaging with near-field scanning optical microscopy." *Appl. Phys. lett.* 67 (17): 2483–2485. https://doi.org/10.1063/1.114615.

n.d. *JASCO.* Accessed June 11, 2020. https://jascoinc.com/products/spectroscopy/raman-imaging-microscope/.

Jiang, N., D. Kurouski, E.A. Pozzi, N. Chiang, and M.C. Hersam. 2016. "Tip-enhanced Raman spectroscopy: From concepts to practical applications." *Chem. Phys. Lett.* 659: 16–24. https://doi.org/10.1016/j.cplett.2016.06.035.

Kauffman, J.F, S.J. Gilliam, and R.S. Martin. 2008. "Chemical Imaging of Pharmaceutical Materials: Fabrication of Micropatterned Resolution Targets." *Anal. Chem.* 80 (15): 5706–5712.

Kimura, S., and T. Wilson. 1991. "Confocal scanning optical microscope using single-mode fiber for signal detection." *Appl. Opt.* 30 (16): 2143–2150.

Kumar, N., S. Mignuzzi, W. Su, and D. Roy. 2015. "Tip-enhanced Raman spectroscopy: principles and applications." *EPJ Techn. Instrum.* 2 (9). https://doi.org/10.1140/epjti/s40485-015-0019-5.

Kurouski, D. 2018. "Tip-Enhanced Raman Spectroscopy: An Emerging Technique for Probing Biology and Electrochemistry at the Nanoscale." *Spectroscopy* 33 (11): 38–46. http://www.spectroscopyonline.com/tip-enhanced-raman-spectroscopy-emerging-technique-probing-biology-and-electrochemistry-nanoscale.

Langer, J., D. Jimenez de Aberasturi, J. Aizpurua, R.A. Alvarez-Puebla, B. Auguié, J.J. Baumberg, G.C. Bazan, et al. 2020. "Present and Future of Surface-Enhanced Raman Scattering." *ACS Nano* 14 (1): 28–117. https://doi.org/10.1021/acsnano.9b04224.

Lee, E. 2012. *Imaging Modes.* Vol. 168, chap. 1 in *Raman Imaging: Techniques and Applications*, edited by A. Zoubir, 1–37. Berlin: Springer. https://doi.org/10.1007/978-3-642-28252-2_1.

Lichtman, J. 2013. "Microscopy: Point Spread Function." YouTube, November 17. Accessed April 28, 2020. https://www.youtube.com/watch?time_continue=1366&v=JQy94K94nL0&feature=emb_logo.

Mark, H., and J. Workman Jr. 2018. *Chemometrics in Spectroscopy.* Academic Press. https://doi.org/10.1016/C2015-0-04023-0.

n.d. *Nanophoton*. Accessed April 30, 2021 https://www.nanophoton.net/products

NIST. 2018. *SRM 2241 - Relative Intensity Correction Standard for Raman Spectroscopy: 785 nm Excitation.* 6 26 2018. https://www-s.nist.gov/srmors/certificates/2241.pdf.

Ou, F.S., M. Hu, I. Naumov, A. Kim, W. Wu, A.M. Bratkovsky, and X. Li. 2011. "Hot-Spot Engineering in Polygonal Nanofinger Assemblies for Surface Enhanced Raman Spectroscopy." *Nano Lett.* 11 (6): 2538–2542. https://doi.org/10.1021/nl201212n.

Pérez-Jiménez, A.I., D. Lyu, Z. Lu, G. Liu, and B. Ren. 2020. "Surface-enhanced Raman spectroscopy: benefits, trade-offs and future developments." *Chem. Sci.* 11: 4563-4577. https://doi.org/10.1039/D0SC00809E.

Pilot, R., R. Signorini, C. Durante, L. Orian, M. Bhamidipati, and L. Fabris. 2019. "A Review on Surface-Enhanced Raman Scattering ." *Biosensors (Basel)* 9 (2): 57. https://doi.org/10.3390/bios9020057.

Puppels, G.J., W. Colier, J.H.F. Olminkhof, C. Otto, F.F.M. de Mul, and J. Greve. 1991. "Description and Performance of a Highly Sensitive Confocal Raman Microspectrometer." *J.Raman Spectrosc.* 22 (4): 217–225. https://doi.org/10.1002/jrs.1250220405

n.d. *Renishaw.* Accessed June 6, 2020. https://www.renishaw.com/en/6150.aspx.

Schrum, K.F., S.H. Ko, and D. Ben-Amotz. 1996. "Description and Theory of a Fiber-Optic Confocal and Super-Focal Raman Microspectrometer." *Appl. Spectrosc.* 50 (9): 1150–1155.

n.d. *SOL Instruments.* Accessed June 11, 2020. https://solinstruments.com/en/analysis/microscopy.

Sourisseau, C., and P. Maraval. 2003. "Confocal Raman Microspectrometry: A Vectorial Electromagnetic Treatment of the Light Focused and Collected Through a Planar Interface and Its Application to the Study of a Thin Coating." *Appl. Spectrosc.* 57 (11): 1324–1332.

Stockle, R.M., Y.D. Suh, V. Deckert, and R. Zenobi. 2000. "Nanoscale chemical analysis by tip-enhanced Raman spectroscopy." *Chem. Phys.*

Lett. 318 (1-3): 131–136. https://doi.org/10.1016/s0009-2614(99)01451-7.

Tabaksblat, R., R.J. Mieer, and B.J. Kip. 1992. "Confocal Raman Microspectroscopy: Theory and Application to Thin Polymer Samples." *Appl. Spectrosc.* 46 (1): 60-68.

n.d. *Thermo Fisher Scientific.* Accessed June 9, 2020. https://www.thermofisher.com/us/en/home/industrial/spectroscopy-elemental-isotope-analysis/molecular-spectroscopy/raman-spectroscopy.html.

Tomba, J.P., L.M. Arzondo, and J.M. Pastor. 2007. "Depth Profiling by Confocal Raman Microspectroscopy: Semi-empirical Modeling of the Raman Response." *Appl. Spectrosc.* 61 (2): 177–185.

Verma, P. 2017. "Tip-Enhanced Raman Spectroscopy: Technique and Recent Advances." *Chem. Rev.* 117 (9): 6447–6466. https://doi.org/10.1021/acs.chemrev.6b00821.

Wallace, W., L.H. Schaefer, and J.R. Swedlow. 2012. "Introduction to Deconvolution." *Deconvilution in optical microscopy.* Olympus America Inc. Accessed April 28, 2020. http://olympus.magnet.fsu.edu/primer/digitalimaging/deconvolution/deconintro.html.

Williams, K. P. J., G. D. Pitt, D. N. Batchelder, and B. J. Kip. 1994. "Confocal Raman Microspectroscopy Using a Stigmatic Spectrograph and CCD Detector ." *Appl. Spectrosc.* 48 (2): 232–235. https://doi.org/10.1366/0003702944028407.

n.d. *WITec.* Accessed June 9, 2020. https://www.witec.de/products/raman-microscopes/alpha300-r-confocal-raman-imaging/.

Zhang, W., Z. Zheyu Fang, and X. Zhu. 2017. "Near-Field Raman Spectroscopy with Aperture Tips." *Chem. Rev.* 117 (7): 5095–5109.

https://doi.org/10.1021/acs.chemrev.6b00337.

Zrimsek, A.B., N. Chiang, M. Mattei, S. Zaleski, M.O. McAnally, C.T. Chapman, A.-I. Henry, G.C. Schatz, and R.P. Van Duyne. 2017. "Single-Molecule Chemistry with Surface- and Tip-Enhanced Raman Spectroscopy." *Chem. Rev*. 117 (11): 7583–7613. https://doi.org/10.1021/acs.chemrev.6b00552.

CHAPTER FOUR

SELECTED EXAMPLES OF RAMAN MICROSCOPY AND IMAGING APPLICATIONS

In recent years, better integrated and compact instruments, a variety of laser sources with different excitation wavelengths, faster detectors and sample scanning methods have significantly improved the technique of confocal Raman microscopy and imaging. Today, it is becoming a generally accepted experimental technique for research and analytical laboratories for a wide range of applications in almost any field of physics, chemistry, geology, biology, agricultural, environmental and life sciences, where molecular spectral analysis is traditionally used.

A remarkably diverse range of applications of Raman microscopy and imaging can be found in contributing chapters of monographs (Zoubir 2012, Toporski, Dieing and Hollricher 2018, Pelletier 1999, Turrel and Corset 1996) and special reviews (Lohumi, et al. 2017, Opilik, Schmid and Zenobi 2013, Stewart, Priore and Nelson 2012, Weng, et al. 2019) written by experts in the relevant fields.

In this chapter, selected applications of confocal Raman microscopy and imaging that the author has worked with are provided to illustrate both traditional and unique tasks. The examples presented in these applications are primarily intended to demonstrate the principal possibilities of this method without an in-depth physicochemical analysis of spectral data and results.

4.1. Polymer composites and laminated polymer films

Raman spectroscopy is a proven method for the identification and characterization of the chemical composition and structure of polymers. Polymer samples may be in any form, including moulded parts, films, coatings, fibres or beads, and can be analyzed nondestructively with little or no sample preparation. Raman spectroscopy is sensitive to the structure of the polymer along the backbone as well as its crystallinity and conformation. Raman microscopy significantly expands the capabilities of this method by analyzing the spatially heterogeneous composite polymers and the materials based on them.

Thermosetting polymers are well known to exhibit structural stiffness and dimensional stability. Epoxy resins (ERs) are among the best thermoset materials for fibre composites, coatings, adhesives, binders for abrasives, automotive and electrical components. However, ERs, like most other thermosets, are rather brittle. The main strategy of toughness enhancement is based on the dispersion of impact modifier (IM) particles in the epoxy matrix. A major feature for the IM/ER blends is the dependence of their impact properties on the composition, size, shape and distribution of the IM particles in the ER matrix.

An example of confocal Raman microscopy applied to a bisphenol-based epoxy resin with inclusions of acrylonitrile rubber is shown in Figure 4-1. The XY map was collected using 532 nm excitation (4 mW of light power at the sample) and 100×/0.9 metallurgical microscope objective from the sample area of about 70 by 40 μm with 1 μm steps (2700 spectra in total) in point-by-point mode, thus, providing approximately par-sampling conditions. The characteristic band at 2238 cm^{-1} assigned to ν(C≡N) clearly

identified acrylonitrile rubber, and the Raman image was generated as the integrated intensity of this band.

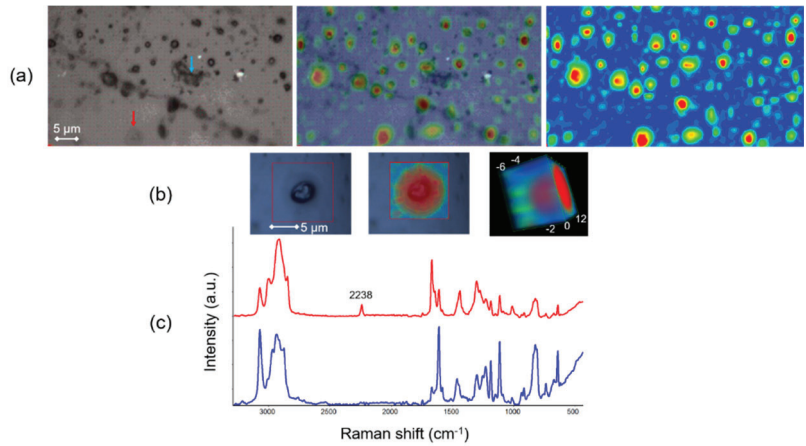

Figure 4-1. Raman images of epoxy resin with rubber inclusions as impact modifiers. (a) Optical image (left), Raman image superimposed on the optical image (centre), and the Raman image (right) generated as the integrated intensity of the band at 2238 cm^{-1} assigned to ν(C≡N) of acrylonitrile rubber. The red, yellow, and green areas on the Raman image represent the values of the intensity, with red representing the highest intensity. (b) Optical image (left), the Raman image superimposed on the optical image (centre), and the 3D Raman image (right) of one of a rubber particle showing the hemispherical shape of the particle. (c) Representative mean Raman spectra obtained from acrylonitrile rubber inclusions (red) and bisphenol-based epoxy resin matrix (blue) normalized and offset for clarity.

The analysis of the Raman spectral image made it possible to clarify that the combined area of the IM inclusions on the surface of the sample is about 20% of the total analyzed area, which slightly exceeds the data obtained from the digital processing of the optical image. Indeed, in the optical

image, some IM rubber inclusions, such as those indicated by the red arrow, are not detected. From the other side, in the optical image, the dark features indicated by the blue arrow might be mistakenly identified as rubber particle agglomerates. The Raman spectral image allowed IM rubber particles as small as about 1 μm to be detected on the surface of the sample. The sizes of the IM particles derived from the Raman image was found to be distributed from 1 to 6 μm.

A 3D dimensional Raman spectral image obtained with 0.2 μm step in XY plane and 1 μm step in the Z direction using a 50 μm confocal pinhole from one of the IM inclusions showed that the rubber formed a hemispherical particle under the surface of the epoxy resin.

One of the most powerful applications of confocal Raman microscopy is an exploration of the interior of samples by optical sectioning. A complex semi-transparent laminated polymer film can be examined by simply focusing the laser beam on progressively deeper layers of the film instead of cutting and analyzing the slice or section of the film. However, as has already been mentioned in Chapter Three, the spectral measurements from a sample using a metallurgical (dry) microscope objective result in the compression of the actual sampling depth, a loss of axial spatial resolution and a decrease in the intensity of the Raman bands with increasing the sampling depth. Axial thickness measurements of individual layers in the laminates performed with the dry objective are therefore not exact.

The spatial distortion and spectral degradation can be addressed by using oil immersion objectives and filling the gap between the objective's lens and the polymer film with oils that have an index of refraction $n \approx 1.5$, similar to many polymer materials.

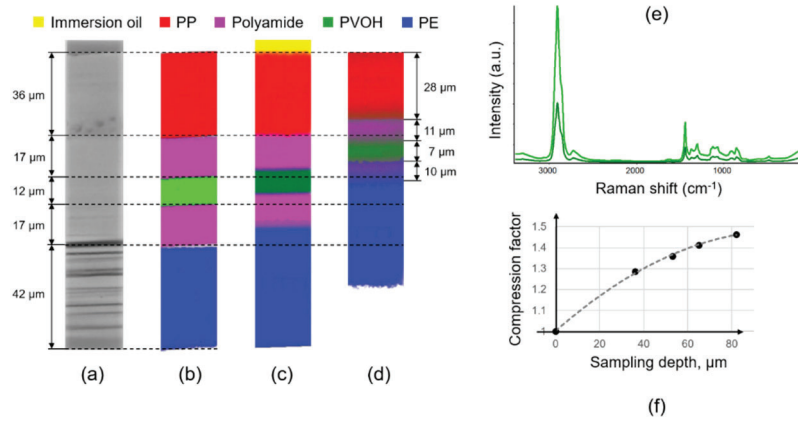

Figure 4-2. Optical and Raman spectral images of a laminate polymer film: (a) optical image of a cross-section cut, (b) Raman image of the cross-section cut, (c) Raman optical section obtained with 100×/1.3 oil immersion objective, (d) Raman optical section obtained with 100×/0.9 metallurgical objective, (e) comparison of the intensity of the Raman spectra obtained from the PVOH layer with the use of the oil immersion (light green) and metallurgical (dark green) objectives; and (f) the compression factor as the function of the sampling depth resulting from the use of the metallurgical objective.

Figure 4-2 shows the optical (a) and the Raman spectral image (b) obtained from a cross-section cut of a composite polymer film that consists of 5 layers. It was found, that the layers from the top to the bottom of the film are composed of polypropylene (PP), polyamide, polyvinyl alcohol (PVOH), polyamide and polyethylene (PE) with thicknesses of about 36, 17, 12, 17 and 42 µm, correspondingly. The Raman optical sections were acquired perpendicular to the surface of the film using a 100×/1.3 oil immersion objective (c) and 100×/0.9 metallurgical objective (d). The measurements were performed using a 532 nm laser for excitation, a 50 µm confocal pinhole and the mapping grid with the equidistant steps of 1 µm.

The spectral components in the Raman images were extracted using the MCR method. These components and their colours are indicated above the images. Note that, in the optical image of the cross-section cut, the central PVOH layer is barely observed while it is clearly identified in its Raman spectral image.

The figure demonstrates that the thicknesses of individual layers, which can be estimated from the Raman optical section acquired with the oil immersion objective, are in good agreement with those measured directly in the spectral image of the cross-section cut, although the axial scale is still slightly compressed. When using the metallurgical objective, there is significant compression of the layers compared to what is observed in the Raman image obtained from the cross-section cut and Raman optical section of the laminate acquired with the oil immersion objective. It can be noticed that the layers in the Raman spectral image obtained with the metallurgical objective are less clearly defined and suffer from blurred focus and loss of spatial resolution. As a result, the spectra at the interfaces between the layers are overlaid, which contributes to additional uncertainty in determining the layers' thicknesses. The oil immersion objective produces better distinguishable Raman spectra of the polymer layers and more realistic estimates of their thicknesses. The inset (e) demonstrates more than 2.5 times higher intensity and, correspondingly, the S/N in the Raman spectrum obtained with the use of the oil immersion objective (light green) in comparison to that obtained with the metallurgical one (dark green). For comparison, the spectra are retrieved from a position in the middle of the PVOH layer observed in the corresponding Raman optical sections.

The inset (f) shows the dependence of the compression factor resulted from the use of the metallurgical objective on the sampling depth, which was

measured from the surface of the film. The compression factor is calculated as the ratio of the true layer thicknesses to the thicknesses derived from the Raman optical section obtained with the metallurgical objective. The compression factor is not linear and is in good agreement with the evaluation made by Everall (N. Everall 2000). It can be used to correct the depth profiles of the polymer laminates when it is necessary to use metallurgical microscope objectives for nondestructive analysis. One may estimate the compression factor in advance for the conditions of a given experiment if it is possible to make a cross-section cut of an analyzed or a similar laminate.

In practice, it is sometimes difficult to prepare slices or sections of very thin laminates or coatings on metal surfaces without inducing artefacts or distortions even when using special microtome tools. Figure 4-3 shows examples of Raman optical sections of a thin separator membrane (a) and a multi-layered polymer coating on aluminium foil (b) obtained with the use of 100×/1.25 oil immersion objective. This method makes it possible to reliably determine the thickness of individual layers and their composition without cutting the samples.

The Raman optical sections were measured perpendicular to the samples' surfaces using a 532 nm laser for excitation, a 25 μm confocal pinhole and a mapping grid with the equidistant steps of 0.4 μm. The Raman images are generated as both the correlations with the mean spectra retrieved from the positions in the middle of the corresponding polymer layers and the components extracted by MCR. The Raman images demonstrate the multi-layered structure of the separator membrane and the polymer coating with well-defined thicknesses. It was determined that the separator membrane represented a tri-layered PP/PE/PP structure with layer thicknesses of about

4/5/5 µm, correspondingly. The coating on the aluminium foil was found to consist of a polyethylene terephthalate (PET) external layer of 14 µm thick and nylon 6 internal layer of 14 µm thick.

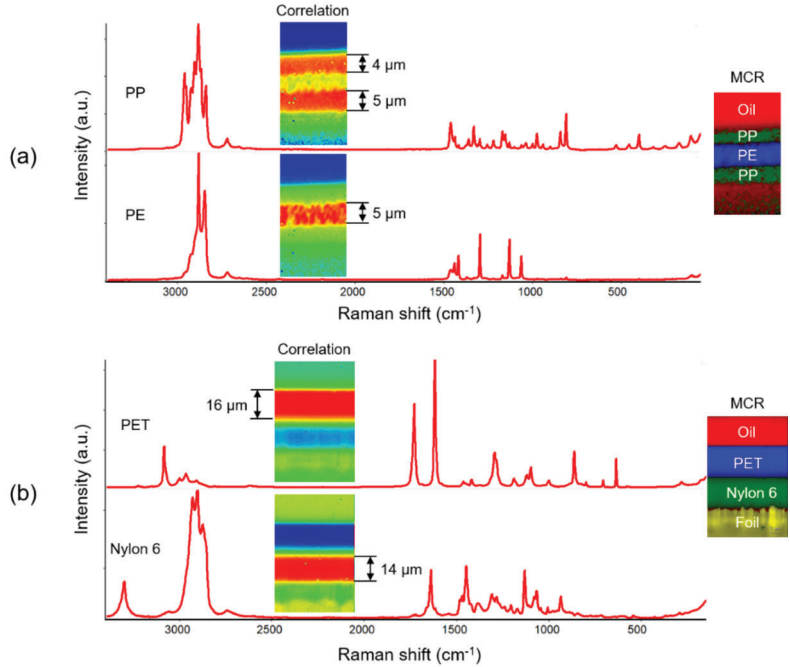

Figure 4-3. Raman spectra and Raman optical sections of a thin separator membrane (a) and a multi-layered polymer coating on aluminium foil (b) obtained using a 100×/1.3 oil immersion objective. The Raman images are constructed as correlations with the spectra of the corresponding polymers and the spectral components extracted by the MCR method. The mean representative Raman spectra are normalized and displayed in the spectral panes above one another.

Increased light collection efficiency and improved spatial discrimination provided by an oil immersion objective can be used to disclose internal structural layers of only a few microns thick in multi-layer polymer films.

Figure 4-4 illustrates the detection of a thin intermediate layer of polyvinylidene chloride (PVDC) sandwiched between the layers of PET and PE in a film. PVDC is often used in food packaging films as it combines high moisture and odour barrier performance with good adhesion to many other polymer materials. The line scan in the direction perpendicular to the film's surface was performed using a 532 nm laser for excitation, 100×/1.3 oil immersion objective, 50 μm pinhole and 1 μm steps along the line. The depth profile of the polymer film is shown in (a). The horizontal axis represents the Raman shift in the range of 150–3300 cm^{-1}. The vertical axis indicates the displacement of the sample stage so that the film's surface starts at 0. The colours in the spectral image correspond to the intensities of the Raman bands, with red indicating the highest intensity. The presence of the PVDC layer was found after the sequential subtraction of the spectra of PET and PE from the spectrum measured at a sampling depth of 8 μm. The resultant difference spectrum and the PVDC spectrum from a commercial library are shown in (b). The individual depth profiles in (a) were generated as the integrated intensities of the Raman bands at 1615 cm^{-1} in the spectrum of PET, 455, 358 and 293 cm^{-1} in the spectrum of PVDC and 1065 cm^{-1} in that of PE. Thicknesses of the layers estimated as the halfwidths of the individual depth profiles were found to be 7, 3 and 43 μm, respectively.

The results demonstrate that the quality of the Raman spectra obtained with the use of oil immersion objective allows the layer of PVDC no thicker than about 3 μm to be detected between the layers of PET and PE, despite the fact that both the polymers produce much more intense Raman spectra than PVDC.

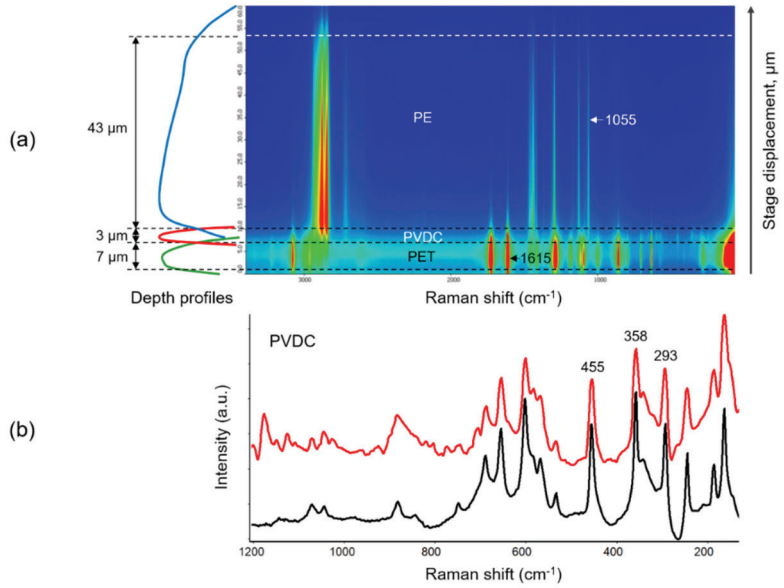

Figure 4-4. The depth profile of a multi-layer polymer film obtained using an oil immersion objective: (a) 2D representation of Raman spectra in a line scan performed perpendicular to the film's surface with green, red and blue curves showing the depth profiles of individual PET, PVDC and PE layers; (b) the Raman spectra of PVDC detected in the film (red) and taken from a commercial library (black) are presented in the spectral range of 100–1200 cm^{-1} for comparison.

Blue and green wavelengths are well appropriate for Raman optical profiling of transparent and colourless polymers because, as a rule, these materials do not fluoresce under the short excitation wavelengths. The microscope objectives with a high NA and the confocal apertures of small diameters are necessary to achieve the best axial resolution for a given excitation wavelength. For depth profiling of multi-layer polymer films, an oil immersion objective is the best option, except when oil contamination may appear to be harmful to the sample. If a metallurgical objective is used,

then one has to correct the observed depth profiles for the distortions in the depth scale, if possible.

A variety of different industries employ polymer composites specifically engineered for particular performance characteristics. Confirming the structure, composition and integrity of the polymer composites is important for both the industries that manufacture these materials and utilize them in their own products. Whether the goal is quality assurance, failure analysis or even reverse engineering of the polymer composites, the confocal Raman microscopy is a valuable analytical tool for these applications.

4.2. Pharmaceutical dosage forms and formulations

The characterization of the dosage forms, such as component identification, mixture consistency and verification of formulation, is becoming increasingly important in the pharmaceutical industry. The structural forms and spatial distribution of the active pharmaceutical ingredient (API) in the pharmaceutical dosage forms are critical factors for delivering effective drugs when consumed. Some APIs take various structural forms that affect the functional behaviour of the drug. Different polymorphs or the degree of the API's crystallinity may affect how the drug is delivered and its therapeutic effectiveness. The homogeneous distribution of APIs is often an important aspect of the development of formulation and processing procedures.

Raman microscopy and imaging can be used to identify and verify APIs and excipients, differentiate polymorphs and display the spatial distribution of the ingredients in various drug products and the processes of a pharmaceutical formulation (Netchacovitch, et al. 2014, Bugay 2001).

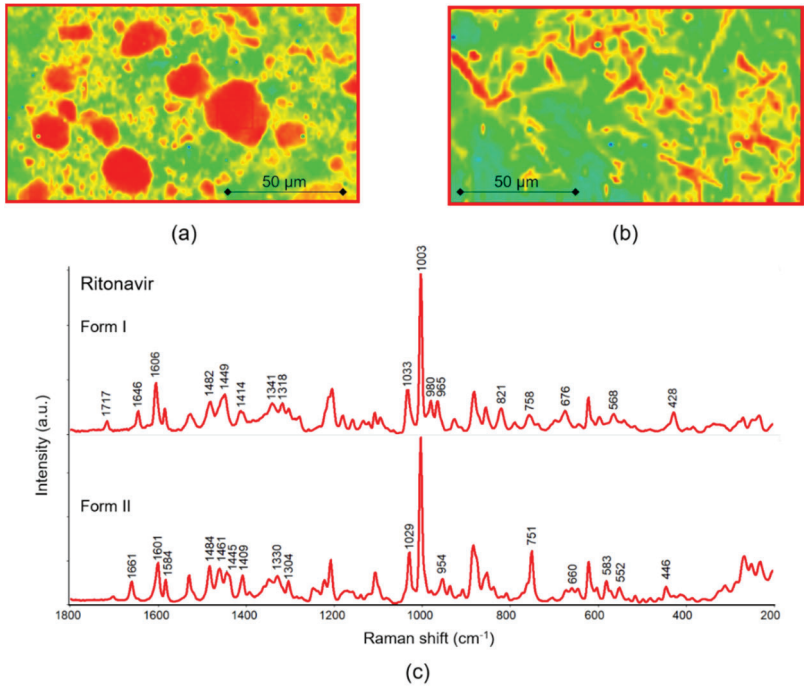

Figure 4-5. Raman images of pharmaceutical suspensions of the crystalline form I (a) and II (b) of ritonavir in medium-chain triglyceride deposited on a metal-coated microscope slide. The images are constructed as spectral correlations with the corresponding Raman spectra of the drug form I and II shown in (c). The spectra of the polymorphs are normalized to the spectral band at 1003 cm^{-1} and displayed in a stacked view in the "fingerprint" region.

Figure 4-5 shows an example of the use of Raman imaging microscopy to characterize two polymorphs of ritonavir drug substance dispersed in a medium-chain triglyceride (MCT) in a suspension for a softgel capsule fill. The suspensions were applied to a metal-coated microscope slide, and the maps were acquired from areas of about 150 × 100 μm^2 with equidistant steps of 2 µm using a 50×/0.75 metallurgical objective and a 50 µm confocal

pinhole. To minimize the fluorescence, a 780 nm laser was selected for excitation with 25 mW of light power at the sample. The Raman images are generated as correlations with the Raman spectra of the drug substance in the crystalline form I (a) and II (b). The representative spectra of the two polymorphs of ritonavir after subtraction of a reference spectrum of MCT are shown in (c).

The Raman spectral images demonstrate the differences in the morphology of the sedimented particles composed of different ritonavir polymorphs. It is evident that form I constitutes particles with a mostly round regular shape and dimensions ranging from several to 40 μm, while form II crystalizes in needle-shaped particles up to 40 μm in length. Although the Raman spectra of both polymorphs manifest a number of bands of very close by intensities and position, these two polymorphs can be easily distinguished. Indeed, the intense band at 1003 cm^{-1}, which is assigned to the breathing vibration of phenyl groups in ritonavir, is well observed in the Raman spectra of both polymorphs, whereas the spectral bands at 1717 and 1646 cm^{-1} manifest only in form I, and the band at 1661 cm^{-1} is specific for form II.

Depending on the formulation conditions, form II with an undesirable therapeutic action can occur as a result of process-induced re-crystallization of ritonavir. The ability to distinguish between the polymorphs makes Raman spectral imaging an effective method for monitoring the unwanted crystalline forms in pharmaceutical drugs.

Raman optical sectioning can be applied to estimate the thickness and integrity of shells in capsule dosage forms. Figure 4-6 illustrates the defects found in the shell of a soft gelatin capsule that may result in subsequent leakage of the inner fill. The Raman spectral sectioning was performed

using a 780 nm laser for excitation (25 mW of light power at the sample), a 50×/0.75 metallurgical objective and a 50 µm confocal pinhole. The sampling step was set to 2 µm in both the horizontal and vertical directions. The obtained Raman images are constructed as a correlation with a reference spectrum of gelatin used in manufacturing the capsules.

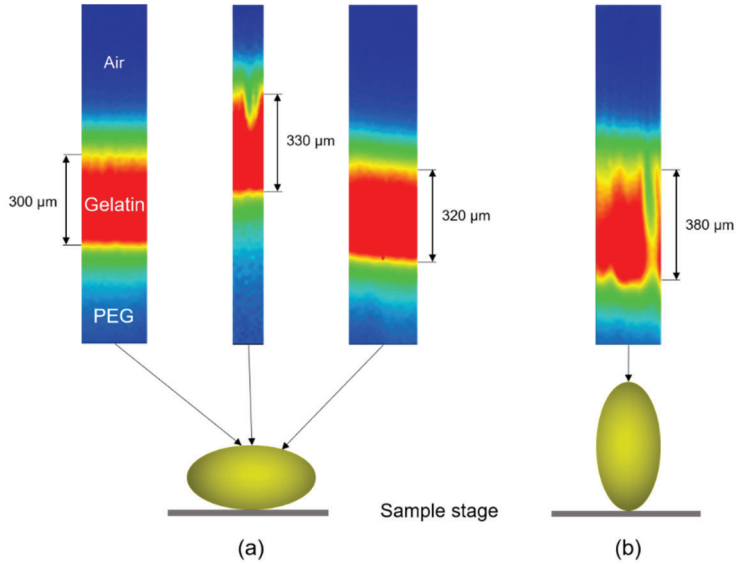

Figure 4-6. The Raman spectral sections of a shell obtained at the locations from the side of the soft gelatin capsule indicated by the arrows (a) and at its pole (b). The images allow the detection of well-type defects and provide an estimate of the shell thickness.

The Raman optical section of the capsule oriented horizontally (a) reveals the well-type defect in the shell formed from the outer side (central inset). The Raman sections at the other two locations (left and right) do not reveal any defects or imperfections in the shell. The images allow the shell thickness to be estimated between 300 and 330 µm (without the axial

correction of the compressed scale). The Raman optical section of the capsule oriented vertically (b) demonstrates a defect in the pole of the capsule, which passes through the entire shell from the outer side almost down to polyethylene glycol filler (PEG). The thickness of the shell at the pole was found to be about 380 μm, that is, a little thicker than on the side.

Examples of Raman spectral imaging for the characterization of the distributions of well-detectable APIs and excipients in solid dosage forms were demonstrated above and in the previous chapter. However, many pharmaceutical dosage forms and formulations contain APIs in relatively low concentrations. The requirements for the Raman micro-spectroscopic analysis of these types of samples are somewhat different from those in which most of the ingredients are APIs. Indeed, collecting the Raman maps in under-sampling conditions or of a relatively small sample area may lead to insufficiently representative and, therefore, not adequate results. Meanwhile, the Raman spectral image obtained in a par-sampling mode from a large enough area can help to intimately characterize the pharmaceutical product and provide detailed information on the API and its spatial distribution in the product. An example of Raman imaging of an antibiotic presented in a relatively low concentration in a surgical mesh is shown in Figure 4-7. The Raman image acquired from a 6.6 x 4.5 mm area of the polypropylene mesh with a low load of ampicillin is constructed as the integrated intensity of the peak at 1004 cm^{-1} of the breathing vibration of the phenyl group in ampicillin. The measurements were performed using a 780 nm laser for excitation (25 mW at the sample), a metallurgical 10×/0.25 objective and a 50 μm pinhole aperture. To match the requirements of the par-sampling, the pixel size was set to 4 μm which resulted in the image composed of about 1.9 million spectra.

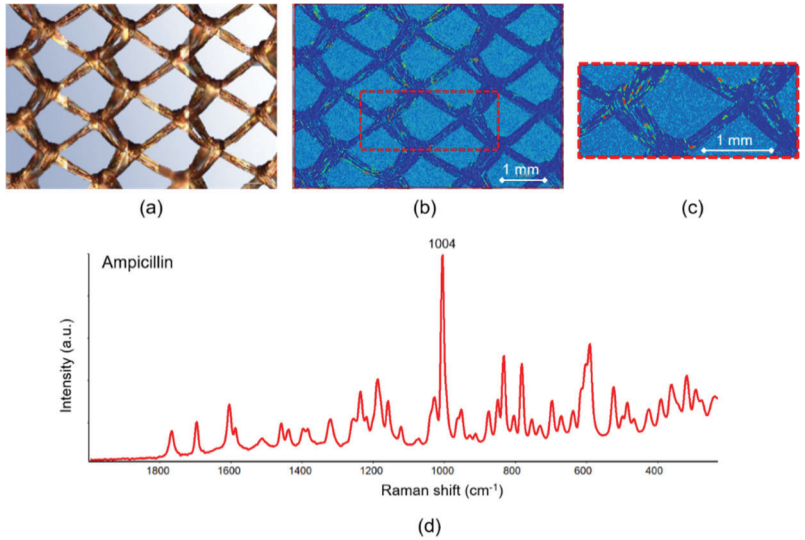

Figure 4-7. Optical (a) and Raman (b) images of a surgical polypropylene mesh with a low load of ampicillin. The inset (c) shows a zoomed area of the Raman image to better visualise the red spots corresponding to the highest concentration of ampicillin. The mean representative Raman spectrum of ampicillin (d) is shown in the fingerprint region after subtracting the spectrum of polypropylene, baseline correcting and smoothing.

Acquisition and comparison of several areas of equal dimensions on the mesh showed that the selected areas were statistically significant for estimating the spatial distribution of ampicillin in the entire mesh. The par-sampling allows for a definitive evaluation of the distribution pattern of ampicillin. The results demonstrate that the amount of ampicillin is quite limited. Ampicillin is spread over the surface of the mesh with a rather high degree of dispersion, probably due to the low wettability of polypropylene. Despite the massive amount of data that needs to be collected under the par-

sampling conditions, the fast Raman imaging makes this kind of analysis practical.

Raman spectral imaging is a powerful analytical tool for the modern pharmaceutical laboratory. One of the advantages of this method is that the great majority of APIs consist of organic molecules containing double and triple chemical bonds, phenyl groups and carbocyclic and heterocyclic structures that typically result in strong bands in Raman spectra. In contrast, the common pharmacologically inert excipients that are combined with APIs to aid their processing into dosage forms are characterized by Raman spectra of relatively low intensity. This particularity often allows the rapid, direct analysis of APIs with very little or no sample preparation, which increases the demand for this technique in the quality control of the pharmaceutical formulations.

As was demonstrated, Raman spectral imaging can be used not only for identification and statistically relevant visualization of the spatial distribution of APIs but also for more detailed spectral analysis, such as the differentiation of polymorphs and the extent of crystallinity. It can also be used to detect and spatially locate lower concentration ingredients. In practice, to avoid possible fluorescence from many common excipients and their mixtures, a longer excitation wavelength, such as 780, 785 or 830 nm, is recommended.

4.3. Biological cells, bacteria and tissues

Raman microscopy has been used for decades and is now well established as one of the most powerful analytical techniques for the characterization of complex biological objects and monitoring biological processes (Antonio and Schultz 2014) at the micro-scale. This technique offers a unique capability for the noninvasive analysis of live cells (Palonpon, Sodeoka and Fujita 2013), bacteria (Lorenz, et al. 2017) and tissues (Movasaghi, Rehman and Rehman 2007) for research, medical and cosmetic applications.

The inelastic scattering of light by different types of biomolecules generates corresponding bands in the Raman spectra, which makes it possible to distinguish between proteins, different classes of lipids, saccharides and certain amino acids, as well as DNA and RNA. In the biological cells, the Raman spectra vary between different cellular compartments and subcellular organelles, such as the nucleus, nucleolus, mitochondria and endoplasmic reticulum. Since the diameter of the focused laser beam in a Raman microscope is smaller than most cellular organelles, the beam can be scanned over a cell to generate Raman images displaying cellular heterogeneity and distinct subcellular structures. However, due to the complexity of the Raman spectra and superposition of spectral bands, the spectral differences between various parts of the cell are quite subtle, which are not easy to identify by visual inspection or by means of univariate analysis.

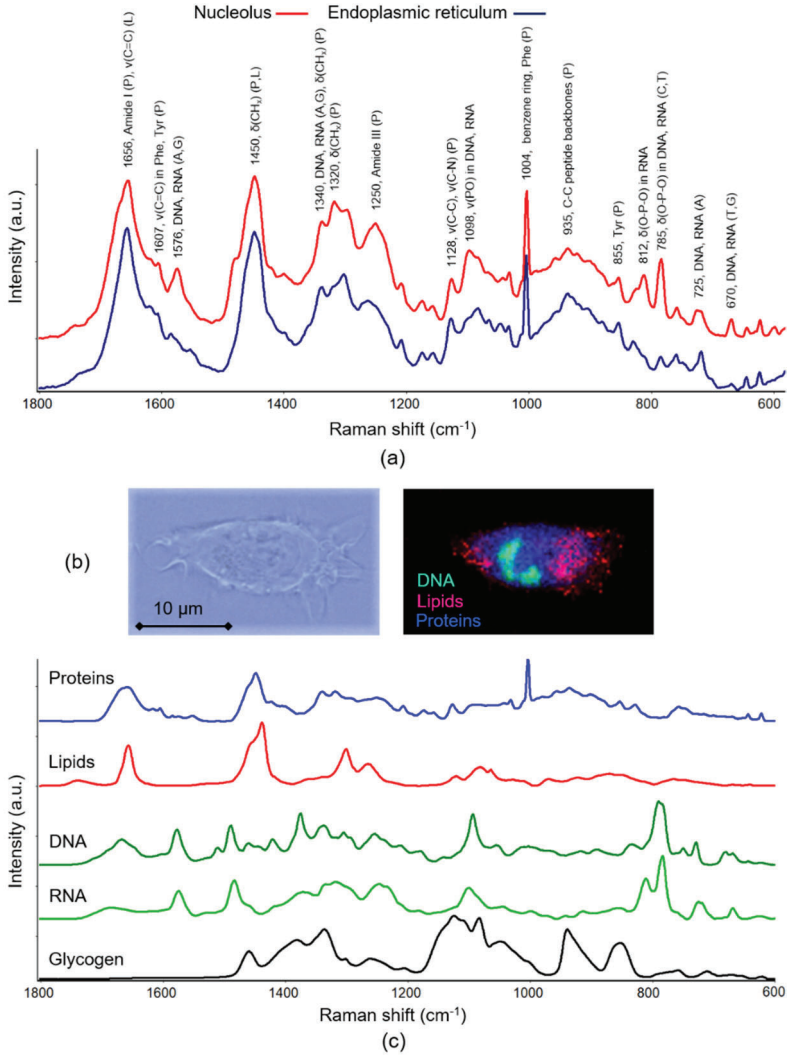

Figure 4-8. Raman spectra and images of live cells: (a) Raman spectra of a HeLa cell and the assignment of the most common spectral bands (P – proteins, L – lipids, and the four nucleobases in the nucleic acids DNA and RNA: A – adenine, C – cytosine, G – guanine, T – thymine); (b) Raman image of an HT1080 cell generated using PCA; and (c) the Raman spectra of five basic biochemical components.

Figure 4-8(a) demonstrates the representative Raman spectra obtained from a nucleolus and endoplasmic reticulum of a live HeLa cell in the fingerprint region. The spectra were obtained using a 633 nm laser (50 mW at the sample), a 60×/1.2 water immersion objective and a 50 μm confocal pinhole. Obviously, these spectra are very similar, despite minor differences in the relative intensities of some bands. The positions and assignment of the most common Raman bands manifested in biological cells and to one degree or another in tissues are given in the figure. As is seen, several biochemical components may contribute to the peaks at the same wavenumbers. Thus, changes in the individual Raman bands result in little understanding of how the relative amounts of the biochemical components vary across each cell. Selective analysis of a specific band or bands in a narrow spectral interval often leads to a loss of important information in the rest of the Raman spectrum.

To effectively use Raman spectral imaging to reconstruct the structure and composition of cells and tissues, it is necessary to apply chemometric methods of multivariate statistics.

Principal component analysis (PCA) is one of the most recognized classic methods of multivariate analysis. PCA reduces a large set of variables in the spectral data to a smaller number of principal components (PCs), which account for the variability in the data and contains major spectral information. Subsequently, all original spectra are expressed as linear combinations of these PCs. The classification of spectral data can be completed by choosing different combinations of PCs to build a new basis set for the data. Figure 4-8(b) shows a Raman image of a live HT1080 cell generated using PCA. The image was acquired using 532 nm excitation (10 mW at the sample), a 60×/1.2 water immersion (WI) microscope objective,

a 50 μm confocal pinhole and a 0.2 μm step. However, while PCA is useful as a classification method that can determine specific spectral differences and changes, it cannot recognize and explicitly quantify the components responsible for these spectral transformations.

Valuable information about the physiological and structural changes in different cells can be extracted with the use of a method known as Biomolecular Component Analysis (BCA). BCA is a technique that quantifies the concentration of biochemical components composing the biological sample (Kuzmin, Pliss and Rzhevskii, et al. 2018, Kuzmin, Pliss and Kachynski 2013). The core of the technique is obtaining the best fit of a Raman spectrum of a biological sample with the linear combination of the weighted spectra of the basic biochemical components, such as proteins, lipids, nucleic acids and polysaccharides. The spectral weights, which are optimized during the fitting procedure, directly yield the concentrations of the biochemical components. The Raman spectra of five selected basic biochemical components are shown in Figure 4-8(c). BCA is an effective method for detailed analysis of molecular content in major organelles, including nucleoli, endoplasmic reticulum, Golgi apparatus and mitochondria of either live or fixed cells.

Recently, the Raman microscopy enhanced by the BCA has been used to quantitate lipid content in late-stage transgenic adenocarcinoma of mouse prostate tumours (TRAMP) and normal (WT) prostate tissues. The increased lipid accumulation in late-stage TRAMP compared to early-stage TRAMP and normal WT prostate tissues was detected. The results of the method correlated with the free fatty acid and total cholesterol content assay in the tissues. The correlation between lipid accumulation in individual tissue cells and tumour stage provided a quantitative marker for prostate cancer diagnosis. Figure

4-9 illustrates that lipid quantification by Raman microscopy combined with BCA analysis is a sensitive and reliable tool for prostate cancer diagnosis and staging.

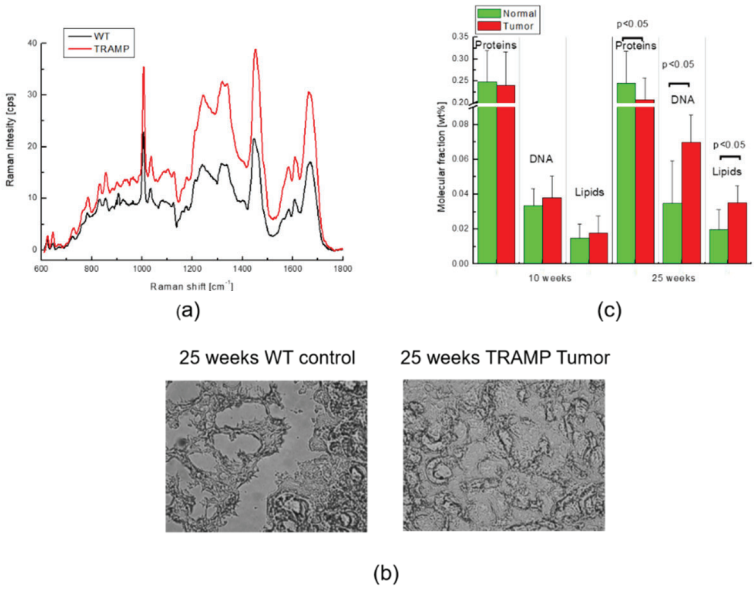

Figure 4-9. Representative mean Raman spectra of the individual cell nucleus in WT and TRAMP tissues (a), optical images of WT and TRAMP tissues (b), and mean value of the weight fraction of proteins, DNA and lipids in normal (WT) and tumour (TRAMP) cell nucleus obtained by BCA (c). The figure was adapted with permission from (O'Malley, et al. 2017).

Other multivariate methods for discriminating the structure of biological samples and generating Raman spectral images include cluster analysis (hierarchical and K-means clustering) and vertex component analysis. These and other algorithms are available in CytoSpec^{TM}, a specialized software package widely used in biomedical applications (CytoSpec n.d.).

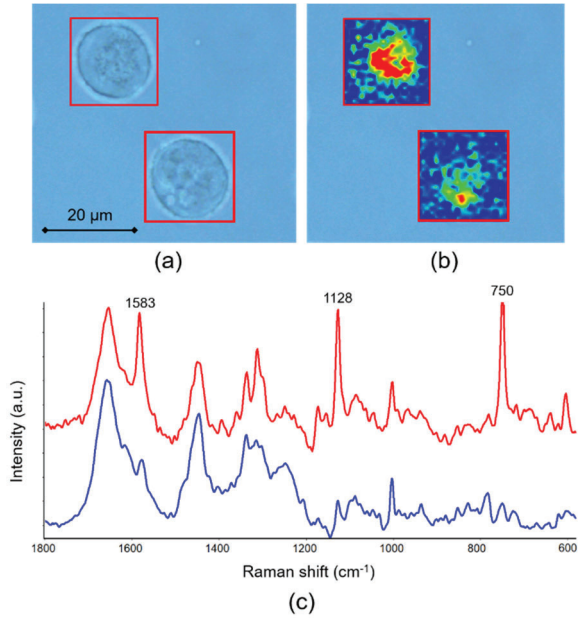

Figure 4-10. Probing cytochrome C in a cancerous cell using RRS with 532 nm laser excitation: (a) optical image captured with a 60×/1.2 WI objective; (b) the Raman images of the cells generated as the integrated intensity of the resonantly enhanced band at 750 cm^{-1} and superimposed on the optical image; and (c) representative mean Raman spectra of the cytochrome C (red) and the rest of the cell (blue). The spectra are shown after baseline correction and offset for clarity.

Selective enhancement of specific Raman bands due to resonance Raman (RRS) scattering offers a sensitive probe for structural changes in biological samples. As mentioned in Chapter One, resonance Raman scattering involves laser excitation within an electronic absorption band. A chromophore's specific vibrational modes, which couple to the electronic transition, are greatly enhanced in the observed spectrum. Figure 4-10 illustrates the detection of cytochrome C in normal and cancerous cells. The

optical image obtained with a 60×/0.9 WI microscope objective is shown in (a). The Raman spectral images (b) of the cells were generated as the integrated intensity of the band at 750 cm^{-1} resonantly enhanced under 532 nm excitation. The representative mean Raman spectra of the cytochrome C manifesting the resonantly enhanced bands at 1583, 1128 and 750 cm^{-1} and the rest of the cell are shown in (c). The chromophore of cytochrome C is the iron complex of porphyrin, and the resonance effect occurs in the heme prosthetic group of porphyrin. The red spot in the lower right Raman image of the normal cell indicates that cytochrome C is localized in the mitochondria. The upper left Raman image of the cancerous cell, however, reveals that cytochrome C is spread throughout the cell, which evidences the mitochondria disrupted by cancer.

Raman microscopy can be effectively applied to detect chemical marker compounds that are characteristic of spore-producing bacteria, including *Bacillus anthracis* (anthrax) and *Clostridium botutinum* (botulism). Figure 4-11 demonstrates the sensitivity and selectivity of Raman spectral imaging to the marker compound, dipicolinic acid (2,6-pyridinedicarboxylic acid, DPA), in an agglomeration of spores. The spores were deposited and dried on a stainless steel μ-RIM™ substrate available from BioTools (BioTools n.d.). The Raman spectral image was acquired using 532 nm excitation, a 100×/0.9 metallurgical objective, a 50 μm confocal pinhole and a 0.2 μm step. The laser power was set to 3 mW to prevent laser-induced modification or carbonization of the spores. The total acquisition time of the Raman image composed of 720 spectra (pixels) was less than 7 min. The representative mean Raman spectra obtained from individual spores demonstrate the appearance of the band at 1017 cm^{-1}, which can be assigned to a chelate of Ca^{2+} of DPA (CaDPA). The Raman image was generated as

the integrated intensity of the band at 1017 cm^{-1} normalized to the band of phenylalanine at 1004 cm^{-1}. Thus, the spectral image reveals that CaDPA is present in the only spore of the agglomerate. The ability of Raman spectral imaging to spatially discriminate individual spores that do not exceed one micron in size and to detect CaDPA in a specific spore demonstrates the technique's high potential for rapid bacterial spores detection and the recognition of biological hazards.

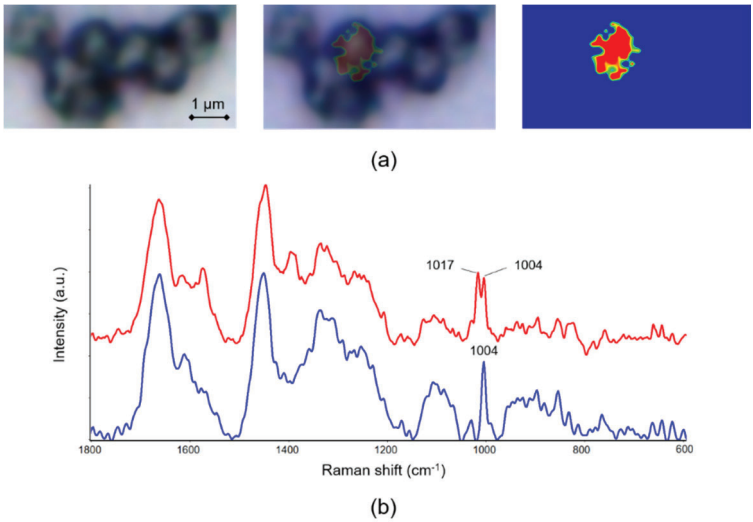

Figure 4-11. Detection of CaDPA in an individual spore by Raman spectral imaging. (a) From left to right: the optical image of the agglomeration of spores, the semi-transparent Raman image superimposed on the optical image, and the Raman image constructed as the integrated intensity of the CaDPA-specific Raman band at 1017 cm^{-1} normalized to the spectral band of phenylalanine at 1004 cm^{-1}. The red area indicates CaDPA content of the specific spore in the agglomeration. (b) The representative mean Raman spectra of the spore containing (red) and without CaDPA (blue) after baseline correction. The spectra are shown in the fingerprint region and offset for clarity.

Fast methods for investigations of biological tissue to diagnose diseases are increasingly required (Rau, et al. 2016). Combining the speed of the EMCCD detectors with the fast sample scanning mechanisms allows for Raman spectral imaging of large-area tissues without chemical labelling, as illustrated in Figure 4-12. The Raman map of a paraffin-embedded tissue section of a whole mouse brain of about 9 × 6 mm^2 was collected using a 780 nm laser for excitation (24 mW power at the sample), a 20×/0.4 metallurgical objective, a 50 µm slit aperture and a 25 µm step. The map was composed of 86,994 spectra acquired for 2.4 hours. The Raman image is constructed as the integrated intensity of the $\nu(CH_x)$ bands in 2800-3200 cm^{-1} spectral region and displays the diverse anatomical macro- and microstructures of the brain.

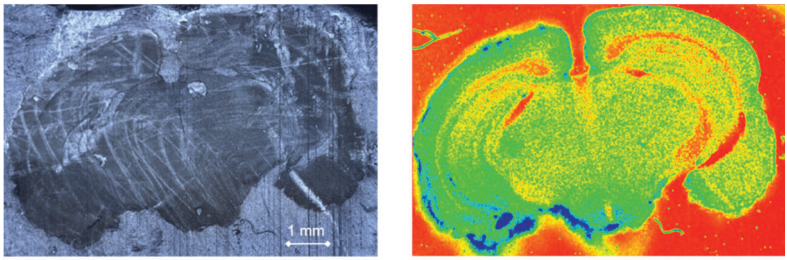

Figure 4-12. Optical (a) and Raman (b) images of the tissue section of a mouse brain.

This example suggests that Raman imaging can be applied to large-area natural tissues and organs, which makes this method a high potential technique for early diagnosis of diseases in clinical and non-clinical conditions.

Confocal Raman microscopy can also be used to obtain information about the molecular composition of tissues down to tens of microns below the tissue surface. The measurements at different depths allow infiltration of foreign substances or variation in concentration of the major constituents to be monitored in the volume of the tissue. Such information is of interest for fundamental research concerning the physiology and pathology of tissues, as well as applied research in the cosmetic and pharmaceutical industries.

Figure 4-13(a) shows representative Raman spectra of virgin and chemically reduced human hairs measured at the surface and in the hair's inner part. The measurements were performed using a 785 nm excitation wavelength (24 mW of laser power at the sample), an oil immersion 100×/1.25 objective and a 50 μm pinhole. A quartz coverslip was placed over the hair to prevent contact with the immersion oil. Since the diameter of hair was about 70 μm, the spectrum of the inner part of the hair fibre was measured at a depth of 34 μm from its surface. The spectra are normalized to the band at 1446 cm^{-1} assigned to $\delta(CH_x)$. The scissoring deformation vibrations of both CH_2 and CH_3 groups are often used as an internal standard for quantitative analysis of the Raman spectra of biological tissues.

The spectra reflect the differences in the hair constituents between the surface and the depth in both the virgin and chemically reduced hair. As can be seen, a band at 1297 cm^{-1} and a couple of bands at 1126 and 1063 cm^{-1} appear in the spectrum of the inner part of the virgin hair. These bands are assigned, respectively, to the twisting $\delta_t(CH_2)$ and stretching skeletal ν(C-C) vibrations of lipids. The manifestation of these bands evidences the relatively high concentration of lipids in the hair's inner (cortex) region. The presence of the Raman band at 510 cm^{-1}, ascribed to the stretching vibration of the disulfide ν(S-S) bond, confirms that the virgin hair is rich in a sulfur-

containing amino acid called cysteine. The relative concentration of S-S cross-links decreases from cuticle to cortex, which is consistent with the proteins in the cuticle being known to contain more sulfur than the cortical region. In contrast, in the spectrum of the chemically reduced (slightly bleached) hair, the relative intensity of the band at 510 cm^{-1} is higher in the cortex. Indeed, the bleach does not penetrate deep into the cortex region, but the bleaching opens the cuticle structure up and decreases the sulfur content in it. In practice, bleaching of human hair is recommended to reduce fluorescence and the dependence of the Raman spectra on pigmentation since it has been proven that light hairs are easier to analyze than dark ones.

Figure 4-13(b) illustrates the capability of confocal Raman microscopy to detect and profile the penetration depth of an active ingredient in a hair fibre. The Raman spectra of a blond natural human hair grafted with alkyl acrylate and its reference spectrum are shown in the 1800–1200 cm^{-1} spectral region. Crosspolymers based on alkyl acrylate are commonly used in cosmetics (shampoo and conditioners) and personal care products as thickening, film-forming, anti-aging agents and texture enhancers. The spectra were measured using the parameters indicated above. An optical micrograph of the hair treated with the active ingredient is presented in Fig. 4-13(c) in support of the fact that no visual signs of hair treatment are usually observed. The red cross denotes the point on the hair surface at which the depth profile was obtained. The Raman spectra measured at the surface of the hair (black), 2 μm (blue) and 4 μm (green) below the surface show the presence of the band at 1724 cm^{-1} ascribed to the stretching vibration ν(C=O) in alkyl acrylate. This band vanishes at a depth of 6 μm (brown) that evidences the depth of penetration of alkyl acrylate is limited by the outer cuticle layer, which is about 5 μm thick.

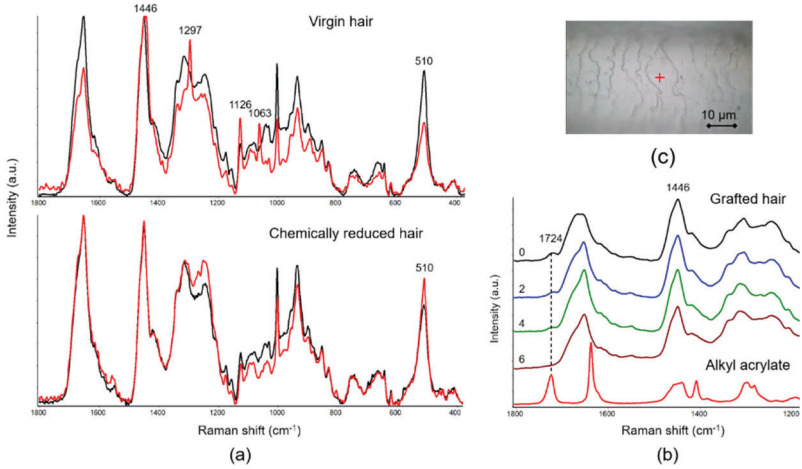

Figure 4-13. Raman spectra of the virgin, chemically reduced and grafted human hairs obtained at the surface and different depths below it. (a) The Raman spectra of the virgin (top) and chemically reduced (bottom) hair measured at the surface (black) and a depth of 34 µm (red) and demonstrated in the fingerprint region. The spectra are baseline-corrected and normalized to the band at 1446 cm^{-1}. (b) The Raman spectra of the natural blond hair grafted with alkyl acrylate measured at the surface (0) and the depths of 2, 4 and 6 µm below the surface of the hair as denoted by the numbers next to the spectrograms. The reference Raman spectrum of alkyl acrylate is shown for comparison. The spectra are shown after baseline correction, normalized to the band at 1446 cm^{-1} and offset for clarity. (c) Optical micrograph of the grafted hair and the point of the measurements indicated by the red cross.

In recent years, many cosmetic companies have intensified research into the deposition of a wide range of functional materials and active ingredients on the skin *in vitro*. Figure 4-14 demonstrates an example of confocal Raman spectral imaging to visualize the spatial distribution of trichloroacetic acid (TCA) as it diffuses into synthetic skin. TCA is a common ingredient in chemical skin peels used to remove moles and blemishes, correct

pigmentation and treat many other cosmetic skin problems. The synthetic testing substrate has been formulated to effectively mimic the properties of human skin in terms of topography, wetting properties, viscoelasticity, etc. The 3D Raman spectral image of the skin substrate treated with 20% aqueous solution of TCA shown in (a) was obtained using 532 nm excitation (10 mW of the laser power at the sample), a 60×/0.9 WI microscope objective and a 50 μm confocal pinhole with 0.5 and 2 μm steps in the horizontal plane and the vertical axis, respectively. The image is constructed as the integrated intensity of the Raman bands at 425 and 280 cm^{-1} normalized to that of the band at 1450 cm^{-1} in the spectra of the treated skin substrate. The reference spectrum of the 10% aqueous solution of TCA is shown in (b) for comparison. The relatively intense Raman bands at 430 and 283 cm^{-1} observed in the spectrum of TCA that do not overlay with the bands assigned to the skin substrate were selected as analytical bands to track the spatial distribution of TCA in the subsurface region of the substrate. The representative mean Raman spectra retrieved from the 3D image demonstrate that the bands are well observed at a depth of 6 μm and not detected at a depth of 18 μm in the substrate. The 3D Raman image demonstrates that TCA penetrates down to about 12 μm, which corresponds to the thickness of the upper portion of the stratum corneum layer. It is worth mentioning that this synthetic skin not only reproduces the properties of the human skin, but its Raman spectrum closely resembles those of the natural biological cells and tissues presented above.

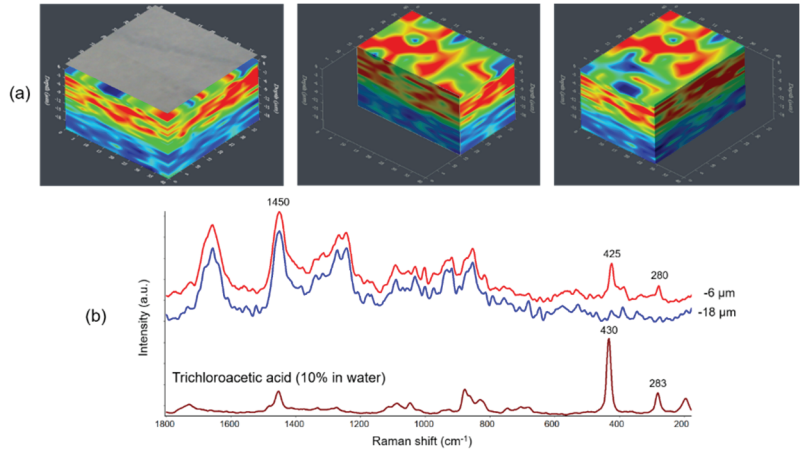

Figure 4-14. Confocal Raman spectrochemical imaging of the spatial distribution of a chemical peel (20% aqueous solution of TCA) in synthetic skin. (a) 3D Raman image displayed with the optical micrograph of the skin surface on top of the Raman image (left), a slice in the XZ plane (centre) and a YZ slice (right). The Raman image was generated as the integrated intensity of the bands at 425 and 280 cm^{-1} of TCA normalized to the peak at 1450 cm^{-1} in the spectrum of the skin substrate. The red portion of the image indicates the subsurface volume in which TCA predominantly accumulates. Diffusion of TCA into the skin reaches the depth of about 12 µm. (b) The representative mean Raman spectra of the treated skin substrate retrieved from the 3D Raman image at a depth of -6 (red) and -18 µm (blue) below the substrate surface and the spectrum of a reference 10% aqueous solution of TCA (brown) in the fingerprint region. The spectra are shown after the baseline correction and offset for clarity.

As there are many physical factors that affect the depth of the chemical peel penetration, completing a thorough Raman spectrochemical profile of the treated skin in vitro is crucial in determining these factors for particular cosmetic ingredient and the skin's properties. Finally, *in vitro*

characterization helps to relate and predict the results that can be obtained on human skin *in vivo*.

The fact that the confocal Raman microscopy and imaging is a technique that provides high spatial resolution and does not require any markers or stains makes it uniquely suitable for the analysis of biological samples. Since Raman spectroscopy works in an aqueous environment, this technique can be applied for studies of live cells and microorganisms and freshly prepared tissues.

The use of immersion objectives is recommended when working with both living biological objects and fixed ones. It improves the spatial resolution and allows for higher laser power to be focused on the sample, reducing the total time of the spectral measurements. Despite the effective heat dissipation when analyzing samples in an aqueous environment, careful control and optimization of laser power are necessary for noninvasive analysis of generally radiation-sensitive biological objects.

The Raman analysis can be carried out with different laser excitation wavelengths. The short wavelengths from UV to green may selectively enhance specific Raman bands, which would result in significant improvement in the detection of the corresponding chemical and structural constituents of biological samples. However, for living biological objects, reducing the "toxicity" of laser radiation on account of the use of red wavelengths (e.g., 633, 638, 647 or 660 nm) can be of crucial importance when biochemical processes, such as metabolic pathways or dynamics are to be studied. The dark red 780/785 nm excitations may help to reduce fluorescence from cell culture media, buffers and process liquids. The NIR

excitation at 830 nm may be particularly effective in mitigating fluorescence in the study of natural skin *in vivo*.

The fast scanning modes in a Raman microscope for 3D confocal imaging provide an essential advantage since information regarding the interior of biological objects (for example, tissues, as demonstrated above) is just as important as information obtained from a flat surface. The analyses of the complex Raman spectra and a large number of data in the spectrochemical images of biological samples can be a challenging endeavour without the proper application of multivariate mathematic and statistic (chemometric) techniques. Such methods can significantly improve the S/N ratio in the representative spectra and facilitate the assignments of the spectral features to the structure and composition of the biological systems.

4.4. Nanomaterials

The research and development of nanomaterials are currently one of the major drivers for the introduction of new materials and technologies into all aspects of the economy and life, as it aims to make the world healthier, cleaner and safer.

According to the generally accepted definition, nanomaterials include objects that have at least one size less than 100 nanometers. A very large volume fraction of interfaces and anisotropy of nanomaterials often contribute to their unique mechanical, optical, electronic, magnetic, chemical and other properties. Since conventional Raman microscopes cannot produce laser spots less than a few hundred nanometers in diameter in accordance with equation (3.1), each Raman spectrum will, therefore, contain the average response of a typically large number of nano-objects. Nevertheless, the sensitivity of Raman spectra to slight differences in short-

range structural changes in these materials can be used to identify and assess these changes. Moreover, if the nano-objects are dispersed or isolated and produce a strong enough Raman signal, then they can be spectroscopically characterized. The individual carbon nanotubes (CNTs) and graphene sheets, as demonstrated in the previous chapter, can be measured by confocal Raman microscopy with the spatial resolution determined by the diffraction limit of light used for the spectral excitation.

There is a fairly extensive literature on the application of Raman spectroscopy for the study of nanomaterials, such as a special issue of the "Journal of Raman Spectroscopy" (Kiefer, Gouadec and Colomban 2007) and the special issue of the open access journal of "Nanomaterials", which is currently being prepared for publication (Vergara 2021).

The discovery of CNTs in 1991 and their subsequent mass production has markedly accelerated interest in Raman spectroscopy as a general method for characterizing carbon nanomaterials. More recently, Raman has been used to characterize graphene, a single layer of carbon atoms arranged in a two-dimensional hexagonal net. Raman spectroscopy using almost any excitation wavelength is highly sensitive to the covalent carbon-carbon bonds that make up these nanomaterials and able to provide a wealth of information about their structure and properties. A mixture of sp^{3-} and sp^{2-} hybridized carbon may have a bandgap up to 6 eV, and the excitation of allotropes of carbon with the wavelength from NIR to deep UV may result in a resonant Raman scattering. The Raman spectra of allotropes of carbon are characterized by only a few distinctive spectral bands, which nevertheless contain useful information about these materials.

Figure 4-15 exemplifies the Raman spectra of graphene and CNTs. Graphene is a fundamental building block of many important carbon nanomaterials, including CNTs. The G-band is a common spectral feature of all sp^2-bonded carbon ascribed to the E_{2g} mode that arises from stretching the C-C bond in the graphene plane. The G-band is located at about 1585 cm^{-1} and, despite the resonance nature, its position is pretty much independent of the excitation wavelength, making it different from the other bands in the Raman spectrum of graphene. The position of the G-band is sensitive to the thickness of the graphene layer in accordance with the empirical formula:

$$\bar{\nu}_G = 1581.6 + \frac{11}{1 + n^{1.6}},$$

where $\bar{\nu}_G$ is the position of the G-band, and n is the number of graphene sheets. As the number of the sheets increases, the position of the G-band shifts to lower wavenumbers representing a slight softening of the C-C bonds. It is worth noting that the position of the G-band is also sensitive to doping and a minor strain. This needs to be considered when using the G-band position to determine the thickness of graphene.

The D-band that appears at approximately 1350 cm^{-1} is caused by disordered structure and defects in graphene. The band represents a ring breathing mode from sp^2-hybridized carbon rings, which is adjacent to a graphene edge or a defect. The presence of disorder in sp^2-hybridized carbons results in a strong resonance that makes Raman spectroscopy one of the most sensitive techniques to characterize disorder in the carbon materials. The D-band exhibits so-called dispersive behaviour. This means that there is a number of spectral modes underlying this band, and the different excitation wavelengths enhance specific modes. The consequence of this relation is

that both the position and shape of the D-band will vary substantially with the excitation wavelengths. As a result, it is important to use the same excitation laser wavelength for all measurements when the D-band is analyzed. The D-band is typically very weak in graphene. If the D-band is significant, it indicates that there are a lot of defects in the sample. The intensity of the D-band is proportional to the number of defects in the carbon nanomaterials.

The 2D-band, which manifests at about 2680 cm^{-1}, is the second-order of the D-band, sometimes referred to as an overtone of the D-band. The 2D-band appears as the result of a second-order two-phonon lattice vibrational process, but, unlike the D-band, it does not need to be activated by proximity to a defect. Consequently, the 2D-band is always a strong band in the Raman spectrum of graphene even when no D-band is present, but it is not associated with defects. The band exhibits a dispersive behaviour and, thus, the dependence of its position and shape on the excitation wavelength. The 2D-band can be used to determine the number of graphene layers. This is mainly because the position and shape of the 2D-band in multi-layer graphene differ from those in single-layer graphene. The 2D-band in single-layer graphene is much more intense and sharper than that in multi-layer graphene. The most prominent observation is that this band has a roughly two times higher peak intensity than the G-band in the spectrum of single-layer graphene. The 2D-band shifts to higher wavenumbers as the number of layers increases. The shift in the peak position results from the interaction between the stacked layers of graphene, which tends to shift the 2D-band to a higher frequency. The spectral profile of the 2D-band in the Raman spectrum of single-layer graphene is composed of a single spectral component, but in double-layer graphene, the profile is formed by four

components. It is worth noting that the 2D-band is very sensitive to graphene folding, which needs to be taken into account when analyzing this band to determine the number of layers in graphene samples.

The other Raman bands that can be observed in the spectra of graphene are the D'-band, which usually appears as a shoulder at about 1620 cm^{-1} on the profile of G-band; the overtone of the D'-band at ~ 3250 cm^{-1}; and the combination of D+G-mode at ~ 2940 cm^{-1}.

The Raman spectrum of a CNT is very similar to graphene, which is not surprising as the CNT is a single-dimensional form of sp^2-hybridized carbon that can be imaged as a rolled up sheet of graphene. There are two main types of CNTs: single-walled (SWCNTs) and multi-walled (MWCNTs). The structure of an SWCNT can be represented as a single graphene sheet rolled into a cylindrical tube with diameters from less than one to a few nanometers, while they can be up to several centimetres in length. When multiple graphene sheets are rolled into concentric tubes, the resulted structure forms an MWCNT.

The G- and 2D(G')-bands are observed in the Raman spectrum of an SWCNT. When considering the Raman spectra of CNTs, the 2D band is sometimes referred to as the G'-band, but both 2D and G' are accepted names for this band. Due to defects in the nanotubes, the D-band is also observed, and its intensity relative to that of the G-band is often used as a measure of the quality and purity of the nanotubes. The unique feature of the Raman spectrum of SWCNTs is a spectral band of the radial breathing mode (RBM). As the name suggests, the RBM originates from an in-phase radial movement of all carbon atoms of the nanotube, that is, from its expansion and contraction as if the nanotube is breathing. The RBM band

is located between 50 and 400 cm^{-1} in the Raman spectrum of an SWCNT. It was empirically established that the position of the band $\bar{\nu}_{RBM}$ is inversely proportional to the nanotube diameter, d_{CNT}:

$$\bar{\nu}_{RBM} = \frac{C_1}{d_{CNT}} + C_2 \,. \tag{4.1}$$

In the case of an isolated SWCNT, the constants C_1 and C_2 are equal to 224 $cm^{-1}\times nm$ and 0 cm^{-1}, correspondingly. For non-isolated (bundled) SWCNTs, the coefficient C_2 was reported to be 14 cm^{-1} (Rao, et al. 2001), as the inter-tube interactions slightly shift the positions of RBM bands to higher wavenumbers. For isolated SWCNTs, the coefficient C_1 has then been refined (Jorio, et al. 2001) to the value of 248 $cm^{-1}\times nm$. It worth noticing that the precise values of these constants are not critical. Indeed, SWCNTs within the same bundle typically possess similar physical properties, and minor variations in the values of C_2 may be attributed to the differences in sample preparation and measurement conditions. As follows from (4.1), an SWCNT with the RBM band at about 250 cm^{-1} in its Raman spectrum has a diameter of approximately 1 nm.

The variety of SWCNTs is determined by a pair of integers (n, m) from which their diameter, chirality and semiconducting or metallic properties can be derived. Chirality describes the orientation of the rolled graphene sheet relative to the main axis of the nanotube. In the spectral region of the manifestation of RBM modes, multiple bands are observed if the sample contains nanotubes of various sizes and chirality.

Figure 2-3 in Chapter Two shows the spectrum of SWCNTs obtained when a nanotube bundle was excited at three laser wavelengths. As was demonstrated, the spectra are highly dependent on the excitation

wavelength, which follows from the resonance behaviour mentioned above. As a result, the spectra were contributed from nanotubes of specific diameters that come into resonance with particular excitation wavelengths. A theoretical relationship between the electronic energy separation that establishes the resonance conditions and the diameter of SWCNTs is presented in the well-known Kataura plot (Kataura, et al. 1999, Dresselhaus, Dresselhaus and Jorio 2007), i.e., the correlation plot of the excitation laser energy vs. the position of RBM band in the Raman spectrum. When the Raman spectra of SWCNTs are recorded, the Kataura plot allows one to determine its semiconducting or metallic properties and estimate their diameters and chirality (n, m).

As is apparent from Figure 4-15, an MWCNT has a very similar spectrum to that of an SWCNT. The major differences are the lack of RBM bands and a much more prominent D-band in the MWCNT. The RBM modes are absent because the multiple outer walls restrict the breathing mode. The more prominent D-band, which indicates more disorder in the structure in MWCNTs, is to be expected due to the higher probability of defect formation given the multi-layered structure of the nanotube.

A detailed interpretation of the Raman spectra of graphene and CNTs has been provided by Rao (Rao, et al. 1997) and Dresselhaus (Dresselhaus, Dresselhaus and Saito, et al. 2005, Malard, et al. 2009, Dresselhaus, Jorio, et al. 2010).

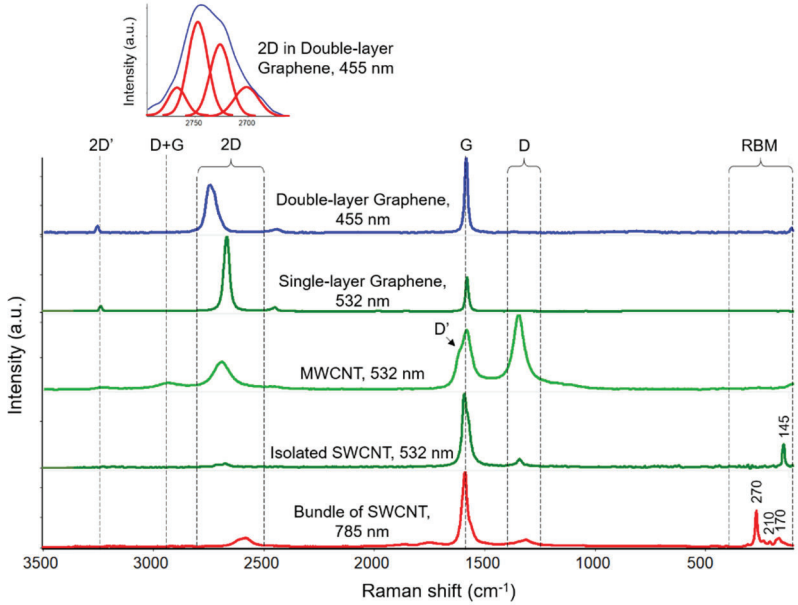

Figure 4-15. Representative Raman spectra of graphene, SWCNTs and MWCNTs obtained using 455, 532 and 785 nm excitation wavelengths. Vertical dotted lines denote the positions of the major spectral bands or the intervals of their manifestation. In the spectrum of the isolated SWCNT, the only RBM band appears at 145 cm^{-1}, while in the spectrum of the SWCNT's bundle, the bands at 270, 210 and 170 cm^{-1} manifest as the result of the resonance with 785 nm laser excitation. Note the shift of the 2D-band towards the lower wavenumbers when increasing the excitation wavelength. The upper left inset shows the result of curve-fitting of the 2D-band by four Gaussian/Lorentzian spectral components that confirm the bilayer structure of graphene.

Figure 4-16 illustrates the application of confocal Raman imaging for tracking changes in the diameter of an isolated SWCNT by the shift in the position of the RBM band. The shift can be caused by the expansion of the nanotube upon absorption of water (Rzhevskii 2019). The map of the SWCNT on the Si substrate was acquired using a 100×/0.9 metallurgical

objective, a 532 nm laser for excitation (4 mW laser power at the sample), a 50 μm pinhole and a 0.2 μm step. The Raman image (a) is generated as the shift of the RBM band from 149 to 145 cm^{-1} (b) thereby evidencing the increase in the diameter of the nanotube in accordance with (4.1). The unique capability of carbon nanotubes to penetrate biological cell membranes makes them a new perspective tool in nanobiotechnology and nanomedicine for delivering therapeutic agents into the cytoplasm and, in many cases, into the nucleus. While the amount of the drug substance loaded into the individual carbon nanotube of a nanometer diameter can scarcely be detected directly by any spectroscopic means, the increase in the carbon nanotube diameter upon "swallowing" the drug is expected to be observed by Raman microscopy. The high spatial resolution Raman imaging may bring further advantages for tracking and real-time monitoring of drug delivery *in vivo*.

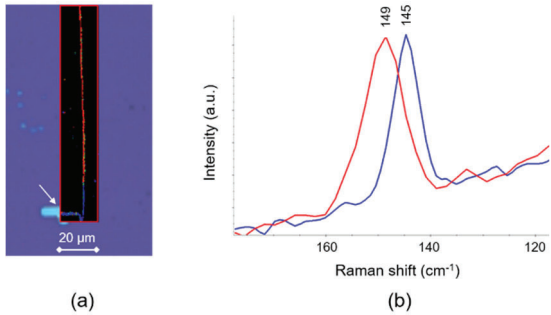

Figure 4-16. The Raman image (a) and the change in the diameter of individual SWCNT (b) upon absorbing water. Blank (red) and loaded (blue) portions of the SWCNT are discovered in the Raman image. The Raman spectra in the region of manifestation of the RBM modes are shown in the colours corresponding to the empty and filled parts of the nanotube in the Raman image. The white arrow points to a micro nozzle used to inject water into the SWCNT.

Advances in the study of graphene and CNTs using Raman microscopy and imaging have facilitated the application of this technique for the characterization of novel two-dimensional transition metal dichalcogenides (TMDCs) and single-dimensional boron nitride nanotubes (BNNTs).

TMDCs, such as MoS_2, $MoSe_2$, WS_2 and WSe_2, are gaining an energetic practical interest in electrochemistry, the construction of high-performance energy storage capacitors and the fabrication of optoelectronic devices. Similar to graphene, these materials can be constituted by monolayer and multi-layered structures, and the number of layers strongly influences their electrical, optical and other properties.

It was found that the most prominent Raman bands of molybdenum disulfide (MoS_2) at about 382 (E_{2g}^1) and 405 cm^{-1} (A_{1g}) exhibited sensitive thickness dependence (Lee, et al. 2010) and that Raman and photoluminescence images can be used to probe spatially varying differences in the structure of this material (Tuschel 2015).

BNNTs have complementary properties to those of CNTs. They can be considered a single sheet of hexagonal boron nitride (wide-gap semiconductor) rolled upon itself. BNNTs are potentially promising materials in structurally reinforced composites due to their unique mechanical, electro-mechanical and thermal properties, as well as for applications in solar cell technology and optoelectronics, based on their high electron mobility and optical transparency. Raman microscopy is just beginning to be actively used for the study of BNNTs. It has been recently demonstrated that the phonon modes of single-walled BNNTs can be measured in resonant conditions using deep-UV excitations (Arenal, et al. 2006) since the electronic gap of BNNTs is estimated to exceed 5.5 eV.

It should be emphasized that, regardless of the excitation wavelength, it is necessary to carefully control the laser radiation aimed at the samples in order to avoid laser-induced modification of the nanomaterials. Many carbon nanomaterials are sensitive to laser power and, when measuring the Raman spectrum of these materials with dry objectives and a high *NA*, the recommended laser power at the point of measurement should not exceed a few mW to ensure reproducible results. Local overheating of the samples may lead to the change of the relative intensities of the G- and D-bands in the Raman spectra of these materials. Meanwhile, the ratio of the peak intensity of the D-band to that of the G-band, I_D/I_G, has been successfully used to evaluate the dimensions of nanocrystallites in carbon materials. A relation between this ratio and the size of the nanocarbon clusters L_g was empirically proposed by Tuinstra and Koenig (Tuinstra and Koenig 1970) for the laser excitation at 514.5 nm:

$$\frac{I_D}{I_G} = \frac{C(\lambda)}{L_g(nm)}, \qquad C(\lambda_{514.5\,nm}) = 44$$

An illustrative example of the importance of a fine laser power control when measuring Raman spectra of nanomaterials is presented is in Figure 4-17. The Raman spectrum of nickel oxide (NiO) nanopowders can only be obtained at a laser power not exceeding 0.1 mW at the sample since the higher laser power results in the thermal decomposition of NiO.

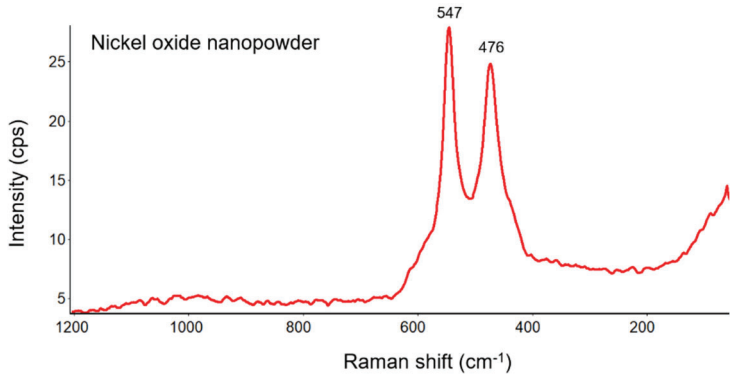

Figure 4-17. The Raman spectrum of the NiO nanopowder obtained with the 532 nm laser at 0.1 mW of the laser power at the sample.

The spectrum was accumulated using a 532 nm laser, a 50×/0.75 metallurgical objective and a 50 μm slit for 10 min. The Raman bands at 547 and 476 cm^{-1} are assigned to the longitudinal optical (LO) and transverse optical (TO) phonon modes of NiO, respectively. The broad and weak spectral feature around 1000 cm^{-1} may be attributed to the overlapped bands originating from the optical overtones (second-order phonon modes) 2LO and 2TO.

4.5. Raman and photoluminescence imaging in mineralogy and gemology

Raman microscopy and imaging have been widely recognized as an effective technique for the analysis of gems, minerals and rock samples (Karr 1975, Andò and Garzanti 2014). Successful applications of this technique cover virtually all sub-disciplines in mineralogy, gemology and geochemistry.

Nondestructive identification, characterization and semi-quantitative analysis of different mineral phases and related materials in rocks and soils can be easily performed using Raman imaging. Figure 4-18 provides a Raman image of a polished surface of metamorphic rock. The spectral map was collected from an area of about 1 × 0.5 mm^2 using a 532 nm laser (10 mW at the sample) for excitation, a metallurgical 50×/0.75 objective, a 50 μm pinhole and a 5 μm sampling step. The map is composed of 21168 spectra collected with an integration time of 0.05 s per spectrum. The different colours in the Raman image (a) correspond to the spectral components extracted using MCR method. Identification of the mineral makeup of the rock by the spectral components was then performed using commercially available Raman libraries of minerals. One of the most useful and valuable spectral libraries for identifying minerals is the RRUFF database (RRUFF n.d.). The spectral components and corresponding minerals identified in the RRUFF library are shown in (b). The Raman image demonstrates the mineral composition and texture of the rock with domains of different shapes and sizes. The MCR method yields the percentage that each spectral component occupies in the imaged area of the sample. The assessment resulted in the following mineral assemblage: actinolite (35%) + albite (24%) + quartz (18%) + epidote (11%) + titanite (7%). The assemblage corresponds to the typical one for greenschist rock, with titanite present in the rock as a likely accessory mineral.

Although the surface of the metamorphic rock was flat and highly polished, it is now possible to analyze untreated natural geological samples. The surface topography tracking capabilities mentioned in Chapter Three minimize the sample preparation and help to characterize geological

samples by acquiring confocal Raman images from almost any shape of their surface.

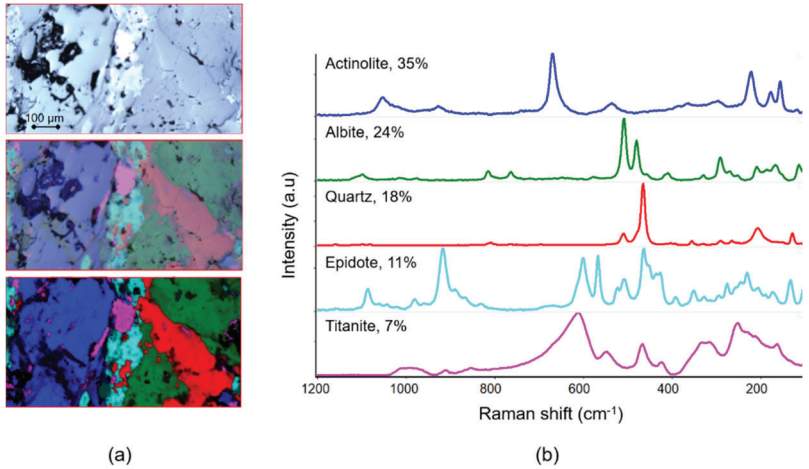

Figure 4-18. Raman image demonstrating the mineral composition and texture of an area of basalt rock. (a) From top to bottom: the optical image of the polished surface of the rock, the semi-transparent Raman image superimposed on the optical image and the colour-coded Raman image generated as the spectral components extracted by the MCR method. (b) The MCR spectral components and the corresponding minerals identified using the RRUFF spectral library. The proportion of the colour-coded areas in the Raman image corresponding to the identified mineral phases is indicated by the percentage next to the mineral names.

Due to the phonon excitations and the involvement of metals and oxygen atoms in the lattice vibration of minerals, the Raman bands of minerals, as a rule, manifest in the fingerprint region of the spectrum. The analysis of Raman spectra in this region can also be applied to art, archaeology and other related disciplines where analytical goals include the identification of mineral pigments in paintings, mineralogical phases of ceramics, sculpture

building materials and mineral constituents in ancient and contemporary objects.

As a nondestructive technique, Raman microscopy is also an ideal tool for analyzing gems and jewels. Aside from the quick identification of stones and distinguishing between genuine gems and fake specimens, Raman microscopy is useful in identifying natural and synthetic minerals. Raman microscopy is able to evidence whether stones, such as diamonds, have been synthesized or artificially processed via high pressure and high temperature (HPHT) or treated with special fillers to enhance their aesthetical look and raise their value.

HPHT treatment mimics the exact same conditions that occur in the volcanic environments where diamonds are usually formed. Synthetically grown HPHT diamonds are subjected to extremely high temperatures and pressures inside special chambers. By refining the process of diamond growth, the producers of synthetic diamonds make all their physical, chemical, optical and aesthetical properties practically identical to those of high quality mined diamonds.

The availability of HPHT diamonds has a different impact on industrial diamond applications and diamond jewellery. From one side, the diamond materials are demanded and can be used in optics (UV and IR windows, laser optical components and lenses for gyrotrons), the semiconductor industry (key elements in diodes, transistors and thyristors, media storage devices for information and quantum computing), and electrochemical sectors of industry (electrode in electrolytes and special sensors) just to name a few. On the other side, the high-yield production and increased sizes of HPHT diamonds, which are cheaper but still of jewellery quality, pose a

threat to the mined diamond industry and jewellery trade. Thus, diamonds need to be confidently identified as genuine natural colourless diamonds or not, and the grading laboratories, members of the diamond trade and consumers must be informed appropriately.

The above-mentioned identity of the properties of HPHT treated and high-quality natural diamonds requires the development of the technologies that could be used to distinguish between these types of diamonds. The sharp peak in the Raman spectrum of the diamond at 1332 cm^{-1} (see Fig. 3-15) is sensitive to its crystallinity, purity, defects and many other properties. However, no effect of HPHT treatment on the spectral parameters of this peak was found. An advanced spectroscopic technique based on photoluminescence (fluorescence) images obtained using a Raman microscope has been recently developed and effectively applied at the Gemological Institute of America to discern synthetic and HPHT treated diamonds (Loudin 2017).

Fluorescence spectroscopy has been successfully used in gemological laboratories to verify whether a diamond specimen is natural, synthetically grown or HPHT treated. This method is based on the detection and identification of defects in the diamond lattice (Fisher and Spits 2000). In gemology, the term photoluminescence (PL) is used to emphasize that PL spectra are measured at liquid nitrogen (LN) temperature using laser excitation, while fluorescence has traditionally been measured at room temperature with a broad-band source. In combination with laser excitation, sample cooling often reveals weak PL peaks that might not be detectable at room temperature.

An essential drawback of conventional PL measurements is that spectra are often collected from a single spot or a few spots of the diamond crystal and may not characterize the entire sample. PL spectral imaging can be used to identify point defects and display their spatial distribution in the whole diamond sample. However, as the diamond must be cooled to the LN temperature (~77 K, or – 196^0C) to produce sharp PL spectral bands, an open bath LN sample holder is commonly used to facilitate the productivity of the analyses. If open bath cooling is used, then high-speed mapping methods are needed because the liquid nitrogen quickly vaporizes at atmospheric temperature and pressure. The fast sample scanning mechanisms combined with EMCCD detectors available in Raman imaging microscopes meet the requirement of a short measurement time and allow for spatially resolved PL images of the diamond.

Figure 4-19 shows the HPHT synthesized 0.49 carat round diamond cut, shortwave UV image and PL images acquired from the table of the diamond (a). The diamond was placed in the open bath LN sample holder, and the mapping was acquired using a 10×/0.25 metallurgical objective, a 50 μm pinhole and a 5 μm step. The total time for the map acquisition was less than 5 min. The PL spectra revealed the doublets at 736.6/736.9 nm and 882.6/884.3 nm (b). The PL images were generated as the integrated intensities of the PL doublets. The doublets are attributed to the silicon split-vacancy defects $[Si\text{-}V]^-$ and nickel impurity centres Ni^+ in the diamond lattice excited using the 633 and 780 nm lasers, respectively. While the $[Si\text{-}V]^-$ defect is common in synthetic diamonds (Clark, et al. 1995), the solvent catalysts used in the HPHT methods to grow the synthetic diamond, either intentionally or unintentionally, contain Ni in varying quantities. Since Ni^+ defects are confined exclusively to the octahedral growth sectors {111} of

the diamond (Lawson and Kanda 1993), the PL spectral images confirmed that the [Si-V]$^-$ defects are bounded to the same octahedral growth sectors. The images reveal that the defects are mostly concentrated along the sector boundaries. The results demonstrate that fast PL spectral imaging of an LN-cooled diamond is the technique of choice for the rapid detection and determination of the spatial distribution of the point defects in the HTHP grown diamond.

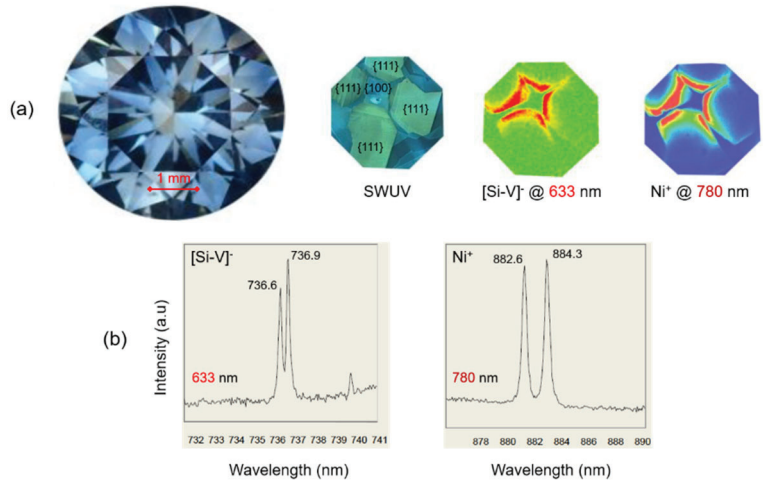

Figure 4-19: Spatial distribution of [Si-V]$^-$ and Ni$^+$ defects in an HPHT synthetically grown diamond of jewellery quality. (a) From left to right: 0.49 carat vivid blue diamond, SWUV image of the diamond top showing the growth sectors {111} and {100}, and PL images revealing the distribution of the [Si-V]$^-$ and Ni$^+$ defects concentrated predominantly at the edges of the growth sectors. (b) PL spectral doublets assigned to the [Si-V]$^-$ and Ni$^+$ defects in the diamond excited using 633 and 780 nm laser excitations.

Since the PL bands of point defects in diamonds manifest in relatively far apart regions of the wavelength scale, Raman microscopes are required to use, as a rule, several excitation wavelengths for measuring these bands.

4.6. The accurate measurement of spectral shifts in the Raman spectrum of Silicon

Strain control in Si and other semiconductors is of great importance in microelectronics to prevent quality problems in integrated circuits and microdevices. Raman microscopy has become a popular technique for local strain measurements in Si-based materials and structures (De Wolf 1996). The position of the band at 520 cm^{-1} in the spectrum of Si is highly sensitive to the strain and is linearly proportional to the amount of deformation. Raman spectral imaging can be applied to monitor strain in Si by measuring a slight shift (typically within 1 cm^{-1}) of this band at different locations in the sample and generating a "strain" image with a micrometre spatial resolution. However, the environmental and instrumental instabilities, which can become especially noticeable during a prolonged imaging acquisition, may lead to some drift of the position of the spectral band in time. Therefore, in order to measure small changes in the position, a reference spectral line is required to calibrate the Raman shift axis in the course of the measurements. One can use the unfiltered plasma lines of the excitation laser, the emission lines of the incandescent Ne lamp, or a line generated by the auxiliary laser as the reference lines. However, neither of these options provide a universal solution for the shift measurement. For example, the sharp and stable plasma lines are only generated by gas lasers. Moreover, the spectral positions of the reference spectral lines follow the drifts in the spectrograph but do not track the instabilities in the laser excitation frequency, as discussed in Chapter Three.

A simple accessory that accounts for all possible instabilities related to the environment, the spectrograph and the excitation laser is outlined in Figure 4-20. The accessory represents an insert with a window made of an optically transparent material that produces a strong and sharp Raman band. The preferable material is diamond, although other materials, such as calcium fluoride, calcite and a combination of these materials, can be used. The insert can easily be attached to a common objective used in a Raman microscope. The position of the window is adjustable along the vertical axis so that the window can be placed close enough to the surface of the sample under study. As a result, the Raman band of the window material will be registered along with the spectral bands of the sample. The position of the spectral band of the window material is used as reference one for the real-time calibration of the Raman shift axis in the course of the measurements. Any drift in the Raman shift wavenumbers caused by temperature or instrumental instability results in a synchronous shift of the bands in the Raman spectra of both the sample and the reference window.

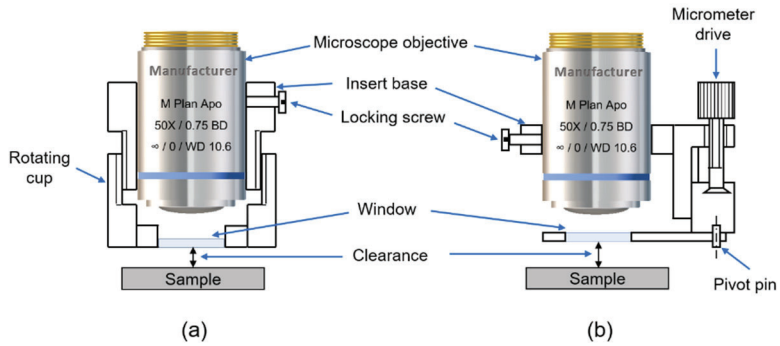

Figure 4-20: Two variants of an accessory design with an optical window that provides reference spectral bands for accurate measurements of Raman shifts. (a) The insert with the window in the rotating cup adjusts the clearance between the window and sample. (b) The window embedded in a slat that can be brought into and out of the optical path by rotating around the pivot pin. The micrometre drive provides positioning of the window relative to the sample.

The typical procedure for installation and adjustment of the accessory with a diamond window is as follows:

1) The accessory is attached to an objective;
2) The diamond window is moved along the vertical axis until its lower surface appears in optical focus: the position of the window corresponds to a zero clearance between the window and a sample surface;
3) The window is moved slightly upward, and the Raman spectrum is recorded until the intensity of the diamond band at 1332 cm^{-1} decreases to a level that still allows accurately determine its position: under this condition, there is sufficient clearance between the window and the sample;
4) The sample under study is brought into the focus.

The diamond window allows direct viewing of the sample through the objective. Depending on the sample, the window position may be finely adjusted to ensure the Raman bands of the sample and the diamond are optimized by intensity.

Figure 4-21 shows the fragment of the structure fabricated in the process of the local oxidation of Si (LOCOS). The LOCOS structure was observed and measured through a 100×/0.8 long working distance metallurgical objective equipped with a 0.5 mm thick diamond window insert. In the figure, the

Raman spectral images generated as the position of the Si band, which varies in the narrow range of 520.9–520.4 cm^{-1}, are superimposed on the optical image of the LOCOS structure in the Si wafer. The Raman images were obtained using a 532 nm laser for excitation (6 mW of the laser power at sample), a 25 μm pinhole and a 0.1 μm step. The total number of spectra in both Raman images was 74462, and the total acquisition time was about 30 min. Compressive stress shifts the Raman peak towards higher wavenumbers, while tensile stress shifts to lower wavenumbers, which appears in Raman spectral images.

Although in this example the shift of the Si band was observed within the range of 0.5 cm^{-1}, the position of spectral bands can be determined with an accuracy better than 0.03 cm^{-1} using the accessory with the diamond window.

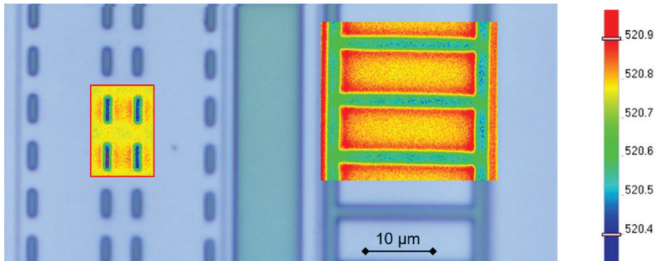

Figure 4-21: Optical and Raman images of the Si wafer fragment with the LOCOS structure obtained using an insert with a diamond window attached to a 100×/0.8 metallurgical objective. The Raman images demonstrate the shift of the Si band at 520 cm^{-1} calculated using the position of the reference spectral peak of the diamond window.

It is recommended to fit the experimentally measured Raman bands by a model spectral profile to determine the positions of the peaks as accurately as possible.

4.7. Fluorescence and Raman imaging for the detection of gunshot residue for forensic purposes

Raman spectroscopy and, especially, microscopy are becoming increasingly popular for forensic evidence analysis. The quantitative and nondestructive nature of Raman spectroscopy ensures the objectivity and reliability of analyzes, as well as the preservation of physical and biological evidence. Raman microscopy is used in a variety of forensic areas for the analysis of trace evidence recovered at crime scenes, including the identification of biological stains (Sikirzhytski, Virkler and Lednev 2010), drugs and other illicit substances (Bumbrah and Sharma 2016), pigments used in automotive paints (Muro, et al. 2015), hairs and fibres.

Recently, it has been shown that Raman microscopy can help link gunshot residue to the type and calibre of its ammunition source (Lopez-Lopez, Delgado and Garcıa-Ruiz 2013, Bueno, Sikirzhytski and Lednev 2012). When a gun is fired, components of the ammunition vaporize and form particles that can settle on the target, shooter or nearby objects. The gunshot residue particles (GSR) contain two distinct subclasses: inorganic gunshot residue (IGSR) and organic gunshot residue (OGSR). IGSR originates from the primer of an ammunition cartridge, whereas OGSR stems from gunpowder.

The most common and standardized technique for GSR analysis is scanning electron microscopy coupled with energy dispersive X-ray spectroscopy (SEM-EDX). This technique aims to detect heavy metals, such as lead, antimony and barium. The particles analyzed using SEM-EDX belong to

the IGSR class and thus originate from the primer component of the ammunition. However, SEM-EDX spectroscopy is extremely time-consuming, as analysts spend a great deal of time searching for and locating the particles. This search time is prolonged due to the large sample areas and the time utilized to analyze non-GSR particles and debris, such as skin and fibres, which can obscure particles of interest. Furthermore, the development of green ammunition, which is lead-free and non-toxic, makes it difficult for forensic science research to rely on metal analysis alone because the characteristic triad of heavy metals is not present in these samples due to the exclusion of lead. As SEM-EDX spectroscopy is not applicable for the analysis of OGSR or GSR particles originating from green ammunition, the characterization and analysis of these particles using Raman microscopy is gaining importance.

Raman imaging combined with multivariate analysis was successfully applied to detect and identify both IGSR and OGSR on an adhesive tape and stab (Lopez-Lopez, Fernandez de la Ossa and Garcıa-Ruiz 2015, Bueno, Halámková, et al. 2018). Collecting GSR particles with lift tapes and stubs is a common procedure in criminal shooting incident investigations. However, other microscopic objects adhering to the tape, as well as folds and irregularities in the adhesive on the tape, can make optical image analysis and GSR particle recognition problematic. A novel method for detecting and identifying GSR has been recently proposed (Khandasammy, Rzhevskii and Lednev 2019). This method involves fast fluorescence imaging of a lift tape to detect potential OGSR particles, followed by measuring Raman spectra and identifying the composition of the detected particles by their spectra. This two-pass technique can ensure that debris fragments are not misidentified and OGSR particles are correctly

recognized. Figure 4-22 (a) demonstrates optical, fluorescence and Raman images of an adhesive lift tape with GSR particles. The fluorescence image was acquired from the area of 6.1×6.4 mm^2 using a metallurgical 10×/0.25 objective, a 455 nm laser for excitation (2 mW of the laser power at the sample), a 50 μm slit aperture and a 4 μm step resulting in about 2.5 million spectra. The total collection time was about 1 hour. The spectral image was generated as the intensity of the fluorescence at 3400 cm^{-1}. Note that the laser wavelength of 455 nm was used as it is well suited for exciting both fluorescence and Raman scattering of GSR particles.

As the OGSR particles fluoresce under excitation in the visible spectral range, fluorescence imaging was applied to find and refine the location of the OGSR particles on an adhesive tape. The subsequent acquisition of Raman spectra of each recognized particle, numbered on the right inset, was performed using an automated particle analysis procedure. The representative mean Raman spectra of particles 2, 3 and 5 are shown in (b). The Raman spectra obtained from particles 1, 4, 6 and 7 are similar to the spectrum of particle 2. The bands at 1287 and 850 cm^{-1} are assigned respectively to the symmetric stretching of $\nu_s(NO_2)$ and scissoring $\delta(NO_2)$ vibrations in the nitrate ester functional group. Modern smokeless ammunition propellants often consist of nitrate ester explosives. The small Raman images superimposed on the particles in the right inset are generated as the integrated intensity of the nitrate ester band at 1287 cm^{-1}.

The noticeable red-coded areas in particles 1, 2, 4, 6 and 7 provide evidence of the presence of the nitrate ester, thereby confirming that these particles belong to the OGSR of the propellants. In the Raman spectrum of the

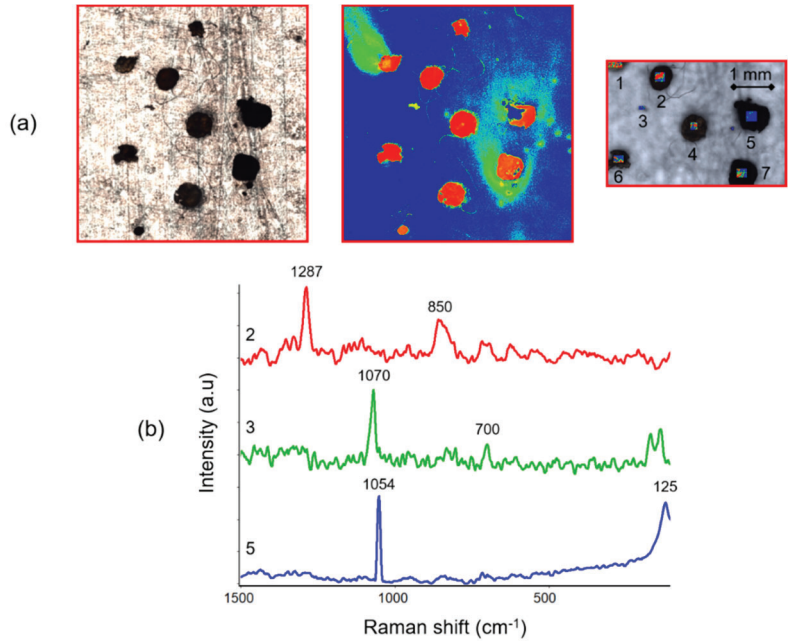

Figure 4-22: Fluorescence and Raman image analysis of GSR particles on adhesive tape. (a) From left to right: the optical image of the adhesive tape, the spectral image with the red colours indicating intense fluorescence from GSR particles, and the optical image of the central region of the adhesive tape with Raman images obtained from areas inside particles 1–7. The Raman images, which are constructed as the integrated intensity of the band at 1287 cm^{-1} ascribed to the nitrate ester functional group, indicate OGSR particles 1, 2, 4, 6 and 7 from the propellant. (b) The representative mean Raman spectra of particles 2, 3 and 5. The Raman bands in particles 3 and 5 can be assigned to heavy metal salts, such as $BaCO_3$ and $PbSO_4$, which are commonly used in ammunition primers.

relatively small particle 3, the two peaks at about 1070 and 700 cm^{-1} are assigned, respectively, to symmetric stretching $\nu_s(CO_3)$ and in-plane bending $\delta(CO_3)$ vibrations. The band at 1054 cm^{-1} in the Raman spectrum

of particle 5 can be assigned to $\nu_s(SO_4)$. These bands may prove the presence of heavy metal salts, such as $BaCO_3$ and $PbSO_4$ commonly used in ammunition primers, in particles 3 and 5, respectively.

Fluorescence and Raman spectral imaging demonstrates great potential for the analysis of both IGSR and OGSR particles. Given the recent advances in fast spectral imaging techniques, this method is a good prerequisite for creating a highly automated routine for detecting and identifying GSR particles by their spectral characteristics.

References

Andò, S., and E. Garzanti. 2014. *Raman spectroscopy in heavy-mineral studies.* Vol. 386, in *Sediment Provenance Studies in Hydrocarbon Exploration and Production, Geological Society, London*, by R.A. Scott, H.R. Smyth, A.C. Morton and N. Richardson, 395–412. London: Geological Society, Special Publications. https://doi.org/10.1144/SP386.2.

Antonio, K.A., and Z.D. Schultz. 2014. "Advances in Biomedical Raman Microscopy." *Anal. Chem.* 86: 30–46. https://doi.org/10.1021/ac403640f.

Arenal, R., A.C. Ferrari, S. Reich, L. Wirtz, J.-Y. Mevellec, and S. Lefrant. 2006. "Raman Spectroscopy of Single-Wall Boron Nitride Nanotubes." *Nano Lett.* 6 (8): 1812-1816. https://doi.org/10.1021/nl0602544.

n.d. *BioTools.* Accessed July 28, 2020. https://biotools.us/.

Bueno, J., L. Halámková, A. Rzhevskii, and I.K. Lednev. 2018. "Raman microspectroscopic mapping as a tool for detection of gunshot residue on adhesive tape." *Anal. Bioanal. Chem.* 410: 7295–7303. https://doi.org/10.1007/s00216-018-1359-1.

Bueno, J., V. Sikirzhytski, and I.K. Lednev. 2012. "Raman Spectroscopic Analysis of Gunshot Residue Offering Great Potential for Caliber Differentiation." *Anal. Chem.* 84 (10): 4334−4339. https://doi.org/10.1021/ac203429x.

Bugay, D.E. 2001. "Characterization of the solid-state: spectroscopic techniques." *Adv. Drug Deliv. Rev.* 48: 43–65.

Bumbrah, G.S., and R.M. Sharma. 2016. "Raman spectroscopy – Basic principle, instrumentation and selected applications for the characterization of drugs of abuse." *Egypt. J. Forensic Sci.* 6 (3): 209–215. https://doi.org/10.1016/j.ejfs.2015.06.001.

Clark., C.D., H. Kanda, I. Kiflawi, and G. Sittas. 1995. "Silicon defects in diamond." *Phys. Rev. B* 51 (23): 16681-16688.

n.d. *CytoSpec.* Accessed July 26, 2020. http://www.cytospec.com/index.php.

De Wolf, I. 1996. "Micro-Raman spectroscopy to study local mechanical stress in silicon integrated circuits." *Semicond. Sci. Technol.* 11: 139–154.

Dresselhaus, M.S., A. Jorio, M. Hofmann, G. Dresselhaus, and R. Saito. 2010. "Perspectives on Carbon Nanotubes and Graphene Raman Spectroscopy." *Nano Lett.* 10 (3): 751–758. https://doi.org/10.1021/nl904286r.

Dresselhaus, M.S., G. Dresselhaus, and A. Jorio. 2007. "Raman Spectroscopy of Carbon Nanotubes in 1997 and 2007." *J. Phys. Chem. C* 111 (48): 17887–17893. https://doi.org/10.1021/jp071378n.

Dresselhaus, M.S., G. Dresselhaus, R. Saito, and A. Jorio. 2005. "Raman spectroscopy of carbon nanotubes." *Phys. Rep.* 409 (2): 47–99. https://doi.org/10.1016/j.physrep.2004.10.006.

Everall, N., J. Lapham, F. Adar, A. Whitley, E. Lee, and S. Mamedov. 2007. "Optimizing Depth Resolution in Confocal Raman Microscopy: A Comparison of Metallurgical, Dry Corrected, and Oil Immersion Objectives." *Appl. Spectrosc.* 61 (3): 251–259.

Everall, N.J. 2000. "Confocal Raman Microscopy: Why the Depth Resolution and Spatial Accuracy Can Be Much Worse than You Think." *Appl. Spectrosc.* 54 (10): 1515–1520.

Fisher, D., and R.A. Spits. 2000. "Spectroscopic evidence of GE POL HPHT-treated natural type IIA Diamonds." *Gems Gemol.* 36 (1): 42–49. https://www.gia.edu/doc/SP00.pdf.

Jorio, A., R. Saito, J.H. Hafner, C.M. Lieber, M. Hunter, T. McClure, G. Dresselhaus, and Dresselhaus M.S. 2001. "Structural (n,m) Determination of Isolated Single-Wall Carbon Nanotubes." *Phys. Rev. Lett.* 86 (6): 1118–1121. https://doi.org/10.1103/PhysRevLett.86.1118.

Karr, C. Jr. 1975. *Infrared and Raman Spectroscopy of Lunar and Terrestrial Minerals.* Academic Press. https://doi.org/10.1016/C2013-0-10938-5.

Kataura, H., Y. Kumazawa, Y. Maniwa, I. Umezu, S. Suzuki, Y. Ohtsuka, and Y. Achiba. 1999. "Optical Properties of Single-Wall Carbon Nanotubes." *Synth. Met.* 103 (1–3): 2555–2558. https://doi.org/10.1016%2FS0379-6779%2898%2900278-1.

Khandasammy, S.R., A. Rzhevskii, and I.K. Lednev. 2019. "A Novel Two-Step Method for the Detection of Organic Gunshot Residue for Forensic Purposes: Fast Fluorescence Imaging Followed by Raman Microspectroscopic Identification." *Anal. Chem.* 91 (18): 11731–11737. https://doi.org/10.1021/acs.analchem.9b02306.

Kiefer, W., G. Gouadec, and P. Colomban, 2007. "Special Issue on the Raman Study of Nanomaterials." *J. Raman Spectrosc.* 38 (6): 597–796.

Kuzmin, A.N., A. Pliss, A. Rzhevskii, A. Lita, and M. Larion. 2018. "BCAbox Algorithm Expands Capabilities of Raman Microscope for Single Organelles Assessment." *Biosensors* 8 (4): 106. https://doi.org/10.3390/bios8040106.

Kuzmin, A.N., A. Pliss, and A.V. Kachynski. 2013. "Biomolecular component analysis of cultured cell nucleoli by Raman microspectrometry." *J. Raman Spectrosc.* 44 (2): 198–204. https://doi.org/10.1002/jrs.4173.

Lawson, S.C., and H. Kanda. 1993. "An annealing study of nickel point defects in high-pressure synthetic diamond." *J. Appl. Phys.* 73 (8): 3967–3973. https://doi.org/10.1063/1.352861.

Lee, C., H. Yan, L.E. Brus, T.F. Heinz, J. Hone, and S. Ryu. 2010. "Anomalous Lattice Vibrations of Single- and Few-Layer MoS2." *ACS Nano* 4 (5): 2695–2700. https://doi.org/10.1021/nn1003937.

Lohumi, S., M.S. Kim, J. Qin, and B-K. Cho. 2017. "Raman imaging from microscopy to macroscopy: Quality and safety control of biological materials." *Trends Anal. Chem.* 93: 183–198. https://doi.org/10.1016/j.trac.2017.06.002.

Lopez-Lopez, M., J.J. Delgado, and C. Garcıa-Ruiz. 2013. "Analysis of macroscopic gunshot residues by Raman spectroscopy to assess the weapon memory effect." *Forensic Sci. Int.* 231 (1–3): 1–-. https://doi.org/10.1016/j.forsciint.2013.03.049.

Lopez-Lopez, M., M.A. Fernandez de la Ossa, and C. Garcıa-Ruiz. 2015. "Fast Analysis of Complete Macroscopic Gunshot Residues on Substrates Using Raman Imaging." *Appl. Spectrosc.* 69 (7): 889–893. https://doi.org/10.1366/14-07816.

Lorenz, B., C. Wichmann, S. Stöckel, P. Rösch, and J. Popp. 2017. "Cultivation-Free Raman Spectroscopic Investigations of Bacteria." *Trends Microbiol.* 25 (5): 413–424. https://doi.org/10.1016/j.tim.2017.01.002.

Loudin, L.C. 2017. "Photoluminescence Mapping of Optical Defects in HPHT Synthetic Diamond." *Gems Gemol.* 53 (2): 1–9. https://www.gia.edu/gems-gemology/summer-2017-photoluminescence-mapping-optical-defects.

Malard, L.M., M.A. Pimenta, G. Dresselhaus, and M.S. Dresselhaus. 2009. "Raman spectroscopy in graphene." *Phys. Rep.* 473: 51–87. https://doi.org/10.1016/j.physrep.2009.02.003.

Movasaghi, Z., S. Rehman, and I. Rehman. 2007. "Raman Spectroscopy of Biological Tissues." *Appl. Spectrosc. Rev.* 42 (5): 493–541.

Muro, C.K., K.C. Doty, J. Bueno, L. Halámková, and I.K. Lednev. 2015. "Vibrational Spectroscopy: Recent Developments to Revolutionize Forensic Science." *Anal. Chem.* 87: 306−327. https://doi.org/10.1021/ac504068a.

Netchacovitch, L., C. De Bleye, P.-F. Chavez, P.-Y. Sacré, P. Hubert, and E. Ziemons. 2014. "Raman hyperspectral imaging: a single tool to characterise pharmaceutical products." *Eur. Pharm. Rev.* 19 (5): 8–11.

O'Malley, J., R. Kumar, A.N. Kuzmin, A. Pliss, N. Yadav, S. Balachandar, J. Wang, K. Attwood, P.N. Prasad, and D. Chandra. 2017. "Lipid quantification by Raman microspectroscopy as a potential biomarker in prostate cancer." *Cancer Lett.* 397: 52–60. doi:10.1016/j.canlet.2017.03.025.

Opilik, L., T. Schmid, and R. Zenobi. 2013. "Modern Raman Imaging: Vibrational Spectroscopy on the Micrometer and Nanometer Scales."

Annu. Rev. Anal. Chem. 6: 379–398. https://doi.org/10.1146/annurev-anchem-062012-092646.

Palonpon, A.F., M. Sodeoka, and K. Fujita. 2013. "Molecular imaging of live cells by Raman microscopy." *Curr. Opin. Chem. Biol.* 17 (4): 708–715. doi:10.1016/j.cbpa.2013.05.021.

Pelletier, M. 1999. *Analytical Applications of Raman Spectroscopy.* Blackwell Science Ltd.

Rao, A. M., J. Chen, E. Richter, U. Schlecht, P. C. Eklund, R. C. Haddon, U. D. Venkateswaran, Y.-K. Kwon, and D. Tomanek. 2001. "Effect of van der Waals Interactions on the Raman Modes in Single Walled Carbon Nanotubes." *Phys. Rev. Lett.* 86 (17): 3895–3898. https://doi.org/10.1103/PhysRevLett.86.3895.

Rao, A.M., E. Richter, S. Bandow, B. Chase, P.C. Eklund, K.A. Williams, S. Fang, et al. 1997. "Diameter-Selective Raman Scattering from Vibrational Modes in Carbon Nanotubes." *Science* 275: 187–191.

Rau, J.V., V. Graziani, M. Fosca, C. Taffon, and M. Rocchia. 2016. "RAMAN spectroscopy imaging improves the diagnosis of papillary thyroid carcinoma." *Sci. Rep.* 6: 1-10.
https://doi.org/10.1038/srep35117.

n.d. *RRUFF.* Accessed August 5, 2020. www.rruff.info.

Rzhevskii, A. 2019. "The Recent Advances in Raman Microscopy and Imaging Techniques for Biosensors." *Biosensors* 9 (1): 25. https://doi.org/10.3390/bios9010025.

Sikirzhytski, V., K. Virkler, and I.K. Lednev. 2010. "Discriminant Analysis of Raman Spectra for Body Fluid Identification for Forensic Purposes." *Sensors* 10 (4): 2869–2884. https://doi.org/10.3390/s100402869.

Stewart, S., R.J. Priore, and M.P. Nelson. 2012. "Raman Imaging." *Annu. Rev. Anal. Chem.* 5: 337–360.

Toporski, J., T. Dieing, and O. Hollricher. 2018. *Confocal Raman Microscopy, 2nd Edition.* Edited by J. Toporski, T. Dieing and O. Hollricher. Springer. https://doi.org/101007/978-3-319-75380-5.

Tuinstra, F., and J.L. Koenig. 1970. "Raman Spectrum of Graphite." *J. Chem. Phys.* 53: 1126–1130. https://doi.org/10.1063/1.1674108.

Turrel, G., and J. Corset. 1996. *Raman Microscopy: Developments and Applications.* Elsevier Ltd.

Tuschel, D. 2015. "Resonance Raman and Photoluminescence Spectroscopy and Imaging of Few-Layer MoS2." *Spectroscopy* 30 (3): 14–29. https://www.spectroscopyonline.com/view/resonance-raman-and-photoluminescence-spectroscopy-and-imaging-few-layer-mos2.

Vergara, A., ed. 2021. "Raman Spectroscopy of Nanomaterials for Application in Photonics." *Nanomaterials.* https://www.mdpi.com/journal/nanomaterials/special_issues/raman_photonics.

Weng, S., W. Zhu, X. Zhang, H. Yuan, L. Zheng, J. Zhao, L. Huang, and P. Han. 2019. "Recent advances in Raman technology with applications in agriculture, food and biosystems: A review." *Artificial Intelligence in Agriculture* 3: 1-10. https://doi.org/10.1016/j.aiia.2019.11.001.

Zoubir, A. 2012. *Raman Imaging: Techniques and Applications.* Edited by A. Zoubir. Vol. 168. New York, Dordrecht, London: Springer. doi:10.1007/978-3-642-28252-2.

APPENDIX

SINGLE VIBRATION AND GROUP FREQUENCIES COMMONLY OBSERVED IN RAMAN SPECTRA

Raman shift, cm^{-1}	**Vibration/Functional group**
5–200	Lattice vibrations in crystals
240–360	ν (Se-Se)
250–400	δ (C-C) aliphatic chains
50–500	ν (Metal-O)
450–550	ν_s (Si-O-Si)
550	Cl_2 gaseous
400–580	ν (S-S)
480–660	ν (C-I)
500–700	ν (C-Br)
670–780	ν (C-S)
550–790	ν (C-Cl)
720–800	ν (C-F)
877	ν (O-O) in H_2O_2
845–900	ν (O-O)
915–945	ClO_3^-
930–950	ClO_4^{2-}
910–990	PO_4^{3-}
960–990	SO_3^{2-}

990–1010	Ring breathing C_6H_5- in mono- and meta-substituted benzenes
950–1040	SO_4^{2-}
1020–1060	Ring breathing C_6H_4- in ortho-disubstituted benzenes
1030–1045	HCO_3^-
1030–1070	NO_3^-
1050–1090	CO_3^-
1080–1100	ν (C-S) in substituted benzenes
1120–1150	ν (C-C)
1020–1230	ν (C=S)
1200–1230	Ring breathing C_6H_4- in para-disubstituted benzenes
1150–1250	$[(PO_3)_n]^{n-}$ metaphosphate
1170–1310	δ_r (CH_2), δ_t (CH_2) in n-alkenes
1320	NO_2 gaseous
1332	-C-C- in diamond
1320–1325	NO_2^-
1080–1360	ν (C-N)
1355–1395, 1430–1470	δ (CH_3)
1285, 1388	CO_2 gaseous, Fermi dyad
1400–1470	δ (CH_2)
1556	O_2 gaseous
1585–1625	ν (C=C) conjugated
1595	δ (H_2O) gaseous
~1640	δ (H_2O) liquid
1580–1610	-C-C- aromatic ring chains

1590–1650	δ (NH_2) in primary amines
1610–1680	ν (C=N)
1620–1680	ν (C=C) nonconjugated
1650–1750	ν (C=O)
2090–2110	ν (Si-H)
2143	CO gaseous
2030–2160	SCN^-
2100–2160	ν (C≡C) in alkyl acetylenes
1990–2200	ν_{as} (N=S=C)
2070–2210	CN^-
2230–2250	ν (C≡N)
2230–2300	ν (C≡C) in dialkyl acetylenes
2329	N_2 gaseous
2200–2500	ν (P-H)
2560–2590	ν (S-H)
2850–2860	ν_s (CH_2) in n-alkenes
2880–2885	ν_{as} (CH_3) in n-alkenes
2910–2930	ν_s (CH_2) in n-alkenes
2965–2970	ν_{as} (CH_3) in n-alkenes
2840–3100	ν (C-H) in n-alkenes
3000–3100	ν (C-H) in benzene derivatives
3270–3330	ν (≡C-H)
3334	NH_3 gaseous
3300–3500	ν (N-H)
3100–3650	ν (O-H) in liquid, H-bonded
3650–3750	ν (O-H) in solid hydroxides, “free”
4156	H_2 gaseous